

SAND76-0347

Unlimited Release

[REDACTED]

[REDACTED]

The Helios Model for the Optical Behavior of Reflecting Solar Concentrators

Frank Biggs, Charles N. Vittitoe

Prepared by Sandia Laboratories, Albuquerque, New Mexico 87185
and Livermore, California 94550 for the United States Department
of Energy under Contract DE-AC04-76DP00769

Printed March 1979



Sandia Laboratories
energy report

*When printing a copy of any digitized SAND
Report, you are required to update the
markings to current standards.*

Issued by Sandia Laboratories, operated for the United States
Department of Energy by Sandia Corporation.

NOTICE

This report was prepared as an account of work sponsored by the United States Government. Neither the United States nor the Department of Energy, nor any of their employees, nor any of their contractors, subcontractors, or their employees, makes any warranty, express or implied, or assumes any legal liability or responsibility for the accuracy, completeness or usefulness of any information, apparatus, product or process disclosed, or represents that its use would not infringe privately owned rights.

Printed in the United States of America

Available from
National Technical Information Service
U. S. Department of Commerce
5285 Port Royal Road
Springfield, VA 22161
Price: Printed Copy \$9.50 ; Microfiche \$3.00

SAND76-0347
Unlimited Release
Printed March 1979

THE HELIOS MODEL FOR THE OPTICAL BEHAVIOR
OF REFLECTING SOLAR CONCENTRATORS*

Frank Biggs
Charles N. Vittitoe
Theoretical Division 4231
Sandia Laboratories
Albuquerque, NM 87185

ABSTRACT

The Helios model simulates the optical behavior of reflecting concentrators. The model follows the incident solar radiation through the system (including the atmosphere) and includes all the factors that influence the optical performance of a collector. An important output is the flux-density pattern (W/cm^2) at a grid of points on a surface such as the absorbing surface of a receiver and its integral (power in watts) over the surface. The angular distribution of sunrays for the radiation incident on a concentrator is modified by convolution, using the fast Fourier transform, to incorporate the effects of other nondeterministic factors such as sun-tracking errors, surface slope errors, and reflectance properties. The analytical methods used for the statistics, the off-axis reflecting optics, the atmospheric effects, and the various coordinate systems are described and illustrated. This model forms a basis for the simulation code HELIOS as well as for other codes under development. Some of the HELIOS routines are described, a few of its capabilities are discussed and illustrated, and comparisons of data with calculations are presented. These capabilities have been used for performance predictions, safety studies, design trade-offs, data analysis problems, the specification and analysis of concentrator quality, and for the general understanding of solar-concentrator technology.

*This work supported by the U. S. Department of Energy.

ACKNOWLEDGMENTS

The quality of the information presented in this document benefited greatly from the cooperative efforts of others. We would like to thank the following Sandia employees: R. B. Pettit, L. K. Matthews, D. J. Kuehl, J. T. Holmes, D. E. Arvizu, and E. A. Igel for many useful discussions; early encouragement was provided by J. V. Otts; more recent encouragement has been provided by B. W. Marshall and J. F. Banas; and J. H. Renken offered consistent support throughout the project. We are also grateful to J. B. Blackman of McDonnell Douglas Co., Fenando Delgado of INITEC, and George Mulholland of New Mexico Tech for several useful suggestions. Interactions with other users of the code HELIOS have been beneficial; especially noteworthy among these is Barbara Levi of Georgia Tech, T. Oliver and W. Hart of Martin Marietta, and S. B. Davis of Sanders Associates. This report was influenced by the publications and helpful discussions of G. L. Schrenk of the University of Pennsylvania.

CONTENTS

	<u>Page</u>
CHAPTER 1 - INTRODUCTION	11
1.1 Modeling	11
1.2 Helios	12
1.3 Purpose, Organization, and Scope	12
Reference	15
CHAPTER 2 - MODEL DESCRIPTION - AN OVERVIEW	17
2.1 Sun Position	18
2.2 Heliostats	18
2.2.1 Heliostat Alignment	18
2.2.2 Prealignment of Facets	18
2.2.3 Facet Focus	19
2.3 Atmosphere	19
2.4 Shadowing and Blocking	20
2.4.1 Shadowing	20
2.4.2 Blocking	20
2.5 Statistics of Reflecting Optics	21
2.5.1 Sunshape	21
2.5.2 Error Cone	21
2.5.3 Effective Sunshape	22
2.5.4 Summary of Reflecting-Concentrator Statistics	22
CHAPTER 3 - HELIOS COORDINATE SYSTEMS	25
3.1 Celestial Coordinates	25
3.1.1 The Solar Declination	25
3.1.2 Elevation and Azimuthal Angles for the Sun	29

CONTENTS (cont)

	<u>Page</u>
3.2 Tower Coordinates	32
3.2.1 Heliostat Geometry	32
3.2.2 Elevation and Azimuthal Angles for the Aim Point and Heliostat	36
3.3 Heliostat Coordinates	39
3.3.1 The Origin	39
3.3.2 Facet Placement and Orientation	40
3.3.3 Heliostat Alignment	42
3.4 The Sun-Concentrator Coordinates	43
3.4.1 Axes	43
3.4.2 Target Points	44
3.4.3 Facet Orientation	45
3.5 Target Coordinates	46
3.5.1 Target Mesh	46
3.5.2 Planar Target Surface	47
3.5.3 Spherical Target Surface	47
3.5.4 Cylindrical Target Surface	48
3.6 Shadowing and Blocking Coordinates	48
 CHAPTER 4 - OPTICS OF REFLECTING CONCENTRATORS	 51
4.1 Specular Reflection of a Light Ray From a Surface Element	51
4.2 Specular Reflection of a Beam of Light From a Surface Element	53
4.3 Spherical or Paraboloidal Concentrators	54
4.3.1 The Tangential-Ray Fan	58
4.3.2 The Sagittal-Ray Fan	60
4.3.3 Focusing by an Astigmatic System	62
4.3.4 Focal Length Versus Slant Range	62
4.3.5 Astigmatic Image Size	64
References	65

CONTENTS (cont)

	<u>Page</u>
CHAPTER 5 - STATISTICS OF REFLECTING OPTICS	67
5.1 The Optical Quality of a Reflecting Concentrator	67
5.2 Two-Dimensional Distributions	69
5.2.1 Reference Planes	69
5.2.2 The Pillbox Distribution	70
5.2.3 The Elliptic-Normal Distribution	71
5.2.4 The Circular-Normal Distribution	73
5.2.5 The Sunshape	74
5.2.6 The General Two-Dimensional Distribution	76
5.3 Convolution of Two-Dimensional Distributions	77
5.3.1 Convolution of Circular-Symmetric Distributions	78
5.3.2 Convolution of Elliptic-Normal Distributions	78
5.3.3 Convolution of Circular-Normal Distributions	81
5.3.4 A Heliostat-Specification Example	82
5.3.5 Numerical Convolution of Two-Dimensional Distributions ..	83
5.3.6 The Central-Limit Theorem	85
5.4 Mapping of Distributions	93
5.4.1 Mapping From a Concentrator Reference Plane to a Reflected-Ray Reference Plane	93
5.4.2 Mapping Elliptic-Normal Distributions From a Concentrator Reference Plane to a Reflected- Ray Reference Plane	96
5.4.3 Mapping Sun-Tracking Errors to a Concentrator Reference Plane	101
5.5 Projecting the Effective Sunshape on the Receiver	104
References	107

CONTENTS (cont)

	<u>Page</u>
CHAPTER 6 - SOLAR IRRADIATION	109
6.1 Atmospheric Parameters	109
6.1.1 The Refraction Model	109
6.1.2 The Relative Optical Airmass Model	110
6.2 Solar Insolation	110
6.2.1 Extraterrestrial Irradiation, the Solar Constant	112
6.2.2 Earth-Orbit Effects Upon Insolation	112
6.2.3 Models of Atmospheric Loss	113
6.2.4 Other Effects on Insolation	117
6.3 Mirror-Receiver Propagation Loss	117
6.3.1 Methods of Calculating Propagation Loss	117
6.3.2 Atmospheric Transmittance	118
6.3.3 Mirror-Receiver Loss Function for Barstow, CA	119
6.4 Sunshape Variation	122
6.4.1 Lawrence Berkeley Laboratory Data	122
6.4.2 Analytical Sunshapes	126
6.4.3 Sunshape Extremes	127
6.4.4 Idealized Cumulative Distribution Functions	127
6.4.5 Actual Cumulative Distribution Functions	133
6.4.6 Sensitivity of Collected Power to Sunshape Variation	137
References	139
CHAPTER 7 - NUMERICAL PROCEDURES	141
7.1 Integration Over the Target Grid	141
7.1.1 Flat Rectangular Target	141
7.1.2 Spherical Targets	147
7.1.3 Cylindrical Targets	147
7.1.4 Circular Target Grid on a Plane Surface	147

CONTENTS (cont)

	<u>Page</u>
7.2 Facet Integration	149
7.3 The Two-Dimensional Fast Fourier Transform	153
7.4 Blocking and Shadowing of Heliostats	156
7.4.1 The Projected Area	156
7.4.2 The Overlap Test	158
7.4.3 Shadowing	159
7.4.4 Blocking	161
7.4.5 Nearest Neighbors	164
References	167
 CHAPTER 8 - AUXILIARY CAPABILITIES	 169
8.1 Reconcentrators	169
8.1.1 Calculation Method Used in HELIOS	171
8.1.2 Four-Panel Reconcentrator	175
8.1.3 Receiver	176
8.1.4 Heliostats for Four-Panel Reconcentrator	178
8.1.5 Results for Heliostat 18 and the Four-Panel Reconcentrator	180
8.1.6 Results for Zones A and B	181
8.2 Plotting Capability	182
8.2.1 The PLO Plotting Package	182
8.2.2 Shadowing and Blocking Movies	182
8.3 NOS Routines	186
8.3.1 NOS Version of HELIOS	187
8.3.2 NOS Input	187
8.3.3 NOS Plotting	187
8.4 Shadowing and Blocking Within a Parabolic Dish	187
8.4.1 The Shadowing Effect	188
8.4.2 The Blocking Effect	190
8.4.3 Receiver Shadowing	191
References	191

CONTENTS (cont)

	<u>Page</u>
CHAPTER 9 - COMPARISONS OF DATA WITH HELIOS PREDICTIONS	193
9.1 Scale-Model Experiment for One Heliostat	194
9.2 A Single-Facet Experiment	194
9.3 A Single-Heliostat Experiment	198
9.4 Remaining Verification	199
References	200
APPENDIX A - GLOSSARY OF TERMS	201
APPENDIX B - THE COMPOSITION OF MEAN-SQUARE VALUES UNDER TWO-DIMENSIONAL CONVOLUTION	211
References	215
APPENDIX C - CONVOLUTION OF ELLIPTIC-NORMAL DISTRIBUTIONS	217
References	228

CHAPTER 1

INTRODUCTION

A vast amount of solar energy is intercepted by the earth each day. Approximately one kilowatt of sunlight irradiates a square meter of land at noon on a clear, dry day in New Mexico. Collection of this valuable energy from its diffuse state is a challenge to today's technology. This source can more than supply future needs of our society. However, the energy is not available at a given location on the earth's surface at night and varies with atmospheric conditions. Because so many factors affect the use we can make of the sun, we must optimize the design of solar collectors to make the best use of available solar energy at the least cost. True optimization requires a thorough understanding of solar systems. An analytical model is a valuable tool in accomplishing this goal.

Rough estimates of collection efficiencies, material costs, conversion efficiencies, etc, recently indicate that electricity from a solar-thermal power plant would cost more than electricity from an oil-fired plant. It is not so clear, however, that this will continue to be the case as oil shortages and world politics combine to drive up the price of crude oil faster than the general inflation rate.

It is important that we compare the cost of solar-thermal energy with the cost of energy from other sources. These relative costs depend on many factors: availability of materials, energy-use patterns, environmental problems, and even changing life styles as energy costs increase. Thus, solar-thermal energy is just one of many alternative sources. To predict the optimum use of these sources, even for a short time into the future, is an exceedingly complex problem. A program of carefully planned experiments combined with computer simulation would provide the knowledge needed to optimize the use of this energy source.

1.1 Modeling

One way to analyze the solar energy alternative is to include it in a model of the entire energy production and utilization system. Such an effective overall model with accurate input from all sources would provide enough information to analyze problems on the production and utilization of energy. A solar-thermal power station is sufficiently complex to benefit from a mathematical model which could be used to quickly analyze its performance. A more general energy utilization model could then use such data as input for further studies.

Computational models also serve other purposes. Such a model is a convenient aid in the design, construction, and operation of a complex solar collector system, such as a solar-thermal power plant. It simulates the behavior of the solar collector and can be used to answer questions on performance predictions, safety problems, and design trade-offs. It can also be used to analyze and interpret experimental data.

A simulation model and experimental work on solar collectors complement each other. Experimental results are used to authenticate the model, after which the model is used to extrapolate experimental results and to provide guidance in planning new measurements. A good simulation model enables the engineer to extract the maximum information from experiments. This is especially important when dealing with experimentation as expensive as a heliostat field of a solar power plant.

1.2 Helios

The Helios model mathematically simulates the solar flux density pattern from reflecting concentrators; the computer program HELIOS implements it. When we wish to refer specifically to the computer program, we will use capital letters (HELIOS). The name Helios is given to both the model and to the computer program because it is a simple name that is easy to pronounce; also it forms the first part of the word heliostat, which is an important subsystem of a central receiver solar power plant. From Greek religion, Helios is the sun god, represented as driving a four-horse chariot through the heavens.

During its development, Helios has been used extensively in analyzing the Central Receiver Test Facility (CRTF) at Sandia Laboratories in Albuquerque, New Mexico. The model has been used to answer questions on safety, to predict facility performance under various conditions of operation, and to provide guidance in identifying and solving design problems. Calculated and measured results are compared whenever feasible to help validate the model.

This model has been used on the design and analysis of solar concentrators, including not only heliostats, but also other concentrators such as the parabolic-dish concentrator. In the evaluation of concentrators it is sometimes convenient to measure the quality of the reflected beam in a convenient measurement geometry, use results from the model to unfold concentrator performance specifications from this data, then use the specifications as an input for simulating the use of the concentrator in other geometries.

1.3 Purpose, Organization, and Scope

The purpose of this report is to present the theory of the Helios model. This is not a user's guide for the program HELIOS; a separate document (Reference 1.1) is available for that purpose.

Since the computer program is still evolving to include new capabilities, to refine or streamline calculations, and to simplify its use, a new edition of the User's Guide is required from time to time. The third edition of it has already been published and other editions will likely follow. This report on the theory is less subject to change.

Although the User's Guide provides adequate information for using program HELIOS, it does not treat the underlying theory that is needed for a thorough understanding of the code. This report is especially useful for anyone interested in making changes in the program.

There are some topics that fall between the central purpose of the User's Guide and that of this document. Some of the "Auxiliary Capabilities" of Chapter 8 are in this category. As new topics of this nature occur, they either will be included in subsequent revisions of the User's Guide or will be discussed in separate reports.

Although this report is useful as a companion document to the HELIOS User's Guide, it is also a valuable reference for its own sake because of the careful treatment of the technology of solar concentrations. It is with this thought in mind that we have developed and illustrated the topics contained in this report.

We have organized this report into chapters for major topics with subheadings for different categories of information within these topics. Although there is no index, a complete Table of Contents is provided to guide the reader to an appropriate chapter or subsection of the document. Also, a Glossary of Terms is given in Appendix A for convenient reference to definitions that may have special meaning in this report.

The major sections of each chapter are numbered with the section number separated from the chapter number by a decimal. For example, Section 3.2 is the second section in Chapter 3. Subsections are numbered within each section by adding another number, again separated by a decimal; i. e., subsection 3.2.1 refers to the first subsection of Section 3.2. Figures and tables are numbered within each chapter and equations are numbered within each major section. A dash is used to separate the equation number from the subsection number (i. e., Eq. 3.2-1 refers to the first equation in Section 3.2). Sometimes the letters (a, b, c, etc.) are appended to the equation number to designate equations that are closely related or to designate members of a system of equations. We often refer to a system of equations by citing the equation number without the letters; for example, Eq. (4.3-10) refers to the system of equations from Eq. (4.3-10a) through (4.3-10e). References are provided at the end of each chapter.

Chapter 2 provides an overview of the Helios model as it applies to the concentrator system of a central-receiver power station. This was used as our overview example because it contains the relevant elements and we have had more experience with this solar collector than with others.

However, neither the Helios theory nor the HELIOS computer program is limited to this application. It has been applied to a growing list of other types of solar collectors.

There are many coordinate systems utilized in the Helios model. Calculations are often done in one coordinate system and then transferred to another coordinate system. This facilitates the development of the program in a modular form with separate subroutines for most major tasks so that changes and extensions can easily be made. Most of the coordinate systems are described in Chapter 3. There are a few other systems, such as the "reference planes" of Chapter 5 that are not included in Chapter 3. These are so uniquely associated with statistics that it is appropriate to define them in conjunction with their utilization in Chapter 5.

Chapter 4 reviews the basic theory of the optics of reflecting concentrators and puts it into a convenient form for use in the Helios model. Most optics texts emphasize on-axis (or nearly on-axis) optical systems for imaging purposes. In solar concentrators, off-axis systems are more the rule than the exception. Therefore, the off-axis effects are carefully developed and illustrated.

The statistics of reflecting optics play a central role in the Helios model. These concepts are also very useful in providing a basis for understanding the effects of nondeterministic factors, such as sun-tracking errors and reflecting-surface slope errors on the performance of solar concentrators. The measurement of the quality of a concentrator and methods for writing specifications, acceptance criteria, etc., also involve these concepts. This material is developed in Chapter 5.

Atmospheric effects impact the Helios model in several ways. The atmosphere absorbs sunlight both before and after its reflection from a concentrator. Refraction changes the apparent direction of the sun. The sunshape is sensitive to atmospheric changes. These topics are treated in Chapter 6.

Chapter 7 describes the numerical procedures used in some of the HELIOS routines. This material will be especially useful to code users who wish to make changes or extensions in any of these routines.

Chapter 8 describes the "Auxiliary Capabilities" developed for the HELIOS program so far. Some of these serve as convenient illustrations of the flexibility of the program.

In Chapter 9 we describe some of the important comparisons of data with HELIOS predictions that have been done to date.

Appendix A contains a Glossary of Terms which provides a convenient reference for special terms used in this report and is also a useful terminology reference for solar concentrator technology. The other two appendices contain derivations that were too lengthy to put in the body of the report.

Finally, we reemphasize that the Table of Contents has been carefully organized for convenience in locating a particular topic of interest. This enhances the usefulness of this document as a reference on both the Helios model and on the corresponding computer program.

Reference

- 1.1 C. N. Vittitoe, F. Biggs, and R. E. Lighthill, HELIOS: A Computer Program for Modeling the Solar-Thermal Test Facility, A User's Guide, SAND76-0346, Third Edition, Sandia Laboratories, Albuquerque, NM, October 1978.

CHAPTER 2

MODEL DESCRIPTION - AN OVERVIEW

In this chapter we describe the Helios model of a concentrator system as it applies to a central receiver, organizing the discussion in roughly the order that a photon from the sun traverses the system. Detailed developments of some parts of the model are contained in separate chapters; some of these are referenced within this chapter. The table of contents is specifically constructed to be a useful aid in locating topics of interest.

Figure 2-1 shows a schematic drawing of a central-receiver solar-collector system emphasizing the important elements. Three heliostats are shown on a small hill to illustrate that the ground may not be level. There are, of course, more than three heliostats in the usual concentrator field but these will be adequate to illustrate some of the main ideas of the model including shadowing and blocking.

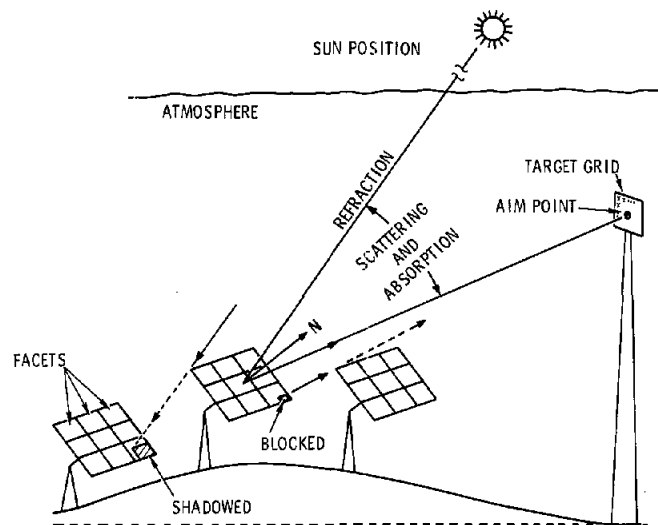


Figure 2-1. Geometry of a Central-Receiver Solar-Collection System

From the time a photon leaves the sun until it reaches the receiver of a solar collector, it is subjected to many effects. Helios is designed to simulate these effects and to determine their consequences on the operation of the system.

First we define the system through a few special terms, then redefine it by describing the important effects. We follow with a brief discussion of how Helios treats them. The "central ray"

from the sun originates from the center of the solar disk. The "sun position" is the direction (azimuth and elevation) of the incoming central ray. Each heliostat consists of one or more reflecting surfaces called "facets." Figure 2-1 shows nine square facets on each heliostat for convenience in drawing. Each heliostat is guided so that a central ray from the sun will reflect from the center of its "reference facet" (center facet) to intercept the "aim point." The distance from the center of a heliostat to the target center is called the "slant range" for that heliostat; the path followed by a central reflected ray is called the "slant path." The individual facets also have slant-ranges which may differ slightly from the corresponding heliostat slant-range. The "target grid" is a grid of points at which HELIOS calculates the incident flux density in watts/cm² and integrates over the target to give the intercepted solar power in watts.

The placement of the aim point and the target grid are arbitrary. Different aim points may be used for different heliostats. The target grid need not contain the aim point within its boundary; for example, it may be positioned off to the side for use in "spillage" calculations. Spillage is defined as solar power that is reflected from the concentrator system but misses the receiver aperture. This feature has been used extensively for safety calculations.

2.1 Sun Position

The geometry of the sun-earth portion of the solar system is used to calculate the direction of the central ray from the sun at any time of the year. This information is needed for heliostat alignment calculations, facet prealignment strategies, and atmospheric transmission effects. A detailed development is given in Chapter 3.

2.2 Heliostats

2.2.1 Heliostat Alignment

The direction of the incoming central ray from the sun and the heliostat-receiver geometry provide information from which the heliostat alignment is calculated. Since the heliostat rotates about two tracking axes that for some systems displace the center of the heliostat, it is necessary to iterate this calculation so the final center position of the aligned heliostat correctly defines the geometry. This is not an undue numerical complication because these heliostat motions are small compared to the corresponding slant ranges and convergence is rapid.

2.2.2 Prealignment of Facets

It is necessary to prealign each facet of a heliostat with respect to the heliostat frame. This provides a focusing capability for the heliostat. One option is to prealign the facets so that a ray from the sun would reflect from the center of each facet to the aim point on the receiver

whenever the heliostat is properly aligned on the aim point. As the sun position changes, the sun-tracking system keeps the reference facet correctly aligned, but the reflected central rays from the other facets do not continue to intersect the aim point. Astigmatic aberrations cause them to spread out about it.

Several options are available for specifying the prealignment geometry for the facets. In one option, the sun position is specified in terms of a date and time from which HELIOS calculates a sun position and, together with the tower-heliostat geometry, then calculates facet prealignment settings. These settings are stored and used in subsequent calculations. Another option causes the facets to be prealigned "on axis." In this geometry each facet center would be tangent to a spherical surface which corresponds to a focal length equal to the heliostat slant range to the prealignment point.

The actual facet prealignments will probably be made in some geometry different from that of the intended use and then related to the geometry of the specified option by computer calculations.

In the Helios model the facet prealignments are exactly calculated according to the option specified. The nondeterministic measurement errors resulting from implementing this alignment option are accounted for statistically in Helios by including them in the facet-alignment error distribution.

2.2.3 Facet Focus

In some cases it is desirable to change the surface shape of an individual facet to improve its ability to concentrate the reflected sunlight on the receiver. The facets are focused to maximize the concentration of reflected light on the receiver under the geometry corresponding to the specified prealignment option. For spherical surfaces this is a matter of specifying the radius of curvature. The facet surface shape may be more complicated, however, and controlled by some parameter such as the distance that the facet center is pulled down relative to the reference plane of the undeflected flat facet. The facet shape and its focusing properties then depend on this pull-down distance. For such a facet it is necessary to use an iterative procedure to calculate the optimum value of the pull-down distance. A similar method can be used when the facet shape is controlled by more than one parameter as long as a computer algorithm can be constructed to determine the shape of the surface as a function of these parameters.

2.3 Atmosphere

The solar insolation at a collector site is strongly affected by atmospheric attenuation. The length of the air path changes with the sun position because of the time-dependent angle at which the sun rays encounter the atmosphere. Also, the attenuation properties of the atmosphere change

with weather conditions (moisture content, haze, etc.). A model of the atmosphere that provides the solar insolation at any position on the earth, for any sun position, and for a variety of atmospheric conditions is useful. This permits the use of the model to predict behavior at any geographical location and to analyze time-of-day variations and weather effects on the design and operation of a solar-power facility.

Measured values of the insolation can also be used. These can be used directly as input or may be used for normalization purposes in one of the atmospheric models.

The Helios model also includes effects of atmospheric attenuation along the slant paths between the heliostats and the target grid. This becomes an important effect for large central receivers where the slant ranges can become large (approximately a kilometer).

2.4 Shadowing and Blocking

2.4.1 Shadowing

In a concentrator field some of the heliostats may interfere with others by partially "shadowing" them from incoming sunlight as indicated in Figure 2-1. This effect is likely to become especially severe when the sun position is low in the sky. The tower or other objects may also shadow part of the concentrator field. In HELIOS the effect of shadowing is calculated by projecting the outlines of the aligned heliostats, the tower, and anything else that casts a shadow onto a plane perpendicular to the central ray from the sun. Shadowed portions of any heliostat will appear in overlapped regions of this projection. A graphic presentation of shadowing as well as a numerical calculation of its effect on heliostat performance is provided by HELIOS.

2.4.2 Blocking

A light ray reflected from one heliostat may be "blocked" by another heliostat or by some other object to prevent it from reaching the target grid. The effects of blocking are calculated by projecting the outlines of the aligned heliostats and any other obstacles that might block reflected light onto a unit sphere centered about the aim point. Blocked portions of any heliostat will appear in overlapped regions on this projection. This projection provides a pictorial representation of the effects of blocking. The effect is also quantified numerically in HELIOS.

An auxiliary program is available in HELIOS to make a movie of the shadowing and blocking projections. This capability will be described in more detail in Chapter 8.

2.5 Statistics of Reflecting Optics

Concentrator optics would be simpler to describe if collimated light were used to irradiate them and if the error tolerances of all system components were small enough to be neglected. Neither of these conditions exists; sunlight is not well collimated and a concentrator system with negligible error tolerances would not be cost effective for most solar-collector applications. It is, therefore, necessary to use statistical methods to analyze the concentrator system. In this section we define terms and give an overview of some important concepts in the statistical analysis of errors for solar reflectors.

2.5.1 Sunshape

A random photon from the sun is drawn from a distribution of directions depending upon where it originated on the sun. The probability density function describing this distribution with respect to the direction of the central ray from the sun is called "sunshape." This directional distribution is widened by atmospheric scattering (aureole scattering), especially during hazy atmospheric conditions. Light clouds can cause considerable broadening of the sunshape. The sunshape plays a key role in defining the upper limit to the concentration level that can be obtained by a given concentrator.

2.5.2 Error Cone

When a light ray undergoes specular reflection from a concentrator surface, the angle of reflection is equal to the angle of incidence. These angles are measured with respect to the surface normal at the point of reflection. However, in solar-collector applications, the direction of the surface normal is not always exactly known. It is subject to errors for a variety of reasons. The surface normal at a given place on the facet may deviate from its design value because of manufacturing defects, focusing errors, wind loading, gravity loading, temperature effects, etc. A facet may also have alignment errors with respect to the heliostat frame. These errors arise from such things as measurement errors during the prealignment procedure or from wind loading of the heliostat. The entire heliostat is subject to alignment errors such as sun-tracking errors. There may be a nonspecular contribution to the reflected light that also contributes to the non-deterministic nature of the reflected light.

These effects are combined and interpreted in terms of their net effect on the uncertainty in direction of a reflected ray that corresponds to a known direction for an incoming ray. This produces a distribution of directions for the reflected ray even though the incoming-ray direction is specified. The probability density function that describes this distribution of reflected rays is called the "error cone."

2.5.3 Effective Sunshape

Since the error cone of reflected rays corresponds to an incoming ray of specified direction, it is necessary to combine the error cone with the sunshape in order to obtain the resultant average distribution of reflected rays corresponding to incident sunlight. The probability density function describing this distribution of directions is called the "effective sunshape." It is obtained by convolving the sunshape with the error cone in a reflected-ray reference system as is described in detail in Chapter 5.

2.5.4 Summary of Reflecting-Concentrator Statistics

The methods used in Helios for handling the statistical analysis warrant some elaboration since statistics form a basis for so much of the model. In this section we provide a descriptive overview of the statistics; a detailed development is provided in Chapter 5. Since concepts utilizing both time averaging and space averaging occur in Helios, it is instructive to use some hypothetical examples to clarify these concepts.

Figure 2-2 depicts a light ray \hat{I} incident on a small plane surface element of surface normal \hat{N} and reflecting along \hat{R} . The three vectors lie in a plane and the angle of incidence μ is equal to the angle of reflection in agreement with the law of specular reflection.

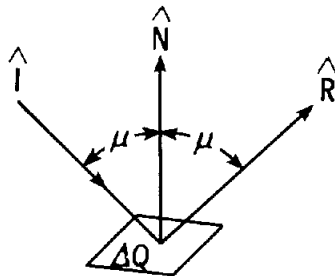


Figure 2-2. Specular Reflection From a Surface Element ΔQ

As a time-average example, suppose that the element ΔQ of Figure 2-2 flutters slightly in the wind so that the surface normal \hat{N} is time dependent. Assume that one photon per second is incident on ΔQ in the fixed direction \hat{I} and reflects to a distant receiver. After a sufficient interval of time, a flux pattern is formed on the receiver by the collected photons. For simplicity in this example we assume that the fluttering motion of ΔQ is a "stationary" (in time) stochastic process. By this we mean that once the flux pattern is established on the receiver, it does not thereafter change its shape. In principle, one could keep track of the time dependence of \hat{N} and calculate the position where each photon strikes the receiver; the integral of this result over time would give the flux pattern. However, in practice (if all you need is the flux pattern on the receiver) keeping track of the time dependence in order to calculate the photon position is neither necessary nor

feasible. To obtain a flux pattern, you need not know the order in which the photons strike the receiver. Therefore, we can relinquish the time-history information about \hat{N} and settle for a distribution function that specifies the fraction of time that \hat{N} spends in any solid-angle increment. This distribution can then be used to determine the time-average flux-pattern on the receiver. If the stochastic fluttering motion is not stationary in time, then the appropriate distribution becomes time dependent. Even a time dependent distribution function is a more convenient description than is a complete time history of the surface normal \hat{N} .

As a space-average example, suppose that a collimated beam of photons is incident on a concentrator that is properly shaped to focus them at a point on the receiver. Now suppose that the concentrator is deformed to produce a small random surface waviness so that the photons no longer come to a point but are spread out into a pattern around it. For simplicity in this example, we assume that the stochastic "slope-error" pattern (surface waviness) is stationary (in space). By this we mean that the shape of the flux patterns resulting from one (large) part of the concentrator is the same as that resulting from another (large) part of the concentrator. In principle one could map out the detailed shape of the concentrator surface and calculate the point of impact on the receiver for photons from each small increment of the concentrator. In practice this is not necessary if all one needs is the flux pattern on the receiver. It is not necessary to know from what part of the concentrator the photons were reflected. Therefore, we can relinquish the detailed slope error versus position information and settle for a distribution of slope errors. This distribution gives the fraction of the concentrator surface that has slope errors in any specified solid-angle increment and then can be used to obtain a flux pattern on the receiver that represents a space average over the concentrator surface. If the stochastic slope errors are not stationary in space, then the distribution function becomes a function of position on the concentrator surface. Such a space-dependent distribution function would still be a simpler description of the surface than would a detailed map.

The direction from which photons from the sun are incident on a concentrator surface is also a stochastic process because of the size of the solar disk. Even without the previously illustrated errors, the flux-pattern of reflected sunlight (solar image) on the receiver has a lower limit to its size. Rather than trying to keep track of where (or when) photons originated on the sun, a distribution (the sunshape) is used to describe them. When sunlight is reflected from concentrators with errors that are described by probability distributions, these distributions are combined with each other and with the sunshape by convolution to obtain the average resultant of the combined effects. The details of this process are given in Chapter 5.

Figure 2-3 is a useful aid in summarizing these statistical concepts. The surface normal of a concentrator element ΔQ that is free of errors would lie along \hat{N} and the incident central ray \hat{I} from the sun would reflect in direction \hat{R} for specular reflection. Also in this ideal error-free case, the sunshape (illustrated in the figure by the cone drawn about \hat{I}) would reflect unchanged in shape as indicated by the dashed cone about \hat{R} . When errors (time dependent or space

dependent) cause the alignment of \hat{N} to become nondeterministic, it is then described by a distribution of directions as shown by the cone drawn about \hat{N} . This cone of directions is mapped into its effect on reflection rays and convolved with the sunshape to obtain a distribution called the "effective sunshape" shown in Figure 2-3 by the solid cone about \hat{R} . The effective sunshape is projected onto the receiver to obtain the flux contribution from the concentrator element ΔQ .

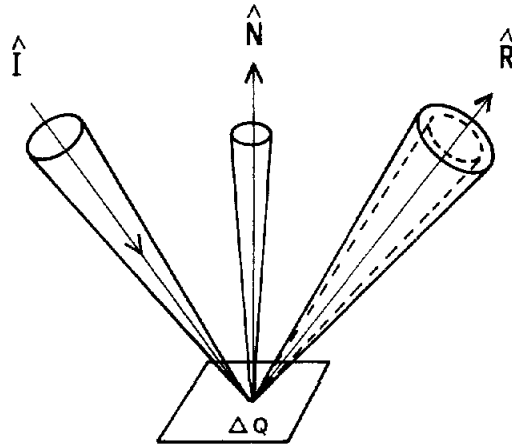


Figure 2-3. Statistics of Solar Reflectors

CHAPTER 3

HELIOS COORDINATE SYSTEMS

A series of coordinate systems are required to fulfill the needs of a concentrator system numerical model for a central receiver. The celestial sphere is used to specify the sun position for given day and time. The latitude of the heliostat array and tower is needed to calculate the elevation and azimuthal angles for the sun. The heliostat and tower bases are distributed in an N-S and E-W array on a nonuniform earth (the tower coordinate system). A rotation and translation then transform the coordinates of an arbitrary point to those in the heliostat coordinate system where the origin is the center of the mirror array with the x axis taken to be horizontal and the z axis taken to be normal to the facet at the heliostat center. The heliostat coordinate system is most convenient for specifying the center position of each facet with respect to the center of the facet array. An additional translation and a slight rotation transform to the sun-concentrator coordinate system where the origin is at an individual facet center, the z axis is normal to the facet center, and the central ray of the incident energy is in the y-z plane. This sun-concentrator system is most convenient for calculating the distribution of reflected energy. However, it is not convenient for observing the collected energy since there are 25 different systems for each heliostat in the CRTF array. The distribution of reflected energy is transformed to the target system before output. Additional coordinate systems are introduced to treat shadowing and blocking. This chapter introduces the coordinate systems involved and gives additional detail concerning their use.

3.1 Celestial Coordinates

3.1.1 The Solar Declination

Imagine a sphere of very large radius centered at the earth's center. The points where the earth's axis intersects the sphere are defined as the north and south celestial poles. The great circle defined by the intersection of the plane of the earth's equator with the sphere is the celestial equator. A star position may be specified by the intersection of the line joining the center of the earth to the star with the celestial sphere. If refraction of light is neglected, the altitude of the celestial pole which is above the horizon is equal to the latitude of the observer. The rotation of the earth gives the appearance of rotation (from east to west) of the celestial sphere as if it were a rigid body. The great circle joining the north and south points of the horizon which passes through the zenith is called the meridian of the observer. A star which is on the meridian of an observer in the northern hemisphere, between the zenith and the southern point on the horizon,

is at its greatest altitude at that moment. This crossing is called the meridian passage. As indicated in Figure 3-1, the prime meridian on the celestial sphere is the one passing through the vernal equinox.

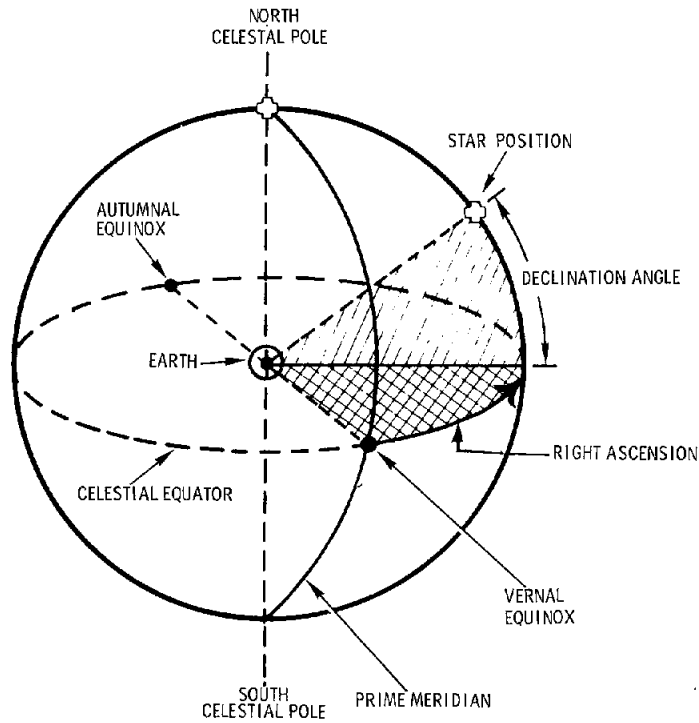


Figure 3-1. The Celestial Sphere

The position of a star on the celestial sphere is given by the coordinates declination and right ascension. The declination, δ , is defined as the angular distance of a point on the celestial sphere north of the celestial equator (points to the south have negative δ). The elevation angle of a star at its meridian passage is

$$\begin{aligned} \zeta_s &= 90^\circ - \varphi_\ell + \delta_1 & \delta_1 < \varphi_\ell, \\ \zeta_s &= 90^\circ + \varphi_\ell + \delta_2 & \delta_2 > \varphi_\ell, \end{aligned} \tag{3.1-1}$$

where φ_ℓ is the latitude of the observation point. As indicated in Figure 3-1, the right ascension is measured from the celestial meridian that passes through the vernal equinox, (i.e., one of the intersections of the celestial equator with the great circle marking the apparent path of the sun across the sky (the ecliptic) during a year). The vernal equinox occurs about March 21 each year (March 20 at 17 h 43 min in 1977). Before defining right ascension we introduce the concept of sidereal time and hour angle.

The time between successive meridian passings for a particular star is called a sidereal day. Each 15° of rotation of the earth in space then corresponds to 1 sidereal hour of time. With the definition that 1 (solar) h is $1/24$ th of a solar day, then a sidereal day is 23 h 56 min 3 s long. The difference between a sidereal day and a solar day occurs because of the earth's motion in its orbit.

The hour angle of a star on the meridian is defined as zero; its hour angle increases by 15° per sidereal hour. The hour angles are positive (negative) for stars to the west (east) of the meridian. Instead of a star, an observer can also determine the local hour angle for the vernal equinox at any moment. This is how the origin for local sidereal time is defined. Local sidereal time at any point and time is the local hour angle of the vernal equinox at that moment. If the observer is at Greenwich, for example, the hour angle he measures for the vernal equinox gives the Greenwich sidereal time.

The right ascension of a star is defined as the local sidereal time for meridian passage of the star. The right ascension runs eastward around the celestial equator from 0 at the vernal equinox to 24 sidereal h at the same point after completing the circle. A star with right ascension 3 sidereal h is 45° to the east of the vernal equinox. Sidereal time is so convenient for astronomers that they often have sidereal clocks to aid in locating specific stars of interest.

The coordinates of the sun are constantly changing. As measured in the ecliptic plane, the time variation of azimuthal angle of the sun is given as

$$\varphi_{se} \approx \frac{2\pi}{365 \text{ days}} (t - 80 \text{ days}) , \quad (3.1-2)$$

where the angle is measured from the sun's position on the 80th day of the year (i.e., March 21 barring leap year, near the vernal equinox). The t here is measured in solar days. The relative orientation of the ecliptic and the celestial equator are indicated in Figure 3-2.

The ecliptic plane intersects the celestial equator plane along the line connecting the vernal and autumnal equinoxes. The 1977 value of the angle between the planes is $\delta_o = 23^\circ.442274$. A perpendicular from the sun position to this intersection line has length $R_o \sin \varphi_{se}$ where R_o is the radius of the celestial sphere. The distance between the sun position and the plane of the celestial equator is $R_o \sin \delta_s$ where δ_s is the declination angle for the sun. The triangle thus formed in Figure 3-2 gives

$$\sin \delta_s = \sin \delta_o \sin \varphi_{se} , \quad (3.1-3)$$

as illustrated. The declination is plotted versus time in Figure 3.3.

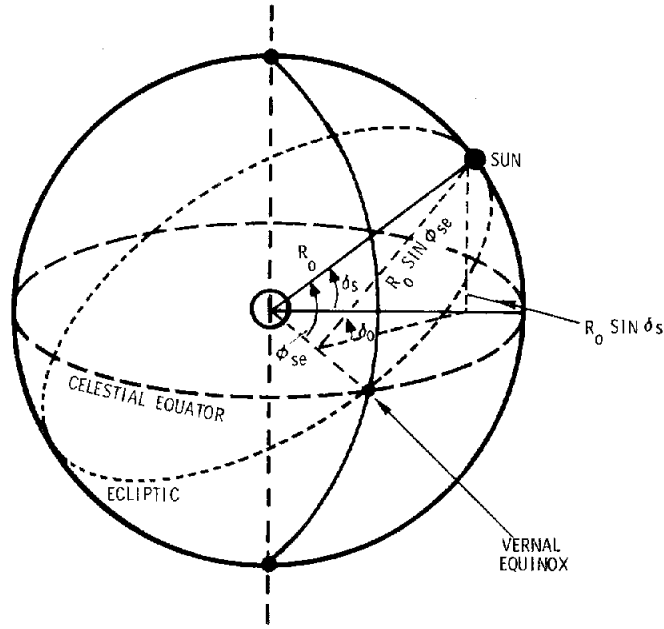


Figure 3-2. The Ecliptic Plane Intersecting the Celestial Sphere

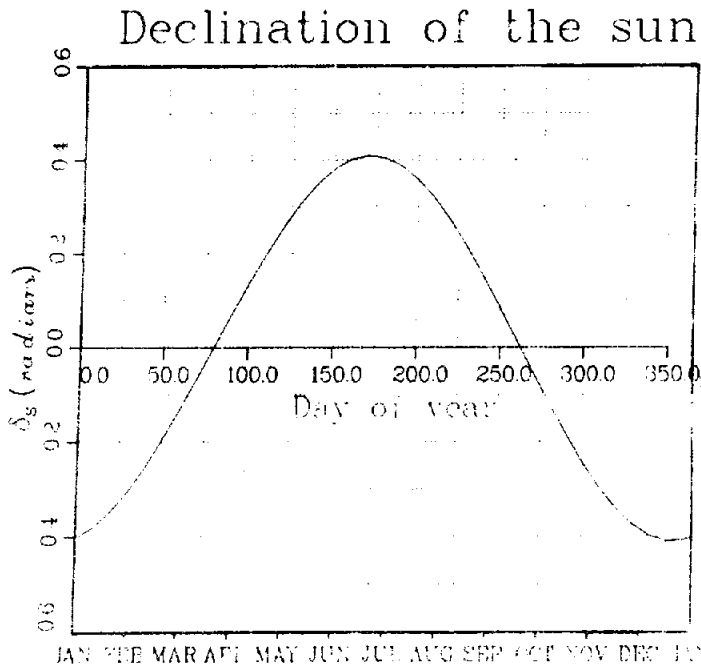


Figure 3-3. Declination of the Sun

The positions of the celestial poles, the celestial equator, the vernal equinox, and the mean obliquity (δ_0) of the ecliptic do change with time, but at extremely slow rates. Because of these changes, astronomers often refer right ascensions and declinations of stars to a given epoch, such as 1800, 1950, or perhaps 1977. The changes are mainly caused by precession of the earth's axis. The gravitational forces of the moon and sun interacting with the earth's bulge at its equator produce a torque that causes the axis to precess westward about the vertical with a complete revolution requiring 25 800 yr. In addition, the plane of the moon's orbit about the earth rotates with respect to the ecliptic with a period of 18.6 yr. This produces an additional oscillation (called nutation) in the earth's axis superimposed upon the precession. Our calendar has been designed to prevent these effects from altering the months that correspond to specific seasons. Leap years help somewhat. Fine tuning is accomplished by abandoning leap year every century year not divisible by 400. The present calendar develops an error of about a day each 3400 yr.

3.1.2 Elevation and Azimuthal Angles for the Sun

The right ascension of the sun continually increases, changing about 1° per day to traverse the ecliptic each year. The hour angle of the sun increases with time as,

$$H_s = \frac{15^\circ}{h} t \quad (3.1-4)$$

where t is the local solar time in hours measured from local noon. As indicated in Figure 3-4, the dot product of \hat{e}_r and a unit vector directed toward the sun gives

$$\cos z = \sin \phi_l \sin \delta_s + \cos \phi_l \cos \delta_s \cos H_s, \quad (3.1-5)$$

where ϕ_l is the observer latitude.

The elevation angle is

$$\zeta_s = \frac{\pi}{2} - z. \quad (3.1-6)$$

The $\cos H_s$ term causes rapid variation in the elevation angle. Under average atmospheric refraction the solar edge will appear on the horizon when the true elevation angle of the sun is about 0.0145 radians (50') below the horizon. The entire sun subtends an angle of about 0.0093 radians (32') when viewed from the earth. Atmospheric refraction accounts for the additional 9.89 mrad (34') leading to early sunrise. Daylight corresponds to $\zeta_s \geq -14.5$ mrad.

Consider in Figure 3-4 the coordinate system where \hat{j}_1 is the vertical direction at local noon on the equator, and \hat{k}_1 is directed along the earth's axis. At the observation point labeled 0, unit vectors to the north, east, and upward are given by

$$\hat{e}_N = -\hat{i}_1 \cos \theta_\ell \cos \varphi_1 - \hat{j}_1 \cos \theta_\ell \sin \varphi_1 + \hat{k}_1 \sin \theta_\ell ,$$

$$\hat{e}_E = -\hat{i}_1 \sin \varphi_1 + \hat{j}_1 \cos \varphi_1 , \quad (3.1-7)$$

$$\hat{e}_u = \hat{i}_1 \sin \theta_\ell \cos \varphi_1 + \hat{j}_1 \sin \theta_\ell \sin \varphi_1 + \hat{k}_1 \cos \theta_\ell ,$$

where

$$\theta_\ell = \pi/2 - \varphi_\ell , \quad (3.1-8)$$

and

$$\varphi_1 = \pi/2 - H_s . \quad (3.1-9)$$

A unit vector directed toward the sun is

$$\hat{e}_s = \hat{j}_1 \cos \delta_s + \hat{k}_1 \sin \delta_s . \quad (3.1-10)$$

The projections of \hat{e}_s to the north and east are

$$\hat{e}_s \cdot \hat{e}_N = -\cos \delta_s \cos \theta_\ell \sin \varphi_1 + \sin \delta_s \sin \theta_\ell$$

$$\hat{e}_s \cdot \hat{e}_E = \cos \varphi_1 \cos \delta_s \quad (3.1-11)$$

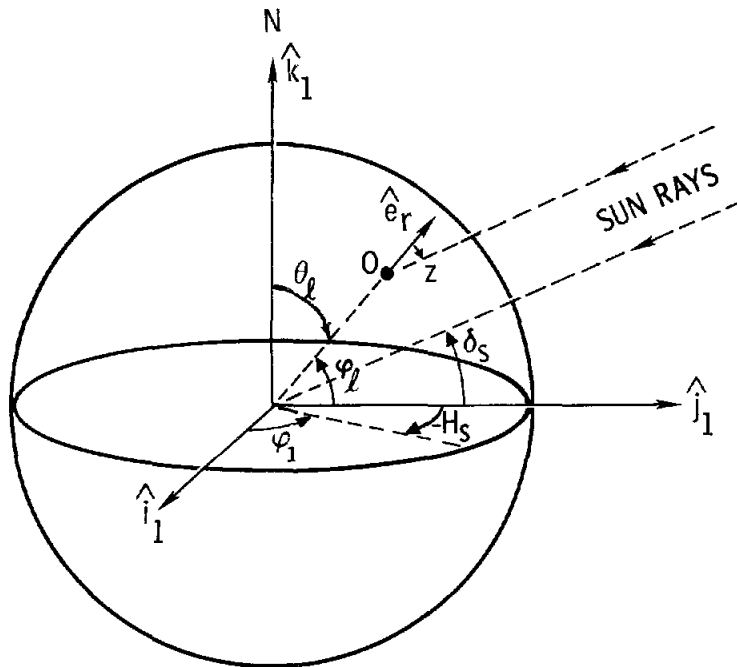


Figure 3-4. Zenith Angle (z) and Hour Angle (H_s) for the Sun

The azimuthal angle for the sun as measured from the east toward the north in the horizontal plane is then given by

$$\varphi_s = \tan^{-1} \left[\frac{\hat{e}_s \cdot \hat{e}_N}{\hat{e}_s \cdot \hat{e}_E} \right], \quad (3.1-12)$$

or

$$\varphi_s = \tan^{-1} \frac{\sin \delta_s \cos \varphi_l - \cos \delta_s \sin \varphi_l \cos H_s}{-\cos \delta_s \sin H_s}. \quad (3.1-13)$$

The cosine may be written in the simpler form

$$\cos \varphi_s = - \frac{\sin H_s \cos \delta_s}{\cos \zeta_s}, \quad (3.1-14)$$

however, computer evaluation from the \tan^{-1} function has the advantage of removing quadrant ambiguities. The ζ and φ_s variations are indicated in Figures 3-5 and 3-6.

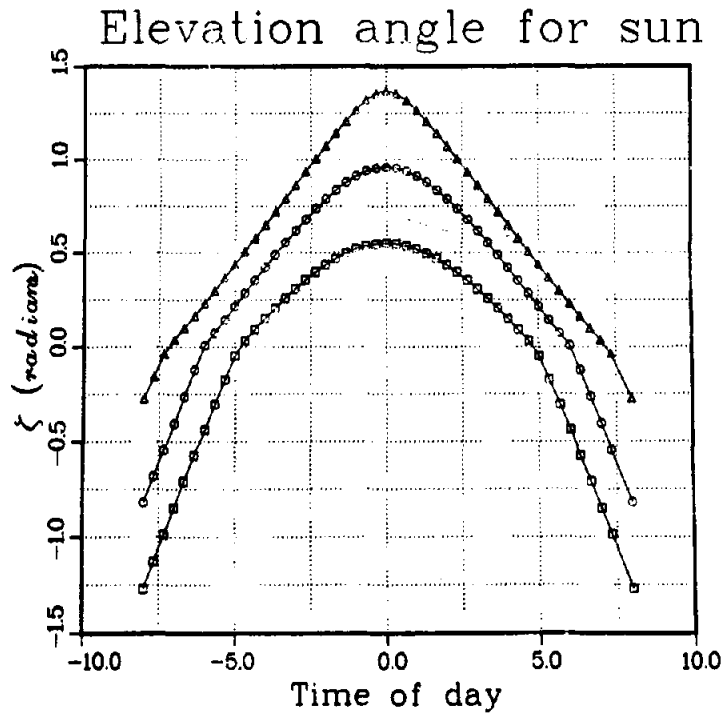


Figure 3-5. The Elevation Angle of the Sun as Seen From Albuquerque, NM on June 21 (Δ), March 21 (\circ), and December 21 (\square). Time is in hours from local noon.

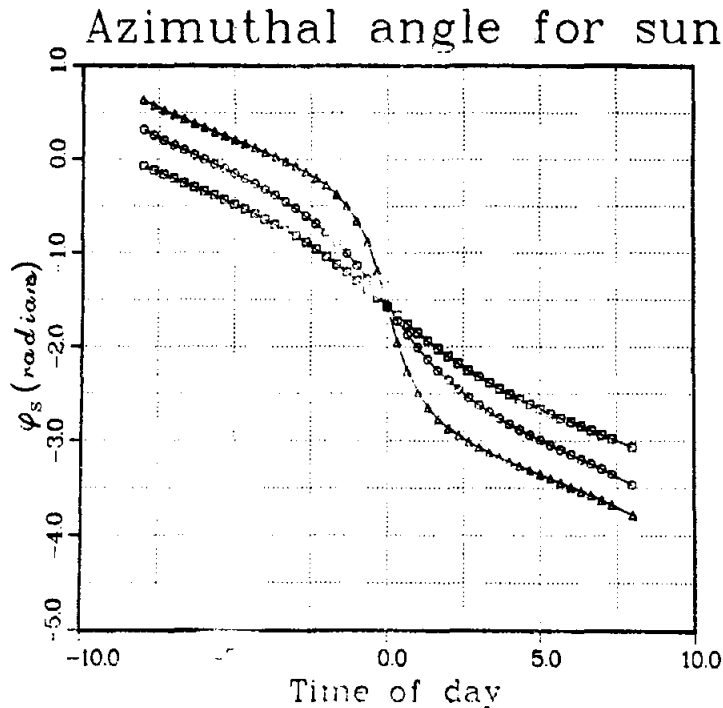


Figure 3-6. The Azimuthal Angle of the Sun as Seen From Albuquerque, NM on June 21 (Δ), March 21 (o), and December 21 (\square). Time is in hours from local noon.

3.2 Tower Coordinates

3.2.1 Heliostat Geometry

In Figure 3-4 let us assume the position O is at the center of the tower base. With this origin we construct an x-y-z Cartesian coordinate system with the axes in the east, true north, and vertical directions. This is the tower coordinate system. The positions of the center for each heliostat base (E_i, N_i, Z_i) are specified in this system as illustrated in Figure 3-7. The top of the tower is specified by $(0, 0, Z_t)$. The Z coordinates should be adjusted to account for the slope of the land. They may also account for the curvature of the earth's surface.

The center of the reflecting surface is given the coordinates (x_1, y_1, z_1) in the same coordinate system. The transformation from (E_1, N_1, Z_1) to (x_1, y_1, z_1) will be dependent upon the method of mounting the heliostat upon the base as well as upon the orientation of the heliostat. With the mounting illustrated in Figure 3-8 we have

$$x_1 = E_1 + l_1 \cos \zeta \cos \varphi ,$$

$$y_1 = N_1 + l_1 \cos \zeta \sin \varphi , \tag{3.2-1}$$

$$z_1 = Z_1 + l_2 + l_1 \sin \zeta ,$$

where the azimuthal angle φ is the angle between the E axis and the projection of l_1 onto the horizontal plane. Azimuthal angles are measured from the east; positive toward the north. The elevation angle of the heliostat is labeled ζ . Figures 3-9 and 3-10 give an actual design of the mirror assembly. This design gives the values $l_1 = 0.318$ m and $l_2 = 3.987$ m. The l_2 is measured between the leveling plate and the center of the tube-support interface in Figure 3-10.

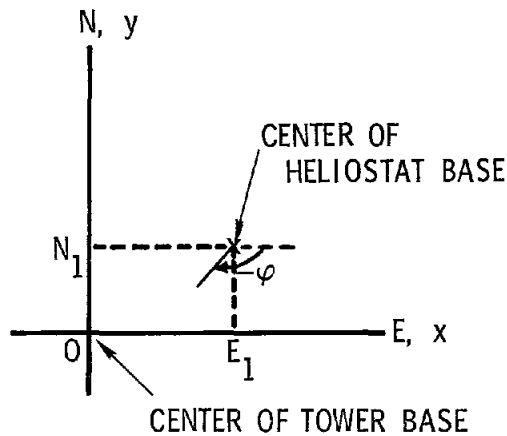


Figure 3-7. Heliostat Deployment in Tower Coordinate System

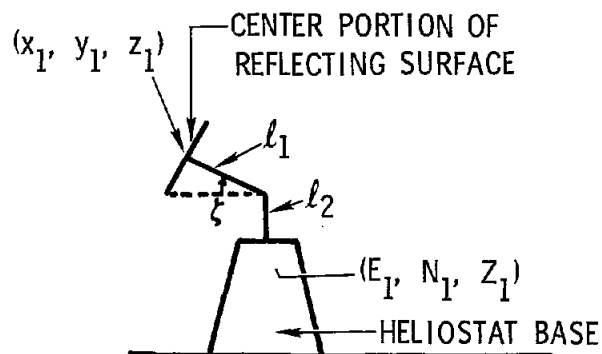


Figure 3-8. Sample Heliostat Mounting

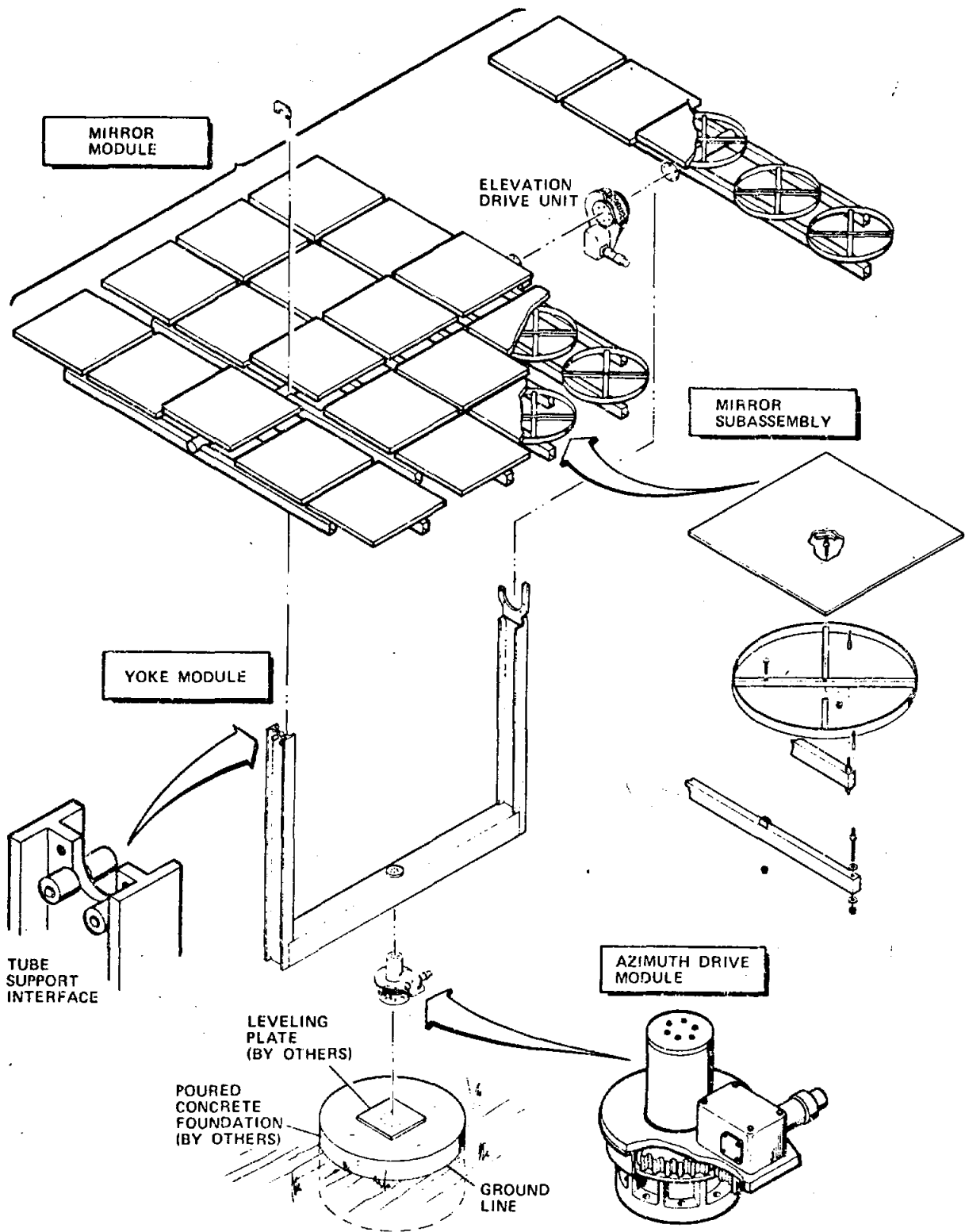


Figure 3-9. Martin-Marietta Heliostat Design for Solar-Thermal Test Facility

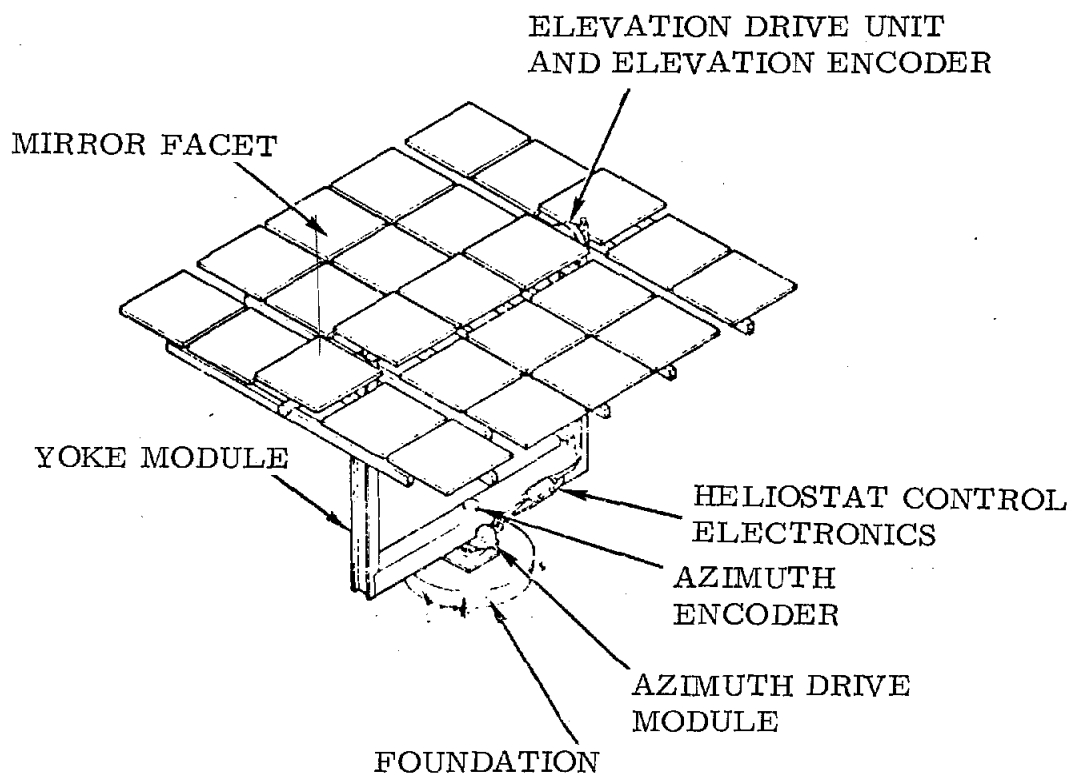


Figure 3-10. Martin-Marietta Heliostat Design for Solar-Thermal Test Facility

The mounting in Figure 3-8 requires rotation about horizontal and vertical axes like a piece of artillery. Several of the largest steerable antennae used in radio astronomy are mounted in this manner. Computers are used to keep the antennae aligned to a certain position in the sky for astronomy work. In this application the computers align the antennae to collect solar energy at the receiver. The necessary azimuthal and elevation angles will vary with the time of day, with the day of the year, with the position of the tower on the earth's surface, and with the receiver design.

3.2.2 Elevation and Azimuthal Angles for the Aim Point and Heliostat

The alignment geometry is indicated in Figure 3-11. The aim point is at (x_a, y_a, z_a) , hence the distance between the heliostat center and the aim point is

$$d = \left[(x_1 - x_a)^2 + (y_1 - y_a)^2 + (z_1 - z_a)^2 \right]^{1/2} \quad (3.2-2)$$

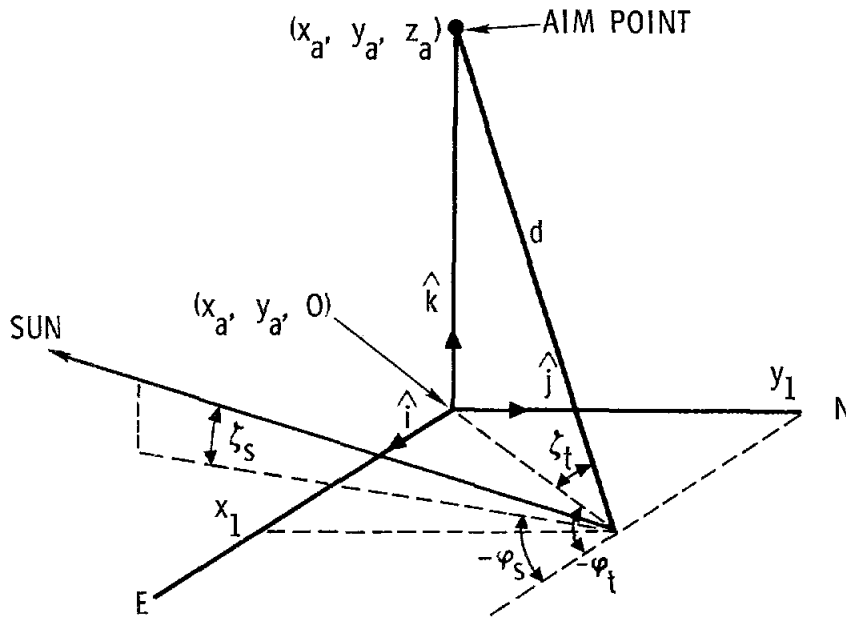


Figure 3-11. Alignment Geometry

The elevation angle of the aim point, ζ_t , and the azimuthal angle, ϕ_t , are defined by

$$\zeta_t = \tan^{-1} \left\{ \frac{z_a - z_1}{\left[(x_1 - x_a)^2 + (y_1 - y_a)^2 \right]^{1/2}} \right\}, \quad (3.2-3)$$

$$\varphi_t = \tan^{-1} \left\{ \frac{y_a - y_1}{x_a - x_1} \right\} . \quad (3.2-4)$$

At the heliostat a unit vector directed toward the sun is given by

$$\hat{V}_s = \hat{i} \cos \zeta_s \cos \varphi_s + \hat{j} \cos \zeta_s \sin \varphi_s + \hat{k} \sin \zeta_s , \quad (3.2-5)$$

while a unit vector toward the aim point is

$$\hat{V}_r = \hat{i} \cos \zeta_t \cos \varphi_t + \hat{j} \cos \zeta_t \sin \varphi_t + \hat{k} \sin \zeta_t . \quad (3.2-6)$$

The sum $\hat{V}_r + \hat{V}_s$ is a vector in the scattering plane which bisects the angle between \hat{V}_r and \hat{V}_s . This is the direction of the arm ℓ_1 in Figure 3-8.

$$\begin{aligned} \hat{V}_{\ell_1} = & \hat{i} \alpha \left[\cos \zeta_s \cos \varphi_s + \cos \zeta_t \cos \varphi_t \right] \\ & + \hat{j} \alpha \left[\cos \zeta_s \sin \varphi_s + \cos \zeta_t \sin \varphi_t \right] \\ & + \hat{k} \alpha \left[\sin \zeta_s + \sin \zeta_t \right] , \end{aligned} \quad (3.2-7)$$

where

$$\begin{aligned} \alpha = & |\hat{V}_r + \hat{V}_s|^{-1} , \text{ or} \\ \alpha^{-2} = & \left(\hat{V}_r + \hat{V}_s \right) \cdot \left(\hat{V}_r + \hat{V}_s \right) \\ = & |\hat{V}_r|^2 + |\hat{V}_s|^2 + 2 \hat{V}_r \cdot \hat{V}_s . \end{aligned} \quad (3.2-8)$$

A unit vector in the horizontal plane directed along the projection of \hat{V}_{ℓ_1} is given by

$$\begin{aligned} \hat{V}_h = & \hat{i} \beta \left[\cos \zeta_s \cos \varphi_s + \cos \zeta_t \cos \varphi_t \right] \\ & + \hat{j} \beta \left[\cos \zeta_s \sin \varphi_s + \cos \zeta_t \sin \varphi_t \right] , \end{aligned} \quad (3.2-9)$$

where

$$\begin{aligned} \beta^{-2} = & \left[\cos \zeta_s \cos \varphi_s + \cos \zeta_t \cos \varphi_t \right]^2 \\ & + \left[\cos \zeta_s \sin \varphi_s + \cos \zeta_t \sin \varphi_t \right]^2 . \end{aligned} \quad (3.2-10)$$

The cosine of the elevation angle for the heliostat, ζ_h , may now be written in terms of the angles of the aim point and sun ($\zeta_h \leq \pi/2$),

$$\cos \zeta_h = \hat{V}_h \cdot \hat{V}_{\ell_1} . \quad (3.2-11)$$

In like manner, the heliostat azimuthal angle, φ_h , is given by

$$\cos \varphi_h = \hat{V}_h \cdot \hat{i} \quad (3.2-12)$$

$$\sin \varphi_h = \hat{V}_h \cdot \hat{j} \quad (3.2-13)$$

where

$$-\pi \leq \varphi_h \leq \pi .$$

The sine of the heliostat elevation angle is given by

$$\sin \zeta_h = \frac{\sin \zeta_s + \sin \zeta_t}{\left[2 \left\{ 1 + \cos \zeta_s \cos \zeta_t \cos (\varphi_s - \varphi_t) + \sin \zeta_s \sin \zeta_t \right\} \right]^{1/2}} . \quad (3.2-14)$$

When $\varphi_s = \varphi_t$,

$$\text{then } \zeta_h = \frac{\zeta_s + \zeta_t}{2} .$$

When $\zeta_s = \pi/2$,

then also

$$\zeta_h = \frac{\zeta_s + \zeta_t}{2}$$

independent of φ_s , φ_t , and ζ_t .

When $\zeta_s = 0$,

$$\sin \zeta_h = \frac{\sin \zeta_t}{\left[2 \left\{ 1 + \cos \zeta_t \cos (\varphi_s - \varphi_t) \right\} \right]^{1/2}} . \quad (3.2-15)$$

Hence in a general case the elevation angle of the heliostat is dependent upon the difference in azimuthal angles of the sun and aim point.

3.3 Heliostat Coordinates

3.3.1 The Origin

The point (x_1, y_1, z_1) in Figure 3-8 is the origin of the heliostat coordinate system. It is a Cartesian system with the u_1 axis horizontal, the u_3 axis along the arm ℓ_1 (normal to the heliostat at its center), and the u_2 axis completing the right-handed system. The positions of facet centers are designated in the heliostat coordinate system by u_{1i}, u_{2i}, u_{3i} where i varies from 1 to the number of facets in the heliostat (25 for the CRTF).

Figure 3-12 gives a plane projection of the heliostat with 25 facets illustrated along with the choice of indices for the facets. Consider an individual facet with center coordinates (u_{1i}, u_{2i}, u_{3i}) . The center of the heliostat was earlier designated by the vector

$$\vec{V}_h = x_1 \hat{i} + y_1 \hat{j} + z_1 \hat{k} \quad (3.3-1)$$

in the tower coordinate system. The unit vector normal to the heliostat is

$$\hat{V}_{\ell_1} = \hat{i}\eta_1 + \hat{j}\eta_2 + \hat{k}\eta_3, \quad (3.3-2)$$

where the η_i are given by Eq. (3.2-7).

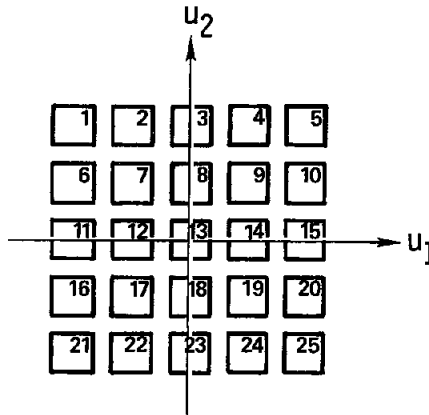


Figure 3-12. Plane Projection of Facet Array on One Heliostat

3.3.2 Facet Placement and Orientation

The center of a facet is given by

$$\vec{V}_f = \vec{V}_h + \vec{u} , \quad (3.3-3)$$

where

$$\vec{u} = u_{1i} \hat{e}_{u_1} + u_{2i} \hat{e}_{u_2} + u_{3i} \hat{e}_{u_3} . \quad (3.3-4)$$

The unit normal to the facet in the heliostat coordinate system is determined by the time at which the facet is positioned for optimum collection of power at the tower. Figure 3-13 illustrates the tower ($\hat{i}, \hat{j}, \hat{k}$) and heliostat (u_1, u_2, u_3) coordinate systems. The u'_1, u'_2, u'_3 axes given are respectively parallel to u_1, u_2, u_3 to illustrate the angles α_{ni} and ϕ_{ni} .

The u_3 axis is in the V_{ℓ_1} direction, hence

$$\hat{e}_{u_3} = \eta_1 \hat{i} + \eta_2 \hat{j} + \eta_3 \hat{k} . \quad (3.3-5)$$

The u_1 axis is taken to be horizontal, hence

$$\hat{e}_{u_1} = -\sin \phi_h \hat{i} + \cos \phi_h \hat{j} , \quad (3.3-6)$$

where ϕ_h is given by Eqs. (3.2-12) and (3.2-13). Then $\hat{e}_{u_2} = \hat{e}_{u_3} \times \hat{e}_{u_1}$, or

$$\hat{e}_{u_2} = -\hat{i} \eta_3 \cos \phi_h - \hat{j} \eta_3 \sin \phi_h + \hat{k} (\eta_2 \sin \phi_h + \eta_1 \cos \phi_h) . \quad (3.3-7)$$

If we let $x'_1, y'_1,$ and z'_1 be the coordinates of the i^{th} facet center in the $\hat{i}, \hat{j}, \hat{k}$ (tower) coordinate system,

$$\begin{aligned} x'_1 &= x_1 - u_{1i} \sin \phi_h - u_{2i} \eta_3 \cos \phi_h + u_{3i} \eta_1 , \\ y'_1 &= y_1 + u_{1i} \cos \phi_h - u_{2i} \eta_3 \sin \phi_h + u_{3i} \eta_2 , \\ z'_1 &= z_1 + u_{2i} (\eta_2 \sin \phi_h + \eta_1 \cos \phi_h) + u_{3i} \eta_3 . \end{aligned} \quad (3.3-8)$$

These small changes will alter the elevation and azimuthal angles for the aim point causing small variation in the direction of the normal for each facet.

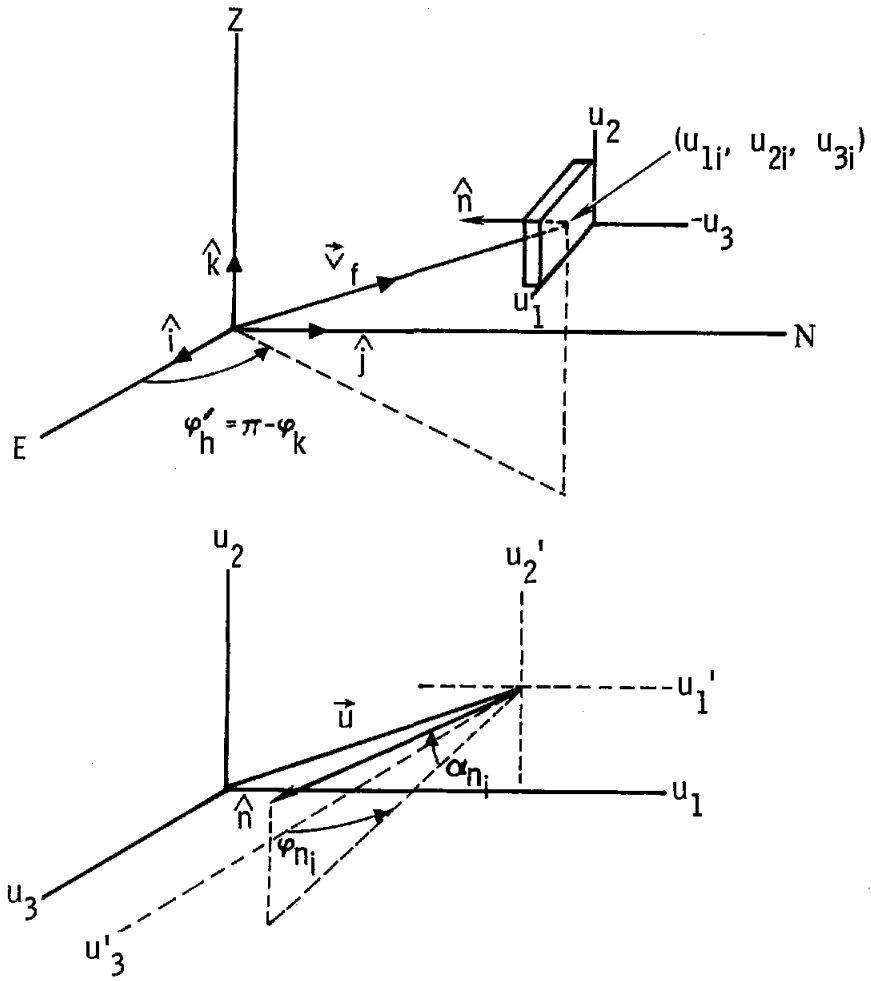


Figure 3-13. Geometry Indicating Normal to Facet in Heliostat and Tower Coordinate Systems

Reference to Figure 3-13 allows the normal to the i^{th} facet center to be written as

$$\hat{\eta}_i = \hat{e}_{u_1} \cos \alpha_{ni} \sin \varphi_{ni} + \hat{e}_{u_2} \sin \alpha_{ni} + \hat{e}_{u_3} \cos \alpha_{ni} \cos \varphi_{ni} . \quad (3.3-9)$$

Assuming for the moment that α_{ni} and φ_{ni} are known, Eqs. (3.3-5) through (3.3-7) allow conversion to the tower coordinate system.

$$\begin{aligned} \hat{\eta}_i = & \hat{i} \left\{ -\sin \varphi_h p_{ni} - \eta_3 \cos \varphi_h q_{ni} + \eta_1 r_{ni} \right\} \\ & + \hat{j} \left\{ +\cos \varphi_h p_{ni} - \eta_3 \sin \varphi_h q_{ni} + \eta_2 r_{ni} \right\} \\ & + \hat{k} \left\{ (\eta_2 \sin \varphi_h + \eta_1 \cos \varphi_h) q_{ni} + \eta_3 r_{ni} \right\} , \end{aligned} \quad (3.3-10)$$

where

$$p_{ni} = \cos \alpha_{ni} \sin \phi_{ni} ,$$

$$q_{ni} = \sin \alpha_{ni} , \quad (3.3-11)$$

$$r_{ni} = \cos \alpha_{ni} \cos \phi_{ni} .$$

3.3.3 Heliostat Alignment

If data for α_{ni} and ϕ_{ni} are not available, they may be determined from the time at which the facets are tuned for maximum reception of solar energy. Substitution of x'_1, y'_1, z'_1 (Eq. (3.3-8)) for x_1, y_1, z_1 in Eqs. (3.2-3) and (3.2-4) and insertion of time data allow calculation of a new vector \hat{v}'_1 which is normal to the facet. Very slight corrections can also be inserted to account for the facet being at a slightly different hour angle from the sun and a different latitude on earth than the heliostat center. These slight corrections are neglected at present. The known normal may then be set equal to Eq. (3.3-10)

$$\eta_x = a_{11} p_{ni} + a_{12} q_{ni} + a_{13} r_{ni} ,$$

$$\eta_y = a_{21} p_{ni} + a_{22} q_{ni} + a_{23} r_{ni} , \quad (3.3-12)$$

$$\eta_z = a_{31} p_{ni} + a_{32} q_{ni} + a_{33} r_{ni} ,$$

where a_{ij} are determined from Eq. (3.3-10). Note $a_{31} = 0$ and the determinate of the matrix of values a_{ij} is $\eta_3^2 + (\eta_1 \cos \phi_h + \eta_2 \sin \phi_h)^2 = 1$. These equations may be solved for p_{ni}, q_{ni} , and r_{ni} . The angles may then be obtained from

$$\alpha_{ni} = \sin^{-1}(q_{ni}) ,$$

$$\phi_{ni} = \tan^{-1}(p_{ni}/r_{ni}) .$$

(3.3-13)

Both α_{ni} and ϕ_{ni} should be small angles, hence the intervals $-\pi/2 \leq \phi_{ni} \leq \pi/2$ and $-\pi/2 \leq \alpha_{ni} \leq \pi/2$ are suitable for computer evaluation of the functions. Of course the p_{ni}, q_{ni}, r_{ni} themselves are used to generate the central normal to each facet surface.

In order to calculate normals when the facets are focused on-axis, the identical equations are used with the angular coordinates of the sun replacing those of the prealignment point.

3.4 The Sun-Concentrator Coordinates

3.4.1 Axes

In this section the geometrical variables are determined for the sun-concentrator coordinate system in terms of the systems introduced earlier. The system has z in the direction of the facet normal at its center, the yz plane contains the facet normal and the central reflected ray from the sun as it would be if no slope error occurs on the facet surface, and x completes the right-handed system. These coordinates are convenient for expressing the reflection properties of the facet (or of the individual reflector).

Let us now form unit vectors along the facet-coordinate axes in terms of the tower coordinates. The z axis is along the facet normal so

$$\hat{e}_z = \hat{\eta}_i = v_{fi}\hat{i} + v_{fj}\hat{j} + v_{fk}\hat{k} \quad (3.4-1)$$

with the coefficients as in Eq. (3.3-10). The unit vector toward the sun is taken from Eq. (3.2-5)

$$\hat{V}_s = s_i\hat{i} + s_j\hat{j} + s_k\hat{k} . \quad (3.4-2)$$

Thus the angle of incidence for the central ray is

$$\mu = \cos^{-1}(\hat{\eta}_i \cdot \hat{V}_s) . \quad (3.4-3)$$

The central reflected ray is reflected at the same angle in the same plane of incidence; hence a unit vector along the central reflected ray is

$$\hat{c}_r = 2 \cos \mu \hat{\eta}_i - \hat{V}_s . \quad (3.4-4)$$

The x axis may now be formed as

$$\hat{e}_x = \hat{c}_r \times \hat{\eta}_i / |\hat{c}_r \times \hat{\eta}_i| , \quad (3.4-5)$$

and the unit vector along the y axis is

$$\hat{e}_y = \hat{\eta}_i \times \hat{e}_x . \quad (3.4-6)$$

The \hat{e}_x , \hat{e}_y , $\hat{\eta}_i$ are illustrated in Figure 3-14.

$$\begin{aligned}
r_1 &= \vec{v}_{gf} \cdot \hat{e}_x , \\
r_2 &= \vec{v}_{gf} \cdot \hat{e}_y , \\
r_3 &= \vec{v}_{gf} \cdot \hat{\eta}_i ,
\end{aligned}
\tag{3.4-8}$$

with each of the vectors in the inner products expressed for convenience in the tower system after translation to the facet center. These components are useful for evaluating the reflected light intensities.

For the present the mesh of target points is assumed to be distributed in a plane. In the tower coordinates, the normal to this plane is designated by \vec{v}_m . This normal is required for calculating the power per unit area falling on the target. In order to find the contribution of each facet the \vec{v}_m must be converted to the coordinates of the individual facet. The facet components are

$$\begin{aligned}
v_{mx} &= \vec{v}_m \cdot \hat{e}_x \\
v_{my} &= \vec{v}_m \cdot \hat{e}_y \\
v_{mz} &= \vec{v}_m \cdot \hat{\eta}_i
\end{aligned}
\tag{3.4-9}$$

3.4.3 Facet Orientation

In some applications the effect of facet orientation may be required. In Figure 3-14 this would appear as variation of the angle β between the x axis and the line that passes between the x and y axes from the facet center orthogonal to the edge of the facet square. Let us assume the bottom edge of the facet remains horizontal. Then a vector in the direction of this edge can be conveniently calculated. The normal to the facet is (in tower coordinates)

$$\hat{\eta}_i = \hat{i}n_x + \hat{j}n_y + \hat{k}n_z ,
\tag{3.4-10}$$

where n_x , n_y , n_z are defined by Eq. (3.3-10). Its projection on the horizontal plane is

$$\vec{h}_i = \hat{i}n_x + \hat{j}n_y
\tag{3.4-11}$$

with conversion to a unit vector

$$\hat{e}_{hi} = \vec{h}_i / \sqrt{n_x^2 + n_y^2} .
\tag{3.4-12}$$

A unit vector in the direction of the bottom edge of the facet is then

$$\hat{e}_B = \hat{\eta}_i \times \hat{e}_{hi} / |\hat{\eta}_i \times \hat{e}_{hi}|. \quad (3.4-13)$$

In the special case when $n_z = 0$, \hat{e}_{hi} may be replaced by \hat{k} in order to define \hat{e}_B . The angle between \hat{e}_B and \hat{e}_x is then

$$\beta = \cos^{-1}(\hat{e}_B \cdot \hat{e}_x). \quad (3.4-14)$$

In order to restrict the angle to the β above, we write

$$\cos \beta = |\hat{e}_B \cdot \hat{e}_x|, \quad (3.4-15)$$

$$\sin \beta = \mp \sqrt{1 - \cos^2 \beta}, \quad (3.4-16)$$

where the upper (lower) sign is appropriate when the sign of $\hat{e}_B \cdot \hat{e}_y$ is positive (negative). The angle β gives the angle of rotation required to align one of the facet edges with the x axis.

3.5 Target Coordinates

3.5.1 Target Mesh

In order to evaluate the coordinates of a target point in the sun-concentrator system (v_{mx} , v_{my} , v_{mz}), the tower coordinates are needed (x_g , y_g , z_g). For comparison with experimental data or for predictions of the energy flux distribution on some aperture, the target coordinates related directly to the target itself are most convenient. Let us divide the target surface into a matrix of points identified by the indices i_x , i_y . The number of points in the surface is $i_t = i_x * i_y$. The points are divided into rows and columns such that the row number is $n_r = (i - 1)/i_x + 1$ and the column number is $n_c = i - (n_r - 1) * i_x$ where $1 \leq i \leq i_t$. The middle row is $m_r = (i_y + 1)/2$ while the middle column is $m_c = (i_x + 1)/2$, i.e., when i_x and i_y are odd numbers.

Let the extent of the target surface be x_{ext} and z_{ext} along the horizontal and the orthogonal direction (in the surface). The origin of the target coordinate system is taken at the target center. In this system the coordinates of a specific target point are given by $x_t = (n_c - m_c) * x_{ext} / (i_x - 1)$ and $z_t = (n_r - m_r) * z_{ext} / (i_y - 1)$. Conversion from these target coordinates to the tower coordinates requires further specification of the target surface. Three shapes are treated here: planar, spherical, and cylindrical.

3.5.2 Planar Target Surface

We assume that tower coordinates are given for three noncolinear points in the target plane. We also assume a vector \vec{V}_{ivmd} is given that is roughly an outward unit vector at the target surface. Vectors $(\vec{V}_1, \vec{V}_2, \vec{V}_3)$ are formed from the origin to the points defining the plane, with \vec{V}_1 directed to the center of the target surface. With $\vec{V}_{12} \equiv \vec{V}_2 - \vec{V}_1$ and $\vec{V}_{13} \equiv \vec{V}_3 - \vec{V}_1$, a normal to the surface is $\vec{V}_n = \vec{V}_{12} \times \vec{V}_{13}$. In order to insure this is an outward-directed normal, the sign of $\vec{V}_n \cdot \vec{V}_{ivmd}$ may be tested. A negative sign is corrected by replacing \vec{V}_n by $-\vec{V}_n$. The \vec{V}_{ivmd} must be sufficiently accurate for the correct \vec{V}_n to pass the test.

A linear combination of \vec{V}_{12} and \vec{V}_{13} is horizontal and is in the target plane.

$$\vec{V}_h = \left(V_{12x} - \frac{V_{12z}}{V_{13z}} V_{13x} \right) \hat{e}_x + \left(V_{12y} - \frac{V_{12z}}{V_{13z}} V_{13y} \right) \hat{e}_y, \quad (3.5-1)$$

where the notation V_{12x} indicates the x component of \vec{V}_{12} in the tower coordinate system. When $V_{13z} \approx 0$, the $\vec{V}_h = \vec{V}_{13}$. The vector in the target plane orthogonal to the horizontal is $\vec{V}_o = \vec{V}_n \times \vec{V}_h$. Normalization converts to the corresponding unit vectors $\hat{V}_h, \hat{V}_o, \hat{V}_n$. Coordinates of the i^{th} target point in the tower coordinates is given by

$$\vec{V}_t = \vec{V}_1 + x_t \hat{V}_h + z_t \hat{V}_o. \quad (3.5-2)$$

The x_{ext} and z_{ext} are the dimensions of the target surface (in metres).

3.5.3 Spherical Target Surface

We assume that the tower coordinates are given for the sphere center (the center of curvature for the spherical surface), that the radius of curvature (r) is given, and that the polar (θ_c) and azimuthal (ϕ_c) angles (as measured from the sphere center) are given for the center of the target surface. We assume \vec{V}_{ivmd} is given as for the planar case. We also assume x_{ext} and z_{ext} are given as the total extent of the azimuthal and polar angles (radians) subtended by the target surface.

A vector, \vec{s} is formed from the origin of the tower coordinates to the sphere center. The azimuthal and polar angles for individual target points are then given by $\phi_i = \phi_c + x_t$ and $\theta_i = \theta_c + z_t$ where x_t and z_t are evaluated as before. In keeping with x_{ext} being a horizontal measurement, azimuthal angles are measured in the horizontal plane. For consistency with the tower coordinates, azimuthal angles are measured from the east and positive toward the north.

Polar angles are measured from the vertical. The position of the i^{th} target point in the tower coordinates is given by

$$\vec{V}_t = \vec{s} + r \cos \theta_i \cos \varphi_i \hat{e}_x + r \cos \theta_i \sin \varphi_i \hat{e}_y + r \sin \theta_i \hat{e}_z . \quad (3.5-3)$$

The normal to the surface is given by

$$\vec{V}_n = (\vec{V}_t - \vec{s})/r . \quad (3.5-4)$$

As in the case of a planar target, the normal is replaced by its negative if it fails the $\vec{V}_n \cdot \vec{V}_{ivmd}$ test.

3.5.4 Cylindrical Target Surface

Only portions of a right-circular cylinder with a vertical axis are considered at present. We assume that the (x, y) tower coordinates (x_a, y_a) are specified for the cylinder axis, that the axis-surface distance (ρ) is given, that the z coordinate of the target center (z_c) is given, and the azimuthal angle (φ_c) is given for the center of the target surface. We also assume x_{ext} is the total extent (radians) of azimuthal angle subtended by the target while z_{ext} is the vertical dimension of the target surface. The azimuthal angle for an individual target point is then given by $\varphi_i = \varphi_c + x_t$ and z_t is the vertical coordinate in the target coordinate system.

A vector, \vec{S} , is formed from the origin of the tower coordinates to the point (x_a, y_a, z_c) . The position of the i^{th} target point in the tower coordinates is given by the vector

$$\vec{V}_t = \vec{S} + \rho \cos \varphi_i \hat{e}_x + \rho \sin \varphi_i \hat{e}_y + z_t \hat{e}_z . \quad (3.5-5)$$

The normal to the cylindrical surface at the i^{th} target point is

$$\pm \vec{V}_n = \cos \varphi_i \hat{e}_x + \sin \varphi_i \hat{e}_y . \quad (3.5-6)$$

The upper (lower) sign is used for the outward (inward) drawn normal. The \vec{V}_{ivmd} is not used for cylindrical target surfaces.

3.6 Shadowing and Blocking Coordinates

In the Central Receiver Test Facility there will be times when the tower and some heliostats interfere with the collection of solar energy. The shadows cast by the tower and the heliostats may fall on other heliostats preventing collection of energy by them. Even though the sun may strike some heliostats, the reflected energy may be blocked from reaching the tower receiver by interference from other heliostats. Accurate models of the performance of the facility must include such effects.

One of the problems which may be addressed by HELIOS is the possibility of improving the distribution of heliostats. As they are spread apart the blocking and shadowing effects are reduced, yet the increase in distance to the receiver may reduce the collected energy. Thus an optimum deployment is expected to exist, likely dependent upon time of use, focusing strategy, reflector surface accuracy, alignment and tracking errors, and perhaps other variables. The search for optimum deployment requires consideration of shadowing and blocking.

As an aid in the shadowing calculation, the outline of each heliostat is projected onto a plane through the origin in Figure 3-11, orthogonal to the direction to the sun (\hat{V}_s). The geometry (tower coordinates) is given in Figure 3-15. The \vec{r}_o represents a specific point of interest on the heliostat (one of the corners). The distance from \vec{r}_o to the plane is $-\hat{V}_s \cdot \vec{r}_o$. The projected point is then

$$\vec{P} = \vec{r}_o - \left[\hat{V}_s \cdot \vec{r}_o \right] \hat{V}_s . \quad (3.6-1)$$

In the new plane, we define x' , z' axes such that all points \vec{P} have $y' = 0$. Hence, $\hat{e}_{y'} = -\hat{V}_s$. The x' axis is chosen to the horizontal, with $\hat{e}_{x'}$, defined by the vector $\hat{e}_z \times \hat{V}_s$ after normalization. The z' axis ($\hat{e}_{z'} = \hat{e}_{x'} \times \hat{e}_{y'}$) completes the right-handed system. In the new coordinates, the components of \vec{P} are $x' = \vec{P} \cdot \hat{e}_{x'}$, $z' = \vec{P} \cdot \hat{e}_{z'}$. In this manner, the (x', z') coordinates are found for each corner of each heliostat.

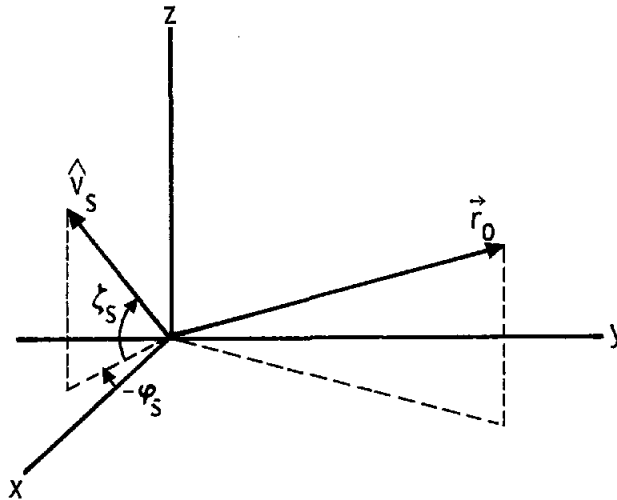


Figure 3-15. \vec{r}_o and \hat{V}_s Vectors in the Tower Coordinate System

As a rough model of the tower, we take 7 m (r_t) for a radius at the top, 8 m (r_b) for a radius at the bottom, and an effective height of 61 m (z_{ef}). The projection of the tower onto the x' , z'

plane gives the corners $(x', z') = (-r_b, 0), (+r_b, 0), (+r_t, z_{ef} * \sqrt{1 - \alpha^2})$, and $(-r_t, z_{ef} * \sqrt{1 - \alpha^2})$ where α is the z component of \hat{V}_s . This x', z' coordinate system is the most convenient for examining shadowing.

A convenient projection for examining the seriousness of heliostat blocking is to project the heliostat outlines onto a unit sphere centered at the aim point. Let us assume in Figure 3-15 that the aim point is $(0, 0, Z_t)$ (a translation converts to the more general case). A line from \vec{r}_o to the aim point intersects the unit sphere at azimuthal angle $\varphi_o = \tan^{-1} Y_o/X_o$ and polar angle $\theta_o = \tan^{-1} \left[(X_o^2 + Y_o^2)^{1/2} / (Z_o - Z_t) \right]$ where $\vec{r}_o = (X_o, Y_o, Z_o)$. Each corner of each heliostat is projected in this manner to generate the blocking diagram on the unit sphere. Any overlap of heliostats here indicates blocking occurs. The methods of calculating shadowing and blocking are given in Chapter 7 on numerical procedures.

CHAPTER 4

OPTICS OF REFLECTING CONCENTRATORS

In this chapter, we develop some relationships that are useful in calculating the optical behavior of a reflecting surface. Some general focusing properties of curved-surface reflectors are given and illustrated analytically for the special case of a spherical reflector used in an off-axis geometry with a collimated incident beam. Even though this special case may not often be realized in practice, it does provide a simple means of illustrating some interesting off-axis optical effects. Similar effects occur for more complicated reflector surfaces. The corresponding calculations, however, must be done numerically. The simple examples used here illustrate some of the important properties of off-axis reflecting optics.

4.1 Specular Reflection of a Light Ray From a Surface Element

We start with the law of reflection of a light ray from an element of surface. This is illustrated in Figure 4-1 where a light ray coming from the direction of the unit vector \hat{A} reflects from an element of surface that has the unit normal \hat{N} . The direction of the reflected ray is indicated by the unit vector \hat{B} . These vectors satisfy the equation

$$\hat{N} = \frac{\hat{A} + \hat{B}}{|\hat{A} + \hat{B}|} . \quad (4.1-1)$$

Note that the laws of specular reflection are satisfied by these directions. The three vectors lie in a plane because \hat{N} is a linear combination of the two vectors \hat{A} and \hat{B} . Also, the angle of incidence is equal to the angle of reflection because $\hat{A} \cdot \hat{N} = \hat{B} \cdot \hat{N}$ and the vectors all have unit magnitude.

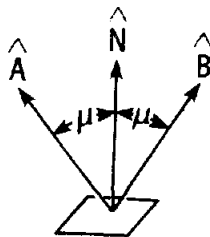


Figure 4-1. Reflection From a Surface Element. The light ray comes from direction \hat{A} and reflects in direction \hat{B} or vice versa. The surface normal is \hat{N} . All three vectors have unit length.

It is useful for our subsequent work to express the unit vector \hat{B} in terms of the unit vectors \hat{A} and \hat{N} . Observe that

$$|\hat{A} + \hat{B}| = 2 \cos \mu = 2 \hat{N} \cdot \hat{A} . \quad (4.1-2)$$

Substituting Eq. (4.1-2) into Eq. (4.1-1), and solving for \hat{B} gives

$$\hat{B} = 2 \hat{N} (\hat{N} \cdot \hat{A}) - \hat{A} . \quad (4.1-3)$$

This equation also applies with unit vectors \hat{B} and \hat{A} interchanged because of the symmetry of the geometry. This is clear from Eq. (4.1-3) using the fact that $\hat{N} \cdot \hat{A} = \hat{N} \cdot \hat{B}$. We write this form of the equation in order to have explicit expressions for each of the unit vectors \hat{A} , \hat{N} , and \hat{B} in terms of the other two.

$$\hat{A} = 2 \hat{N} (\hat{N} \cdot \hat{B}) - \hat{B} . \quad (4.1-4)$$

Another useful result is obtained by using dyadics to render Eq. (4.1-3) into a form that expresses \hat{B} as a matrix operating on \hat{A} . The elements of this matrix operator depend only on the components (direction cosines) of \hat{N} . The result is

$$\begin{bmatrix} B_x \\ B_y \\ B_z \end{bmatrix} = \begin{bmatrix} 2N_x^2 - 1 & 2N_x N_y & 2N_x N_z \\ 2N_y N_x & 2N_y^2 - 1 & 2N_y N_z \\ 2N_z N_x & 2N_z N_y & 2N_z^2 - 1 \end{bmatrix} \begin{bmatrix} A_x \\ A_y \\ A_z \end{bmatrix} \quad (4.1-5)$$

or in matrix notation

$$\hat{B} = \mathcal{N} \hat{A} \quad (4.1-6)$$

where

$$\mathcal{N} = \begin{bmatrix} 2N_x^2 - 1 & 2N_x N_y & 2N_x N_z \\ 2N_y N_x & 2N_y^2 - 1 & 2N_y N_z \\ 2N_z N_x & 2N_z N_y & 2N_z^2 - 1 \end{bmatrix} . \quad (4.1-7)$$

Because of the problem's symmetry we can also write

$$\hat{A} = \mathcal{N}\hat{B} \quad (4.1-8)$$

which means that the matrix \mathcal{N} is its own inverse. This is also evident from other considerations. The unit vector \hat{A} can be obtained by rotating the unit vector \hat{B} 180° about \hat{N} , the same rotation \mathcal{N} takes \hat{A} into \hat{B} . Therefore, \mathcal{N} is its own inverse. Also, since \mathcal{N} represents a rotation, it is an orthogonal matrix, moreover, inspection of Eq. (4.1-7) reveals that it is symmetric. A symmetric orthogonal matrix is its own inverse.

4.2 Specular Reflection of a Beam of Light From a Surface Element

We now extend our treatment to a beam of light reflecting from a surface. Consider the geometry shown in Figure 4-2 where a beam of collimated light incident from direction \hat{A} reflects from the element dQ to strike the receiver element dS . The light ray that strikes point C in the center of dQ reflects about the surface normal \hat{N} and goes in direction \hat{B} to intercept the receiver at point D in accordance with the results given in the previous section. Such a ray trace can, of course, be done for any single light-ray in the beam. For the beam of light rays striking dQ , however, there can be divergence or convergence of the beam upon reflection, depending upon the curvature properties of the surface element dQ . It is of interest to explain the behavior of the reflected beam in terms of the intrinsic properties of the reflecting surface.

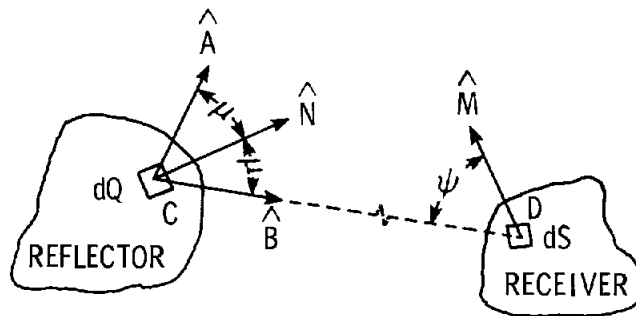


Figure 4-2. Reflector-Receiver Geometry

To be specific, we ask what is the flux density at point D on the receiver when the reflector is irradiated at point C with a collimated beam of light from direction \hat{A} ? This question is addressed in sufficient detail by Shealy and Burkhard (Refs. 4.1 and 4.2) so that it suffices for us to begin with some of their results.

Consider a beam of collimated light incident on the reflector from direction \hat{A} . The flux density F , at point D on the receiver in terms of the intrinsic geometry of the reflecting surface at point C of the reflector is

$$F = \frac{\omega \sigma \cos \mu \cos \psi}{|a_2 r^2 + a_1 r + a_0|} \quad (4.2-1)$$

where ω is the flux density on the reflector at point C , σ is the coefficient of specular reflectance of the surface element dQ , and r is the distance from point C to point D ; the angles μ and ψ are defined in Figure 4-2, and

$$a_0 = \cos \mu \quad (4.2-2a)$$

$$a_1 = -2 \left(2H \cos^2 \mu + K_N \sin^2 \mu \right) \quad (4.2-2b)$$

$$a_2 = 4K \cos \mu, \quad (4.2-2c)$$

where H and K are the mean and the Gaussian curvatures, respectively, of the reflecting surface at point C . The parameter K_N is the normal curvature of the line generated by the intersection of the plane of incidence with the reflecting surface at point C . These curvatures are defined in Kreyszig^{4.3} and illustrated in an example below.

4.3 Spherical or Paraboloidal Concentrators

We now illustrate the use of Eq. (4.2-1) in an example. Figure 4-3 shows a portion of a concentrating reflector that is illuminated from above by a collimated light beam. Consider a sphere of radius, R , centered at point P on the z -axis a distance $z = R$ above the origin. In cylindrical coordinates with

$$\rho^2 = x^2 + y^2 \quad (4.3-1)$$

the equation of this surface is

$$G(\rho, z) = z - R + \sqrt{R^2 - \rho^2} = 0. \quad (4.3-2)$$

For the purposes of this illustration, it is sufficient to limit our attention to a small enough portion of the spherical surface that $\rho/R \ll 1$ and to neglect higher powers of ρ/R than the first. With this restriction, Eq. (4.3-2) simplifies to

$$G(\rho, z) = z - \frac{\rho^2}{2R} = 0, \quad \rho/R \ll 1 \quad (4.3-3a)$$

or in rectangular Cartesian coordinates

$$G(x, y, z) = z - \frac{(x^2 + y^2)}{2R} = 0, \quad x/R \ll 1 \text{ and } y/R \ll 1. \quad (4.3-3b)$$

This is the equation of a parabola of revolution about the z-axis with a focal length of

$$f = R/2. \quad (4.3-4)$$

The focal point, as we shall prove later, is on the z-axis a distance f above the origin.

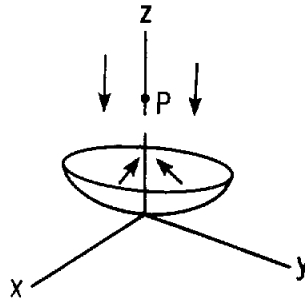


Figure 4-3. A Concentrating Reflector

In order to use results from Kreyszig^{4,3} to evaluate the curvatures of Eqs. (4.2-2), it is convenient to express the surface of Eqs. (4.3-3) in terms of a position vector $\vec{P}(x, y)$ to get

$$\vec{P}(x, y) = \left(x, y, \frac{x^2 + y^2}{2R} \right), \quad (4.3-5)$$

where the z-component of this vector has been written in terms of x and y . Note that

$$\frac{\partial^2 \vec{P}}{\partial x \partial y} = (0, 0, 0). \quad (4.3-6)$$

This will be useful in simplifying subsequent curvature equations.

The mean curvature is

$$H = \left(g_{xx} b_{yy} + g_{yy} b_{xx} \right) / 2g, \quad (4.3-7)$$

the normal curvature is

$$K_N = \frac{b_{xx}}{g_{xx}} \cos^2 \alpha + \frac{b_{yy}}{g_{yy}} \sin^2 \alpha , \quad (4.3-8)$$

and the Gaussian curvature is

$$K = \frac{b_{xx} b_{yy}}{g_{xx} g_{yy}} , \quad (4.3-9)$$

where

$$b_{xx} = \hat{\eta} \cdot \frac{\partial^2 \vec{P}}{\partial x^2} , \quad (4.3-10a)$$

$$b_{yy} = \hat{\eta} \cdot \frac{\partial^2 \vec{P}}{\partial y^2} , \quad (4.3-10b)$$

$$g_{xx} = \left| \frac{\partial \vec{P}}{\partial x} \right|^2 , \quad (4.3-10c)$$

$$g_{yy} = \left| \frac{\partial \vec{P}}{\partial y} \right|^2 , \quad (4.3-10d)$$

$$g = g_{xx} g_{yy} , \quad (4.3-10e)$$

α is the angle between the normal section considered and the x axis, and $\hat{\eta}$ is the unit normal to the surface. To get a normal to the reflecting surface, we take the gradient of Eq. (4.3-3b) to get

$$\nabla G = \left(-\frac{x}{R}, -\frac{y}{R}, 1 \right) \cong \hat{\eta} . \quad (4.3-11)$$

Note that the magnitude of this vector differs from unity only by powers of x/R and y/R higher than the first so we neglect them.

From Eq. (4.3-5)

$$\frac{\partial \vec{P}}{\partial x} = (1, 0, x/R) , \quad (4.3-12a)$$

$$\frac{\partial \vec{P}}{\partial y} = (0, 1, y/R) , \quad (4.3-12b)$$

and

$$\frac{\partial^2 \vec{P}}{\partial x^2} = (0, 0, 1/R) = \frac{\partial^2 \vec{P}}{\partial y^2} . \quad (4.3-12c)$$

Using these derivatives and $\hat{\eta}$ in Eqs. (4.3-10) gives the parameters needed to calculate the mean curvature

$$H = \frac{1}{R} \quad (4.3-13)$$

the normal curvature

$$K_N = \frac{1}{R} \cos^2 \alpha + \frac{1}{R} \sin^2 \alpha = \frac{1}{R} , \quad (4.3-14)$$

and the Gaussian curvature

$$K = \frac{1}{R^2} . \quad (4.3-15)$$

Substituting these curvatures into Eqs. (4.2-2), then using the results in Eq. (4.2-1) and using Eq. (4.3-4) gives the flux density

$$F = \frac{\omega \sigma \cos \psi}{\left| \left(\frac{r}{f} - \cos \mu \right) \left(\frac{r}{f} - \sec \mu \right) \right|} . \quad (4.3-16)$$

Note that the denominator of this equation vanishes at the distances

$$r = f \cos \mu \quad (4.3-17a)$$

and

$$r = f \sec \mu . \quad (4.3-17b)$$

When the angle of incidence $\mu = 0$, both of these equations give $r = f$ corresponding to the well-known result in geometric optics that collimated light incident on a paraboloidal reflector along its axis of symmetry is reflected through the focal point of the parabola of revolution. When a collimated bundle of rays is incident from an off-axis direction ($\mu \neq 0$), astigmatic aberration results and two line focuses occur. The distance to the tangential focal line is given by Eq. (4.3-17a) and the distance to the sagittal focal line is given by Eq. (4.3-17b).

A geometric derivation of these focal distances is given in Longhurst^{4,4} Section 16-7.

4.3.1 The Tangential-Ray Fan

In order to illustrate and clarify some of the preceding concepts, we use results from Section 4.1 to demonstrate some of the results in Section 4.2. We also elucidate some of the terminology used in describing solar concentrators.

Consider the fan of rays incident on the spherical reflector of Figure 4-3 in the y - z plane when a collimated beam of light is incident on the reflector from an off-axis direction. Figure 4-4 shows two rays from this fan; one incident on the center of the reflector at the origin and the other incident on the reflector at the small distance $y = \delta \ll f$ from the origin along the y -axis. We have neglected to show the curvature of the reflector along the y -direction because we intend this result to apply only in the limit $\delta/f \rightarrow 0$. These two rays are said to be in the tangential-ray fan because they are in the plane that contains the incoming principal ray (the ray incident at the origin of Figure 4-3) and the central normal of the reflector (parallel to the z -axis of Figure 4-3). These rays converge upon reflection from the spherically concave surface to intersect as shown in Figure 4-4. It is of interest to use geometry to verify and to interpret Eq. (4.3-17a).

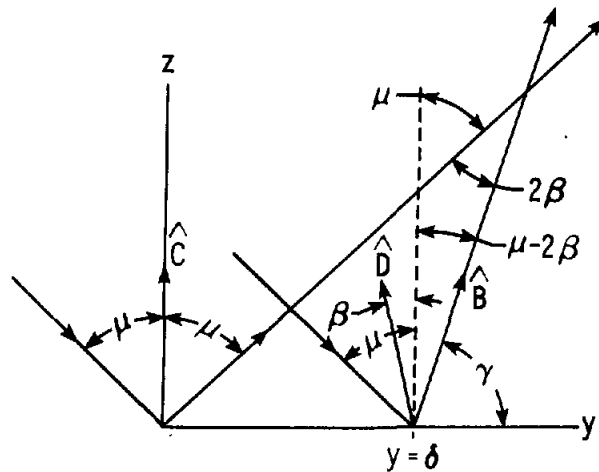


Figure 4-4. Geometry for the Tangential Focus of an Astigmatic System

Figure 4-4 can be thought of as a magnified view of a slice of Figure 4-3 in the y - z plane and near the origin. One ray is incident at the origin where the reflecting-surface unit-normal \hat{C} is along the z -axis. The other ray in the incoming beam is parallel to the first one but is incident at $y = \delta$ where the surface unit-normal is not parallel to the z -axis but is rotated a small angle β as shown schematically in the figure. Using the fact that the angle of reflection is equal to the angle of incidence together with a little geometry involving the angles labeled in Figure 4-4, it is easy to conclude that the two reflected rays intersect at an angle of 2β as indicated in the figure.

In order to calculate the distance, r , from the origin to the point of intersection, we use the law of sines from trigonometry to write

$$\frac{\delta}{\sin(2\beta)} = \frac{r}{\sin\left(\frac{\pi}{2} + \mu - 2\beta\right)} = \frac{r}{\cos(\mu - 2\beta)} \quad (4.3-18)$$

Now use Eq. (4.3-11) and the fact that β is small to get $\beta = \delta/R$, giving an angle of intersection of

$$2\beta = 2\delta/R = \delta/f \quad (4.3-19)$$

and for small δ Eq. (4.3-18) reduces to

$$r = f \cos \mu \quad (4.3-20)$$

in agreement with Eq. (4.3-17a).

Before proceeding to analyze the reflection in the sagittal-ray fan, it is instructive to rederive the above result using formalism developed in Section 4.1. We first use Eq. (4.1-5) to derive the direction of the reflected ray \hat{B} of Figure 4-4; then compare this direction with the direction of the ray reflected from the origin. The incident beam comes from the direction

$$\hat{A} = (0, -\sin \mu, \cos \mu) \quad (4.3-21)$$

Recall that the convention used for the unit-vector directions is defined in Figure 4-1. The surface normal at $Y = \delta$ is according to Eq. (4.3-11)

$$\hat{D} = \left(0, -\frac{\delta}{R}, 1\right) \quad (4.3-22)$$

Applying Eq. (4.1-5) with vectors written as columnar matrices and neglecting powers of δ/R higher than the first gives

$$\begin{bmatrix} B_x \\ B_y \\ B_z \end{bmatrix} = \begin{bmatrix} -1 & 0 & 0 \\ 0 & -1 & -\frac{2\delta}{R} \\ 0 & \frac{-2\delta}{R} & 1 \end{bmatrix} \begin{bmatrix} 0 \\ -\sin \mu \\ \cos \mu \end{bmatrix} = \begin{bmatrix} 0 \\ \sin \mu - \frac{2\delta}{R} \cos \mu \\ 2 \frac{\delta}{R} \sin \mu + \cos \mu \end{bmatrix} \quad (4.3-23)$$

We can now compare the slopes of the two reflected rays of Figure 4-4 to determine their angle of intersection. Let the angle between the Y-axis and the reflected-ray direction \hat{B} be γ as

indicated in Figure 4-4, then

$$\tan \gamma = \frac{B_z/B_y}{\sin \mu - \frac{\delta}{f} \cos \mu} = \frac{\frac{\delta}{f} \sin \mu + \cos \mu}{\sin \mu - \frac{\delta}{f} \cos \mu} \quad (4.3-24)$$

where we have used $f = R/2$. Note that at $\delta/f = 0$, $\tan \gamma = \cot \mu$ as it should. The change in γ corresponding to a small change in δ near $\delta = 0$ is obtained by differentiating Eq. (4.3-24)

$$d\gamma = \frac{d\delta}{f} \frac{\cos^2 \gamma}{\left(\sin \mu - \frac{\delta}{f} \cos \mu\right)^2} \quad (4.3-25)$$

When $\delta/f \ll 1$, the change in γ corresponding to $\Delta\delta = \delta$ is

$$\Delta\gamma = \frac{\delta}{f} \frac{\cos^2 \gamma}{\sin^2 \mu} = \frac{\delta}{f} \quad (4.3-26)$$

as obtained before in Eq. (4.3-19).

4.3.2 The Sagittal-Ray Fan

The sagittal-ray fan also contains the principal ray, but it lies in a plane perpendicular to the tangential-ray fan. Note that the incident tangential-ray fan is in the same plane as the corresponding reflected-ray fan, whereas this is not true of the sagittal-ray fan. It is, therefore, more difficult to visualize the geometry for the sagittal focus of an astigmatic system.

Figure 4-5 shows two rays in the sagittal fan incident on the spherical reflector of Figure 4-3 from an off-axis angle ($\mu \neq 0$). Ray 1 strikes the reflector at the origin and Ray 2 at a small distance δ along the x-axis from the origin. These rays reflect to intersect at the sagittal focus as indicated in the figure. The intersection occurs in the y-z plane because incoming Ray 1 and the surface normal \hat{C} at the origin are both in the y-z plane.

The incoming rays come from the direction of the unit vector \hat{A} of Eq. (4.3-21). The surface normal at $(x, y, z) = (\delta, 0, 0)$ from Eq. (4.3-11) is

$$\hat{D} = \left(-\frac{\delta}{R}, 0, 1 \right), \quad (4.3-27)$$

which has unit length to first order in the small quantity δ/R . The direction of reflected Ray 2 using Eq. (4.1-5) (to first order in δ/R) is

$$\begin{bmatrix} B_x \\ B_y \\ B_z \end{bmatrix} = \begin{bmatrix} 1 & 0 & -2\frac{\delta}{R} \\ 0 & -1 & 0 \\ -2\frac{\delta}{R} & 0 & 1 \end{bmatrix} \begin{bmatrix} 0 \\ -\sin \mu \\ \cos \mu \end{bmatrix} = \begin{bmatrix} -2\frac{\delta}{R} \cos \mu \\ \sin \mu \\ \cos \mu \end{bmatrix} \quad (4.3-28)$$

Reflected Ray 2 intercepts the y-z plane when the x-component of \hat{B} is renormalized so that

$$B_x = -\delta \quad (4.3-29a)$$

The other components of \hat{B} corresponding to this normalization are

$$B_y = f \tan \mu \quad (4.3-29b)$$

and

$$B_z = f \quad (4.3-29c)$$

where we have again used $R = 2f$.

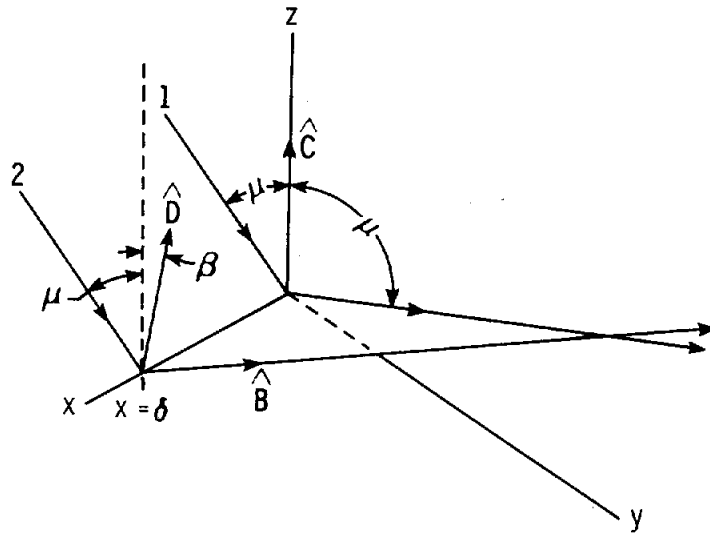


Figure 4-5. Geometry for the Sagittal Focus of Astigmatic System

Note that

$$B_z/B_y = \cot \mu \quad (4.3-30)$$

is also the slope of reflected Ray 1 in the y-z plane. Therefore, these two reflected rays intersect at the point

$$(x, y, z) = (0, f \tan \mu, f) \quad (4.3-31)$$

in the y-z plane which is a distance

$$r = f \sqrt{\tan^2 \mu + 1} = f \sec \mu$$

from the origin. This agrees with Eq. (4.3-17b).

4.3.3 Focusing by an Astigmatic System

In order to summarize the results of the last two sections, we show the reflected portions of both the tangential-ray fan and the sagittal-ray fan in Figure 4-6. The collimated incident beam (not shown) is from an off-axis ($\mu \neq 0$) direction. The tangential-ray fan is roughly vertical, whereas the sagittal-ray fan is roughly horizontal in the perspective drawing of the figure. If the reflector were rotated toward a zero angle of incidence, the two focal lines would become shorter and closer together until at $\mu = 0$ one focal point at f would be obtained at a distance f from the center of the spherical reflector.

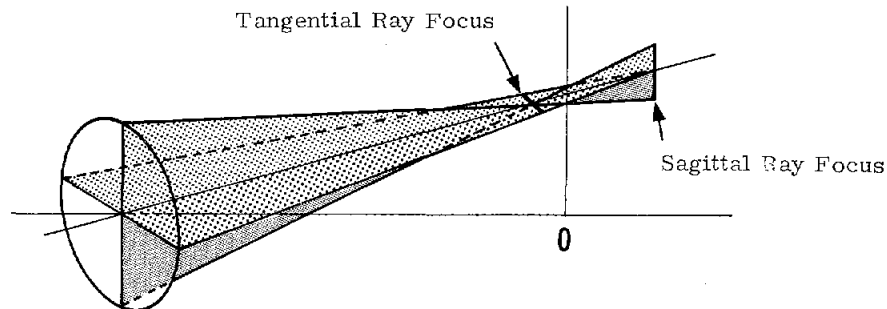


Figure 4-6. Reflected Tangential-Ray Fan and Sagittal-Ray Fan and the Corresponding Focal Lines for an Off-Axis Spherical Reflector

4.3.4 Focal Length Versus Slant Range

In order to address the question of what the focal length should be for a given slant range from the heliostat to the receiver aperture and for a given off-axis geometry, we again consider a spherical mirror. This illustrates the concept and provides analytical results. For reflectors with more complicated shapes than spherical, HELIOS calculates the optimum focal properties numerically.

Figure 4-7 shows the tangential-ray fan in the top of the figure. A collimated beam is incident at an angle of incidence μ . The bottom part of the figure shows the sagittal-ray fan; in this case only the reflected rays are in the plane of the page. The appropriate distance for the slant range D in most applications is such that the image height h_1 in the tangential-ray fan is equal to the image width h_2 in the sagittal-ray fan. This puts the receiver aperture at the "circle-of-least-confusion."

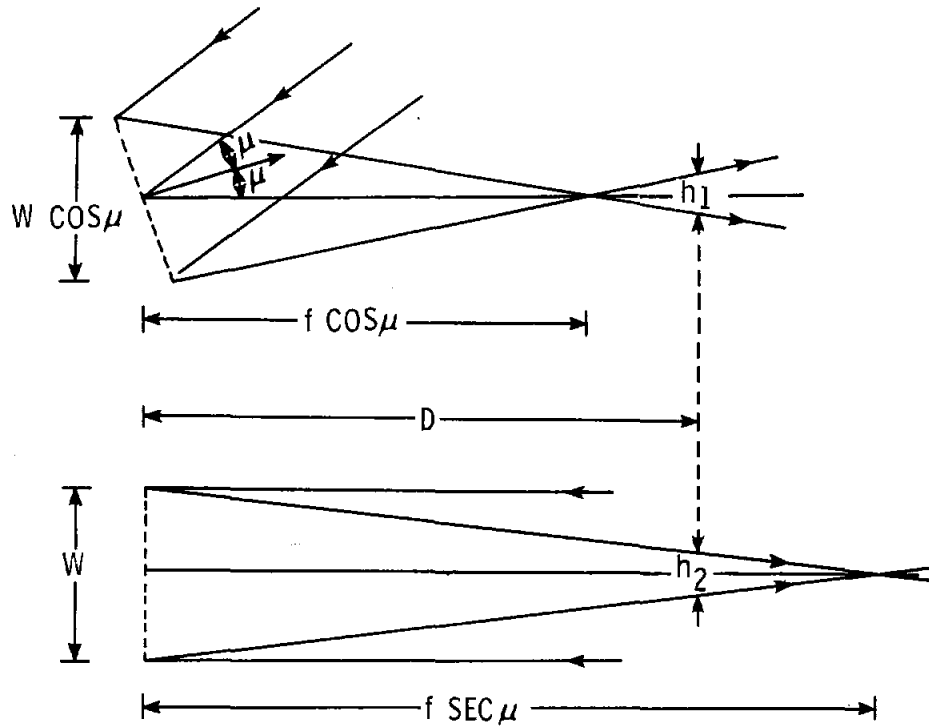


Figure 4-7. The Tangential-Ray Fan (top) and the Sagittal-Ray Fan (bottom). In the sagittal-ray fan the incident rays are not in the plane of the page.

From the geometry of Figure 4-7

$$\frac{W \cos \mu}{f \cos \mu} = \frac{h_1}{D - f \cos \mu} \quad (W \ll D) \quad (4.3-33)$$

from which

$$h_1 = \frac{W}{f} (D - f \cos \mu) \quad (4.3-34)$$

and

$$\frac{h_2}{f \sec \mu - D} = \frac{W}{f \sec \mu} \quad (4.3-35)$$

from which

$$h_2 = \frac{W}{f} (f - D \cos \mu) . \quad (4.3-36)$$

If we impose the condition

$$h_1 = h_2 \quad (4.3-37)$$

then

$$f = D \quad (4.3-38)$$

is the relationship that places the circle-of-least-confusion at the receiver aperture. It does not depend on the angle of incidence μ .

4.3.5 Astigmatic Image Size

When $D = f$, then from Eqs. (4.3-34) and (4.3-36)

$$h_1 = h_2 = W(1 - \cos \mu) = 2W \sin^2\left(\frac{\mu}{2}\right) . \quad (4.3-39)$$

Since this applies to collimated incident light, it must be modified for sunlight which is not well collimated. The envelope of the height H_1 of the solar image at the focal distance in the tangential plane is

$$H_1 = h_1 + \beta D = \frac{W}{f} (D - f \cos \mu) + \beta D , \quad (4.3-40)$$

where β is the angle subtended by the sun. The width of the solar image at the focal distance in the sagittal plane is

$$H_2 = h_2 + \beta D = \frac{W}{f} (f - D \cos \mu) + \beta D . \quad (4.3-41)$$

At the slant range $D = f$, both of the above dimensions become

$$H_1 = H_2 = 2W \sin^2\left(\frac{\mu}{2}\right) + \beta f . \quad (4.3-42)$$

These equations can be used to approximate image sizes resulting from individual facets when W is taken to be a facet diameter (or average diameter) or for entire heliostat effects when W is the average heliostat diameter. The derivation is based on a spherical or almost spherical reflector. The heliostat facets approximate a spherical surface when the facets are prealigned with respect to the heliostat frame in an on-axis ($\mu = 0$) geometry.

Since the effects of astigmatic aberrations are calculated numerically in HELIOS without the need for any of these special-case analytical approximations, we shall not pursue this topic further here. More details on the effects of astigmatic aberrations on the performance of central-receivers including effects of prealigning the heliostat facets off-axis ($\mu \neq 0$) is given by Igel and Hughes.^{4,5}

References

- 4.1 David L. Shealy and Donald G. Burkhard, "Flux Density for Ray Propagation in Discrete Index Media Expressed in Terms of the Intrinsic Geometry of the Deflecting Surface," *Optica Acta* 20, 287, 1973.
- 4.2 Donald G. Burkhard and David L. Shealy, "Flux Density for Ray Propagation in Geometrical Optics," *Journal of the Optical Society of America*, 63: 299, 1973.
- 4.3 Erwin Kreyszig, Introduction to Differential Geometry and Riemannian Geometry, University of Toronto Press, 1968.
- 4.4 R. S. Longhurst, Geometrical and Physical Optics, Second Edition, John Wiley & Sons, Inc., 1967.
- 4.5 E. A. Igel and Robert L. Hughes, Optical Analysis of Solar Facility Heliostats, SAND77-0582, Sandia Laboratories, Albuquerque, NM, May 1977.

CHAPTER 5

STATISTICS OF REFLECTING OPTICS

Many solar energy applications require focussing concentrators to increase the concentration of solar radiation. The shape of the concentrator surface, the geometry under which it operates, and the angular distribution of incoming sunrays (sunshape) combine to define an upper limit to the concentration levels that can be obtained.^{5.1} In practice, however, other factors degrade the average concentration to values below this ideal limit. Thus, it is appropriate to include these effects in specifying the optical quality of a concentrator; this should be done in such a way that the optical performance can be determined for any operating geometry using its specification parameters.

In this chapter we describe a scheme for specifying the optical quality of a reflecting concentrator in terms of error distributions. We give the statistical methods needed to analyze the error distributions required for the various nondeterministic factors. We develop the mapping of error distributions from a reference system that is convenient for specifying the quality of a concentrator to a reference system suitable for reflected beam-quality analysis. Finally, a method for projecting the effective sunshape onto a receiver or other reference surface is derived.

5.1 The Optical Quality of a Reflecting Concentrator

As a hypothetical example, suppose that the reflecting surface of a solar concentrator is composed of a thin sheet of material, one surface of which is reflective. When this sheet is attached to its supporting structure, various distortions occur in the surface. Assume that the resulting surface has a wavy pattern and that the average shape obtained by averaging out the waves also differs from the desired surface. Finally, assume that the reflecting surface has a small-scale structure consisting of a grainy texture plus a striation pattern. A given concentrator may not exhibit all of the surface effects assumed in the example. However, the method developed here encompasses all of these features and allows freedom to include other nondeterministic effects such as sun-tracking errors as well.

There are three categories of surface features in this example. The average shape of the surface is a "large scale" feature. The surface waviness is a "medium-scale" feature. The grainy texture and the striation pattern are "small-scale" effects. Figure 5-1 pictures these three categories of surface features. The dashed curve shows a cross section of the large-scale average shape of the surface which is designated as the "reference surface" for brevity. The solid curve represents the actual surface emphasizing its medium-scale wavy nature. There is

no attempt to show the small-scale surface irregularities directly; instead, this effect is implied by the small arrows which depict a collimated beam incident on a small sample of surface but reflected into a cone of directions designated as the "reflectance cone."

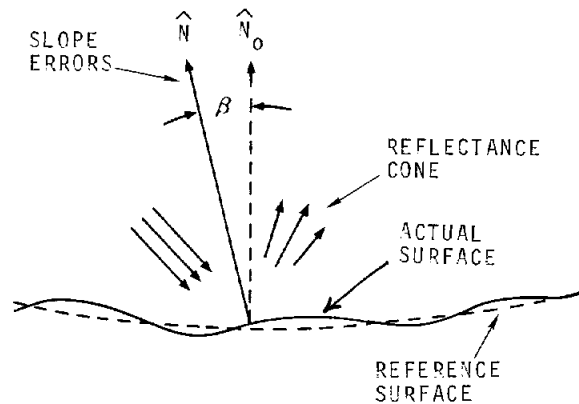


Figure 5-1. Large-Scale (reference surface), Medium-Scale (slope errors), and Small-Scale (reflectance errors) Features of a Concentrator Surface

The medium-scale surface errors are quantified by "slope errors" such as the angle β shown in Figure 5-1. The slope error is the angle between the normal \hat{N}_0 to the reference surface and the normal \hat{N} to the reflecting surface. It is not necessary to specify the slope error at each point on the reference surface. Rather, it is adequate to specify a statistical distribution of slope errors that apply, on the average, to some portion (or perhaps all) of the concentrator surface. Effects of wind turbulence or gravity loading may even cause slope errors to be time dependent, but a distribution of slope errors (perhaps time dependent) is still an appropriate and convenient way to describe the effect.

We assume that the small-scale surface irregularities are modeled the same way as the medium-scale slope-errors; i. e., they are caused by variations in the directions of surface normals but on a smaller scale. The reason for distinguishing them is primarily for convenience in their measurement and in clarifying the meaning of specular-reflectance measurements. The small-scale effects including surface reflectance may usually be measured from samples of the reflecting material in the laboratory. However, the medium and large-scale features must be measured in the field on a fully assembled concentrator in order to include defects that occur during assembly. We refer to the small-scale effects as "reflectance errors" and the corresponding cone of directions as the "reflectance cone" because surface reflectance refers to the integral of reflected light over this cone of directions.

Although we have indicated a clear-cut distinction between small-scale and medium-scale surface errors, this is not always the case. There could be, for example, a continuous gradation of surface waviness extending into the small-scale category. In this case it is necessary to specify a "test area"; medium-scale measurements would average over this test area whereas the small-scale description would apply within it. It is necessary to coordinate the small-scale and the medium-scale measurements to be sure that some surface errors are neither missed nor included in both categories.

The procedure used to relate reflected-beam quality to these error specifications will be described and illustrated after we summarize some statistical optics.

5.2 Two-Dimensional Distributions

5.2.1 Reference Planes

In order to describe an angular distribution of errors in the direction of a unit vector, it is convenient to use a reference plane as suggested by Schrenk.^{5.2} To illustrate this concept, suppose we wish to specify a distribution of slope errors for a reflector. Let the z-axis of the coordinate system in Figure 5-2 be perpendicular to the reference surface of the reflector at a point of interest. The x-y plane is tangent to the reference surface with the x-axis oriented in some convenient direction with respect to the reflector, such as parallel to an edge. If the reflector is a part of a heliostat, the x-axis might be parallel to the horizontal sun-tracking axis. We define the r-s plane to be perpendicular to the z-axis, to intercept it at $z = 1$, and to have its r-axis parallel to the x-axis as indicated in the figure. It is the concept that is important here, not the names of the variables used as coordinates. Later on, we define other reference planes for specifying distributions (the P-Q and U-V planes of Figure 5-22). Although the concepts are the same as described here, it is convenient to use different variable names.

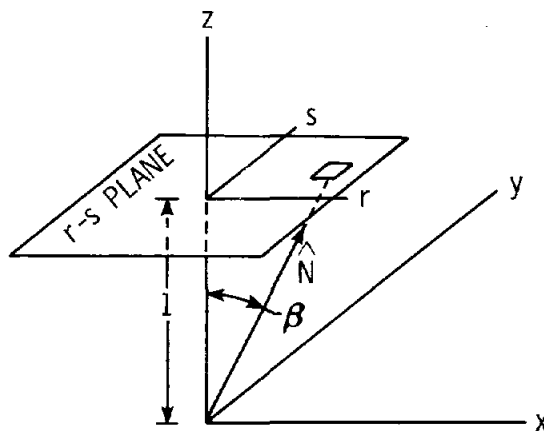


Figure 5-2. The r-s Reference Plane for Specifying Slope-Error Distributions in the Reflector Coordinate System x-y-z

Suppose that \hat{N} is a unit normal to the actual surface at the origin of the coordinate system of Figure 5-2 where the slope error is β as indicated. The direction of \hat{N} is specified by the coordinates (r, s) of the point where the unit vector \hat{N} (extended) intercepts the r - s plane. The probability that this intersection occurs in the element $dr ds$ about the point (r, s) is $[F(r, s) dr ds]$ where F is a probability density function which is normalized to unity when integrated over the entire r - s plane. However, we will usually call such a function as F , a "distribution."

In general, the slope-error distribution is a function of the two variables r and s , but in some special cases circular symmetry reduces the distribution to a function of one variable ρ where

$$\rho = \tan\beta = (r^2 + s^2)^{1/2} . \quad (5.2-1)$$

Note from the geometry of Figure 5-2 that ρ is the radial distance from the origin of the r - s plane to the point (r, s) .

5.2.2 The Pillbox Distribution

Let ρ be the radial distance to the point (r, s) as defined by Eq. (5.2-1) and assume that F has a nonzero constant value over a disk but vanishes outside of it. Then

$$F(\rho) = \begin{cases} \frac{1}{\pi a^2} & , \quad \rho \leq a \\ 0 & , \quad \rho > a \end{cases} \quad (5.2-2)$$

is called a pillbox distribution of disk radius a .

The mean square radius of the pillbox distribution is

$$\langle \rho^2 \rangle = 2\pi \int_0^a \rho^3 F(\rho) d\rho = \frac{a^2}{2} \quad (5.2-3)$$

from which its root-mean-square radius is

$$\sqrt{\langle \rho^2 \rangle} = a/\sqrt{2} . \quad (5.2-4)$$

This distribution is sometimes used as an approximation to the sunshape with the parameter a equal to the angular radius of the solar disk as viewed from the earth ($a \approx 4.2$ mrad as illustrated in Section 5.2.5).

5.2.3 The Elliptic-Normal Distribution

In the r - s plane of Figure 5-2 the elliptic-normal distribution which has its principal axes along r and s is

$$F(r, s) = \frac{1}{2\pi\sigma_r\sigma_s} \exp \left\{ -\frac{1}{2} \left[\frac{r^2}{\sigma_r^2} + \frac{s^2}{\sigma_s^2} \right] \right\} . \quad (5.2-5)$$

The parameters σ_r and σ_s are standard deviations in the r and s directions, respectively. This is a two-dimensional "normal" distribution for the independent random variables r and s . The mean values of r and s are taken to be zero which is adequate for our purposes here. However, these mean values can be changed to \bar{r} and \bar{s} by replacing r by $r - \bar{r}$ and s by $s - \bar{s}$ in Eq. (5.2-5).

The mean square value of r is

$$\langle r^2 \rangle = \left\{ \frac{1}{\sqrt{2\pi}\sigma_r} \int_{-\infty}^{\infty} r^2 \exp \left[-\frac{r^2}{2\sigma_r^2} \right] dr \right\} \left\{ \frac{1}{\sqrt{2\pi}\sigma_s} \int_{-\infty}^{\infty} s^2 \exp \left[-\frac{s^2}{2\sigma_s^2} \right] ds \right\} . \quad (5.2-6)$$

Using the result

$$\int_0^{\infty} \exp[-\lambda x^2] x^k dx = \frac{1}{2} \lambda^{-(k+1)/2} \Gamma\left(\frac{k+1}{2}\right) , \quad k > -1, \lambda > 0 \quad (5.2-7)$$

from page 64 of Grobner and Hofreiter^{5,3} to evaluate this, gives

$$\langle r^2 \rangle = \sigma_r^2 \quad (5.2-8a)$$

or

$$\sqrt{\langle r^2 \rangle} = \sigma_r . \quad (5.2-8b)$$

In a similar way we get

$$\sqrt{\langle s^2 \rangle} = \sigma_s . \quad (5.2-9)$$

The root-mean-square values of r and s are, therefore, equal to their standard deviations for the elliptic-normal distribution of Eq. (5.2-5).

The mean-square radius of the elliptic-normal distribution is

$$\langle \rho^2 \rangle = \langle r^2 \rangle + \langle s^2 \rangle = \sigma_r^2 + \sigma_s^2 . \quad (5.2-10)$$

A continuous random variable v is normally distributed (normal) with mean ξ and variance σ^2 (standard deviation σ) if

$$Q(v, \sigma, \xi) = \frac{1}{\sigma \sqrt{2\pi}} \exp \left\{ -\frac{1}{2} \left(\frac{v - \xi}{\sigma} \right)^2 \right\} . \quad (5.2-11)$$

Refer to Korn and Korn,^{5.4} Section 18.8-3. This distribution is, of course, normalized to unity when integrated over the interval $-\infty < v < +\infty$.

The distribution $F(r, s)$ of Eq. (5.2-5) is a product of two of these normal distributions

$$F(r, s) = Q(r, \sigma_r, 0) Q(s, \sigma_s, 0) . \quad (5.2-12)$$

It is useful to calculate the probability that $|r| < a$ for arbitrary s using the distribution F of Eq. (5.2-5). This probability is given by

$$P(|s| < a) = \int_{s=-a}^{s=a} \int_{r=-\infty}^{\infty} F(r, s) dr ds \quad (5.2-13)$$

Using Eq. (5.2-12) in Eq. (5.2-13) we observe that the integration over r yields unity leaving

$$P(|s| < a) = \int_{s=-a}^a Q(s, \sigma_s, 0) ds = \operatorname{erf} \left\{ \frac{a}{\sigma_s \sqrt{2}} \right\} \quad (5.2-14)$$

where erf denotes the error function (page 297 of Abramowitz and Stegun^{5.5}). The probability that $|r| < a$ is obtained by integrating over the variable s to get Eq. (5.2-14) with $|s|$ replaced by $|r|$ and σ_s by σ_r .

In line-focus concentrators, it is convenient to integrate the effective sunshape in strips parallel to the focal line to obtain a one-dimensional description of the statistics. The above results are useful in analyzing such systems.

5.2.4 The Circular Normal Distribution

In the special case of circular symmetry we have

$$\sigma_r = \sigma_s = \sigma \quad (5.2-15)$$

and the elliptic-normal distribution of Eq. (5.2-5) reduces to the circular-normal distribution

$$F(\rho) = \frac{1}{2\pi\sigma^2} \exp \left\{ -\frac{\rho^2}{2\sigma^2} \right\} \quad (5.2-16)$$

where (using the terminology of Korn and Korn^{5.4}) the parameter σ is called the dispersion. The root-mean-square (rms) radius of this distribution is from Eqs. (5.2-10) and (5.2-15)

$$\sqrt{\langle \rho^2 \rangle} = \sigma \sqrt{2} \quad (5.2-17)$$

The rms width of the sunshape appropriate for a clear day in New Mexico is near 3.5×10^{-3} .

When the root-mean-square radii of the pillbox and the circular-normal distributions are equated, we get

$$\sigma = a/2. \quad (5.2-18)$$

The circular-normal distribution with dispersion given by Eq. (5.2-18) is designated as the circular-normal approximation "associated" with the pillbox distribution of disk radius a . This associated approximation is sometimes useful in convolution calculations as will be illustrated later in some examples involving the Central Limit Theorem.

The probability that $\rho < a$ for the circular normal distribution of Eq. (5.2-16) is

$$P(\rho < a) = 2\pi \int_0^a \rho F(\rho) d\rho = 1 - \exp \left\{ -\frac{a^2}{2\sigma^2} \right\} \quad (5.2-19)$$

A useful form of this result is obtained when the radius a is expressed as a multiple of σ

$$a = \eta\sigma \quad (5.2-20)$$

which gives

$$P(\rho < a) = 1 - \exp \left\{ -\frac{\eta^2}{2} \right\}. \quad (5.2-21)$$

Now consider a circular-normal effective sunshape of dispersion σ . The fraction, f , of reflected power that falls within a cone of radius a is given by $P = f$. Note that the "radius of the cone" as used here is the radius ρ in a reference plane such as the $r - s$ plane of Figure 5-2. Because of the usefulness of the result, we rewrite Eq. (5.2-21) in terms of $f = P$.

$$f = 1 - \exp \left\{ -\frac{\eta^2}{2} \right\}. \quad (5.2-22)$$

Solving this for η^2 gives

$$\eta^2 = -2 \ln (1 - f). \quad (5.2-23)$$

As an example of these results, suppose that a circular-normal effective sunshape has dispersion σ . What is the radius, a , of the reflected cone that contains 90% of the reflected power? Setting $f = 0.9$ in Eq. (5.2-23) gives $\eta = 2.15$ from which Eq. (5.2-20) gives $a = 2.15 \sigma$. Therefore, 90% of the reflected power is contained in a cone of radius equal to 2.15 dispersions of the circular-normal effective sunshape.

5.2.5 The Sunshape

A distribution that plays a central role in the Helios model is the sunshape. It describes the angular distribution of incoming sunrays with respect to the central ray from the sun. Although this distribution does not describe errors such as sun-tracking errors or surface-slope errors, it does represent a stochastic process, the position of origin of photons on the solar disk. The sunshape is convolved with the error cone in a reflected-ray reference plane to obtain the effective sunshape. The purpose of this subsection is to show a typical measured sunshape and discuss briefly some of its properties.

Figures 5-3a and 5-3b show a sunshape S versus ρ in milliradians (since $\rho = \tan\beta \approx \beta$) by the solid curve with squares on it. The quantity $2\pi\rho S d\rho$ gives the fraction of the solar radiation in $d\rho$ about ρ . The squares represent measurements by the Lawrence Berkeley Laboratory Circumsolar Telescope taken in Albuquerque, NM on August 7, 1976 at 11.72-h solar time. Part (a) of the figure has a linear ordinate whereas that of part (b) is logarithmic in order to better resolve differences at small values of S .

A treatment of how the sunshape varies with atmospheric conditions is given in Section 6.4. This sunshape is used in a convolution example later in this chapter where Figure 5-14 shows the distribution in three dimensions.

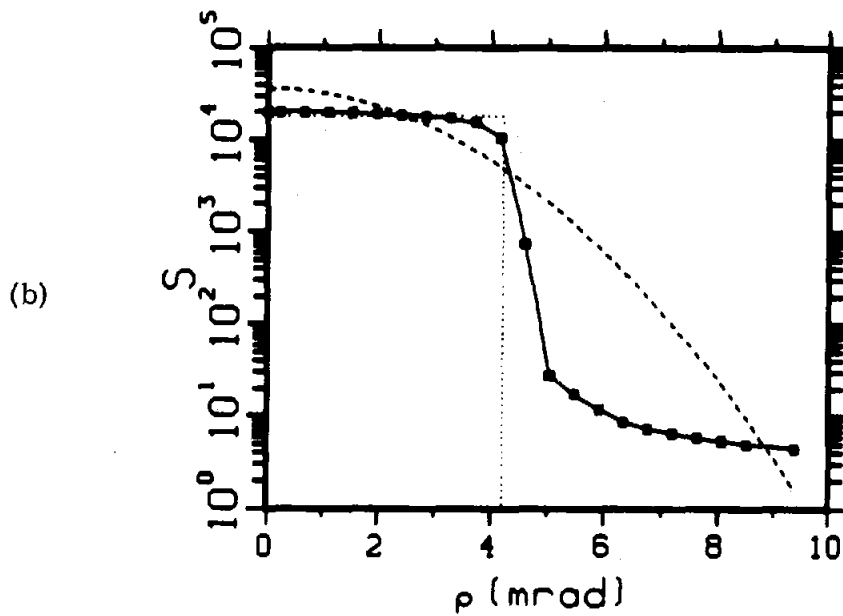
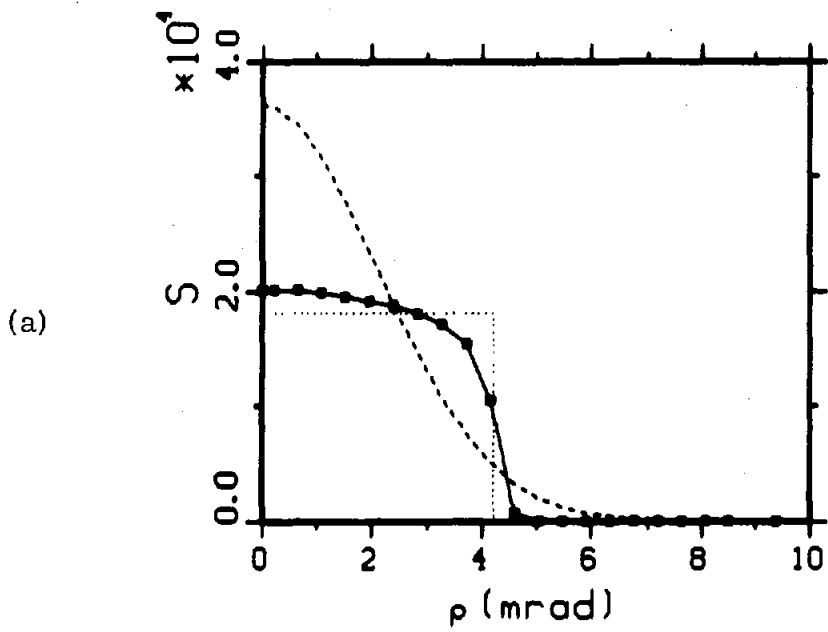


Figure 5-3. A Measured Sunshape (solid curve), Pillbox (dotted), and Circular Normal (dashed) With Mean-Square Radii Equal to That of the Measured Sunshape. The squares represent measurements of the LBL Circumsolar Telescope

The mean-square radius of the sunshape is calculated by

$$\langle \rho^2 \rangle = 2\pi \int_0^{0.01} S(\rho) \rho^3 d\rho = 8.76 \times 10^{-6} \quad (5.2-24a)$$

from which results

$$\sqrt{\langle \rho^2 \rangle} = 2.96 \times 10^{-3} \approx 2.96 \text{ mrad} . \quad (5.2-24b)$$

We terminated the integration in this example at 10 mrad because that represents the maximum ρ for which the sunshape is plotted in Figure 5-3; also in some concentrator applications the radiation at larger values of ρ would not strike the receiver. The Lawrence Berkeley Laboratory (LBL) measurements extend out to nearly 50 mrad, however, and it is arbitrary where one cuts off the sunshape except for some changes in numerical complexity in convolving sunshapes with error cones.

By comparing Eqs. (5.2-4) and (5.2-24b) we obtain a pillbox with a root-mean-square radius equal to that of S at $a = 4.19$ mrad. This pillbox distribution is shown in Figure 5-3 by the dotted rectangles.

By comparing Eqs. (5.2-17) and (5.2-24b) we obtain the circular-normal approximation associated with the sunshape at a dispersion of $\sigma = 2.09$ mrad. This distribution is shown for comparison purposes by the dashed curves in Figure 5-3.

5.2.6 The General Two-Dimensional Distribution

For use in this subsection we denote a general distribution in the r - s plane by $G(r, s)$. As mentioned earlier, this is a probability-density function normalized so that

$$\int_{r=-\infty}^{\infty} \int_{s=-\infty}^{\infty} G(r, s) dr ds = 1 . \quad (5.2-25)$$

The mean-square width of this distribution in the r direction (mean-square value of r) is defined by

$$\langle r^2 \rangle = \int_{s=-\infty}^{\infty} \int_{r=-\infty}^{\infty} r^2 G(r, s) dr ds . \quad (5.2-26)$$

The mean-square width in the s direction is defined in the same way with s^2 replacing r^2 . The root-mean-square widths are the square roots of these quantities.

The "mean-square radius" of the distribution is given by

$$\langle \rho^2 \rangle = \int_{r=-\infty}^{\infty} \int_{s=-\infty}^{\infty} \rho^2 G(r, s) dr ds = \langle r^2 \rangle + \langle s^2 \rangle \quad (5.2-27)$$

where we have used Eqs. (5.2-1) and (5.2-26) as applied to both r and s . Note that the result obtained earlier in Eq. (5.2-10) for the elliptic-normal distribution is a special case of this.

If the distribution G has circular symmetry, then the mean-square values of the two rectangular coordinates r and s are equal

$$\langle r^2 \rangle = \langle s^2 \rangle . \quad (5.2-28)$$

In the case, the root-mean-square radius of the distribution G (root-mean-square value of the polar radius ρ) is related to the root-mean-square values of the rectangular coordinates r and s by

$$\sqrt{\langle \rho^2 \rangle} = \sqrt{2} \sqrt{\langle r^2 \rangle} = \sqrt{2} \sqrt{\langle s^2 \rangle} . \quad (5.2-29)$$

These results are useful when investigating line-focus systems where the desired distribution is often one-dimensional and is obtained by taking lateral slices across the two-dimensional distribution and integrating out the variable along the slices.

5.3 Convolution of Two-Dimensional Distributions

Suppose there are two independent distributions of surface errors such as the slope errors and reflectance errors of Section 5.1. If each direction in a distribution, F , of slope errors is subject to a distribution, G , of reflectance errors, what is the resultant distribution H that describes the combination of these effects? There are many ways the arguments of F and G add up to give a point (r, s) . Combining these by integration gives

$$H(r, s) dr ds = dr ds \int_{-\infty}^{\infty} \int_{-\infty}^{\infty} F(r - \eta, s - \xi) G(\eta, \xi) d\eta d\xi \quad (5.3-1)$$

or the two-dimensional convolution integral

$$H(r, s) = \int_{-\infty}^{\infty} \int_{-\infty}^{\infty} F(r - \eta, s - \xi) G(\eta, \xi) d\eta d\xi = F * G . \quad (5.3-2)$$

The manner in which the mean-square values of the rectangular coordinates add under convolution is derived in Appendix B. In the important special case where either one or both of the averages $\langle r \rangle_F$ or $\langle r \rangle_G$ is zero, the mean-square value of r with respect to the distribution $F * G$ is

$$\langle r^2 \rangle_{F*G} = \langle r^2 \rangle_F + \langle r^2 \rangle_G \quad (5.3-3)$$

If either one or both of the averages $\langle s \rangle_F$ or $\langle s \rangle_G$ is zero, the mean-square value of s with respect to the distribution $F * G$ is

$$\langle s^2 \rangle_{F*G} = \langle s^2 \rangle_F + \langle s^2 \rangle_G \quad (5.3-4)$$

5.3.1 Convolution of Circular-Symmetric Distribution

When a distribution $F(r, s)$ has circular symmetry about the origin, the mean values of both r and s are zero with respect to this distribution. Therefore, when F is convolved with any other distribution G Eqs. (5.3-3) and (5.3-4) apply. Now using these results together with Eq. (5.2-1) leads to

$$\langle \rho^2 \rangle_{F*G} = \langle \rho^2 \rangle_F + \langle \rho^2 \rangle_G \quad (5.3-5)$$

Additional details of this development are given in Appendix B.

If both F and G have circular symmetry, then the convolution $F * G$ also has circular symmetry.

5.3.2 Convolution of Elliptic-Normal Distributions

When two elliptic-normal distributions are convolved, the result is also elliptic normal. This is a very useful result for the analytical convolution of the various error distributions. The results of this convolution are summarized here for convenience, but the details of the proof are relegated to Appendix C.

Suppose that the two elliptic-normal distributions to be convolved are

$$F(u, v) = \frac{1}{2\pi\sigma_u\sigma_v} \exp \left\{ -\frac{1}{2} \left[\frac{u^2}{\sigma_u^2} + \frac{v^2}{\sigma_v^2} \right] \right\} \quad (5.3-6a)$$

and

$$G(x, y) = \frac{1}{2\pi\sigma_x\sigma_y} \exp \left\{ -\frac{1}{2} \left[\frac{x^2}{\sigma_x^2} + \frac{y^2}{\sigma_y^2} \right] \right\} \quad (5.3-6b)$$

where the $u - v$ and $x - y$ systems are related to each other by a rotation as shown in Figure 5-4. It is convenient to picture an elliptic-normal distribution by the contour where the argument of the exponential term is equal to $-1/2$ because the axis intercepts of this curve are equal to the corresponding standard deviations. A portion of this elliptical contour is shown for F by the dashed curve and for G by the solid curve in Figure 5-4.

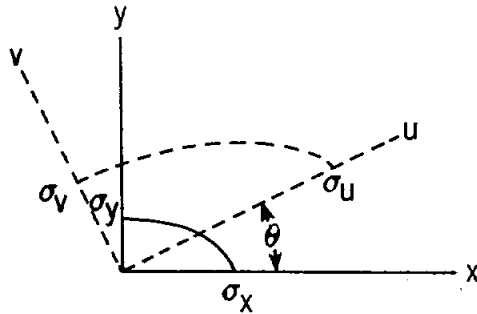


Figure 5-4. Elliptic-Normal Distributions
F and G of Eq. (5.3-6)

The resultant distribution H obtained by convolving F with G is

$$H(x, y) = \frac{1}{2\pi\sigma_x\sigma_y} \left(\frac{D + 1 - A - B}{D} \right)^{1/2} \exp \left\{ -\frac{1}{2} \left[ax^2 + 2kxy + by^2 \right] \right\}, \quad (5.3-7)$$

where

$$a = \frac{D - B}{D\sigma_x^2} \quad (5.3-8a)$$

$$k = \frac{C}{D\sigma_x\sigma_y} \quad (5.3-8b)$$

$$b = \frac{D - A}{D\sigma_y^2} \quad (5.3-8c)$$

and

$$A = 1 + e^2 + g^2 \quad (5.3-9a)$$

$$B = 1 + f^2 + h^2 \quad (5.3-9b)$$

$$C = ef - gh \quad (5.3-9c)$$

$$D = AB - C^2 \quad (5.3-9d)$$

and finally

$$e = \frac{\sigma_x}{\sigma_u} \cos \theta \quad (5.3-10a)$$

$$f = \frac{\sigma_y}{\sigma_u} \sin \theta \quad (5.3-10b)$$

$$g = \frac{\sigma_x}{\sigma_v} \sin \theta \quad (5.3-10c)$$

$$h = \frac{\sigma_y}{\sigma_v} \cos \theta \quad (5.3-10d)$$

The principal axes of the equal probability-density contours (ellipses) are given by the eigenvectors of the matrix

$$M = \begin{bmatrix} a & k \\ k & b \end{bmatrix} \quad (5.3-11)$$

where a, k, b are given in Eq. (5.3-8). The standard deviations σ_i associated with the directions of these eigenvectors are related to the corresponding eigenvalues λ_i by

$$\sigma_i^2 = \frac{1}{\lambda_i}, \quad i = 1, 2 \quad (5.3-12)$$

Analytically, the eigenvalues are

$$\lambda = \frac{1}{2D} \left\{ \frac{D-B}{\sigma_x^2} + \frac{D-A}{\sigma_y^2} \pm \left[\left(\frac{D-B}{\sigma_x^2} - \frac{D-A}{\sigma_y^2} \right)^2 + \left(\frac{2C}{\sigma_x \sigma_y} \right)^2 \right]^{1/2} \right\} \quad (5.3-13)$$

in which one eigenvalue results from the plus sign in front of the bracketed term, and the other eigenvalue from the negative sign. The angle η between the x-axis and the eigenvector (principal axis) t_1 corresponding to λ_1 is

$$\eta = \arctan \left[\frac{\lambda_1 - a}{k} \right]. \quad (5.3-14)$$

The resultant elliptic-normal distribution is shown in Figure 5-5.

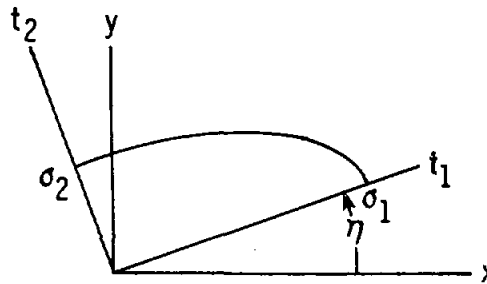


Figure 5-5. The $\exp(-1/2)$ Contour of H in its Principal-Axis System $t_1 - t_2$

In the special case where $\theta = 0$, the results simplify to give $\eta = 0$ and

$$\sigma_1^2 = \sigma_u^2 + \sigma_x^2 \quad (5.3-15a)$$

$$\sigma_2^2 = \sigma_v^2 + \sigma_y^2. \quad (5.3-15b)$$

Also if $\theta = \pi/2$, the result can be written with $\theta = 0$ if we interchange the roles of the σ_u and σ_v to get

$$\sigma_1^2 = \sigma_v^2 + \sigma_x^2 \quad (5.3-16a)$$

$$\sigma_2^2 = \sigma_u^2 + \sigma_y^2. \quad (5.3-16b)$$

5.3.3 Convolution of Circular-Normal Distributions

Since the circular-normal distribution is a special case of the elliptic-normal distribution, we can use the results of the previous section by changing the notation and simplifying the results. Let ϵ be the dispersion of one of the distributions to be convolved and γ the dispersion

of the other distribution. In order to use the results of the previous section, let

$$\epsilon = \sigma_x = \sigma_y \quad (5.3-17)$$

and

$$\gamma = \sigma_u = \sigma_v . \quad (5.3-18)$$

Because of the circular symmetry, the value of θ (Figure 5-4) between principal directions of the two distributions is arbitrary. We therefore, set $\theta = 0$ and use the results of Eq. (5.3-15). First, note that

$$\sigma_1^2 = \gamma^2 + \epsilon^2 = \sigma_2^2 . \quad (5.3-19)$$

Therefore, the convolved distribution is also circular normal. We designate its dispersion by σ and use Eq. (5.2-10) together with Eq. (5.3-15) to get the mean-square radius

$$\langle \rho^2 \rangle = 2(\gamma^2 + \epsilon^2) . \quad (5.3-20)$$

Finally, using Eq. (5.2-17) to relate the mean-square radius of a circular-normal distribution to its dispersion, gives

$$\sigma^2 = \gamma^2 + \epsilon^2 . \quad (5.3-21)$$

5.3.4 A Heliostat-Specification Example

We now use an example to illustrate some uses of the concepts developed above. Suppose that the response function of an error-free heliostat when convolved with the sunshape and projected on the target grid gives a flux-density pattern corresponding approximately to a circular-normal distribution of dispersion γ . (The response-function of a heliostat is its ideal response [no errors] to a collimated incident beam.) Now assume that a fraction, f , of the reflected power would fall within a radius a of this cone. Suppose a requirement is made so that when errors are included the average reflected power falls within a radius b of an enlarged "resultant" cone where b (or $b - a = \delta$) is specified. How wide can an error cone be and still satisfy this requirement?

We assume that the error cone is circular normal with dispersion ϵ . Therefore, the resultant cone is also circular normal and we designate its dispersion by σ so that Eq. (5.3-21) relates the three dispersions. The radius, a , is related to γ by $a = \eta\gamma$ and the radius b is related to σ by $b = \eta\sigma$ where η is in turn related to the fraction, f by Eq. (5.2-23). Now multiply Eq. (5.3-21) by η^2 and substitute these quantities to get

$$b^2 = a^2 + \eta^2 \epsilon^2 \quad (5.3-22)$$

or

$$\epsilon^2 = \frac{b^2 - a^2}{\eta^2} = \frac{b^2 - a^2}{-2 \ln(1-f)} = \frac{\delta(2a + \delta)}{-2 \ln(1-f)}, \quad (5.3-23)$$

where we have used Eq. (5.2-23) and the definition $\delta = b - a$. This shows that for a given value of δ , ϵ increases with the conical radius, a . For example, if $\delta = 1$ mrad, $a = 3$ mrad, and $f = 0.9$ this gives $\epsilon = 1.23$ mrad. But if $a = 10$ mrad for the same values of δ and f , Eq. (5.3-24) gives $\epsilon = 2.14$ mrad.

5.3.5 Numerical Convolution of Two-Dimensional Distributions

The numerical convolution of two-dimensional distributions is a matter of evaluating the double integral of Eq. (5.3-2). Fourier transform methods are useful in performing convolutions because the operation reduces to multiplication in the transform space. In order to do this operation numerically, it is convenient to convert the continuous distribution functions to a series of discrete data samples and to do numerical operations on these samples. Since we use the finite Fourier transform to convolve the resulting data samples, it is expedient to use the fast Fourier transform. The use of the fast Fourier transform to compute convolution integrals is discussed by Cooley et al.^{5,6} The fast Fourier transform routine FOURT used in HELIOS is taken from the Sandia Numerical Subroutine Library.^{5,7}

Since the theory of the Fourier transform is amply described elsewhere,^{5,6,5.8,5.9} and the routine we are using is described in Reference 5.7, we will simply illustrate the use of the two-dimensional fast Fourier transform on an example in this section and relegate a description of numerical procedures to Section 7.3.

In this example we show the results of convolving the distribution of two variables using a fast Fourier transform routine. One of the functions is the rectangular pillbox

$$F(x, y) = \begin{cases} \frac{1}{4ab}, & |x| < a \text{ and } |y| < b \\ 0, & |x| \geq a \text{ or } |y| \geq b \end{cases} \quad (5.3-24)$$

and the other one is

$$G(t_1, t_2) = \begin{cases} \frac{9}{16 cd} \left[1 - \left(\frac{t_1}{c} \right)^2 \right] \left[1 - \left(\frac{t_2}{d} \right)^2 \right], & |t_1| < c \text{ and } |t_2| < d \\ 0, & |t_1| \geq c \text{ or } |t_2| \geq d \end{cases} \quad (5.3-25)$$

This equation is written in terms of the rectangular coordinates t_1 and t_2 with the understanding that the $t_1 - t_2$ system is rotated by an angle θ with respect to the $x - y$ system. The angle θ is measured from the x -axis to the t_1 - axis.

A plot of Eq. (5.3-24) with $a = 3$, $b = 1$, and $\theta = 0$ is shown in Figure 5-6.

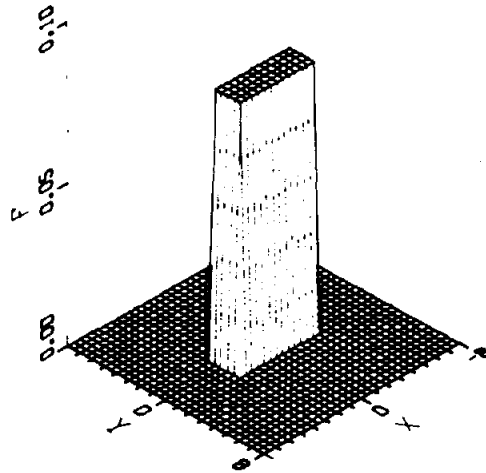


Figure 5-6. A Plot of Eq. (5.3-24) With $a = 3$, $b = 1$, and $\theta = 0$. (θ is the angle between the x -axis and the t_1 -axis)

A plot of Eq. (5.3-25) is shown in Figure 5-7. The parameters used for this plot are $c = 5$, $d = 2$, and the angle θ between the x -axis and the t_1 -axis is 60° . The $t_1 - t_2$ axes are called the principal axes (or principal directions) of this distribution because of its symmetry about them.

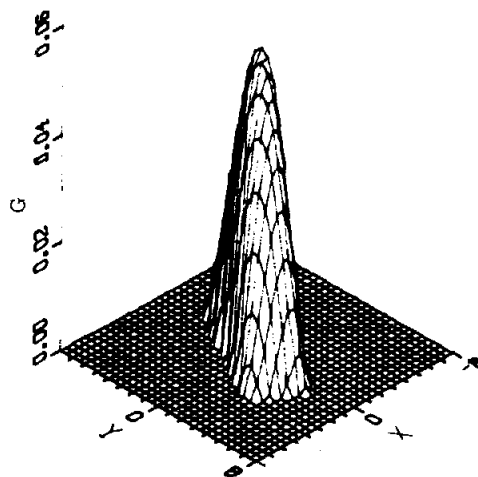


Figure 5-7. A Plot of Eq. (5.3-25) With $c = 5$, $d = 2$, and $\theta = 60^\circ$. (θ is the angle between the x -axis and the t_1 -axis.)

These functions are normalized to unit volume in order to properly simulate two-dimensional probability density functions. The convolution of these distributions

$$H = F * G \tag{5.3-26}$$

is shown graphically in Figure 5-8.

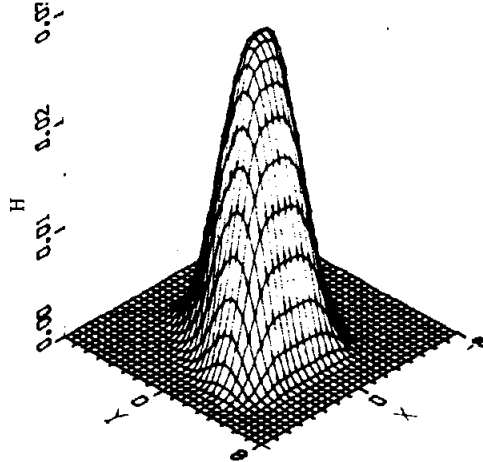


Figure 5-8. A Plot of $H = F * G$

This convolution was calculated numerically using subroutine CONV of program HELIOS. The essential part of the calculation is done within this routine by the fast Fourier transform routine FOURT which is described in Reference 5.7. More details on the use of FOURT to calculate two-dimensional convolutions are given in Section 7.3.

5.3.6 The Central-Limit Theorem

As more and more distributions are convolved together (two-dimensional convolution is defined by Eq. (5.3-2), the resultant distribution tends toward a normal distribution. This is a result of the Central Limit Theorem. Rather than go through an extended discussion, we refer the reader to the literature (see Section 11.3 of Papoulis).^{5.9} In this section we illustrate some consequences of the Central Limit Theorem that are relevant to applications of the Helios model.

As our first example, consider the distribution G of Eq. (5.3-25). A plot of this with $c = 3$, $d = 1.5$, and $\theta = 0$ (θ is the angle between the x-axis and the t_1 - axis) is shown in Figure 5-9. The mean-square widths of the distribution G along its principal axes are

$$\langle t_1^2 \rangle = \iint x^2 G(x, y) dx dy = \frac{c^2}{5} \tag{5.3-27}$$

and

$$\langle t_2^2 \rangle = \iint y^2 G(x, y) dx dy = \frac{d^2}{5} . \quad (5.3-28)$$

For the parameters of the distribution used in this example ($c = 3$, $d = 1.5$, $\theta = 0$), we get

$$\sqrt{\langle x^2 \rangle} = \sqrt{\langle t_1^2 \rangle} = \frac{c}{\sqrt{5}} = 1.34 \quad (5.3-29)$$

and

$$\sqrt{\langle y^2 \rangle} = \sqrt{\langle t_2^2 \rangle} = \frac{d}{\sqrt{5}} = 0.67 . \quad (5.3-30)$$

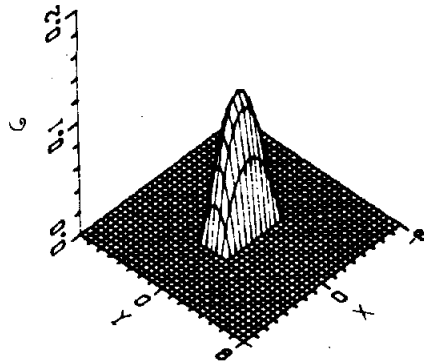


Figure 5-9. A Plot of G in Eq. (5.3-25) With $c = 3$, $d = 1.5$, and $\theta = 0^\circ$

Comparing the results of Eqs. (5.3-29) and (5.3-30) with Eqs. (5.2-8b) and (5.2-9), we get $\sigma_x = 1.34$ and $\sigma_y = 0.67$ as the standard deviations of an elliptic-normal distribution with the same mean-square widths along its principal axes. A plot of the elliptic-normal distribution is shown in Figure 5-10. The elliptic-normal distribution that has the same principal axes as another distribution and has the same root-mean-square widths along these principal axes shall hereafter be designated as the elliptic-normal approximation "associated" with the other distribution. The associated elliptic-normal approximation is often useful in convolution calculations.

In order to indicate more clearly how distribution G of Figure 5-9 differs from its associated circular-normal approximation of Figure 5-10, we show a plot of slices across the center of both of these distributions in Figure 5-11. The slices are in the x and y directions. The solid curves correspond to G of Figure 5-9 and the dashed curves correspond to its associated elliptic-normal approximation of Figure 5-10.

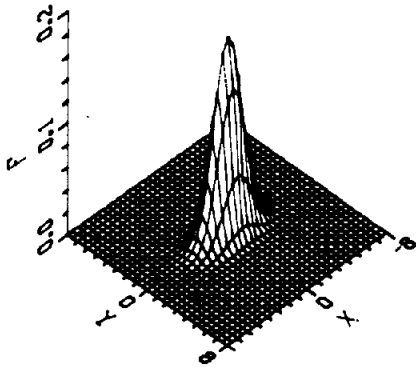


Figure 5-10. The Elliptic-Normal Approximation Associated With the Distribution of Figure 5-9

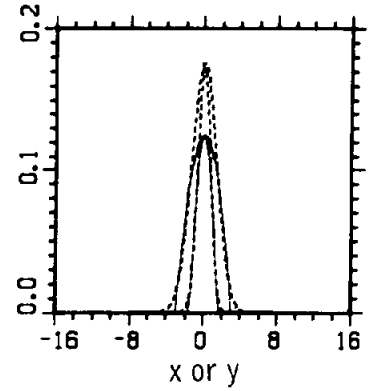


Figure 5-11. Slices in the x and y Directions Across the Centers of the Distributions of Figure 5-9 (solid curves) and Figure 5-10 (dashed curves)

When the distribution G of Figure 5-9 is convolved with itself, the result shown in Figure 5-12 is obtained.

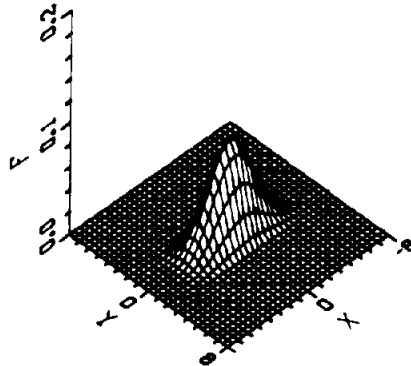


Figure 5-12. The Result of Convoluting Distribution G (of Figure 5-9) With Itself

The mean-square widths of the convolution $G * G$ are equal to twice those of the distribution G . The associated elliptic-normal distribution with mean-square widths matching that of $G * G$, looks much the same as the plot of Figure 5-12. Rather than show a separate three-dimensional plot, we show a graph of slices in both the x and the y directions across the center of both distributions in Figure 5-13. The solid curves represent the convolution $G * G$ whereas the dashed curves represent its associated elliptic-normal approximation.

Note that although the distribution G differs significantly from its associated elliptic normal as shown in Figure 5-11, the convolution $G * G$ is better represented by its associated elliptic normal as seen in Figure 5-13,

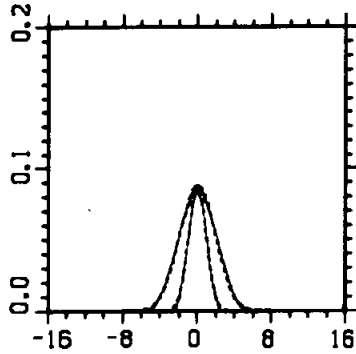


Figure 5-13. Slices Across the Center of the Convolution $G * G$ (solid curves) and Across the Center of the Associated Elliptic-Normal Approximation (dashed curves)

As another illustration of the Central Limit Theorem, we convolve the sunshape with an elliptic-normal error cone to obtain the effective sunshape. This is an especially useful example because the sunshape is sometimes approximated by its associated circular-normal distribution to expedite convolving it with the error cone. We illustrate this convolution with two error cones, one that is wider and one that is narrower than the sunshape.

We now illustrate the Central Limit Theorem using the measured sunshape previously described in Section 5.2.5 and graphed in Figure 5-3. This sunshape (for $\rho \leq 10$ mrad) has a root-mean-square radius equal to 2.96 mrad and its associated circular-normal approximation (equal mean-square radius) has a dispersion of $\sigma = 2.09$ mrad. A three-dimensional plot of this sunshape is shown in Figure 5-14.

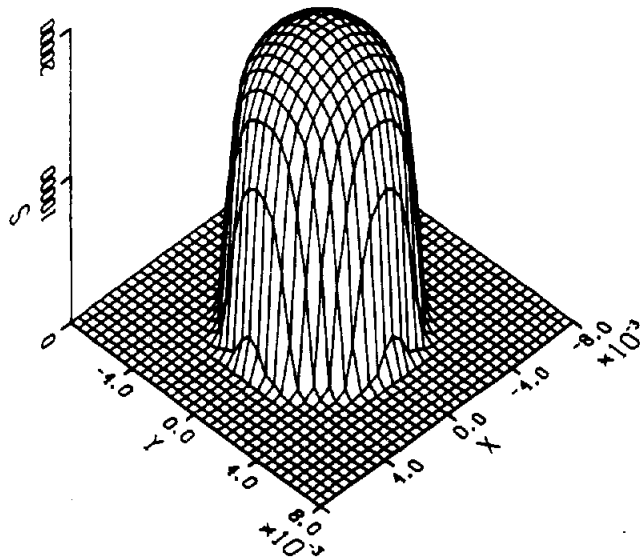


Figure 5-14. Measured Sunshape

The circular-normal approximation associated with the sunshape of Figure 5-14 is shown in Figure 5-15. The difference between the distributions is obvious from the three-dimensional plots. Figure 5-3 is also useful for observing this difference.

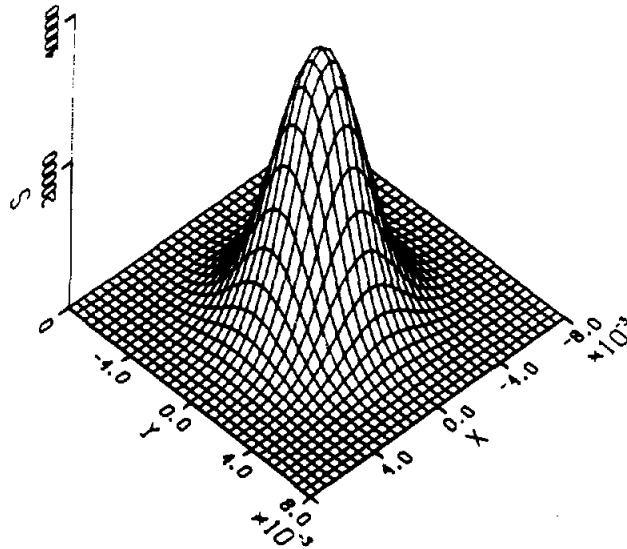


Figure 5-15. Circular-Normal Distribution ($\sigma = 2.09$ mrad)
Associated With the Measured Sunshape of
Figure 5-14

Now suppose we convolve this sunshape with an elliptic-normal error cone, F , with standard deviations $\sigma_x = 4$ mrad and $\sigma_y = 3$ mrad. This error cone is shown in Figure 5-16.

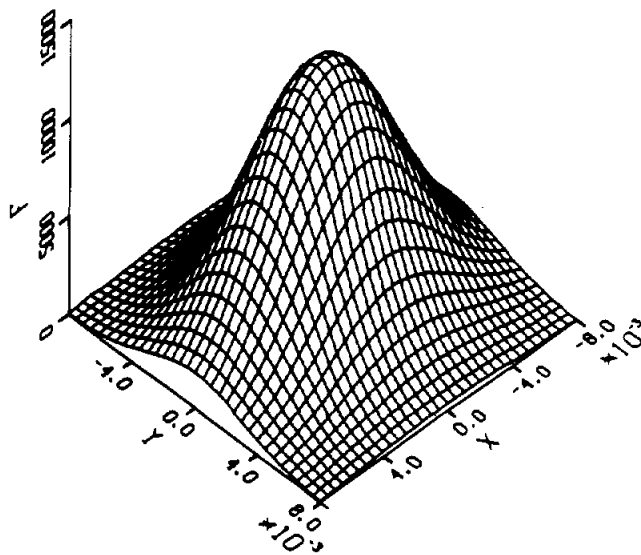


Figure 5-16. Elliptic-Normal Error Cone
With $\sigma_x = 4$ mrad and $\sigma_y = 3$ mrad

The convolution of the sunshape with this error cone gives the effective sunshape shown in Figure 5-17. For convenience in comparing this effective sunshape with its associated elliptic-normal approximation they are plotted together in Figure 5-18. The solid curves show slices across the center of the effective sunshape in the x and y directions. The dashed curves show the same slices across the associated elliptic normal distribution. The elliptic-normal approximation to the effective sunshape has standard deviations,

$$\sigma_x = \left[(2.09 \text{ mrad})^2 + (4.0 \text{ mrad})^2 \right]^{1/2} = 4.51 \text{ mrad} \quad (5.3-31a)$$

and

$$\sigma_y = \left[(2.09 \text{ mrad})^2 + (3.0 \text{ mrad})^2 \right]^{1/2} = 3.66 \text{ mrad} . \quad (5.3-31b)$$

These were obtained by using results of Section 5.3.2 to analytically convolve the elliptic-normal error cone with the elliptic normal approximation associated with the sunshape.

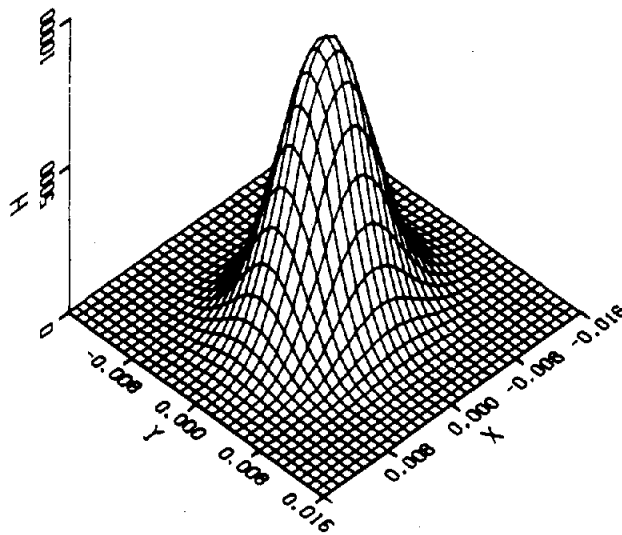


Figure 5-17. The Effective Sunshape Obtained by Convoluting the Sunshape of Figure 5-14 With the Error Cone of Figure 5-16 .

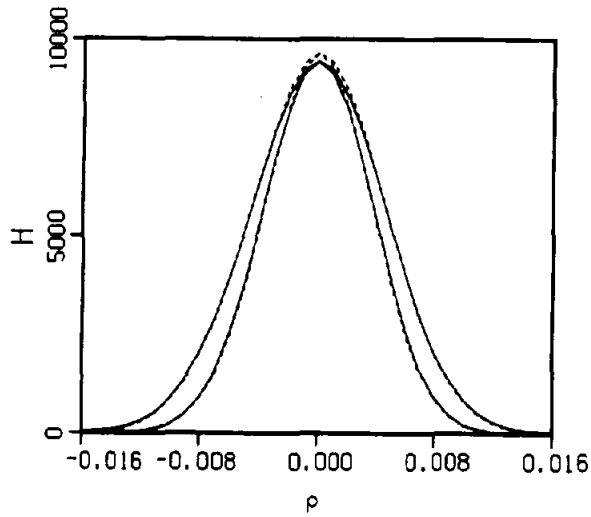


Figure 5-18. Slices Across the Center of the Effective Sunshape (solid curves) in the x and y Directions and Across Its Associated Elliptic-Normal Approximation (dashed curves)

In this illustration the root-mean-square widths of the error cone along both principal axes are larger than the corresponding root-mean-square widths of the sunshape. The resulting effective sunshape is in good agreement with its associated circular-normal approximation. In the next example we illustrate the reverse situation in which the error cone is narrower than the sunshape.

Consider the elliptic-normal error-cone, F, shown in Figure 5-19 where $\sigma_x = 1$ mrad and $\sigma_y = 0.5$ mrad.

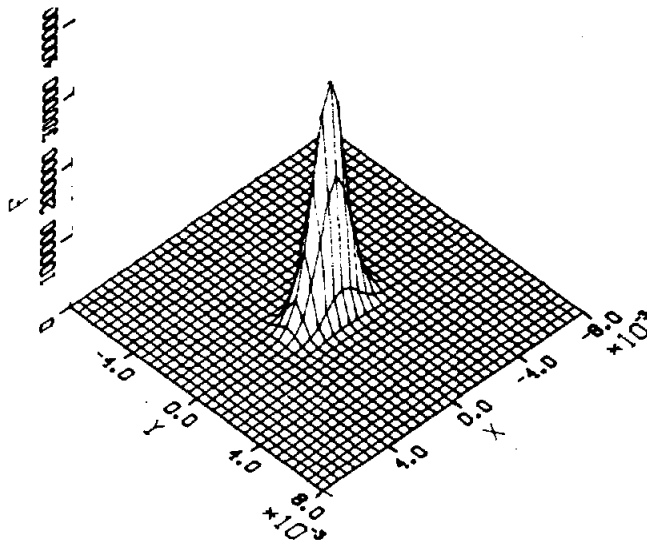


Figure 5-19. Elliptic-Normal Error Cone With $\sigma_x = 1.0$ mrad and $\sigma_y = 0.5$ mrad

Convolving this error cone with the sunshape of Figure 5-14 gives the effective sunshape, H , shown in Figure 5-20.

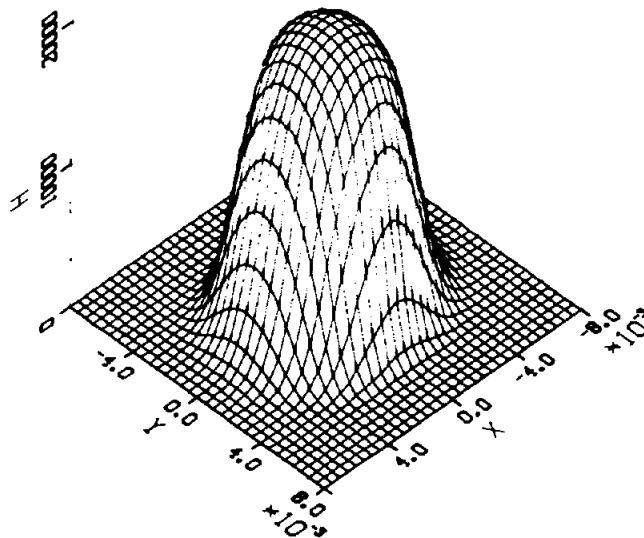


Figure 5-20. The Effective Sunshape Resulting From Convolution of the Sunshape of Figure 5-14 With the Error Cone of Figure 5-19

In order to compare this effective sunshape with its associated elliptic-normal approximation, we show curves in Figure 5-21 that represent slices across the center of both distributions in both the x and y directions. The solid curves correspond to the effective sunshape of Figure 5-20 and the dashed curves represent its associated elliptic-normal approximation in which

$$\sigma_x = \left[(2.09 \text{ mrad})^2 + (1.0 \text{ mrad})^2 \right]^{1/2} = 2.32 \text{ mrad} \quad (5.3-32a)$$

and

$$\sigma_y = \left[(2.09 \text{ mrad})^2 + (0.5 \text{ mrad})^2 \right]^{1/2} = 2.15 \text{ mrad} . \quad (5.3-32b)$$

In this example where the error cone is narrower along both principal axes than is the sunshape, the resulting effective sunshape is not well approximated by its associated elliptic normal.

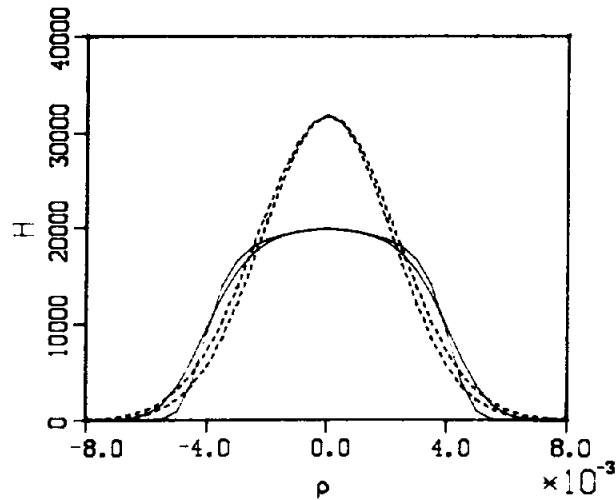


Figure 5-21. Slices Across the Center of the Effective Sunshape of Figure 5-20 (solid curves) in the x and y Directions and Corresponding Slices of its Associated Elliptic-Normal Approximation (dashed curves)

5.4 Mapping of Distributions

Earlier in the chapter we described a technique for specifying the optical quality of a reflecting concentrator in terms of error distributions. We defined a reference-plane method for use in representing these distributions and discussed convolution of two-dimensional distributions. In order to make use of these concepts in the Helios model, it is frequently necessary to map a distribution from one reference system to another. In this section we develop some of the most common mappings that occur in the analysis of solar reflectors.

It is convenient to specify surface slope errors in a system that is defined with respect to the concentrator, but these errors must be interpreted in a system that is defined with respect to the reflected rays in order to determine their effect on reflected-beam quality. This involves a mapping of error distributions from a concentrator reference system to a reflected-ray reference system. Sun-tracking errors are naturally specified using separate angular distributions for errors about each tracking axis. These errors must be mapped into a concentrator reference system, then further mapped into the reflected-ray reference system in order to determine their effect on the quality of the reflected beam.

5.4.1 Mapping From a Concentrator Reference Plane to a Reflected-Ray Reference Plane

Figure 5-22 shows a small increment of the reflector reference surface at the origin of a rectangular coordinate system x-y-z. The reference-surface unit normal \hat{N}_O is along the z-axis. A ray of light incident on this area along unit vector \hat{A} at an angle of incidence μ would

reflect along \hat{B}_O . The coordinate system is oriented so that the plane of incidence (plane containing \hat{A} , \hat{N}_O , \hat{B}_O) coincides with the y-z plane. This is the sun-concentrator coordinate system described in Chapter 3. It is a convenient system for use in describing the reflection of light rays because the tangential fan lies in a coordinate plane (the y-z plane). When the actual surface normal \hat{N} differs from \hat{N}_O (nonzero slope error), what happens to the reflected ray \hat{B} ? In addition, what is the corresponding distribution of reflected rays for a given distribution of slope errors? To facilitate answering these questions we have defined two reference planes. The P-Q plane at unit distance from the origin is perpendicular to the reference surface normal \hat{N}_O and has its P axis parallel to the x axis. The U-V plane at unit distance from the origin, is perpendicular to the reflected reference ray \hat{B}_O with its U axis parallel to the x-axis.

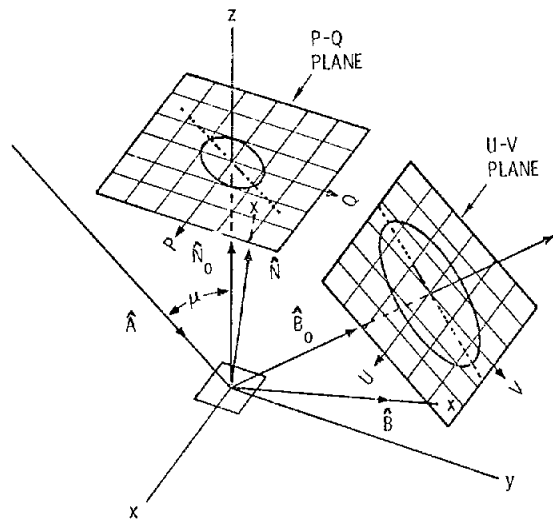


Figure 5-22. The Concentrator Reference Plane (P-Q) and the Reflected-Ray Reference Plane (U-V) Showing the $\exp(-1/2)$ Contour of an Elliptic-Normal Slope-Error Distribution in Both Planes. In the P-Q plane (Fig. 5-23) $\theta = 57.9^\circ$, $\sigma_1 = 1.29$ mrad, and $\sigma_2 = 0.92$ mrad. In the U-V plane (Fig. 5-24) $\beta = 74.8^\circ$, $\eta_1 = 2.45$ mrad, and $\eta_2 = 1.36$ mrad

We designate a distribution of slope errors in the P-Q plane by $G(P, Q)$ and wish to determine the corresponding distribution $H(U, V)$ of reflected rays in the U-V plane, assuming that the direction of the incoming ray \hat{A} is held fixed. This mapping from the P-Q plane to the U-V plane is determined by the law of specular reflection and by the geometry of Figure 5-22. The basis for this transformation is

$$|Gds_1| = |Hds_2| \quad (5.4-1)$$

where ds_2 is the area swept out in the U-V plane by the reflected ray \hat{B} whenever the surface normal \hat{N} sweeps out the area ds_1 in the P-Q plane. An equivalent but more convenient form of this expression is

$$H = G \left| \frac{ds_1}{ds_2} \right| = G \left| \frac{\partial(P, Q)}{\partial(U, V)} \right|, \quad (5.4-2)$$

where we have used the Jacobian of the variable P and Q with respect to U and V in the last term of the equation.

The unit vector \hat{N} (extended) intercepts the P-Q plane at the point (P, Q) and the unit vector \hat{B} (extended) intercepts the U-V plane at the point (U, V). The unit vectors \hat{N}_O and \hat{B}_O point to the origins of the P-Q and U-V planes, respectively, as mentioned earlier. From the geometry of Figure 5-22, the column vector consisting of the x, y, z components of the difference $\hat{B} - \hat{B}_O$ to first order in the small quantities U and V is

$$\hat{B} - \hat{B}_O = \begin{bmatrix} U \\ V \cos \mu \\ -V \sin \mu \end{bmatrix}, \quad (5.4-3)$$

where μ is the angle of incidence of incoming ray \hat{A} with respect to the reference surface normal \hat{N}_O . Next we use Eq. (4.1-5) to express this same difference but in terms of the coordinates P and Q. To first order in the small quantities P and Q, the result is

$$\hat{B} - \hat{B}_O = \begin{bmatrix} 0 & 0 & 2P \\ 0 & 0 & 2Q \\ 2P & 2Q & 0 \end{bmatrix} \begin{bmatrix} 0 \\ -\sin \mu \\ \cos \mu \end{bmatrix} = \begin{bmatrix} 2P \cos \mu \\ 2Q \cos \mu \\ -2Q \sin \mu \end{bmatrix}. \quad (5.4-4)$$

Equating corresponding components in the two preceding equations gives

$$U = 2P \cos \mu \quad (5.4-5a)$$

and

$$V = 2Q. \quad (5.4-5b)$$

From this result we evaluate the Jacobian needed in Eq. (5.4-2) to get

$$\frac{\partial(P, Q)}{\partial(U, V)} = \frac{1}{4 \cos \mu} \quad (5.4-6)$$

and finally

$$H(U, V) = \frac{G \left[\frac{U}{2 \cos \mu}, \frac{V}{2} \right]}{4 \cos \mu}. \quad (5.4-7)$$

This is a useful result for mapping a distribution G from the concentrator reference plane P-Q to obtain the corresponding distribution H in the reflected-ray reference plane U-V.

5.4.2 Mapping Elliptic-Normal Distributions From a Concentrator Reference Plane to a Reflected-Ray Reference Plane

In this section we apply the results of the preceding section to map a general elliptic-normal distribution from the P-Q plane of Figure 5-22 to the U-V plane. This is especially useful because a common way to specify slope errors is to use an elliptic-normal distribution or its special case, the circular-normal distribution.

We specify an elliptic-normal distribution in the P-Q plane by writing an equation for it in terms of its principal-axis coordinates t_1 and t_2 and an angle of rotation θ . The angle θ is measured from the P axis to the t_1 axis. In its principal axis system, the elliptic-normal distribution is

$$F(t_1, t_2) = \frac{1}{2\pi\sigma_1\sigma_2} \exp \left\{ -\frac{1}{2} \left[\frac{t_1^2}{\sigma_1^2} + \frac{t_2^2}{\sigma_2^2} \right] \right\} \quad (5.4-8)$$

where σ_1 and σ_2 are standard deviations along the t_1 and t_2 axes, respectively. Figure 5-22 shows the $\exp(-1/2)$ contour for F of Eq. (5.4-8) in the P-Q plane for the case where the axis t_1 is along the dotted line, $\sigma_1 = 1.29$ mrad, $\sigma_2 = 0.92$ mrad, and $\theta = 57.9^\circ$. Principal axis t_2 is perpendicular to t_1 , but it is not drawn in the figure. The grid spacing in the reference planes of Figure 5-22 is 0.001 in each direction. When the slope error β between \hat{N}_0 and \hat{N} is a few milliradians or less, the radial distance from the origin in the P-Q plane to the point (P, Q) that identifies \hat{N} is approximately equal to the angle β in radians. This occurs because

$$\rho = \tan \beta = \beta + \beta^3/3 + \dots \quad (5.4-9)$$

and β is a good approximation to $\tan \beta$ when $\beta \ll 1$. We, therefore, sometimes use the terminology milliradians for ρ as a convenient means of designating intervals of 0.001 in a reference plane.

Figure 5-23 shows the orientation of the $t_1 - t_2$ system in the P-Q plane. A portion of the $\exp(-1/2)$ contour of an elliptic-normal distribution with standard deviations σ_1 and σ_2 is also shown.

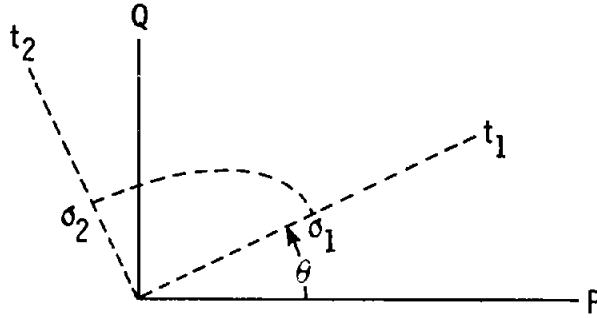


Figure 5-23. A Portion of the $\exp(-1/2)$ Contour of an Elliptic-Normal Distribution With Standard Deviations σ_1 and σ_2 Along Principal Axes t_1 and t_2 , Respectively

The P-Q variables are related to the principal-axis coordinates t_1 and t_2 by

$$t_1 = P \cos \theta + Q \sin \theta \quad (5.4-10a)$$

$$t_2 = -P \sin \theta + Q \cos \theta \quad (5.4-10b)$$

We now designate the quadratic form inside the brackets of the exponential of Eq. (5.4-8) by Z , use the system of Eqs. (5.4-10) to eliminate t_1 and t_2 , then use the system (5.4-5) to eliminate the P and Q to finally get a description of Z in the U-V plane.

$$Z = aU^2 + 2kUV + bV^2, \quad (5.4-11)$$

where

$$a = \frac{1}{4 \cos^2 \mu} \left[\frac{\cos^2 \theta}{\sigma_1^2} + \frac{\sin^2 \theta}{\sigma_2^2} \right] \quad (5.4-12a)$$

$$k = \frac{\sin \theta \cos \theta}{4 \cos \mu} \left[\frac{1}{\sigma_1^2} - \frac{1}{\sigma_2^2} \right] \quad (5.4-12b)$$

$$b = \frac{1}{4} \left[\frac{\sin^2 \theta}{\sigma_1^2} + \frac{\cos^2 \theta}{\sigma_2^2} \right]. \quad (5.4-12c)$$

The principal axes w_1 - w_2 of this quadratic form Z in the U-V plane are along the eigenvectors of the matrix

$$M = \begin{bmatrix} a & k \\ k & b \end{bmatrix} . \quad (5.4-13)$$

In this system the cross term vanishes and Z becomes

$$Z = \lambda_1 w_1^2 + \lambda_2 w_2^2 = \frac{w_1^2}{\eta_1^2} + \frac{w_2^2}{\eta_2^2} \quad (5.4-14)$$

where λ_1 and λ_2 are eigenvalues of M corresponding to the eigenvectors along the axes w_1 and w_2 , respectively. The standard deviations η_1 and η_2 are associated with the axes w_1 and w_2 , respectively, in the U - V plane. The eigenvalues are related to the standard deviations by

$$\lambda_1 = \frac{1}{\eta_1^2} \quad (5.4-15a)$$

and

$$\lambda_2 = \frac{1}{\eta_2^2} . \quad (5.4-15b)$$

The theory of quadratic forms used in this development is given in Chapter 12 of Noble.^{5,10}

Figure 5-24 shows the w_1 - w_2 system in the U - V plane. The angle β specifies the orientation of the w_1 axis with respect to the U axis.

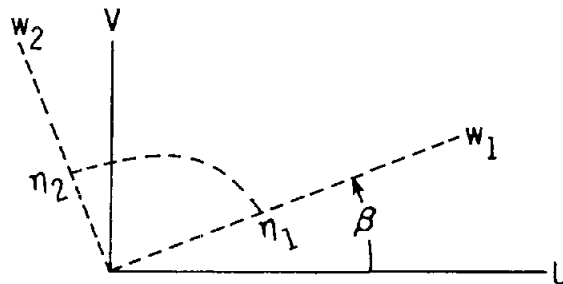


Figure 5-24. Principal Axes w_1 - w_2 in the U - V Plane Showing Part of the $\exp(-1/2)$ Contour

The eigenvalues of M are

$$\lambda = \frac{1}{2} \left[a + b \pm \sqrt{(a - b)^2 + 4k^2} \right], \quad (5.4-16)$$

where λ_1 corresponds to one of the signs in front of the square root and λ_2 to the other sign.

The angle β is given by

$$\beta = \arctan \left[\frac{\lambda_1 - a}{k} \right] \quad (5.4-17)$$

Figure 5-22 shows an example of this mapping. As mentioned earlier, the ellipse in the P-Q plane is the $\exp(-1/2)$ contour of an elliptic-normal distribution with $\theta = 57.9^\circ$, $\sigma_1 = 1.29$ mrad, and $\sigma_2 = 0.92$ mrad. The dotted line indicates the direction of the t_1 axis in the P-Q plane. The corresponding distribution in the U-V plane is specified by $\beta = 74.8^\circ$, $\eta_1 = 2.45$ mrad, and $\eta_2 = 1.36$ mrad. The direction of the w_1 axis is indicated by the dotted line. The grid spacing in Figure 5-22 is 1 mrad. The $\exp(-1/2)$ contours were drawn by computer using DISSPLA graphics. ^{5.11}

In the special case, $\theta = 0$, the quadratic form Z of Eq. (5.4-11) is already in its principal axis system so $\beta = 0$ and from Eq. (5.4-12b) $k = 0$. Comparing Eq. (5.4-11) with Eq. (5.4-14) we get $\lambda_1 = a$ and $\lambda_2 = b$. Combining this with Eqs. (5.4-12) and (5.4-15), we obtain

$$\eta_1 = 2\sigma_1 \cos \mu \quad (5.4-18a)$$

and

$$\eta_2 = 2\sigma_2 \quad (5.4-18b)$$

When σ_1 and σ_2 are equal, the distribution in the P-Q plane becomes circular normal and the value selected for θ is arbitrary. We, therefore, set $\theta = 0$ and use the result above with $\sigma_1 = \sigma_2 = \sigma$ to get

$$\eta_1 = 2\sigma \cos \mu \quad (5.4-19a)$$

$$\eta_2 = 2\sigma \quad (5.4-19b)$$

Therefore, when a circular-normal distribution is mapped from the P-Q plane to the U-V plane, it becomes elliptic normal except at normal incidence ($\mu = 0$). For example, at $\mu = 60^\circ$, a circular-normal distribution of dispersion $\sigma = 1$ mrad in the P-Q plane corresponds to an elliptic-normal

distribution in the U-V plane with a standard deviation $\eta_1 = 1$ mrad in the U direction, and a standard deviation $\eta_2 = 2$ mrad in the V direction.

It is instructive to calculate the mean-square radius of the elliptic-normal distribution in the U-V plane that corresponds to an arbitrary elliptic-normal distribution in the P-Q plane. Applying Eq. (5.2-10) to an elliptic-normal distribution in the U-V plane gives

$$\langle \rho^2 \rangle = \eta_1^2 + \eta_2^2 . \quad (5.4-20)$$

Now using Eqs. (5.4-15) gives

$$\langle \rho^2 \rangle = \frac{1}{\lambda_1} + \frac{1}{\lambda_2} = \frac{\lambda_1 + \lambda_2}{\lambda_1 \lambda_2} . \quad (5.4-21)$$

From the theory of matrices

$$\text{Tr}M = \lambda_1 + \lambda_2 \quad (5.4-22)$$

and

$$\text{Det} M = \lambda_1 \lambda_2 . \quad (5.4-23)$$

These results enable us to express the mean-square radius in terms of the trace and determinant of the matrix, M (Eq. (5.4-13)), to get

$$\langle \rho^2 \rangle = \frac{\text{Tr}M}{\text{Det} M} = \frac{a + b}{ab - k^2} \quad (5.4-24)$$

where a, b, k are defined in Eqs. (5.4-12). Eliminating these parameters and simplifying the result gives

$$\langle \rho^2 \rangle = 4\sigma_1^2 \left[\sin^2 \theta + \cos^2 \mu \cos^2 \theta \right] + 4\sigma_2^2 \left[\cos^2 \theta + \cos^2 \mu \sin^2 \theta \right] . \quad (5.4-25)$$

In the special case where $\theta = 0$, this reduces to

$$\langle \rho^2 \rangle = 4\sigma_1^2 \cos^2 \mu + 4\sigma_2^2 \quad (5.4-26)$$

which agrees with the result obtained from Eqs. (5.4-18) and (5.4-20).

Another special case of interest is when $\sigma_1 = \sigma_2 = \sigma$. Here Eq. (5.4-25) reduces to

$$\langle \rho^2 \rangle = 4\sigma^2 (1 + \cos^2 \mu) \quad (5.4-27)$$

from which the root-mean-square width of a reflected-ray distribution corresponding to a circular-normal slope-error distribution of dispersion σ is

$$\sqrt{\langle \rho^2 \rangle} = 2\sigma \sqrt{1 + \cos^2 \mu} . \quad (5.4-28)$$

If we select a circular-normal distribution in the U-V plane that has this same root-mean-square radius, its dispersion $\tilde{\sigma}$ is related to the P-Q plane dispersion σ by using Eq. (5.2-17) to get

$$\tilde{\sigma} = 2\sigma \sqrt{\frac{1 + \cos^2 \mu}{2}} . \quad (5.4-29)$$

At normal incidence ($\mu = 0$), this gives the well-known result $\tilde{\sigma} = 2\sigma$. At nonnormal incidence ($\mu \neq 0$), $\tilde{\sigma} < 2\sigma$. At $\mu = 30^\circ$, for example, $\tilde{\sigma} = 1.87\sigma$.

5.4.3 Mapping Sun-Tracking Errors to a Concentrator Reference Plane

In order to keep the reflected solar radiation fixed on the receiver as the sun position varies, a typical heliostat utilizes two axes of rotation. The sun-tracking mechanism has error tolerances. Our purpose here is to interpret these errors in terms of their effect on the reflected central ray so that sun-tracking errors can be combined with other kinds of errors for use in the Helios model.

Figure 5-25 shows a schematic drawing of a heliostat frame that follows the sun by rotating about the horizontal axis u_1 and about the vertical axis \tilde{Z} . The heliostat coordinate system has its origin at the center of the heliostat reference surface, its u_1 and u_2 axes are perpendicular to its sides as shown in the figure, and u_3 is along the normal \hat{N}_O to the reference surface at the origin. Assume that a central ray from the sun is incident on the center of the heliostat along \hat{A} . The intersection of the plane of incidence with the heliostat frame is indicated by the dashed line in the figure. The sun-concentrator system for the center of the heliostat is indicated by the axes x-y-z.

We designate the angle between the reference-surface normal \hat{N}_O and the vertical sun-tracking axis \tilde{Z} by β , and the angle between the x-axis of the sun-concentrator system and the u_2 axes of the heliostat system by θ as indicated in Figure 5-25. Suppose that sun-tracking errors are specified separately using distributions about the tracking axes u_1 and \tilde{Z} . How do we map this description to the reflector reference plane P-Q? (Figure 5-22 defines this P-Q plane in the sun-concentrator system.)

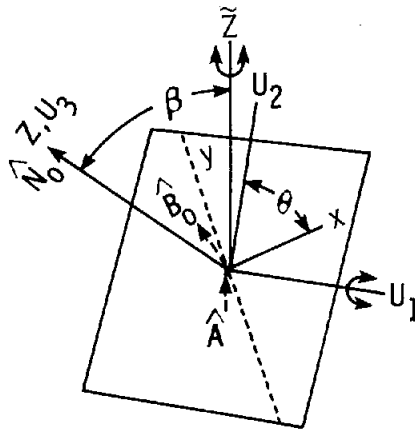


Figure 5-25. Heliostat System $u_1 - u_2 - u_3$;
Sun-Concentrator System x, y, z ;
and Sun-Tracking Axes u_1 and
 \tilde{z}

First consider motion about the u_1 sun-tracking axis. When sun-tracking errors cause the heliostat frame to rock back and forth about its correct alignment on the u_1 axis, the surface normal \hat{N} will deviate from its correct direction \hat{N}_0 and trace out a line in the P-Q reference plane as indicated by the axis t_1 in Figure 5-26. When the heliostat frame rotates through an angle, α , the position of \hat{N} in the U-V plane moves a distance $\tan \alpha$ along the axis t_1 to give $t_1 = \tan \alpha$.

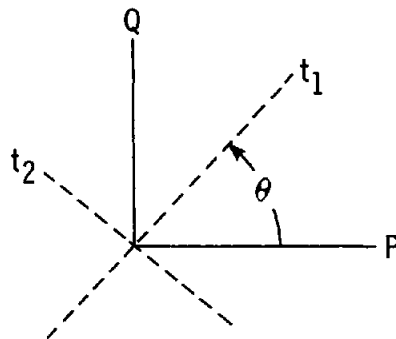


Figure 5-26. Sun-Tracking Errors
in the P-Q Plane

Now consider the rocking motion of the heliostat frame about its vertical tracking axis \tilde{z} . This causes the tip of the vector \hat{N} to move in a circular arc. It is convenient to view this motion from the top as shown in Figure 5-27 where the \tilde{z} axis is perpendicular to the page at 0. A sun-tracking error δ causes \hat{N} to move along an arc that is tangent to t_2 . The value of t_2 corresponding to δ is

$$t_2 = \sin \beta \tan \delta. \quad (5.4-30)$$

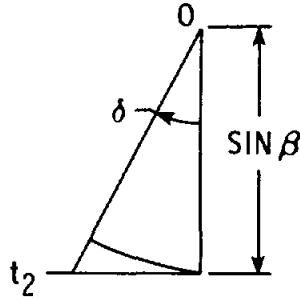


Figure 5-27. The Geometry for Rotation About Sun-Tracking Axis \tilde{Z} as Viewed From the Top

We designate the distribution of sun-tracking errors α about the horizontal axis u_1 by $F(p)$ where $p = \tan \alpha$ and the distribution of sun-tracking errors about the vertical axis \tilde{Z} by $G(s)$ where $s = \tan \delta$. The sun-tracking errors α and δ are measured in radians. The one-dimensional distributions F and G are normalized to unity when integrated from minus infinity to plus infinity. If the sun-tracking errors about these two axes are independent of each other, the corresponding P-Q plane description H becomes

$$H(t_1, t_2) = \frac{1}{\sin \beta} F(t_1) G\left(\frac{t_2}{\sin \beta}\right) \quad (5.4-31)$$

where t_1 and t_2 are related to P and Q by a rotation θ as indicated in Figure 5-26. The factor $1/\sin \beta$ is needed to preserve the unit normalization of the distribution.

For the important special case of normally distributed sun-tracking errors

$$F(p) = \frac{1}{\sqrt{2\pi} \sigma_p} \exp \left\{ -\frac{1}{2} \left(\frac{p}{\sigma_p} \right)^2 \right\} \quad (5.4-32)$$

and

$$G(s) = \frac{1}{\sqrt{2\pi} \sigma_s} \exp \left\{ -\frac{1}{2} \left(\frac{s}{\sigma_s} \right)^2 \right\} . \quad (5.4-33)$$

The corresponding distribution H is the elliptic-normal distribution

$$H(t_1, t_2) = \frac{1}{2\pi\sigma_1\sigma_2} \exp \left\{ -\frac{1}{2} \left[\frac{t_1^2}{\sigma_1^2} + \frac{t_2^2}{\sigma_2^2} \right] \right\} \quad (5.4-34)$$

where

$$\sigma_1 = \sigma_p \quad (5.4-35a)$$

and

$$\sigma_2 = \sigma_s \sin \beta . \quad (5.4-35b)$$

Note that even when the sun-tracking errors are normally distributed about the tracking axes with equal standard deviations $\sigma_p = \sigma_s$, this does not lead to a distribution in the P-Q plane with equal standard deviations because of the $\sin \beta$ factor in Eq. (5.4-35b).

These results can be expressed in the P-Q system using a rotation of the coordinate system through the angle θ as shown in Figure 5-23. Then the results of the previous section are applicable to further map the sun-tracking errors to the reflected-ray reference plane (U-V plane of Figure 5-22).

5.5 Projecting the Effective Sunshape on the Receiver

The reference surface of the concentrator is divided into an integration mesh and the effective sunshape from each integration zone is projected onto the receiver. This result is weighted according to the zone size and concentrator reflectance for sunlight at the angle of incidence involved, then integrated over the entire reference surface of the concentrator. In this section we develop a method for evaluating the effective sunshape for use in this projection.

Let ΔQ of Figure 5-28 be an integration mesh zone on the concentrator-reference surface and define the "sun-concentrator" coordinate system x-y-z to have its origin centered on ΔQ , its z-axis along the normal \hat{N}_O to the reference surface at the mesh point, and its y-z plane coincide with the plane containing the incident central ray from the sun \hat{A} , the reference surface normal \hat{N}_O , and the reflected central-reference ray \hat{B}_O . In the presence of sun-tracking errors, \hat{N}_O is defined as the nominal direction of the reference-surface normal. The reflected-ray reference plane (the U-V plane) is perpendicular to the reflected central-reference ray \hat{B}_O and is at unit distance from the origin. Let P be a point on the receiver in the surface element ΔS and let \hat{M} be the outward surface normal to ΔS . Our objective here is to develop an expression for the flux density in W/cm^2 at P in terms of the effective sunshape $E(U, V)$ and the geometry of Figure 5-28.

The element of receiver area ΔS defines a solid-angle cone with respect to the origin that intercepts the U-V plane as indicated by $\Delta S'$. The areas ΔS and $\Delta S'$ are related by

$$\Delta S' = \Delta S \left(\frac{\cos \psi}{\cos \alpha} \right) \left(\frac{\sec \alpha}{r} \right)^2 , \quad (5.5-1)$$

where r is the distance from O to P and the angles α and ψ are indicated in Figure 5-28. Since the element $\Delta S'$ lies in the U-V reference plane, its normal is parallel to \hat{B}_O and makes an angle α with the reflected ray \hat{B} . The ratio in the first parenthesis on the right side of Eq. (5.5-1) corrects for the angular alignments of the two surface elements and the next factor accounts for their distances from O .

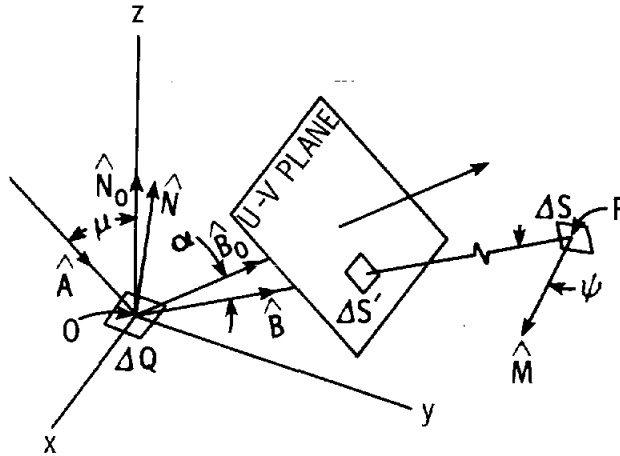


Figure 5-28. Reflected Ray Reference Plane (U-V) in the Sun-Concentrator Coordinate System x - y - z

The power reflected from ΔQ is $\rho a \Delta Q \cos \mu$ where a is the incident solar insolation in W/cm^2 , and ρ is the specular reflectance of ΔQ for sunlight at an angle of incidence μ . The fraction of this reflected power that strikes ΔS is $E \Delta S'$ giving a power contribution of

$$\Delta H = E \Delta S' a \rho \Delta Q \cos \mu = \frac{a \rho E \Delta Q \Delta S \cos \mu \cos \psi}{r^2 \cos^3 \alpha} \quad (5.5-2)$$

The corresponding contribution to the power per unit area (flux density) F at P is $\Delta F = \Delta H / \Delta S$. The flux density F at P is obtained by combining contributions received from different elements of the concentrator surface by integration to get

$$F = a \iint \frac{\rho \cos \mu \cos \psi E_Q(U, V) dQ}{r^2 \cos^3 \alpha} \quad (5.5-3)$$

The subscript Q is used to emphasize the fact that the effective sunshape E may change during integration over the concentrator surface.

The effective sunshape E is described mathematically in terms of coordinates in the reflected-ray reference plane (the $U-V$ plane of Figure 5-28). In order to project the effective sunshape on a receiver it is necessary to determine the intersection of line \overline{OP} in Figure 5-28 with the $U-V$ plane. This provides values of the variables U and V for use in E to evaluate the integrand of Eq. (5.5-3).

Figure 5-29 shows the geometry of the mesh point O , the receiver point P at coordinates (x, y, z) , and the reference plane $U-V$ in the sun-concentrator system again in a form that is convenient for the present calculation. The projection of the line \overline{OP} on the $y-z$ plane is indicated by a dashed line in the direction of the unit vector \hat{C} . The angle γ between \hat{C} and the reflected central reference ray \hat{B}_0 is given by

$$\gamma = \arctan (y/z) - \mu . \quad (5.5-4)$$

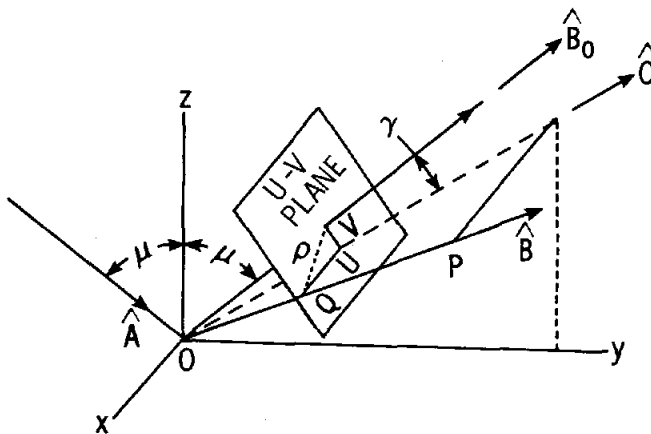


Figure 5-29. The Geometry of Receiver Point P and the Reflected-Ray Reference Plane ($U-V$) in the Sun-Concentrator System

The V coordinate of the intersection of line \overline{OP} with the $U-V$ plane is

$$V = \tan \gamma \quad (5.5-5)$$

which can be written

$$V = \frac{\frac{y}{z} - \tan \mu}{1 + \frac{y \tan \mu}{z}} \quad (5.5-6)$$

From the geometry of Figure 5-29 we can also write

$$U = x \left[\frac{1 + V^2}{y^2 + V^2} \right]^{1/2} \quad (5.5-7)$$

It is useful to express the quantities U , V , and $\rho = \tan \alpha$ (α is the angle between \hat{B}_0 and \hat{B}) in terms of the unit vectors \hat{B} , \hat{B}_0 , and \hat{C} . Also from the geometry

$$U = \frac{\sqrt{1 - (\hat{B} \cdot \hat{C})^2}}{(\hat{B} \cdot \hat{C})} \quad (5.5-8)$$

$$V = \frac{\sqrt{1 - (\hat{C} \cdot \hat{B}_0)^2}}{\hat{C} \cdot \hat{B}_0} \quad (5.5-9)$$

and

$$\rho = \sqrt{U^2 + V^2} = \frac{\sqrt{1 - (\hat{B} \cdot \hat{B}_0)^2}}{\hat{B} \cdot \hat{B}_0} \quad (5.5-10)$$

When the effective sunshape has circular symmetry, it becomes a function of the one variable ρ and it is not necessary to calculate the quantities U and V to evaluate the integrand of Eq. (5.5-3).

References

- 5.1 A. Rabl, "Comparison of Solar Concentrators," Solar Energy, 18: 93, 1976.
- 5.2 G. M. Schrenk, Analysis of Solar Reflectors - Mathematical Theory and Methodology for Simulation of Real Reflectors, GMC-AO-EDR3693, December 1963.
- 5.3 W. Grobner and N. Hofreiter, Integraltafel (zweiter teil), Springer-Verlag, 1961.
- 5.4 G. A. Korn and T. M. Korn, Mathematical Handbook for Scientists and Engineers, McGraw-Hill Book Company, Inc., 1961.
- 5.5 M. Abramowitz and I. A. Stegun, Handbook of Mathematical Functions with Formulas, Graphs, and Mathematical Tables, National Bureau of Standards Applied Mathematics Series 55, U.S. Government Printing Office, June 1965.
- 5.6 James W. Cooley, Peter A. W. Lewis, and Peter D. Welch, "Application of the Fast Fourier Transform to Computation of Fourier Integrals, Fourier Series, and Convolution Integrals," IEEE Transactions on Audio Electroacoustics, AU-15: 79, June 1967.
- 5.7 Karen H. Haskell and Rondall E. Jones, Brief Instructions for Using Mathlib (Version 7.2), SAND77-1441, June 1978.

- 5.8 Ron Bracewell, The Fourier Transform and its Applications, McGraw-Hill Book Company, Inc., 1965.
- 5.9 Athanasios Papoulis, The Fourier Integral and Its Applications, McGraw-Hill Book Company, Inc., 1962.
- 5.10 Ben Noble, Applied Linear Algebra, Prentice-Hall, Inc., 1969.
- 5.11 No personal author, DISSPLA (Display Integrated Software System and Plotting Language), Integrated Software Systems Corporation, P.O. Box 9906, San Diego, CA 92109, July 1975.

CHAPTER 6
SOLAR IRRADIATION

6.1 Atmospheric Parameters

At the present time, there are two atmospheric models that are built into HELIOS: the models for atmospheric refraction and for relative optical airmass. It is possible that future versions will relax these limitations.

6.1.1 The Refraction Model

Refraction of the visible light from the sun affects its apparent zenith angle. For angles less than 1.396 radians (80°), the true zenith angle is \leq 1.6 mrad greater than the apparent value. Table 6-I gives the refraction model used in HELIOS. The data were taken from Allen.^{6.1} Temperature and pressure effects are taken into account by multiplying the difference by

$$\left[\frac{P(\text{torr})}{760 \times \{0.962 + 0.0038 T (^{\circ}\text{C})\}} \right]$$

TABLE 6-I
Refraction Data

Apparent Elevation Angle (radians)	True Elevation Angle (radians)*	Difference
0.000000	-0.010288	.010288
.017453	.010259	.007194
.034907	.029540	.005367
.052360	.046993	.005367
.069813	.066386	.003427
.087266	.084392	.002874
.104720	.102252	.002468
.122173	.120020	.002153
.139626	.137716	.001910
.157080	.155368	.001712
.174533	.172986	.001547
.261799	.260757	.001042
.349066	.348295	.000771
.436332	.435726	.000606
.523599	.523109	.000490
.698132	.697792	.000340
.872665	.872427	.000238
1.047198	1.047033	.000165
1.221730	1.221628	.000102
1.396263	1.396215	.000048
1.570796	1.570796	.000000

* 1 atm pressure, 10°C. Data from Reference 6.1.

6.1.2 The Relative Optical Airmass Model

Degradation in the solar energy as it propagates through the atmosphere is exponentially dependent upon the amount of air traversed. This amount is described by the relative optical airmass, m . Consider a monochromatic energy flux, S_λ . In traveling a distance, ds , through the atmosphere, the energy flux will be attenuated by an amount, $dS_\lambda = -a_\lambda S_\lambda \rho ds$, where a_λ is the mass attenuation coefficient for wavelength λ and where ρ is the air density. The optical thickness of the atmosphere along a ray path from sea level to the sun is $\delta = \int_0^\infty a_\lambda \rho ds$. The optical thickness in the vertical direction is $\delta_0 = \int_0^\infty a_\lambda \rho dh$ where dh is the vertical element of path length. The relative optical airmass along the path from sea level to the sun is defined by $m = \delta/\delta_0$. If the observer is not at sea level or if weather conditions have altered the standard pressure (P_0), the effective relative airmass is given by mP/P_0 where P is the air pressure.

Photon attenuation is wavelength dependent. Even though the mass attenuation coefficient appears in the numerator and denominator of $m = \delta/\delta_0$, the relative optical airmass varies with wavelength because of variation in the path taken by photons with different wavelengths. Since these refraction effects are small, the wavelength dependence of m is neglected. In the approximation of straight-line ray paths $dh = ds \cos \zeta$ where ζ is the zenith angle for the element of ray path. Then $m = 1/\cos \zeta$ for observers at sea level. This is reasonably accurate until the zenith angle approaches $\pi/2$. Kondratyev^{6.2} furnishes data on the variation of m with the apparent zenith angle of the sun. These data are the present model used in HELIOS. The model is dependent upon the clear, dry atmosphere assumed by Kondratyev.^{6.2} The m values resulting from several atmospheric models are compared in Figure 6-1. Allen^{6.1} gives data for relative optical airmass variation in addition to his refraction data. His m values agree with the more extensive tables of Kondratyev,^{6.2} indicating their atmospheric models are consistent.

6.2 Solar Insolation

A data base of the solar energy incident upon the earth's surface is necessary if the energy collected by any solar collector is to be predicted. The atmosphere itself is the most important variable that leads to large uncertainty in predictions. ERDA (now DOE) supported a solar-energy data network extending over the continental US.^{6.4} After sufficient data are available, good estimates should be possible for sunshape and for solar insolation as a function of time-of-day, day-of-year, and weather conditions. HELIOS models for solar insolation are described here.

Scattering and absorption in the atmosphere greatly alter the sun's insolation and shape. The most important processes involved are Rayleigh scattering, Mie scattering, absorption by O_3 and H_2O , and slight absorption by O_2 , CO_2 , and CH_4 . The Rayleigh scattering occurs from various molecules in the air. The Mie scattering occurs in the aerosols (dust, water droplets) present in the atmosphere. This aerosol scattering and absorption are rather involved phenomena that depend upon the particle density, the distribution of particle size (which varies with altitude), the

complex index of refraction of the particles, and the spectral content of the radiation. Some aerosols exhibit layering phenomena where separate indices of refraction must be assigned to a core and to an outer layer. The meteorological terms "visibility" and "meteorological range" are sometimes used as an indication of particle density after a particle-size distribution is assumed. Since these effects are sensitive to the wavelength of radiation, they depend upon the extraterrestrial solar spectrum.

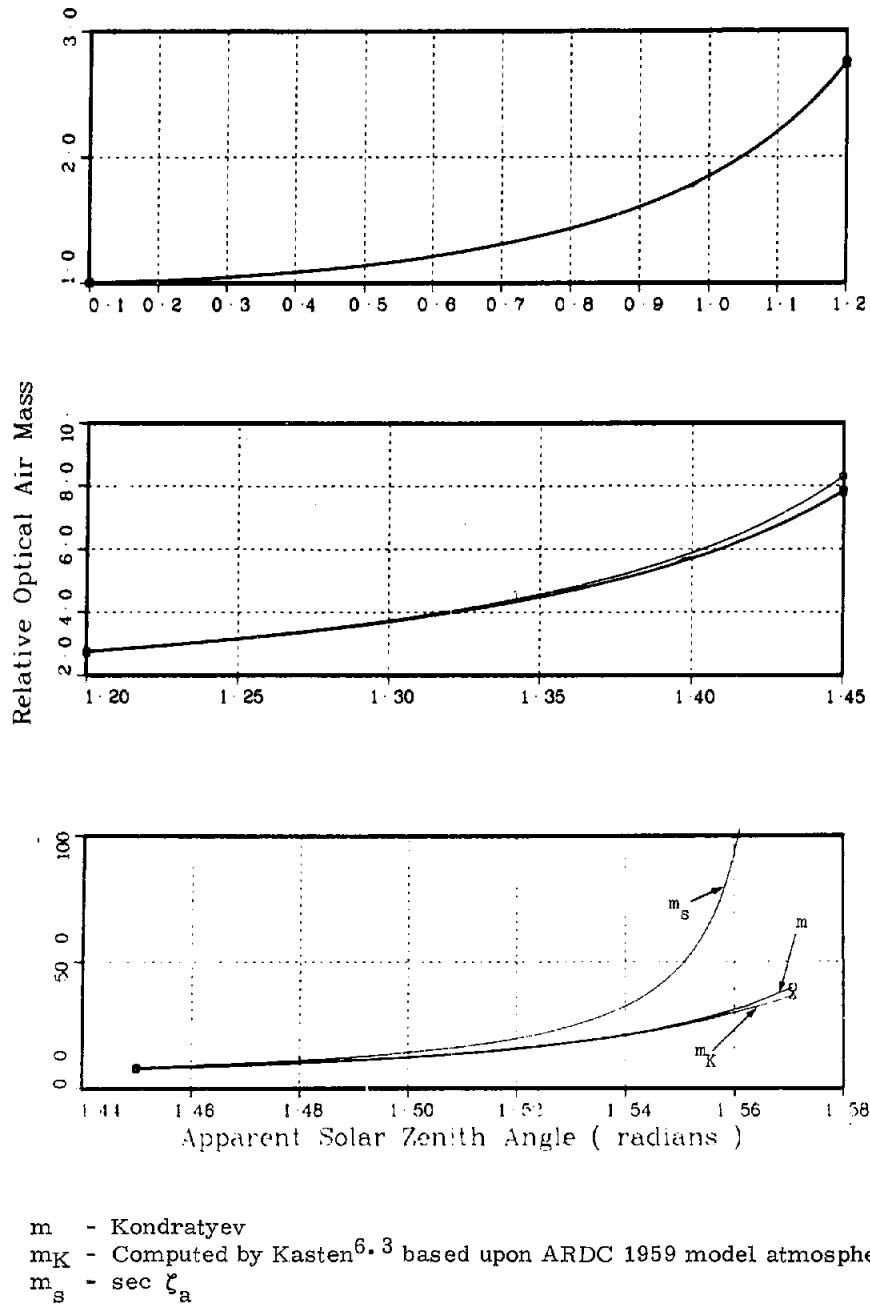


Figure 6-1. Relative Optical Airmass Variation With Apparent Solar Zenith Angle

6.2.1 Extraterrestrial Irradiation, the Solar Constant

One of the latest determinations of the solar spectrum gives the data in Figure 6-2. The data are the result of efforts of the Standards Subcommittee of the Solar Radiation Committee of the Institute of Environmental Sciences. It is appropriate for normal incidence at the earth's mean distance (one astronomical unit: $R_0 = 149.5 \times 10^6$ km) from the sun. The solar constant is the rate at which solar-radiant energy passes a unit area normal to the rays at this distance. Integration over wavelength in Figure 6-2 gives the value $S_{00} = 1353 \pm 21 \text{ W/m}^2$ or $1.940 \pm 0.03 \text{ cal min}^{-1} \text{ cm}^{-2}$.

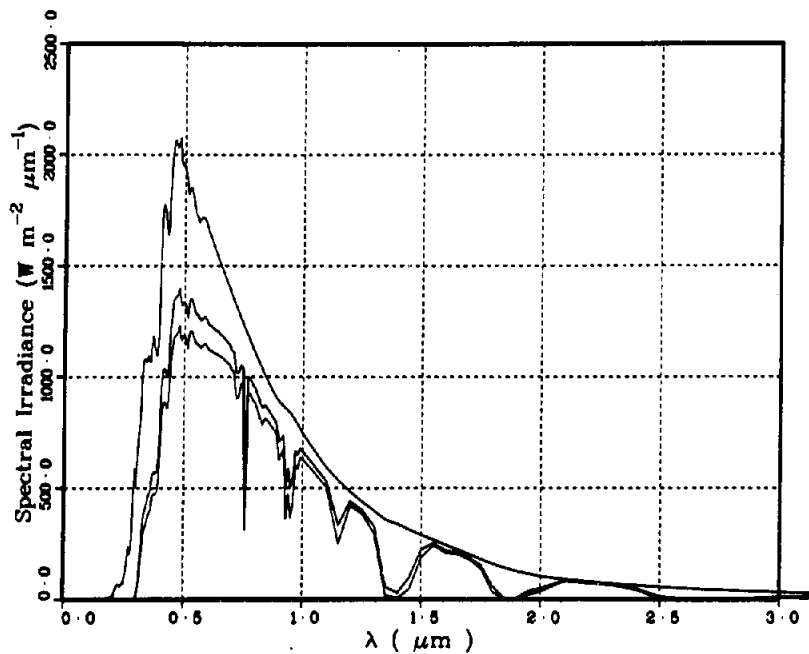


Figure 6-2. Solar Spectral Irradiance. The extraterrestrial solar spectral irradiance (Ref. 6.5), the irradiance after propagation through one choice of atmosphere, and the irradiance after further propagation through 1 km of the atmosphere from elevation 0.62 to 0.72 km

6.2.2 Earth Orbit Effects Upon Insolation

The actual distance, R , between the earth and the sun is approximated by

$$\left(\frac{R_0}{R}\right)^2 \approx 1 + 2e \cos \left[\frac{2\pi (D + 10)}{365} \right] \quad (6.2-1)$$

where R_0 is the mean separation, the orbit eccentricity $e = 0.01675$, and where D represents the day of the year (starting with 1 for January 1). Neglecting the earth's atmosphere, the solar

insolation is given by

$$S_o = S_{oo} \left(\frac{R_o}{R} \right)^2 \cos \zeta \quad (6.2-2)$$

where ζ is the angle between the unit normal to the element of area and the rays coming from the sun.

6.2.3 Models of Atmospheric Loss

Atmospheric effects upon solar insolation have been modeled in a variety of ways. Thomas and Thekaekara^{6.6} have modeled the solar insolation as a function of airmass traversed for a large number of combinations of atmospheric parameters describing the content of ozone, water vapor, and aerosols. Their comparisons with data indicate that atmospheric opacity is less in the afternoon than in the morning. Their model is cumbersome to use because the detailed spectral character of the attenuation is treated. The data are more convenient after integration over wavelengths of interest. Such results have been gathered by Kondratyev,^{6.2} Allen,^{6.1} Moon,^{6.7} and Gates^{6.8} for a series of atmospheres.

Kondratyev gives the reduction factor caused by transmission of the solar insolation through relative optical airmass, m .

$$S/S_o = 1.041 - 0.160 \sqrt{m \left(0.949 \frac{P}{P_o} + 0.051 \right)}, \quad (6.2-3)$$

where $P(P_o)$ is the atmospheric pressure at the observer (sea level) position and m is the relative optical airmass. This empirical formula includes ozone absorption, Rayleigh molecular scattering, and corrections for the portion of solar energy absorbed by constant gases (mostly oxygen) in the atmospheric model for a clear, dry day.

Vant-Hull has devised analytic functions that represent this factor (S/S_o) for the Allen, Moon, and Gates data.^{6.9} The functions fit the data within $\pm 0.5\%$ ($\pm 5 \text{ W/m}^2$). Allen's data are represented by

$$\frac{S}{S_o} = A \equiv 1 - 0.263 \left[\frac{w + 2.72}{w + 5.00} \right] \left(\frac{mP}{P_o} \right)^\gamma, \quad (6.2-4a)$$

where

$$\gamma = 0.367 \left[\frac{w + 11.53}{w + 7.88} \right]. \quad (6.2-4b)$$

The variable, w , is the total precipitable water overhead (in mm).

The fit to Moon's cloudless atmosphere, appropriate for $w = 20$ mm, ozone = 2.8 mm, and 300 aerosol particles/cm³ is

$$\frac{S}{S_0} = M \equiv 0.183 \exp \left[- \frac{mP}{0.48 P_0} \right] + 0.715 \exp \left[- \frac{mP}{4.15 P_0} \right] + 0.102 . \quad (6.2-5)$$

The Gates data are based upon $w = 10$ mm, ozone = 3.5 mm, and 200 aerosol particles/cm³. They also are consistent with a clear day. The analytic representation of these data is

$$\frac{S}{S_0} = G \equiv 0.135 \exp \left[- \frac{mP}{uP_0} \right] + 0.805 \exp \left[- \frac{mP}{3.033 P_0} \right] + 0.06 . \quad (6.2-6)$$

Here u is an unknown constant < 0.3 so the first term yields $< 5 W/m^2$ for $m = 1$. All these models have been incorporated into HELIOS. The default model used is that of Moon. The models are compared in Figure 6-3.

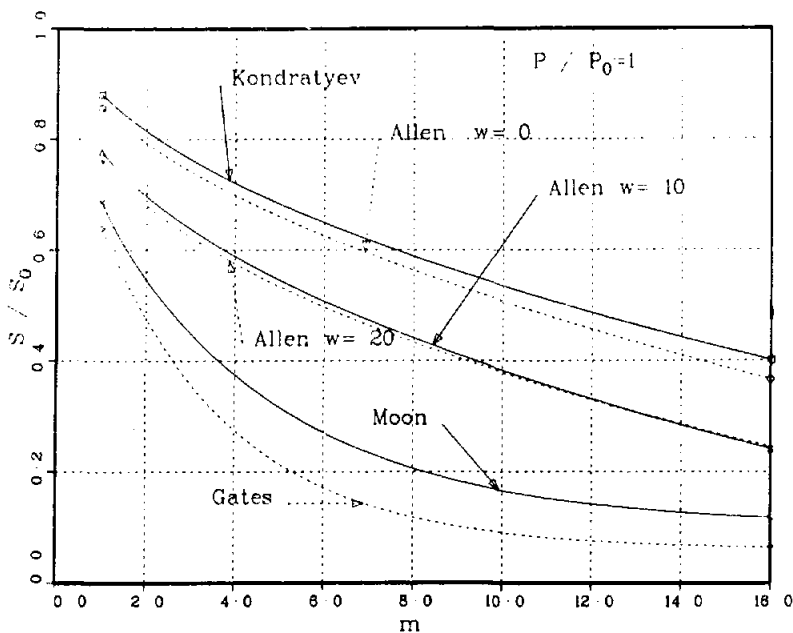


Figure 6-3. The Effect of Relative Optical Airmass Upon Solar Insolation

The variation of m with time of day is shown in Figure 6-4. This representation is that used by Kondratyev^{6.2} and is evaluated by table-look-up in HELIOS. More extensive work is required to make the m vs t , S/S_0 vs t , refraction vs t , and S/S_0 vs m representations all consistent with each other. Improvements may be added later. Solar flux variation with time is illustrated in Figure 6-5 for the Moon model. Comparison indicates the experimental data can be matched by the proper choice of atmosphere.

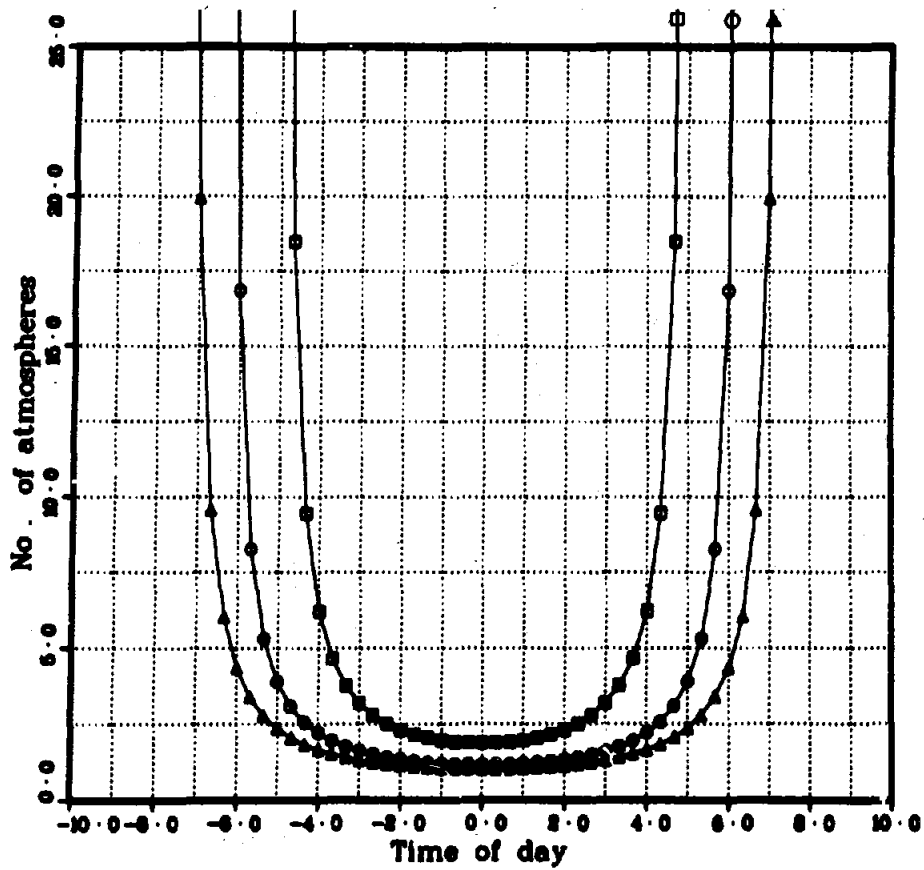


Figure 6-4. Atmospheric Mass Traversed. The number of atmospheric masses traversed by the sun's rays as a function of time-of-day (hours from local noon) for days 183 (▲), 90 (○), and 1 (□) of the year for observers in Albuquerque, NM. The atmospheric model used is for a very clear, dry atmosphere

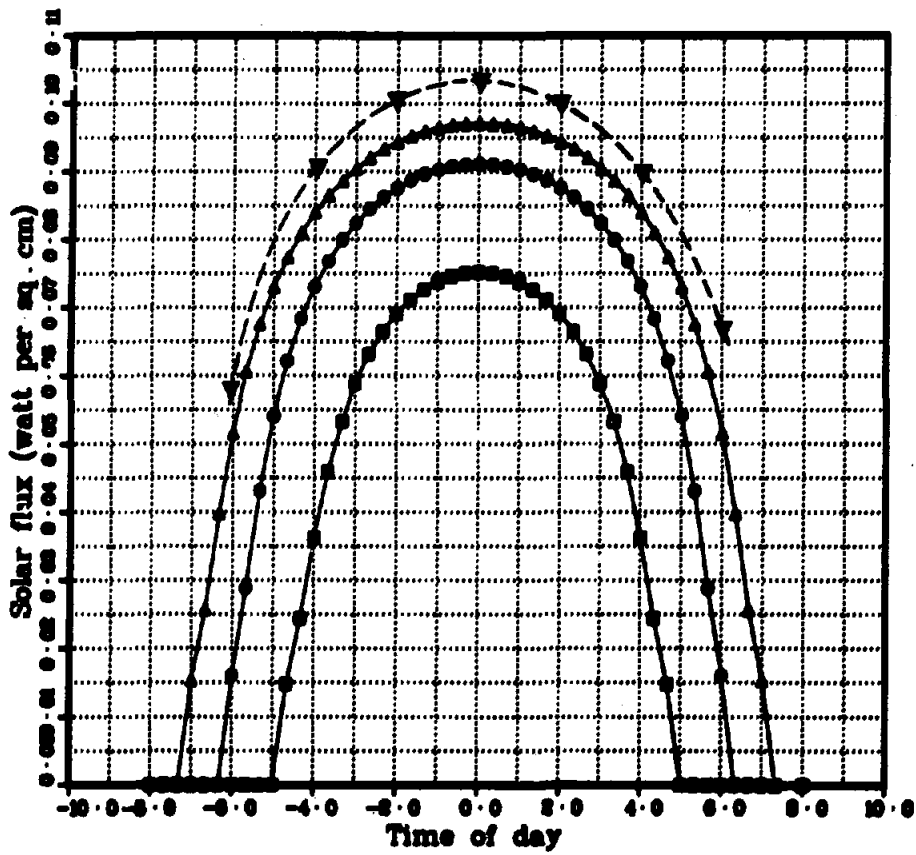


Figure 6-5. Incident Solar Flux. These are variations with time-of-day for January 1 (□), March 31 (○), and July 2 (▲) as predicted by the Moon model for Albuquerque, NM. The experimental data (▼) were measured on July 2.

6.2.4 Other Effects on Insolation

The solar insolation is dependent upon variations in solar emission. Sunspot activity gives large changes in radio wavelengths emitted. Only negligible change occurs in the solar constant. In addition to factors already noted, there are variations in the number density and size distribution of aerosols with time of day and with observer position. Solar insolation variations of 5% have been found in data collected in a large city and in that collected in the country on clear days. A much more involved treatment is required along with additional data before such effects can be predicted by the calculational HELIOS model.

6.3 Mirror-Receiver Propagation Loss

As the goals increase for electrical-power generation from solar energy, the arrays of mirrors surrounding tower receivers extend to larger distances from the towers. This expansion increases the distance that solar energy must be propagated from each mirror before it can be collected. Planned propagation distances are ≤ 700 m for the 10-MW pilot plant now being built at Barstow, CA. Resulting propagation losses are significant.

The purpose here is to estimate the propagation loss for central receiver solar collectors as a function of range, examine sensitivity of the results to choice of atmosphere, and find the variation of these losses with height of the tower receiver. The calculations are done for the 10-MW pilot plant at Barstow, CA. Receiver heights of interest vary from 100 to 300 m. Propagation distance is studied from 0.1 to 1.0 km. A simple functional representation of the loss is found for convenient computer simulation of the effect in the models of solar-energy collection by central receivers.

6.3.1 Methods of Calculating Propagation Loss

Methods of determining the propagation loss have been reviewed by La Rocca and Turner.^{6.10} The methods that have greatest adaptability (easiest alteration of boundary conditions, and physical and geometrical parameters) are stated to be the Monte Carlo and LOWTRAN methods; i. e., if the atmospheric models built into the computer codes are acceptable. The Monte Carlo method suffers from large computer-time requirements. The LOWTRAN method only includes the direct component of the transmitted radiation; the scattered contribution is ignored. Codes are readily available that implement these methods.^{6.11-6.13} Ease of input, computation speed, and direct applicability influenced the choice of LOWTRAN III for the present study. Omission of the scattered energy results in a conservative (upper) bound on the transmission losses. This neglect is not thought to be serious; most of the scattered energy will not be directed toward the receiver. Later the more detailed Monte Carlo calculations could be used to predict correlation between the sun-shape (including scattering effects) and the choice of atmosphere and time of day. LOWTRAN uses a scheme for determining atmospheric absorption and scattering with about 20 cm^{-1} wave-number

resolution across the spectral region.^{6.14} This low resolution is satisfactory for the present study where integrations over wavelength are required. At specific wavelengths--such as for laser propagation studies--the LOWTRAN model may underestimate or overestimate the actual value of transmittance. Other methods are then recommended.^{6.14}

All the propagation methods considered are wavelength dependent. Hence, the propagation loss between each mirror and the receiver is dependent upon the spectral irradiance of the energy originating at the sun.

6.3.2 Atmospheric Transmittance

Before calculating the propagation loss between mirror and receiver, the spectral irradiance must be determined at ground level. The transmittance is found from LOWTRAN III.^{6.11} As input, we set altitude = 0.6096 km, sun zenith angle = 22°, haze model visual range = 23.0 km, wave-number range of interest from 350 to 40 000 cm⁻¹ in steps of 20 cm⁻¹, and atmosphere = the midlatitude winter model built into LOWTRAN III. The altitude is appropriate for the location of the 10-MW electrical pilot plant being built at Barstow, CA. The resulting transmittance for the slant range to space is given in Figure 6-6. Folding this data with the extraterrestrial solar-spectral irradiance gives the center curve in Figure 6-2.

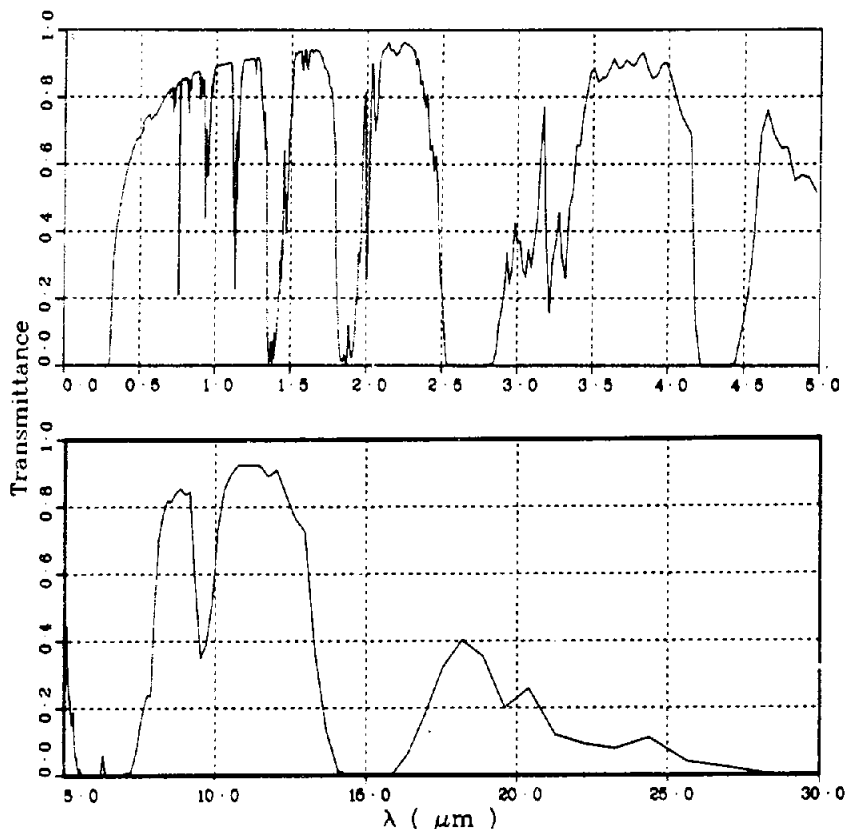


Figure 6-6. Atmospheric Transmittance for Midlatitude Winter Model Atmosphere and for 22° Slant Range to Space From Altitude 0.6069 km With Visual Range of 23 km

In this section we assume specular reflection without energy loss for the solar energy that is incident upon the mirror surfaces. Hence, no calculation is required to account for wavelength and angle of incidence variations of the spectral irradiance upon reflection. Integration over wavelengths here gives a solar insolation of 925 W/m^2 (insolations are given normal to the incoming beam). This is a high value of insolation (corresponding to an unrealistically small 22° zenith angle) for winter at Barstow, CA. The midlatitude summer atmospheric model gives 891 W/m^2 under these conditions while the 1962 US standard atmosphere gives 912 W/m^2 .

LOWTRAN III could also be used to furnish data given by the models of atmospheric loss (paragraph 6.2.3) used in HELIOS. This may be included as a future, expanded option on choice of atmosphere. However, it would require integration over the solar spectrum which is not now required in HELIOS. The new method would automatically yield airmass and refraction data consistent with the choice of atmosphere.

6.3.3 Mirror-Receiver Loss Function for Barstow, CA

After the significant loss of energy the solar insolation suffers in propagating to the earth's surface, negligible further loss might be expected in propagating the distances from heliostats to receiver apertures in the pilot plant. Such is not the case. For ranges $\sim 1 \text{ km}$, losses greater than 10% are encountered. Thus the 925 W/m^2 solar insolation at Barstow, with the midlatitude winter atmospheric model, is reduced to 823 W/m^2 after propagation over 1 km to a tower elevation of 100 m. The lower curve in Figure 6-2 gives the resulting solar spectrum after traversing this path. The loss results primarily from the larger concentration of water vapor and aerosols at lower elevations. Pressure broadening also increases the attenuation at low altitudes.

LOWTRAN III calculations were performed for a series of slant ranges between the altitudes 0.6096 and 0.9096 km above sea level (corresponding to a tower receiver altitude of $\sim 300 \text{ m}$). The results of folding the transmittance with the spectral irradiance and integration over wavelength are summarized in Table 6-II. The tabulated losses are caused only by the propagation along the slant range between the altitudes 0.6096 and 0.9096 km.

The water-vapor densities for the 1962 US Standard Atmosphere correspond to relative humidities of approximately 50% for altitudes up to 10 km, while the relative humidity values for the other models decrease with altitude from approximately 80% at sea level to approximately 30% at 10-km altitude. These humidities are rather high for typical locations for solar central-receiver power stations. LOWTRAN does have a convenient option for relative humidity input along a chosen horizontal path. For altitude 0.6096 km and relative humidity of 10%, the (range, loss) values are (0.2 km, 3.1%), (0.4 km, 5.3%), (0.6 km, 7.4%), (0.8 km, 9.3%), (1.0 km, 11.1%). The data are reasonably consistent with the earlier models as indicated in Figure 6-7.

TABLE 6-II

Solar Insolation After Atmospheric Transmission*

Slant Range R (km)	Midlatitude Winter Atmosphere		Midlatitude Summer Atmosphere		1962 Standard Atmosphere	
	S (W/m ²)	Loss (percent)	S (W/m ²)	Loss (percent)	S (W/m ²)	Loss (percent)
0	925	0.0	891	0.0	912	0.0
0.30	888	4.0	852	4.4	874	4.2
0.47	871	5.8	836	6.2	858	5.9
0.65	856	7.5	821	7.9	843	7.6
0.82	843	9.0	806	9.5	829	9.1
1.00	828	10.5	793	11.0	816	10.5

*The Propagation path through the atmosphere is along a 22° slant range to altitude 0.6096 km and then along a slant range from altitude 0.6096 to 0.9096 km. The nonphysical R = 0 values give the direct solar insolation at 0.6096-km altitude.

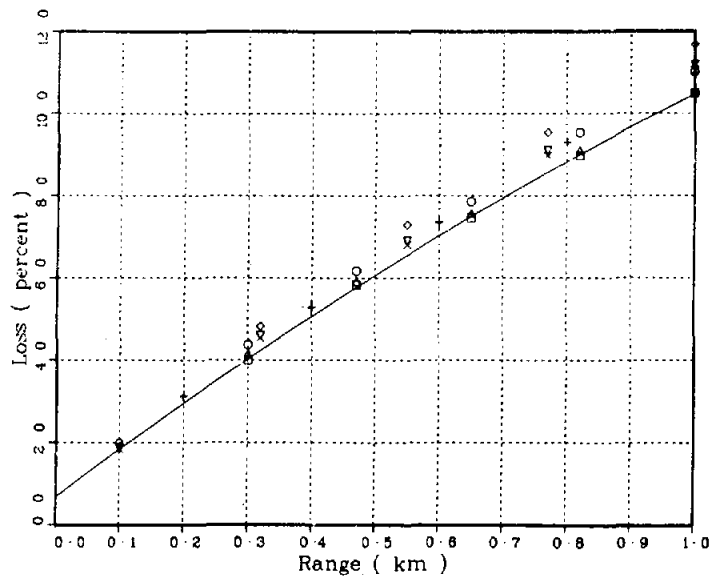


Figure 6-7. Propagation Loss as a Function of Slant Range for Four Choices of Atmosphere: (□, x) midlatitude winter, (○, ◇) midlatitude summer, (△, ▽) 1962 US Standard, and (+) 10% relative-humidity path

For $0.30 \leq R \leq 1.00$ km, the percent loss, L_s , for the midlatitude winter atmosphere is well represented by the standard loss:

$$L_s = -1.97 R^2 + 11.76 R + 0.679 \quad (6.3-1)$$

as shown by the solid curve in Figure 6-7. Loss data have also been generated for a slant range from altitude 0.6096 to 0.7096. These data correspond to a lower tower receiver, and allow data points in Figure 6-7 to extend down to 0.1 km. Loss differences from the standard are given in Figure 6-8. The paths are somewhat different. Symbols \square , \circ , and Δ correspond to paths between 0.6096 and 0.9096 km; symbols \times , \diamond , and ∇ correspond to paths between 0.6096 and 0.7096 km; and symbol $+$ corresponds to a horizontal path at 0.6096-km altitude. All the data in Figure 6-7 are within 1.2% of L_s for $0.1 \leq R \leq 1.0$ km. Consistency with L_s is not changed if the slant range to space is altered from 22° to 50° .

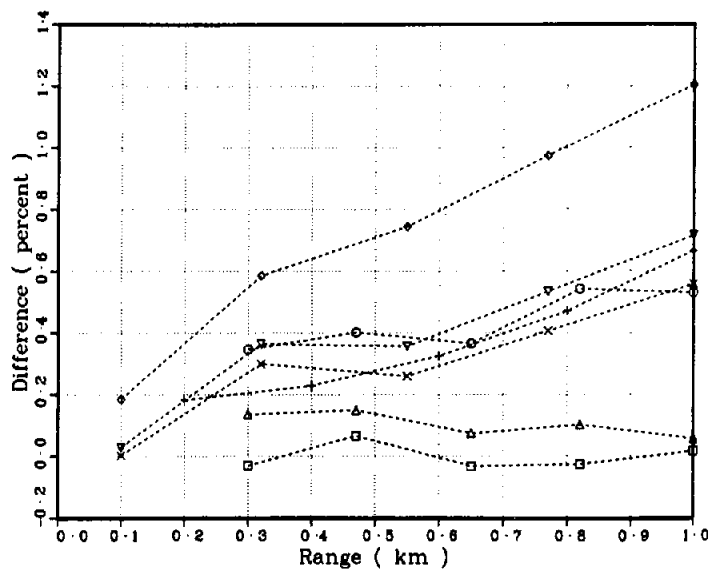


Figure 6-8. Loss Variation From Standard. Difference between propagation loss and standard for four choices of atmosphere: (\square , \times) midlatitude winter, (\circ , \diamond) midlatitude summer, (∇ , Δ) 1962 US Standard, and ($+$) 10% relative-humidity path

The energy loss (percent) caused by propagation of solar energy from mirrors to receiver is estimated by

$$L_s = -1.97 R^2 + 11.76 R + 0.679 \quad 0.1 \leq R \leq 1.0 \text{ km}, \quad (6.3-2)$$

$$L_s = 100 \exp(-0.1852 R) \quad 0 \leq R < 0.1 \text{ km}, \quad (6.3-3)$$

where the propagation distance, R , is in km, the tower elevation is 100 to 300 m, and the site altitude is ~ 0.61 km above sea level in the midlatitude appropriate for the continental US. This

function is presently in use in HELIOS. As data appropriate to other tower elevations, site altitudes, and site latitudes become available, they may be incorporated into HELIOS.

The reader may object to the choice of a function (in Figure 6-7) such that most of the data lie above L_s . L_s was chosen as the lower limit of the data because scattered energy is ignored. Hence, the loss should be somewhat overestimated by LOWTRAN III.

6.4 Sunshape Variation

A set of 16 standard sunshapes has been generated by Lawrence Berkeley Laboratory.^{6.15} The data are intended to span the shapes that may be of interest for central receivers. The data were taken for a range of wind direction and speed, pressure, temperature, and dew point. The data are discussed here to indicate the wide variations that are possible and their consequences.

6.4.1 Lawrence Berkeley Laboratory Data

Parameters describing the sunshapes from LBL^{6.15} are listed in Table 6-III. The I (4.80 mrad) is the solar radiation (W/m^2) tabulated by LBL for the $\sim 0.55^\circ$ subtended by the sun plus the angular resolution of the measuring system. The I (55.2 mrad) results from numerical integration of the LBL sunshape profiles out to the limit of the data furnished; i. e., a cone angle of 55.2 mrad. The circumsolar ratio is the ratio of the power received from one solar radius (taken as 4.8 mrad) out to ~ 55.2 mrad to the total power received. The circumsolar ratio can be estimated from I (4.80 mrad) and I (55.2 mrad). Differences that occur are thought to result from factors such as the finite width (0.41 mrad) of the detector aperture or slight differences in integration procedure. The I (55.2) < I (4.80) impossibility in data set 9 is thought to result from these same factors. The δ (rms) is the root-mean-square width of the distribution with an assumed cut-off at the extent of the data (55.2 mrad). The table appears limited in the season of data collection, with over half the data being collected on December 14 or 29, 1976, or on January 25, 1977. The data have the advantage of indicating how quickly the insolation can vary in addition to spanning the distributions that naturally occur. Sunshape variation is not systematic with time of day or with season.

The possibility of correlation between I (55.2 mrad) and δ (rms) is tested in Figure 6-9. The solid curve is an analytic fit to a second degree polynomial that minimizes the relative error of the data. The curve is given by

$$\delta_{rms} \text{ (mrad)} = 3.7648 - 0.0038413 (I - 1000) + 1.5923 \times 10^{-4} (I - 1000)^2 \quad (6.4-1)$$

where I is in W/m^2 . Three of the points (data sets 9, 10, and 16 in Table 6-III) are chosen for additional study in Section 6.4.5 to determine the effect of sunshape variation.

TABLE 6-III

Sun Parameters

Data Set	Date	Solar Times (hour)	Location	I (4.80 mrad) (W/m ²)	I (55.2 mrad) (W/m ²)	Circumsolar Ratio C	δ (rms) (mrad)
1	Aug 25, 1976	9.36	Fort Hood, TX	708.9	716.4	0.0100	3.98
2	Nov 20, 1976	11.22	Fort Hood, TX	894.8	920.7	0.0270	3.55
3	Nov 22, 1976	14.89	Fort Hood, TX	775.8	798.9	0.0290	5.19
4	Dec 29, 1976	10.39	Fort Hood, TX	168.1	353.3	0.5260	22.63
5	Dec 29, 1976	12.74	Fort Hood, TX	40.5	97.7	0.5870	19.15
6	Dec 29, 1976	13.64	Fort Hood, TX	217.5	361.4	0.3990	12.05
7	Dec 29, 1976	14.00	Fort Hood, TX	705.4	788.1	0.1061	6.36
8	Dec 29, 1976	15.45	Fort Hood, TX	714.9	760.4	0.0571	7.21
9	Aug 07, 1976	11.72	Albuquerque, NM	947.8	943.7	0.0082	3.86
10	Dec 14, 1976	10.21	Albuquerque, NM	340.6	480.4	0.2938	10.53
11	Dec 14, 1976	11.29	Albuquerque, NM	919.5	943.0	0.0345	4.68
12	Dec 14, 1976	12.92	Albuquerque, NM	699.8	816.2	0.1461	8.99
13	Jan 25, 1977	9.34	Albuquerque, NM	736.6	806.3	0.0888	6.13
14	Jan 25, 1977	9.88	Albuquerque, NM	164.0	309.7	0.4708	14.66
15	Jan 25, 1977	10.79	Albuquerque, NM	517.3	649.3	0.2042	8.31
16	Jan 25, 1977	12.78	Albuquerque, NM	29.5	95.3	0.6920	18.94

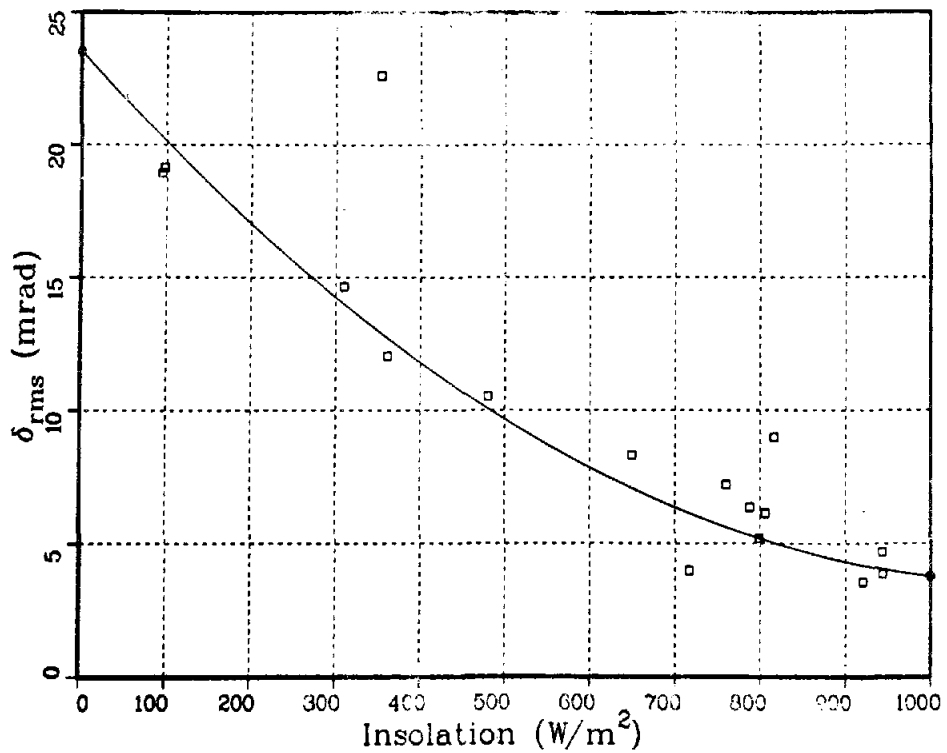


Figure 6-9. Variation of Solar Width With Insolation

Variation of the rms width with the circumsolar ratio, C , is shown in Figure 6-10. A linear least-square fit constrained to pass through $\delta = 3.5$ mrad at $C = 0$ with equal weighting of all the points gives

$$\delta_{\text{rms}} \text{ (mrad)} = 3.5 + 26.2 C. \quad (6.4-2)$$

Note that δ_{rms} and C are correlated.

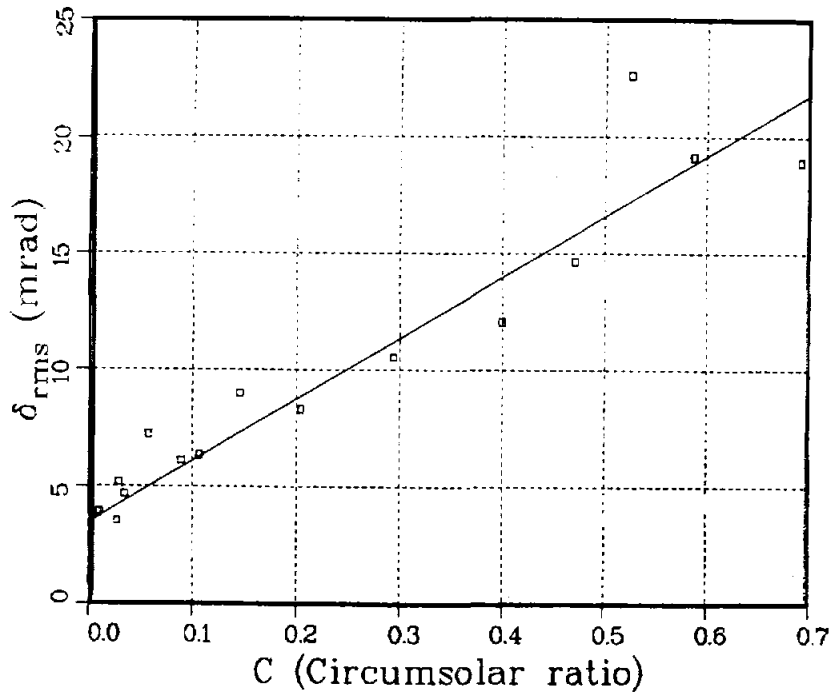


Figure 6-10. The Root-Mean-Square Radius of the Sunshape vs Circumsolar Ratio

The δ_{rms} refers to a two-dimensional sunshape. However, line-focus collectors require a one-dimensional description. The appropriate description is formed by taking lateral slices across the two-dimensional shape. Since the sunshape has circular symmetry, the one-dimensional root-mean-square width W is related to δ_{rms} by

$$W = \delta_{\text{rms}} / \sqrt{2} \quad (6.4-3)$$

in accordance with the result of Eq. (5.2-29). Therefore,

$$W = 2.47 + 18.5 C \quad (6.4-4)$$

describes the the appropriate measure of width as a function of the circumsolar ratio for line-focus collectors.

We also examined the extent to which the circumsolar effects can be identified with the broadening effects of error cones on a basic, narrow sunshape. By using b as the rms radius of the basic sunshape and convolving another distribution of rms radius, ηb , with it, the rms radius of the resultant is

$$\delta^2 = b^2 + \eta^2 b^2 = b^2(1 + \eta^2), \quad (6.4-5)$$

Combining Eqs. (6.4-2) and (6.4-5), setting $b = 3.5$ mrad, and solving for η gives

$$\eta = \sqrt{(1 + 7.49 C)^2 - 1}. \quad (6.4-6)$$

A plot of η versus C is given in Figure 6-11. The data points are obtained by rewriting δ^2 as

$$\eta_i = \sqrt{\left(\frac{\delta_i}{b}\right)^2 - 1}, \quad (6.4-7)$$

setting $b = 3.5$, and using values of δ from Table 6-III. It may be surprising to note that at $C = 0.3$, a value of $\eta \simeq 3$ results. This means that at 30% circumsolar, the sunshape is broadened by an amount approximated by convolving a distribution about three times as wide as the sunshape together with the sunshape.

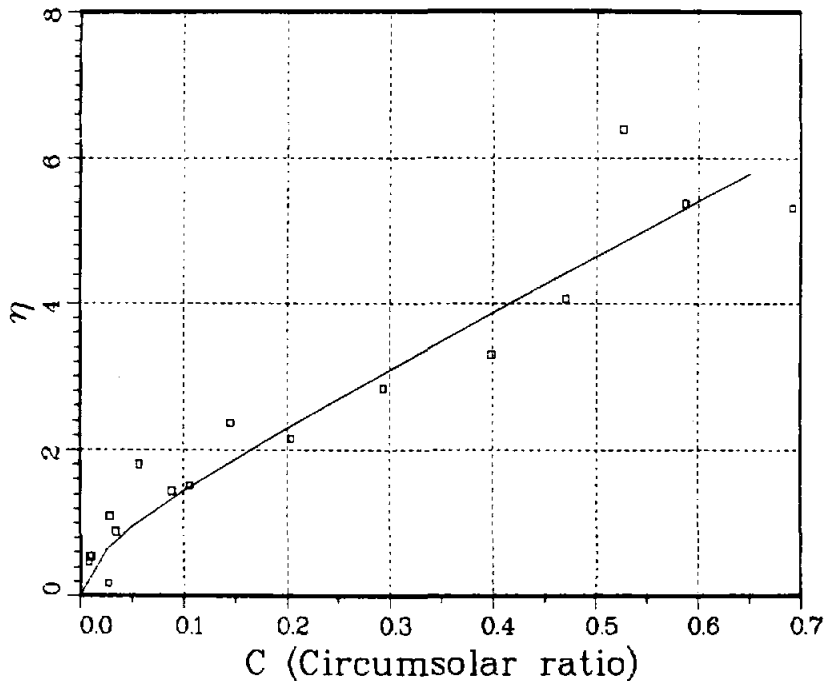


Figure 6-11. A Graph of η (Eq. 6.4-6) vs C (solid curve) and the Corresponding Data (Eq. 6.4-7) From Table 6-III

6.4.2 Analytical Sunshapes

A convenient analytical form representing the sunshape has been adapted from that given by Minnaert;^{6.16} i. e. ,

$$\frac{I}{I_0} = \frac{1 + \beta \cos \theta}{1 + \beta} , \quad (6.4-8)$$

where θ is the angle between rays from the center of the sun going to the observation point and to the observed position on the solar surface. The β is a wavelength-dependent adjustable parameter ($\beta = 2.2$ at $0.5 \mu\text{m}$). If we let α represent the angle between rays from the observer toward the solar center and toward the position on the solar surface, and let δ represent $\tan \alpha$ for the solar edge, then the θ variation may be expressed in terms of $\tan \alpha$.

$$\frac{I}{I_0} = \frac{1 + \beta \sqrt{1 - \tan^2 \alpha / \delta^2}}{1 + \beta} . \quad (6.4-9)$$

Normalization of the brightness to a unit integral over the solar surface yields the probability distribution function for the brightness.

$$P = \left\{ \begin{array}{ll} \frac{1 + \beta \sqrt{1 - \tan^2 \alpha / \delta^2}}{\pi \delta^2 (1 + 2\beta/3)} & \alpha \leq \delta \\ 0 & \alpha > \delta \end{array} \right\} . \quad (6.4-10)$$

This distribution has been called the Kuiper sunshape.^{6.17} In the cases examined to date, measured sunshapes have been represented by this analytical form to within an error that is small compared to the daily sunshape variations found in the LBL data. The proper representation is found from curve fitting with β and δ as adjustable parameters. Typical values of β range from 0.6 to 4.8 with $\tan^{-1} \delta$ near 4.65 mrad. In the cases examined, the fits are for the integrated solar spectrum, rather than for separate spectral regions.

At the edge of the solar disk, the shape is widened by small-angle scattering of the direct beam from atmospheric aerosols with dimensions on the order of or slightly larger than the optical wavelengths. This broadening produces the circumsolar radiation that is sometimes referred to as the solar aureole. At the edges the sunshape is poorly represented by the analytical form of P given in Eq. (6.4-10).

The aureole effect is typically represented by smoothing functions (such as linear, exponential, or cosine functions) to reduce the brightness to zero at the solar edge. At times the shapes are exceptionally wide. However, numerical convolutions with the error cones noted in

Chapter 5 require matrix-dimension limits on computer representation of the sunshape. Hence, outer limits are sometimes employed beyond which the brightness is taken as zero. The aureole effect slightly alters the normalization of P.

In application to those systems that are particularly sensitive to the sunshape and those that use only a small portion of the solar spectrum, detailed treatment is required. Then each portion of the solar spectrum may be treated separately, each with its appropriate insolation, sunshape, and wavelength.

Several other sunshape forms have been treated in the literature (Ref. 6.1 p 170 and Ref. 6,18). However, the forms are generally more complicated. A simple analytical form (even if it involved a series of terms) would allow shape specification with only a few parameters rather than a table of intensity variation with the tangent of the angle measured from the solar center. A sufficiently simple form would allow analytical expressions to be formed for the convolution with elliptic normal distributions to quickly find the effective sunshape. Relatively simple expressions would also be expected for the one and two dimensional cumulative distribution functions. Effort to find appropriate analytical forms is in progress at the present time.

6.4.3 Sunshape Extremes

One of the narrowest sunshapes furnished by LBL is that provided by Data Set 9 in Table 6-III. This set also has the smallest circumsolar ratio. Its rms width of 3.86 mrad is somewhat larger than that for a uniform brightness over the solar disk of halfangle 4.6525 mrad ($\delta = 4.6525/\sqrt{2} = 3.29$ mrad). Data Set 16 in Table 6-III has the largest circumsolar ratio tabulated, as well as one of the largest δ (rms) values. These distributions are given in Figure 6-12 after reducing the cut-off angle to 46.03 mrad and normalizing to an integrated brightness of 1 W/cm^2 .

6.4.4 Idealized Cumulative Distribution Functions

One of the parameters of interest to designers of solar energy collectors is the portion of the solar energy within various acceptance angles. This portion is given by the cumulative distribution function. The acceptance angles may be either one or two dimensional as for parabolic trough or for heliostat methods for energy collection. Consider the circular normal distribution of dispersion σ .

$$G(\rho) = \frac{1}{2\pi\sigma^2} \exp\left(-\frac{\rho^2}{2\sigma^2}\right), \quad (6.4-11)$$

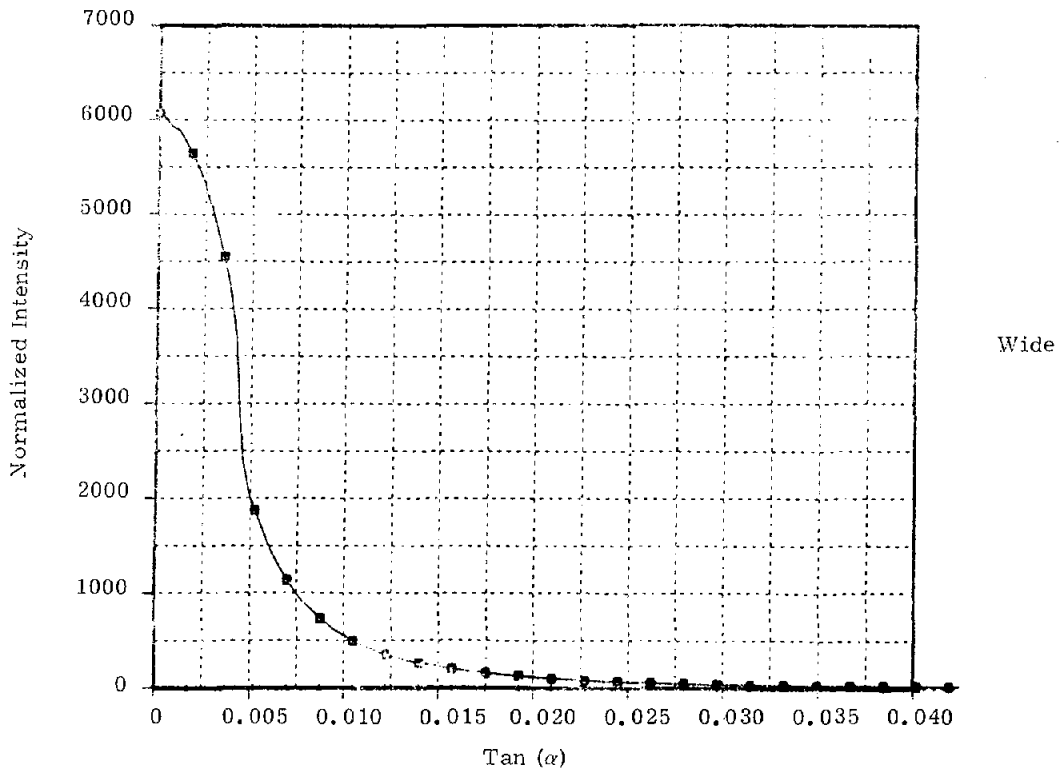
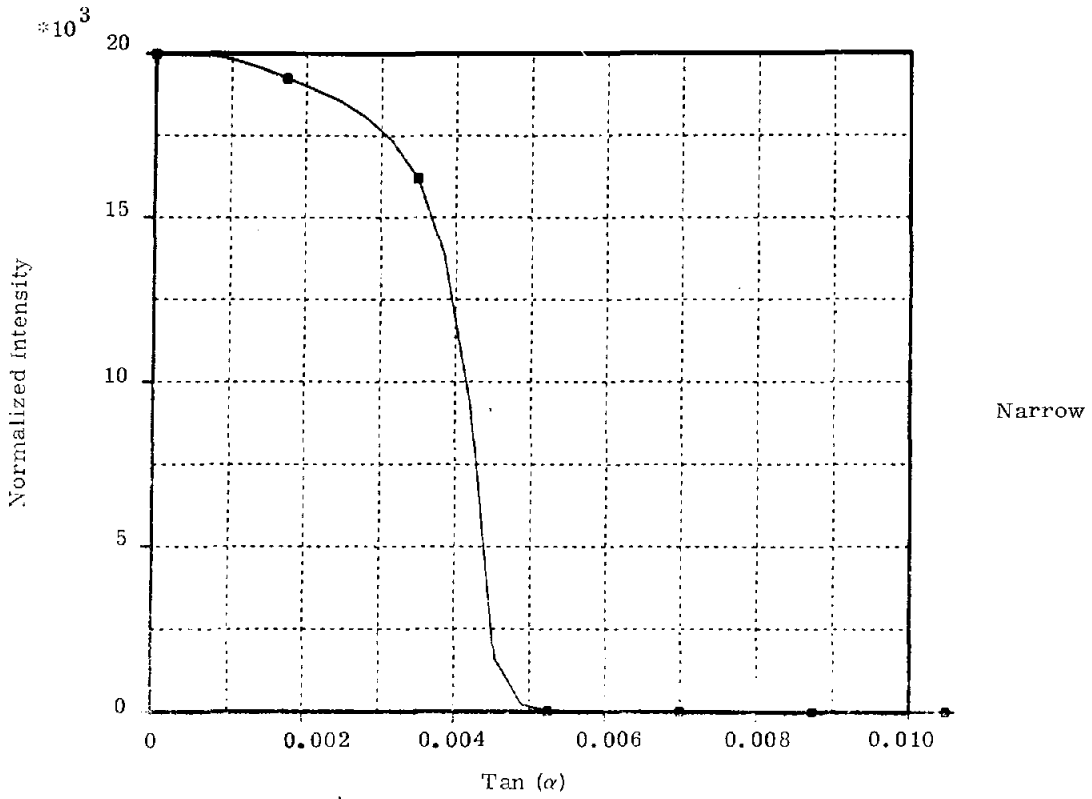


Figure 6-12. Extremes of Narrow and Wide Sunshapes

where $\rho = \tan \alpha$. It is normalized with $\int_0^{\infty} 2\pi\rho G(\rho) d\rho = 1$. The cumulative distribution function is given by

$$C(\rho) = \int_0^{\rho} G(\rho') 2\pi\rho' d\rho' , \quad (6.4-12a)$$

or

$$C(\rho) = 1 - \exp\left(-\frac{\rho^2}{2\sigma^2}\right). \quad (6.4-12b)$$

If the sun is viewed from a slot where all the energy is accepted in one direction (say the y direction), then the one-dimensional cumulative distribution function is

$$C_1(x) = \int_{-x}^x \int_{-\infty}^{\infty} G(x', y') dy' dx' \quad (6.4-13)$$

where $G(x, y) = \frac{1}{2\pi\sigma^2} \exp\left(-\frac{x^2 + y^2}{2\sigma^2}\right)$. Substitution gives

$$C_1(x) = \frac{2}{\sqrt{\pi}} \int_0^{x/\sqrt{2\sigma}} e^{-t^2} dt = \operatorname{erf}\left(\frac{x}{\sqrt{2\sigma}}\right). \quad (6.4-14)$$

When the sunshape is convolved with an error cone as discussed in Chapter 5, a cut-off radius is employed to limit the dimension statements necessary for the fast Fourier transforms. Existence of this cut-off alters the cumulative distributions. Consider the distribution

$$G_c(\rho) = \begin{cases} \frac{N}{2\pi\sigma^2} \exp\left(-\rho^2/2\sigma^2\right) & \rho \leq R \\ 0 & \rho \geq R \end{cases} . \quad (6.4-15)$$

Although σ was defined to be the dispersion when $R = \infty$, we retain that nomenclature for this more general case. N provides the normalization

$$\int_0^R G_c(\rho') 2\pi\rho' d\rho' = 1 .$$

The two-dimensional cumulative distribution function is now altered to

$$C_c(\rho) = \begin{cases} \frac{1 - \exp(-\rho^2/2\sigma^2)}{1 - \exp(-R^2/2\sigma^2)} & \rho \leq R \\ 1 & \rho \geq R \end{cases} . \quad (6.4-16)$$

In one dimension for $x \leq R$, we have

$$C_{cl}(x) = \int_{-x}^x \int_{-\sqrt{R^2+x'^2}}^{\sqrt{R^2+x'^2}} \frac{N}{2\pi\sigma^2} \exp\left(-\frac{x'^2+y'^2}{2\sigma^2}\right) dy' dx' , \quad (6.4-17)$$

where $1/N = 1 - \exp(-R^2/2\sigma^2)$. This may be reduced to the form

$$C_{cl}(x) = \sqrt{\frac{2}{\pi}} \frac{N}{\sigma} \int_0^x \exp\left(-\frac{x'^2}{2\sigma^2}\right) \operatorname{erf}\left(\sqrt{R^2+x'^2}\right) dx' . \quad (6.4-18)$$

Although not convenient for analytic integration, numerical integration can be easily employed.

As an additional example, let us consider the pillbox distribution, $F(\rho)$ (Eq. 5.2-2), with half angle a . The two-dimensional cumulative distribution function is

$$C_p(\rho) = \begin{cases} \rho^2/a^2 & \rho \leq a \\ 1 & \rho > a \end{cases} . \quad (6.4-19)$$

In one dimension, the cumulative distribution function becomes

$$C_{lp}(x) = \begin{cases} \frac{2}{\pi} \sin^{-1} \frac{x}{a} & x \leq a \\ 1 & x > a \end{cases} . \quad (6.4-20)$$

Even after convolution with error cones, actual sunshapes do not match the idealized distributions presented here. However, numerical integration can be used for rather arbitrary shapes experienced in practice. The analytic results form a convenient check upon the numerical procedures used for the more general cases. Consider the pillbox sunshape in Figure 6-13. An error cone of 4-mrad dispersion is also given along with the convolution of the two distributions. In Figure 6-14, the two-dimensional cumulative distribution function is given for six effective sunshapes, i. e., for the pillbox shape convolved with circular normal distributions of dispersion 0, 2, 4, 6, 10, and 20 mrad. The $\sigma = 0$ case has the characteristic $\sim \rho^2$ dependence for $0 \leq \rho \leq a$. The corresponding cumulative distributions for one dimension are in Figure 6-15. Unless the acceptance angle of the solar collector is very large, uncertainty in the aim can cause significant loss of efficiency.

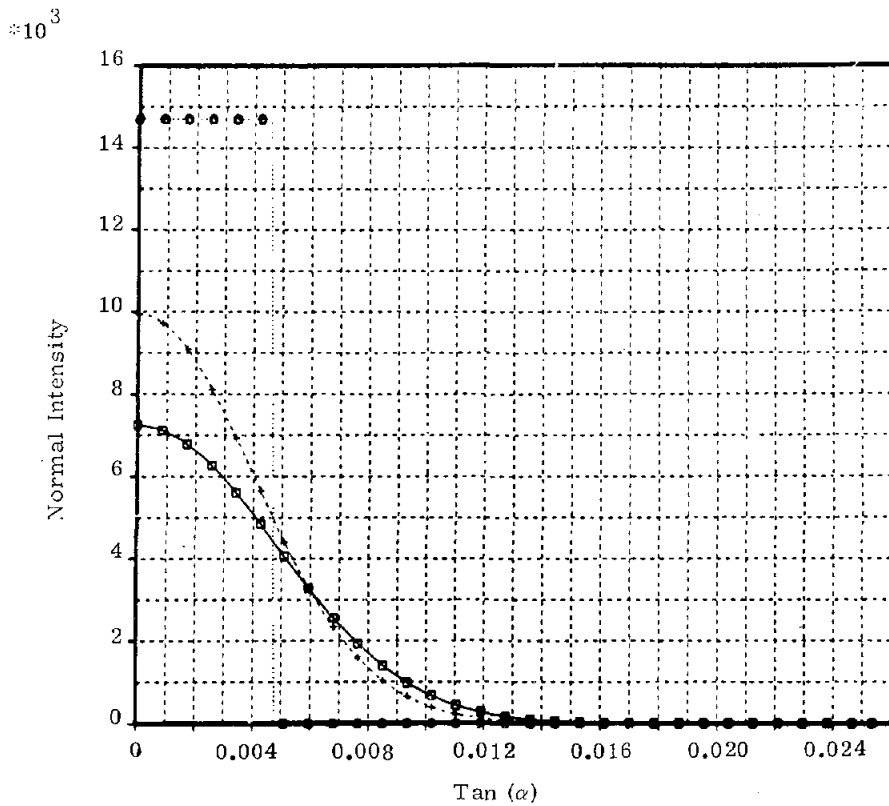


Figure 6-13. Distributions for a Pillbox Sunshape, a Circular Normal of Dispersion 4 mrad, and Their Convolution

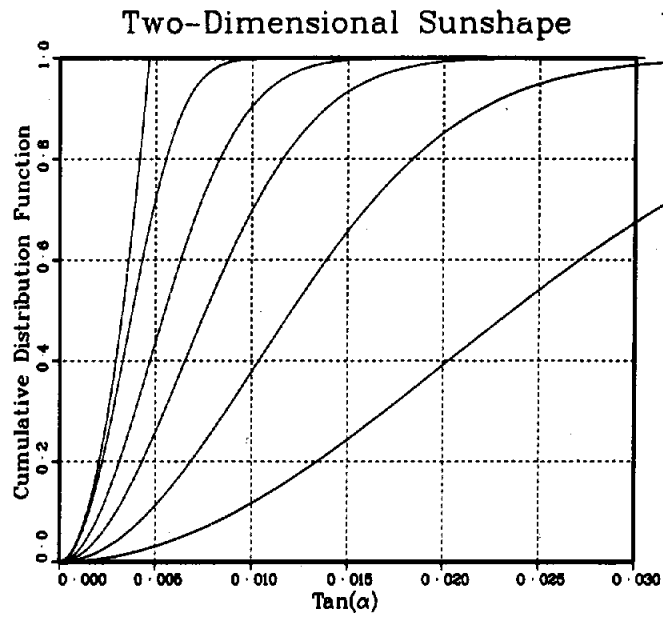


Figure 6-14. Two-Dimensional Cumulative Distribution Functions for a Series of Effective Sunshapes

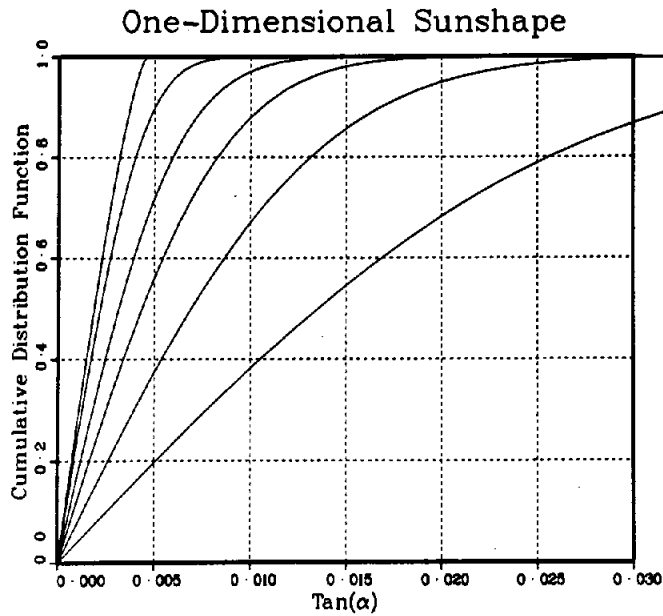


Figure 6-15. One-Dimensional Cumulative Distributions for a Series of Effective Sunshapes

If the error cone were sufficiently wide and cylindrically symmetric, one would expect the effective sunshape to be well approximated by a circular normal distribution. Then simple analytic forms could be used to evaluate the distribution function. However, the proper method for choosing the appropriate dispersion of the effective sunshape is not obvious. One could match rms widths or perhaps match the ρ 's at which both cumulative distribution functions are one (i.e., within a chosen number of significant figures). The presence of the cut-off, R, further complicates the choice.

Using a circular normal distribution with a cut-off, R, the mean square width is given by

$$\langle \rho^2 \rangle_{\text{effective}} = \frac{\int_0^R \rho^3 \exp(-\rho^2/2\sigma^2) d\rho}{\int_0^R \rho \exp(-\rho^2/2\sigma^2) d\rho} \quad (6.4-21)$$

The σ that produces a given $\langle \rho^2 \rangle_{\text{effective}}$ is then obtained from the zero of the function

$$f(\sigma) = \langle \rho^2 \rangle - 2\sigma^2 - e^{-\gamma} \left[\langle \rho^2 \rangle - 2\sigma^2 (1 + \gamma) \right] \quad (6.4-22)$$

where $\gamma = R^2/2\sigma^2$. Note that as $R \rightarrow \infty$, $\langle \rho^2 \rangle \rightarrow 2\sigma^2$ as required for a circular normal distribution. By Eq. (5.3-5), this choice for σ is equivalent to a mean square width given by

$$\langle \rho^2 \rangle = \langle \rho^2 \rangle_{\text{error cone}} + \langle \rho^2 \rangle_{\text{sunshape}} \quad (6.4-23)$$

Also, one could just take $\sigma = \sqrt{\langle \rho^2 \rangle_{\text{effective}}/2}$ for comparison of cumulative distribution functions, or just choose $\sigma = \sigma_{\text{error cone}}$ to find where the actual sunshape has negligible effect. For many applications such differences are of little consequence. In others, the differences require additional care in interpretation.

6.4.5 Actual Cumulative Distribution Functions

Data Sets 9, 10, and 16 (narrow, medium, and wide widths) referred to in Table 6-III have been processed to find their cumulative distribution functions. These functions have also been generated for the effective sunshapes after convolution with a series of error cones. The results are recorded in Figures 6-16 through 6-18. The dashed lines give the cumulative distribution function for a circular normal of the same $\langle \rho^2 \rangle$ and the same cut-off R as for the corresponding effective sunshape. The rms width of the error distribution given in the caption would be $\sqrt{2}$ x the half angle (or dispersion) of the error distribution if R were infinite.

The rms widths noted in the one-dimensional distributions are one-dimensional widths. The figures indicate that for sufficiently large error cones, the effective sunshapes are well represented by circular normal distributions.

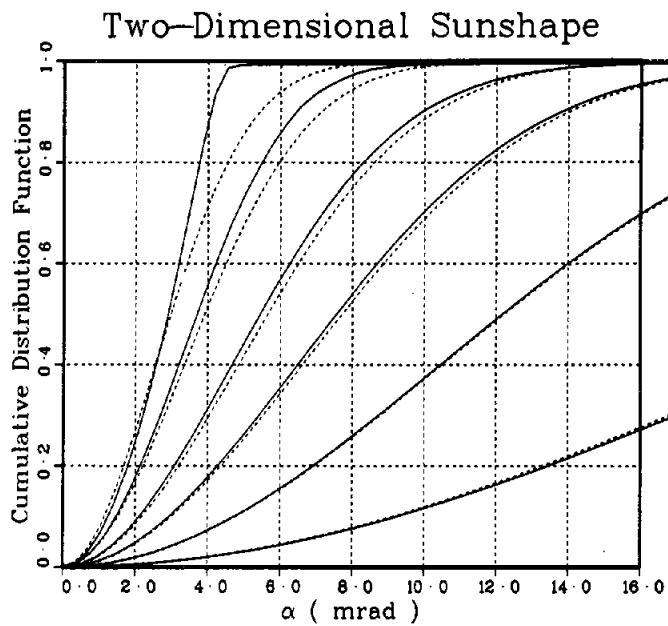
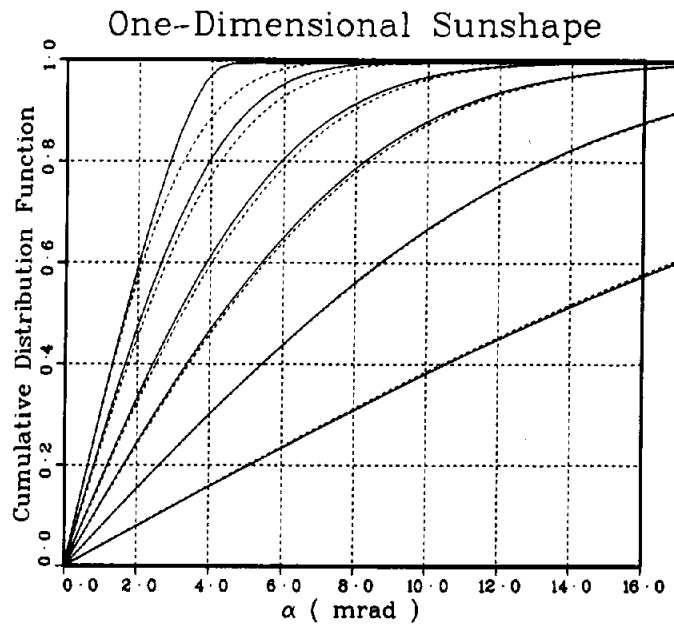


Figure 6-16. Cumulative Distribution Functions for the One- and Two-Dimensional Effective Sunshapes Generated by Convolution of the Narrow Sunshape (Data Set 9) With Error Cones of Dispersion 0, 2, 4, 6, 10, and 20 mrad

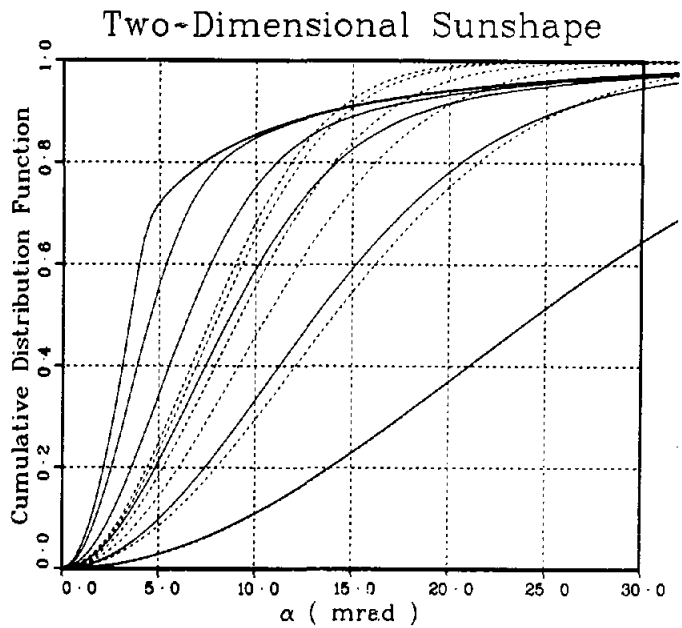
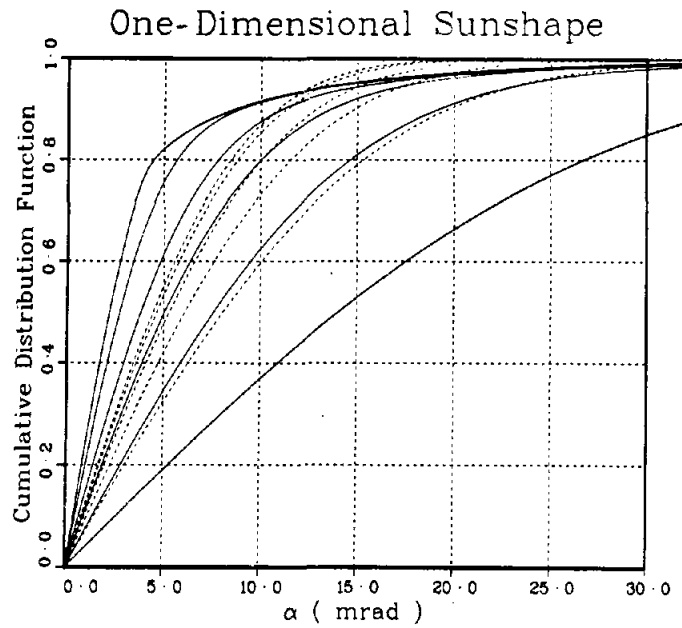


Figure 6-17. Cumulative Distribution Functions for the One- and Two-Dimensional Effective Sunshapes Generated by Convoluting the Medium Width Sunshape (Data Set 10) With Error Cones of Dispersion 0, 2, 4, 6, 10, and 20 mrad

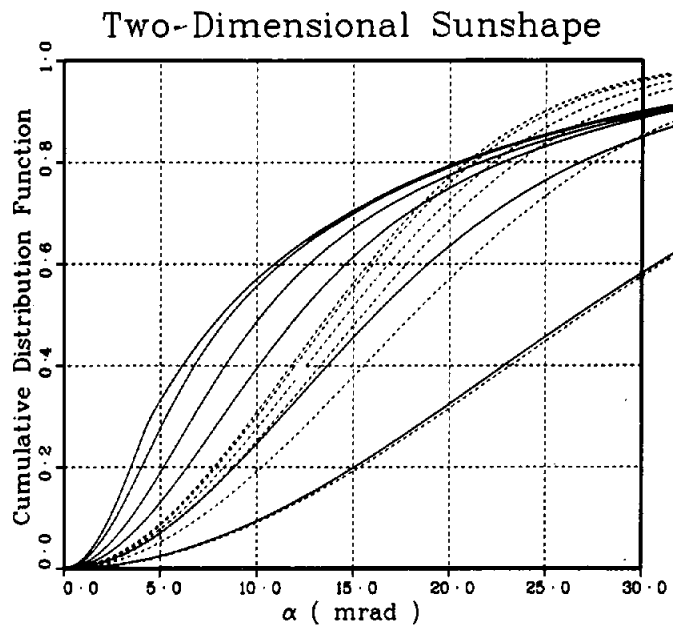
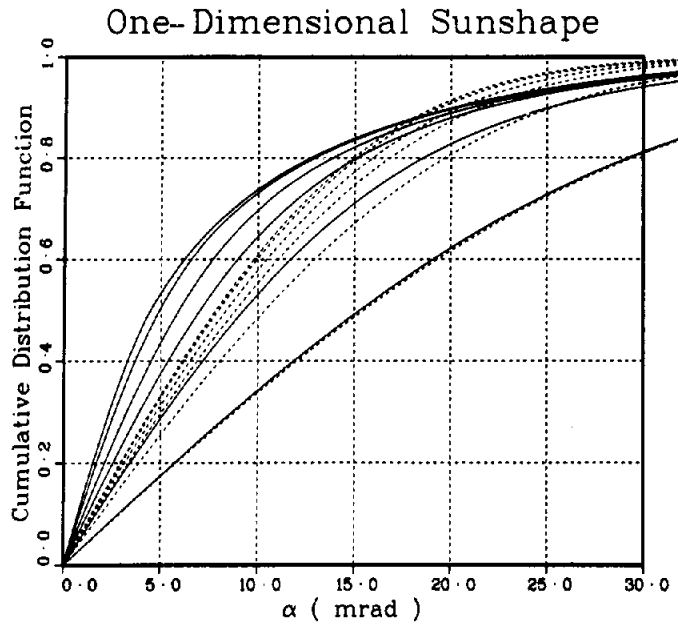


Figure 6-18. Cumulative Distribution Function for the One- and Two-Dimensional Effective Sunshapes Generated by Convoluting the Wide Sunshape (Data Set 16) With Error Cones of Dispersion 0, 2, 4, 6, 10, and 20 mrad

6.4.6 Sensitivity of Collected Power to Sunshape Variation

The power collected by a central receiver is dependent upon many related variables. If the receiver is sufficiently large, sunshape variation will matter only slightly. If the receiver barely accepts the intensity pattern produced by the narrowest possible sun, then slight changes in sunshape or in alignment or surface uncertainties will have a significant effect upon the results. As an illustration of the effect of sunshape, HELIOS results for the 78 heliostats (2902.4 m² of glass) in the north field (Zone A) of the Central Receiver Test Facility are presented in Table 6-IV. The 1 x 1-m Martin-Marietta 1-MW receiver aperture at 44.5-m altitude is used as the target. Solar insolation is normalized to 800 W/m² and facet reflectivity is set to 0.80 to remove these variations. Prealignment is set for noon on March 21 at the target center. Because of this prealignment, the sensitivity should be most pronounced on March 21. Error-cone dispersions are taken as 0 and as the more realistic 2.82 mrad, since the sensitivity must vary with the size of uncertainties in the system of heliostats.

TABLE 6-IV

Comparison for Sunshape Variation, $S = 800 \text{ W/m}^2$, $\rho = 0.8$,
78 Heliostats in Zone A, 1-MW Martin-Marietta Receiver.
 $\sigma \equiv$ error cone dispersion

Sunshape	Power Collected (MW)								
	March 21			June 21			December 21		
	8 AM	10 AM	Noon	8 AM	10 AM	Noon	8 AM	10 AM	Noon
Pillbox $\sigma = 0$	0.79	1.40	1.72	0.66	1.21	1.48	0.41	1.19	1.46
Narrow Data Set 9 $\sigma = 0$	0.87	1.45	1.69	0.75	1.25	1.44	0.45	1.29	1.52
Wide Data Set 16 $\sigma = 0$	0.43	0.67	0.77	0.39	0.60	0.68	0.23	0.59	0.68
Pillbox $\sigma = 2.82 \text{ mrad}$	0.69	1.12	1.30	0.57	0.98	1.17	0.34	0.94	1.12
Narrow $\sigma = 2.82 \text{ mrad}$	0.71	1.15	1.34	0.62	1.01	1.16	0.37	1.01	1.19
Wide $\sigma = 2.82 \text{ mrad}$	0.37	0.57	0.65	0.34	0.52	0.60	0.20	0.49	0.56

Table 6-IV indicates that the CRTF collected power can vary by more than a factor of 2 because of sunshape variation. If insolation variation is also included (rather than the 800 W/m² normalization in the table), then Table 6-III data indicate the factor 2 can change to $2 \times 943.7 / 95.3$, i. e., 19.8. Just the effective sunshape variation caused by altering the error cone dispersion from 0 to 2.82 mrad can produce 30% reduction in the collected power. The data indicate that the 1-MW receiver is not sufficiently large to make collected power independent of sunshape variation.

In addition to the collected power, the distribution of power on the receiver aperture is also affected by the effective sunshape. Data are given in Figure 6-19. The ratio of the peak to the average power density varies from 2.9 to 2.1 (2.0 to 1.6) as the error cone dispersion goes from 0 to 2.82 mrad for the narrow (wide) sunshape. Hence, importance of the distribution of power on the receiver can also determine the criticality of sunshape variation. Of course, the power may be distributed more evenly by allowing various sections of the heliostat field to be aimed at slightly different points in the receiver. Depending upon specific parameters chosen, such a design approach could certainly alter the data in Table 6-IV.

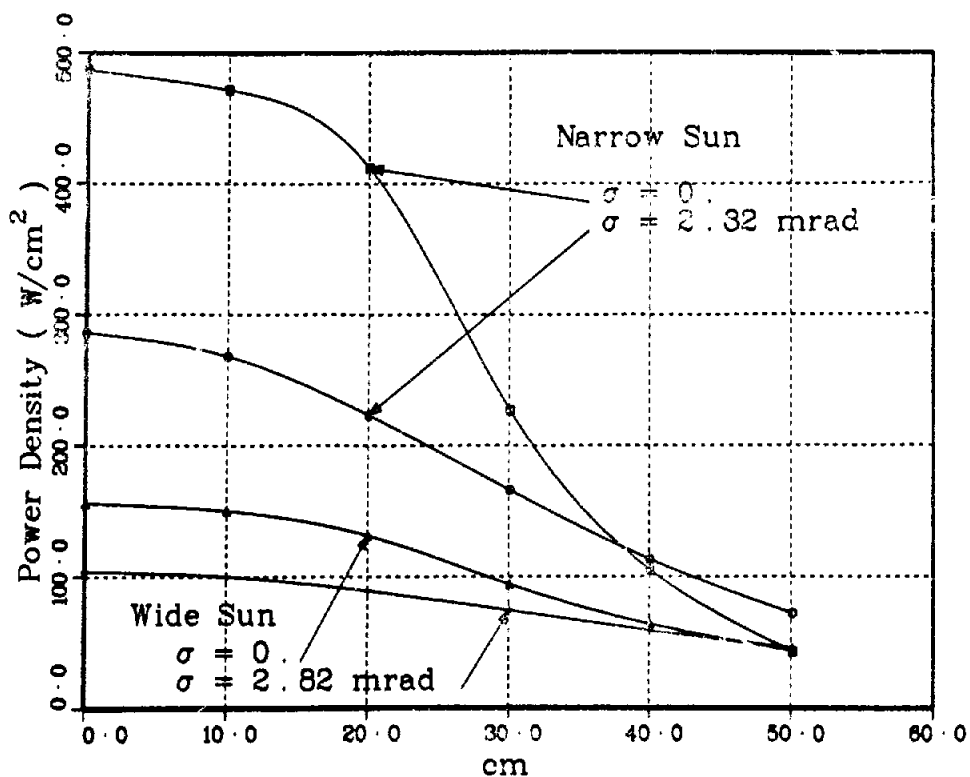


Figure 6-19. Distribution of Power Density Along a Horizontal Line to the West of the Martin-Marietta 1-MW Receiver Center for March 21 at Noon. Insolation is normalized to 800 W/m²; reflectivity is 0.80. The narrow and wide sunshapes correspond to Data Sets 9 and 16 in Table 6-III

References

- 6.1 C. W. Allen, Astrophysical Quantities, Oxford University Press, Inc., New York, NY, p 120, 1964.
- 6.2 K. Ya. Kondratyev, Radiation in the Atmosphere, Academic Press, New York, NY, 1969.
- 6.3 F. Kasten, "A New Table and Approximation Formula for the Relative Optical Air Mass," Arch Meteorol. Geophys. Bioklim, B14: 206, 1966.
- 6.4 F. A. Koomanoff, "Monitoring the Solar Resources," Vol. 1, Proceedings of the Sharing the Sun Solar Technology in the Seventies Joint Conference of the International Solar Energy Society and the Solar Energy Society of Canada, Inc., Winnipeg, Canada, August 15-20, 1976, p 120a (edited by K. W. Boer).
- 6.5 M. P. Thekaekara, "Extraterrestrial Solar Spectral Irradiance," Chapter 4 of The Extraterrestrial Solar Spectrum, Edited by A. J. Drummond and M. P. Thekaekara, published by the Institute of Environmental Sciences, Mount Prospect, IL, p. 114, 1973.
- 6.6 A. P. Thomas and M. P. Thekaekara, "Experimental and Theoretical Studies on Solar Energy for Energy Conversion," Vol. 1, Proceedings of the Sharing the Sun Solar Technology in the Seventies Joint Conference of the International Solar Energy Society and the Solar Energy Society of Canada, Inc., Winnipeg, Canada, August 15-20, 1976, p 338 (edited by K. W. Boer).
- 6.7 P. Moon, "Proposed Standard Solar Radiation Curves for Engineering Use," Journal of Franklin Institute 230, No. 1379, November 1940.
- 6.8 D. M. Gates, "Spectral Distribution of Solar Radiation at the Earth's Surface," Science 151, No. 3710, February 4, 1966.
- 6.9 L. L. Vant-Hull, "Methods for Estimating Total Flux in the Direct Solar Beam at Any Time," Vol. 1, Proceedings of the Sharing the Sun Solar Technology in the Seventies Joint Conference of the International Solar Energy Society and the Solar Energy Society of Canada, Winnipeg, Canada, August 15-20, 1976, p 369 (edited by K. W. Boer).
- 6.10 A. J. La Rocca and R. E. Turner, Atmospheric Transmittance and Radiance: Methods of Calculation, Environmental Research Institute of Michigan Report 107600-10-T, June 1975.
- 6.11 J. E. A. Selby and R. A. McClatchey, Atmospheric Transmittance From 0.25 to 28.5 μ m: Computer Code LOWTRAN III, Report AFCRL-TR-75-0255, Air Force Cambridge Research Laboratories, May 7, 1975.
- 6.12 D. G. Collins and M. B. Wells, Monte Carlo Codes for Study of Light Transport in the Atmosphere, Vol. I Description of Codes, and Vol. II Utilization, ECOM-00240-FI, ECOM-00240-FII, 1965.
- 6.13 W. G. M. Blattner and D. G. Collins, Utilization Instructions for Operation of the Polo Monte Carlo Programs on the Sandia CDC-6600 Computer, Radiation Research Associates, Inc., Research Note RRA-N7515, September 2, 1975.
- 6.14 R. A. McClatchey, R. W. Fenn, J. E. A. Selby, F. E. Volz, and J. S. Garing, Optical Properties of the Atmosphere, Report AFCRL-72-0497, Third Edition, Air Force Cambridge Research Laboratories, August 1972.
- 6.15 D. Grether and A. Hunt, Description of the LBL Reduced Data Base and Standard Profiles, Lawrence Berkeley Laboratory, August 9, 1977. A. Hunt also furnished punched card data for the sunshapes.

- 6.16 M. Minnaert, "The Photosphere," a Contribution to The Sun, The Solar System I, Edited by G. P. Kuiper, University of Chicago Press, Chicago, IL, 1953.
- 6.17 C. N. Vittitoe, F. Biggs, and R. E. Lighthill, HELIOS: A Computer Program for Modeling the Solar Thermal Test Facility A Users Guide, SAND76-0346, Sandia Laboratories, Albuquerque, NM, June 1977.
- 6.18 D. I. Teplyakov, "Concentrating Power of Solar-Energy Paraboloids in Various Spectral Ranges," Geliotekhnika, Vol 9: 20-26, 1973.

CHAPTER 7

NUMERICAL PROCEDURES

7.1 Integration Over the Target Grid

HELIOS calculates the flux density (W/cm^2) at a grid of target points. The resulting flux-density pattern can be displayed by drawing contour, and three-dimensional plots, and by other methods. The pattern is also used to integrate the flux density over portions of the target grid to determine the power (in watts) incident upon a specified area. In this section we discuss the numerical scheme used in HELIOS to perform these surface integrals.

Integrating a smooth kernel over a surface has properties similar to those of one-dimensional integrals in that the integration errors can be reduced by decreasing the grid spacing between the points at which the integrand is evaluated or by going to a more elaborate quadrature formula. Certain quadrature formulas require that the integrand be evaluated at a prescribed mesh of points. The optimum mesh of points for quadrature purposes is not an optimum mesh for displaying the flux-density patterns. Since we wish to use the same values of the flux density for displaying the flux-density pattern that we use for calculating the integral over this pattern, we use a regular grid pattern. Whenever necessary the grid spacing is decreased in order to improve the accuracy of integration. The integration is performed by two different approximations in order to provide an estimate of the integration error.

7.1.1 Flat Rectangular Target

Consider a rectangle of length $2a$ and height $2b$ centered on an $x - y$ coordinate system as shown in Figure 7-1. The area of this rectangle is

$$A = 4ab \tag{7.1-1}$$

and the integral of a function $F(x, y)$ over this rectangle is

$$I = \int_{-a}^a \int_{-b}^b F(x, y) dx dy . \tag{7.1-2a}$$

Approximations to this integral can be constructed which evaluate F at discrete points. One such approximation, I_1 , is defined by

$$I \simeq I_1 = \frac{A}{6} [2F(0, 0) + F(a, 0) + F(0, b) + F(-a, 0) + F(0, -b)] . \tag{7.1-2b}$$

A convenient short-hand way to express this approximation is

$$I_1 = \frac{A}{6} \left[2 \text{ center} + \sum \text{ edge centers} \right]. \quad (7.1-2c)$$

The circled numbers in Figure 7-1 are the weights used to evaluate the expression inside the brackets of approximation I_1 [Eq. (7.1-2b and c)]. Thus the integral of F over a rectangle is evaluated in the approximation I_1 by multiplying the value of F at the center of the rectangle by 2, adding the values of F at the center of each of the four sides, and multiplying this sum by one-sixth of the area of the rectangle.

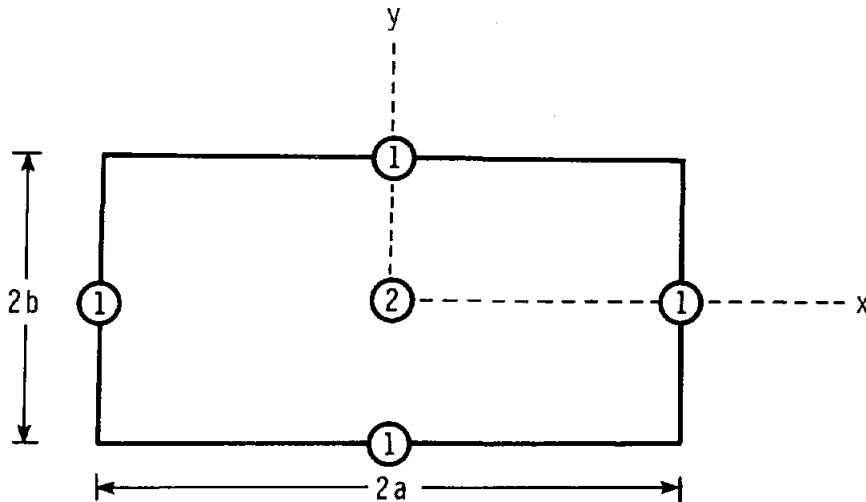


Figure 7-1. Weighting Scheme for the Surface-Integral Approximation I_1 for Eq. (7.1-2)

The approximation I_1 is due to Tyler.^{7.1} It is also discussed by Stroud.^{7.2} The formula has a degree of exactness equal to 3 in that it is exact when the integrand F is any linear combination of monomials $x^\alpha y^\beta$ where α and β are nonnegative integers such that $0 \leq \alpha + \beta \leq 3$.

Another approximation that also has a degree of exactness equal to 3 is

$$I \approx I_2 = \frac{A}{12} \left[8F(0, 0) + F(a, b) + F(-a, b) + F(-a, -b) + F(a, -b) \right]. \quad (7.1-3a)$$

The shorthand notation for this is

$$I_2 = \frac{A}{12} \left[8 \text{ center} + \sum \text{ corners} \right]. \quad (7.1-3b)$$

Figure 7-2 shows the I_2 weighting scheme for the terms inside the brackets. Note that the sum in brackets is obtained by taking 8 times the value of the integrand at the center of the rectangle and adding the value of the integrand from each of the four corners. This sum is then multiplied by one-twelfth the area of the rectangle to complete the calculation. This approximation is due to Ewing,^{7.3} but it is also discussed by Tyler^{7.1} and by Stroud.^{7.2}

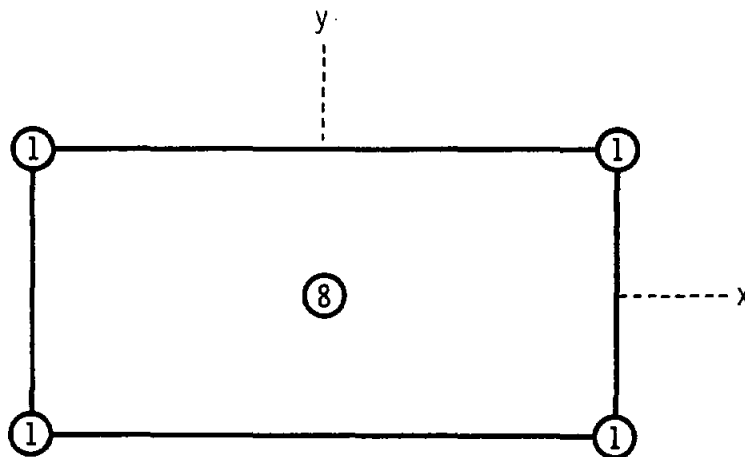


Figure 7-2. Weighting Scheme for the Surface-Integral Approximation I_2 of Eq. (7.1-3)

Other approximations can be constructed by forming combinations of I_1 and I_2 . The approximation

$$I_3 = \frac{2}{3} I_1 + \frac{1}{3} I_2 \quad (7.1-4a)$$

is an interesting one because it can be obtained by applying Simpson's rule twice: once to integrate the rectangle in one direction and again to integrate these results in the other direction. It is, therefore, referred to as the Product Simpson's Rule formula. In our shorthand notation it becomes

$$I_3 = \frac{A}{36} (16 \text{ center} + \sum \text{corners} + 4 \sum \text{edge centers}) . \quad (7.1-4b)$$

The approximation

$$I_4 = \frac{3}{4} I_1 + \frac{1}{4} I_2 \quad (7.1-5a)$$

is due to Albrecht and Collatz^{7.4}; it is also discussed in Stroud.^{7.2} In our shorthand notation this becomes

$$I_4 = \frac{A}{48} (20 \text{ center} + \sum \text{corners} + 6 \sum \text{edge centers}) . \quad (7.1-5b)$$

In order to illustrate the use of these approximations, we consider an example. A flux density that is similar to some that we have encountered in practice is

$$F(x, y) = \exp(-x^2 - y^2). \quad (7.1-6)$$

We integrate this over each of the two squares shown by solid lines in Figure 7-3. Each square has sides of length $2a$. One square is centered at the origin and the other one adjoins it along the x -axis as shown. The integral over the square centered on the origin is

$$E_1(a) = \int_{-a}^a e^{-x^2} dx \int_{-a}^a e^{-y^2} dy = \pi \operatorname{erf}^2(a) \quad (7.1-7)$$

and the integral of F over the other square is

$$E_2(a) = \int_a^{3a} e^{-x^2} dx \int_{-a}^a e^{-y^2} dy = \frac{\pi}{2} \operatorname{erf}(a) [\operatorname{erf}(3a) - \operatorname{erf}(a)]. \quad (7.1-8)$$

These analytical results are useful in illustrating the adequacy of our quadrature approximations. We can illustrate the effect of mesh-size variations by changing the size of a . Note that the integrand [Eq. (7.1-6)] changes by a factor of $\exp(a^2)$ between the center of the square and the center of one side for the square centered on the origin. We cannot expect the quadrature formulas to give good approximations when the integrand changes too much between adjacent grid points.

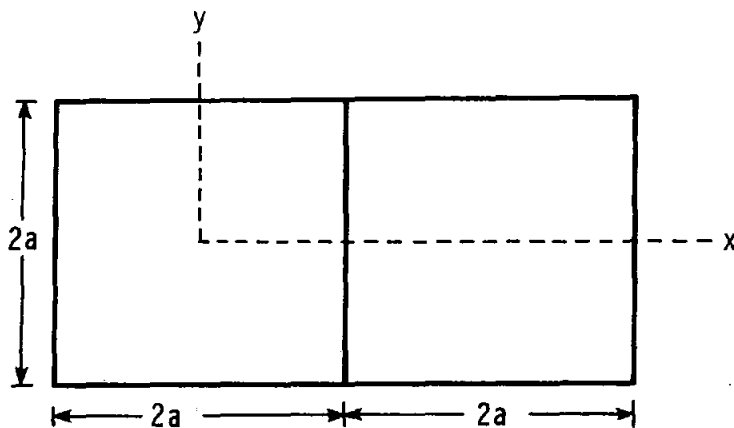


Figure 7-3. Regions in the $x - y$ Plane for Using the Quadrature Approximations as an Example

In order to illustrate this effect and to estimate how much variation can be tolerated between grid points and still give satisfactory accuracy, we evaluate E_1 and E_2 using all of the approximations at several values of a . The results are shown in Tables 7-I and 7-II. The values of a are given in the first column. In Table 7-I, the next column gives the value of E_1 as obtained analytically from Eq. (7.1-7) and is therefore correct to the number of significant places shown. The next four columns give the numbers as calculated from the indicated approximations. The last column gives values of $\exp(a^2)$. Table 7-II is organized the same way as Table 7-I except that it applies to values of E_2 from Eq. (7.1-8).

TABLE 7-I
Estimates of E_1

a	E_1					
	Exact Eq. (7.1-7)	I_1 Eq. (7.1-2)	I_2 Eq. (7.1-3)	I_3 Eq. (7.1-4)	I_4 Eq. (7.1-5)	$\exp(a^2)$
2	3.127	5.38	10.7	7.15	6.71	54.6
1	2.338	2.31	2.85	2.49	2.45	2.72
0.5	0.8511	0.8525	0.8688	0.8579	0.8566	1.28
0.25	0.23988	0.23990	0.24020	0.2400	0.2400	1.06

TABLE 7-II
Estimates of E_2

a	E_2					
	Exact Eq. (7.1-8)	I_1 Eq. (7.1-2)	I_2 Eq. (7.1-3)	I_3 Eq. (7.1-4)	I_4 Eq. (7.1-5)	$\exp(a^2)$
2	0.0073	0.049	0.00089	0.033	0.037	54.6
1	0.2079	0.279	0.139	0.232	0.244	2.72
0.5	0.3643	0.3655	0.3600	0.3637	0.3641	1.28
0.25	0.18874	0.18875	0.18887	0.18879	0.18878	1.06

Several things should be observed about the results of these tables:

- a. At $a = 2$, all the approximations overestimate the value of E_1 by a considerable margin. This is probably caused by the highly peaked nature of the integrand at the center of the corresponding square.

- b. At $a = 0.25$, where $\exp(a^2) = 1.06$, all the approximations give good accuracy. The accuracy is reasonable at $a = 0.5$ where $\exp(a^2) = 1.25$. We expect quadrature errors to be within 1% when the integrand changes by less than 25% between grid points. This, of course, assumes that the integrand is in some sense as smooth as that [Eq. (7.1-7)] used in this example.
- c. Eq.(7.1-2b or 2c) (I_1) generally gives better approximations to the integral than does Eq.(7.1-3) (I_2). One reason for this is that there is less fractional variation in the integrand between adjacent integration-grid points for the first approximation than for the latter.
- d. If the difference between the values obtained from the two approximations I_1 and I_2 is taken as an error estimate, then the estimate obtained from either I_3 or I_4 is within plus or minus this error for the Tables 7-1 and 7-II results. Note, however, that if the difference between I_3 and I_4 is used as an estimate of the error, then neither I_3 nor I_4 is within this error of the true value for most of the examples of Tables 7-I and 7-II. This probably results from the fact that the weights used in Eq. (7.1-4a) do not differ enough from those used in Eq. (7.1-5a)

The recommended procedure is to calculate the approximations I_1 and I_2 , use their difference as an error estimate, and then form one of the linear combinations of either Eq. (7.1-4a) or Eq. (7.1-5a) to obtain either the I_3 or I_4 estimate to use as the best estimate of the integral. Although all of these approximations have a degree of exactness equal to 3, we prefer either I_3 or I_4 as a final estimate of the integral over I_1 or I_2 because they use more function evaluations on the rectangle. However, I_1 and I_2 are still required to obtain error estimates.

The current version of HELIOS evaluates the flux density at an 11 by 11 grid of points. A 5 by 5 array of nonoverlapping rectangles are used to calculate the integral over the entire target grid. The integral is evaluated using each of the approximations I_3 and I_4 separately. The error in each rectangle is now estimated by comparing results from the two approximations.

The error in the integral over the entire grid can be estimated by comparing the integrals for the entire grid. Another estimate is obtained by squaring the error of each rectangle, adding them all together and taking the square root. A more conservative estimate of the total error is to add up the absolute errors from the individual rectangles.

7.1.2 Spherical Targets

Options are also available in HELIOS for specifying the receiver surface in terms of spherical or cylindrical surfaces; in these options new coordinate systems are used to specify the grid points at which the flux densities in W/cm^2 are calculated. The integration over these surfaces to get intercepted power must take the surface properties into account. An element of area on the surface of a sphere of radius R is

$$dS = R^2 \sin \theta \, d\theta d\phi \quad (7.1-9)$$

where θ is the polar angle and ϕ is the azimuthal angle. The surface integral of the flux density F over region \mathcal{R} of the surface of a sphere of radius R is

$$I = \iint_{\mathcal{R}} [F(\theta, \phi) R^2 \sin \theta] \, d\theta d\phi \quad (7.1-10)$$

If the flux density is specified at a regular grid of points in the coordinates θ and ϕ , then we define the integrand

$$\hat{F} = F R^2 \sin \theta \quad (7.1-11)$$

and proceed as we did in the rectangular coordinates.

7.1.3 Cylindrical Targets

In cylindrical coordinates the surface integral over a region \mathcal{R} on a cylinder of radius R is

$$I = \iint_{\mathcal{R}} F(\phi, Z) R \, d\phi dz \quad (7.1-12)$$

Here we define the integrand

$$\hat{F} = F R \quad (7.1-13)$$

and proceed as before.

7.1.4 Circular Target Grid on a Plane Surface

For receivers with a circular aperture it may be convenient to use a target grid with circular symmetry. In this section we develop a procedure for using the previous approximations

to estimate the surface integral of a function specified in polar coordinates. The integral of a function $G(r, \theta)$ is

$$I = \iint G(r, \theta) r d\theta dr = \iint F(r, \theta) d\theta dr \quad (7.1-14)$$

where

$$F(r, \theta) = G(r, \theta)r . \quad (7.1-15)$$

This puts the problem into the same form as discussed in Section 7.1.1; hence, the same approximations can be used after applying the transformation of Eq. (7.1-15).

As an illustration, consider the function

$$G = e^{-.1r^2} \quad (7.1-16)$$

which gives

$$F = re^{-.1r^2} . \quad (7.1-17)$$

The weighting scheme corresponding to Figure 7-1 is shown in Figure 7-4. We use a segment between the radii $r = 1$ and $r = 3$ of an angular width $2\Delta\theta$. The quantity corresponding to A of Eq. (7.1-1) is

$$A = 4\Delta\theta \Delta r = 4\Delta\theta . \quad (7.1-18)$$

The approximation Eq. (7.1-2b) gives

$$I_1 = \frac{4\Delta\theta}{6} \left[2(2e^{-.4}) + 3e^{-.9} + 2e^{-.4} + e^{-.1} + 2e^{-.4} \right] = 4.99\Delta\theta . \quad (7.1-19)$$

Evaluating the same integral analytically gives

$$I = 4.983\Delta\theta . \quad (7.1-20)$$

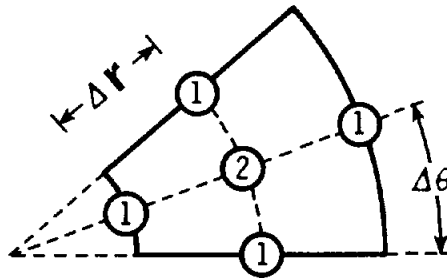


Figure 7-4. Weighting Coefficients for Eq. (7.1-2) for Area Segments in Polar Coordinates

It is clear from this illustration how to use the approximation (7.1-3) on an area segment such as the one shown in Figure 7-4. The center node is weighted by 8 and nodes at the corners of the segment are weighed by 1 corresponding to the scheme depicted in Figure 7-2. When this approximation is applied to the numerical example given above, exactly the same result is obtained; this means the difference between the approximations of Eqs. (7.1-2b) and (7.1-3) is not a good estimate of the error in this example.

7.2 Facet Integration

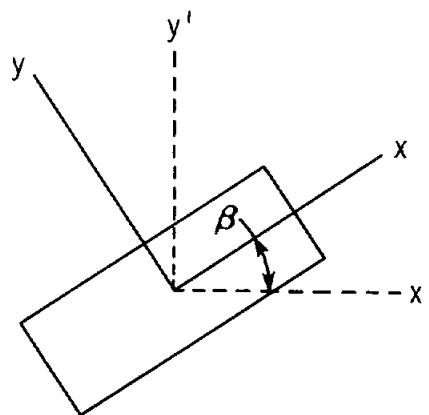
In Section 5.5 an integral [Eq. (5.5-3)] is given for calculating the flux density at a target point. In order to do the integration (numerically) it is necessary to set up a grid on each facet of the reflecting surface that forms a part of the concentrator field. In HELIOS, subroutine FACET performs this integration.

Options are available for facets that are square, rectangular, triangular, or circular. A square facet is, of course, a special case of a rectangular facet but separate options are available in the code. The square-facet option was built into the initial version of the code whereas the rectangular-facet option was added later.

In the square-facet option (KORD = 1), an N- by N-grid is used to divide the facet into surface elements corresponding to the ΔQ of Figure 5-28. In the rectangular-facet option (KORD = 3), both the length (ELENX) and the width (ELENY) of the facet are specified; also the number of strips into which the facet is divided is specified separately for the two directions. The facet coordinate system has its z-axis perpendicular to the reference surface at the center of the facet. (Refer to Section 5.1 for a description of the reference surface.) Its x-axis is horizontal (i. e., nearly parallel to the elevation axis of the heliostat).

As explained in Chapter 3, the x-axis of the facet coordinate system makes an angle β with the x-axis of the sun-concentrator system. This relationship is shown in Figure 7-5 where primes are used to designate the axes of the sun-concentrator system. The z and z' axes coincide and are perpendicular to the plane of the page.

Figure 7-5. The Facet System
x - y and the Sun-
Concentrator System
x' - y'



In the circular-facet option, the facet is divided into circular strips and the strips are divided into segments. Each segment is weighted in the calculation in proportion to its area, and the centroid of the segment is taken as the point of reflection for the radiation striking the segment. In this option (KORD = 2) the parameter ELEN is the radius of the facet in meters. The parameter N (in common block /CKORD/ is used to divide the facet into circular strips. The first element of area is taken to be a circle of radius

$$R = \text{ELEN}/(2N) . \quad (7.2-1)$$

The rest of the facet is then divided into $N - 1$ circular strips of width equal to

$$\Delta R = \frac{\text{ELEN} - R}{N - 1} . \quad (7.2-2)$$

These strips are then divided into segments. Figure 7-6 shows a schematic of one such segment in one of the circular rings defined by concentric circles of radii $r = a$ and $r = b$. The angular width of each segment in the strip is

$$\Delta \theta = 2\alpha = 2\pi/M \quad (7.2-3a)$$

where

$$M = \text{INT} (2\pi b/\Delta R) + 1 . \quad (7.2-3b)$$

We have used Fortran notation for the function INT which truncates its argument to an integer. Observe that this procedure produces M segments of equal area such as the cross-hatched segment of Figure 7-6 so that the arc length $b\Delta\theta$ is less than or equal to the strip width ΔR . The number of segments M increases in moving from one circular strip out to another one defined by larger radii.

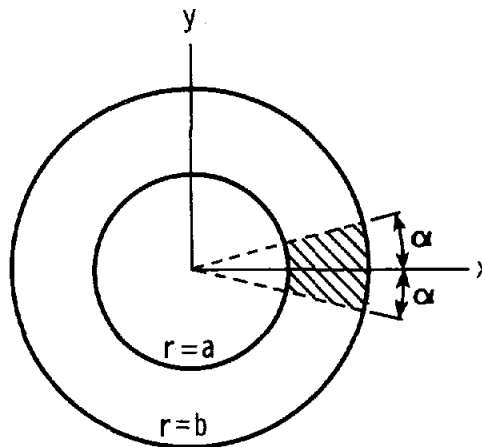


Figure 7-6. An Integration Segment for a Circular Facet

The x coordinate of the segment centroid shown in Figure 7-6 is

$$\begin{aligned}\bar{x} &= \frac{1}{A} \int_{-\alpha}^{\alpha} d\theta \int_a^b xrdr = \frac{1}{A} \int_{-\alpha}^{\alpha} \cos \theta d\theta \int_a^b r^2 dr \\ &= \frac{2 \sin \alpha}{3A} (b^3 - a^3)\end{aligned}\tag{7.2-4a}$$

where the area of the segment is

$$A = \alpha(b^2 - a^2)\tag{7.2-4b}$$

which gives

$$\bar{x} = \frac{2}{3} \frac{(a^2 + ab + b^2) \sin \alpha}{(a + b) \alpha}.\tag{7.2-4c}$$

The y coordinate of the segment shown in Figure 7-6 is

$$\bar{y} = 0\tag{7.2-5}$$

which is obvious from the symmetry of the segment. The polar coordinates of a centroid are given by an angle θ for a ray passing through the center of the segment and a radial coordinate equal to \bar{x} of Eq. (7.2-4c).

In the "super-smart" facet-curvature option (IOPT = 5), the problem is treated as if the entire contribution of reflected power comes from the facet center. This is equivalent to using $N = 1$ for the square or circular facets or $N_X = N_Y = 1$ in the rectangular-facet option. This option, of course, decreases computation time by about a factor of N^2 .

The equilateral-triangle facet option (KORD = 5) divides the triangular surface into an $N_x \times N_x$ grid of elementary equilateral triangles. The facet coordinate system has its x -axis along the bottom edge which is assumed to be horizontal. This x -axis makes an angle β with the x -axis of the sun-concentrator system. As earlier, the y -axis is in the plane of the facet corners, orthogonal to the x -axis. The divisions are indicated in Figure 7-7 for $N_x = 6$.

Before conversion to the sun-concentrator system the origin must be translated to the triangle centroid. For integration over the facet surface, the centroid of each elementary triangle must be specified. For equilateral triangles of side 1 the centroid is at $\sqrt{3}/2$ from each side.

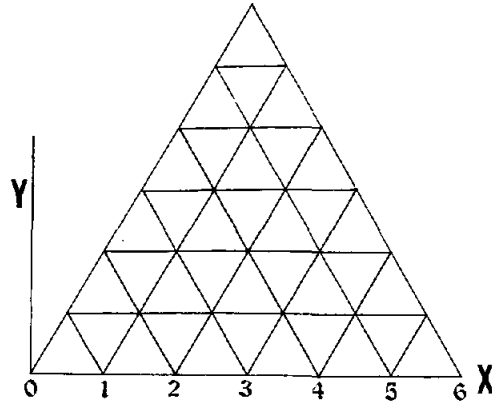


Figure 7-7. Integration Segments for a Triangular Facet

There are $2N_x - 1$ rows for y values for triangle centroids. They are located at

$$y_{i+1} = y_i + A * \sqrt{3} \text{ DX}/2 \quad (7.2-6)$$

for $i = 1$ to $2N_x - 2$. Also

$$y_1 = \sqrt{3} \text{ DX}/2 , \quad (7.2-7)$$

$$\text{DX} = \text{ELENX}/N_x , \quad (7.2-8)$$

ELENX = length of triangle side,

$$A = \begin{cases} 1 & i \text{ odd} , \\ 2 & i \text{ even} \end{cases} . \quad (7.2-9)$$

Replacement of y_i by $-y_i$ will rotate the triangle 180° in the facet coordinate system.

The initial value of x for each row of elementary triangles is given by

$$x_{in} = \text{INT} \left(\frac{N_{row} + 2}{2} \right) * \frac{\text{DX}}{2} \quad (7.2-10)$$

for $1 \leq N_{row} \leq 2N_x - 1$, where again the INT notation indicates truncation of the argument to

an integer. The following x values in each row are separated from each other by DX . The number of elementary triangles in each row is given by

$$N_{\text{col}} = N_x - \text{INT}(N_{\text{row}}/2) . \quad (7.2-11)$$

Thus the x values in each row are given by

$$x_j = (x_{\text{in}} - DX) + j * DX \quad (7.2-12)$$

for $1 \leq j \leq N_{\text{col}}$. The translation to the facet centroid is given by converting (x_j, y_i) to $(x_j - \text{ELENX}/2, y_i - \text{ELENX} * \sqrt{3}/2)$. Now that the elements of area $(\sqrt{3} * DX * DX/4)$ and their centroids are specified, the integration over the facet surface proceeds as before.

7.3 The Two-Dimensional Fast Fourier Transform

The convolution of two-dimensional distributions plays an important role in the HELIOS model. After sun-tracking error distributions are mapped to a reflector reference plane, they are combined with the distribution of surface slope errors by convolution to obtain the error cone in this system. This error cone is then mapped into the reflected-ray reference system where convolution is again used to combine it with the sunshape. These mappings and convolutions can all be done analytically when all of the distributions are elliptic normal. Although an elliptic-normal distribution is probably an adequate approximation for surface slope errors and perhaps even for sun-tracking errors, it is not a very good approximation to the sunshape. Therefore, if a careful calculation of the flux pattern on a receiver is to be made, at least part of the convolution calculations must be done numerically. In this section we describe the use of the fast Fourier transform (FFT) to calculate two-dimensional convolutions.

Suppose we wish to convolve the two distributions F and G to get the resultant distribution H .

$$H(x, y) = F(x, y) * G(x, y) . \quad (7.3-1)$$

In order to use the FFT to approximate this result, a few of its properties are explained. Although none of the distributions F , G , or H are periodic in x or in y , the FFT treats them all as being periodic in both x and y . Since we are free to select the periods, we can insure that the periodic extensions \hat{F} , \hat{G} , and \hat{H} of these functions are adequate approximations to F , G , and H , respectively, in a region of the $x - y$ plane (function space) of interest to us.

Consider a slice across the center of the distribution F as shown by the solid curve in Figure 7-8. The dashed curve shows a portion of its periodic extension \hat{F} of period ELX .

The function \hat{F} is equal to F inside the interval $|x| < |ELX/2|$ and equal to its periodic extension of period ELX outside this interval.

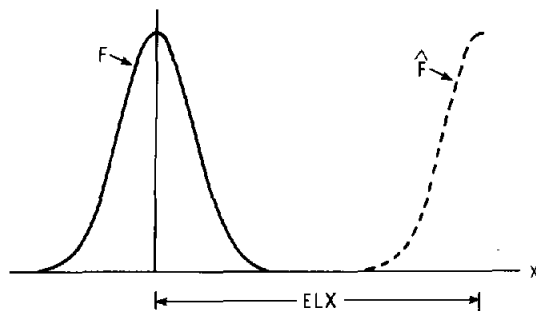


Figure 7-8. A Slice of Distribution F and a Portion of its Periodic Extension \hat{F} of Period ELX

Although we have illustrated this property in only the x -direction for the distribution F , it occurs in both the x and y directions of all the distributions F , G , and H .

The period for the y direction is herein designated as ELY . For a given convolution problem the same values of ELX and ELY must be used for all three distributions. These parameters should be large enough that each of these distributions has negligible value whenever $|x| > ELX/2$ or $|y| > ELY/2$. Otherwise aliasing will occur and degrade the approximation. This requirement is the most stringent on H since it is wider than either F or G .

To use the FFT to approximate the Fourier integral transform of the distribution F , its periodic extension \hat{F} is evaluated at an array of points in the rectangle $0 \leq x < ELX$ and $0 \leq y < ELY$. The spacing in the x direction is $\Delta x = ELX/NX$ and in the y direction $\Delta y = ELY/NY$ where NX and NY are input parameters. The FFT calculation is more efficient if these numbers are both equal to some integer power of two.

The parameter NX should be large enough that when a value of ELX is selected that is large enough to prevent aliasing of H in the x direction, the corresponding $\Delta x = ELX/NX$ is small enough to adequately sample F in the x direction. The same considerations apply to NY and ELY and to the other distribution G being convolved. The computer memory and time requirements increase rapidly with increasing NX and NY .

The HELIOS subroutine CONV numerically performs the convolution of Eq. (7.3-1). It evaluates the periodic extension \hat{F} of F in the rectangle $0 \leq x < ELX$ and $0 \leq y \leq ELY$ at the points (x_i, y_j)

where

$$\left. \begin{array}{l} x_i = (i - 1) \text{ELX/NX}, \quad i = 1, \dots, \text{NX} \\ \text{and} \\ y_j = (j - 1) \text{ELY/NY}, \quad j = 1, \dots, \text{NY} \end{array} \right\} . \quad (7.3-2)$$

CONV obtains \hat{F} from F by replacing x by $x - \text{ELX}$ whenever $x > \text{ELX}/2$ and by replacing y by $y - \text{ELY}$ whenever $y > \text{ELY}/2$. These function values are stored in the real parts of the blank common array GF ; the imaginary parts of this array are set to zero. The same procedure is used on G to fill the blank common array GG .

These arrays are transformed to the transform space by the FFT routine FOURT in CONV . This FFT routine is described in Reference 5.7. In transform space the arrays are multiplied together to effect convolution. The result is then inverted by again using FOURT to obtain the periodic extension \hat{H} of H back in function space.

When the FFT is used to approximate the Fourier integral transform as is the case here, it is necessary to multiply the result by the function-space area-element $\Delta x \Delta y$ where

$$\Delta x = \text{ELX/NX} \quad (7.3-3a)$$

and

$$\Delta y = \text{ELY/NY} . \quad (7.3-3b)$$

In inverting the transform, the multiplier is the transform-space area-element Δf_x times Δf_y where

$$\Delta f_x = 1/\text{ELX} \quad (7.3-4a)$$

and

$$\Delta f_y = 1/\text{ELY} . \quad (7.3-4b)$$

These multipliers are all applied at one place in CONV when the two arrays are multiplied together.

The distributions F and G are normalized to unit volume and the convolved result H should theoretically also have unit volume. Since round-off errors and aliasing can disturb this normalization, a correction is applied during the transform-space multiplication. The correction is obtained by using the property that the function space volume of a distribution is equal to the corresponding transform evaluated at the origin.

The convolved result is transformed back to function space where values of \hat{H} are contained in the real parts of the blank common array GF . The x and y coordinates corresponding to this array of \hat{H} values are the same points (x_i, y_i) defined previously to evaluate \hat{F} and \hat{G} . This result of the convolution is communicated back to program HELIOS through this blank-common block.

In HELIOS it is necessary to obtain a table of the distribution H from the \hat{H} values stored in the real parts of the complex array GF . The values of \hat{H} in the interval $ELX/2 < x < ELX$ are translated to the left by the period ELX to give values of H in the interval $-ELX/2 < x < 0$. The same kind of translation is also used in the y -direction where the period is ELY .

When three distributions are to be convolved, two of them are first convolved together as described above by setting the $CONV$ input parameter $NOPT = 2$. Then $CONV$ is called again with $NOPT = 1$ and with the third distribution to be convolved entered as the second function argument of $CONV$. (The first function argument is not used in this case.) In this option the array GF , which already contains the result of the first convolution, is not changed. The new distribution is put into the array GG and the calculation proceeds as before. Of course, this procedure can be repeated as many times as needed to do multiple convolutions.

We have only mentioned argument parameters of subroutine $CONV$ as needed to clarify the discussion, because different versions of HELIOS have slightly different programming details. The discussion here applies to the most general version of the routine. The comment cards given in each version of $CONV$ adequately describe its argument parameters for using the routine.

In transform space, the increments in the f_x and f_y directions are $\Delta f_x = 1/ELZ$ and $\Delta f_y = 1/ELY$ where f_x and f_y are the transform variables corresponding to x and y respectively. The FFT versions of the transformed arrays also exhibit periodicity in both directions. The period in the f_x direction is $ELFX = NX/ELX$ and the period in the f_y direction is $ELFY = NY/ELY$. However, because of the same kind of "folding" effect shown in Figure 7-8 for F , only half of these periods represent effective frequencies. Therefore,

$$|\text{Max } f_x| = ELFX/2 \quad (7.3-5)$$

and

$$|\text{Max } f_y| = ELFY/2 \quad (7.3-6)$$

Since aliasing can also occur in transform space, it is sometimes necessary to also examine these relationships when specifying the parameters NX , NY , ELX , and ELY .

7.4 Blocking and Shadowing of Heliostats

7.4.1 The Projected Area

Earlier discussion in Chapters 2 and 3 gave the basic approach to shadowing and blocking and introduced the appropriate surfaces; i. e., the $X' - Z'$ plane through the tower base orthogonal to the sun's central ray and the unit sphere centered about the target center. The projections of the four corners of a heliostat onto these surfaces were also considered. These projections are used to estimate the effect of blocking and shadowing.

Let us consider the shadowing ($X' - Z'$) plane first. If we assume the edges of a heliostat lie in a plane, the projection of the four edges onto the $X' - Z'$ plane will result in a quadrilateral. One such quadrilateral is illustrated in Figure 7-9 where the corners are labeled. Overlap between the quadrilaterals for neighboring heliostats indicates shadowing is occurring.

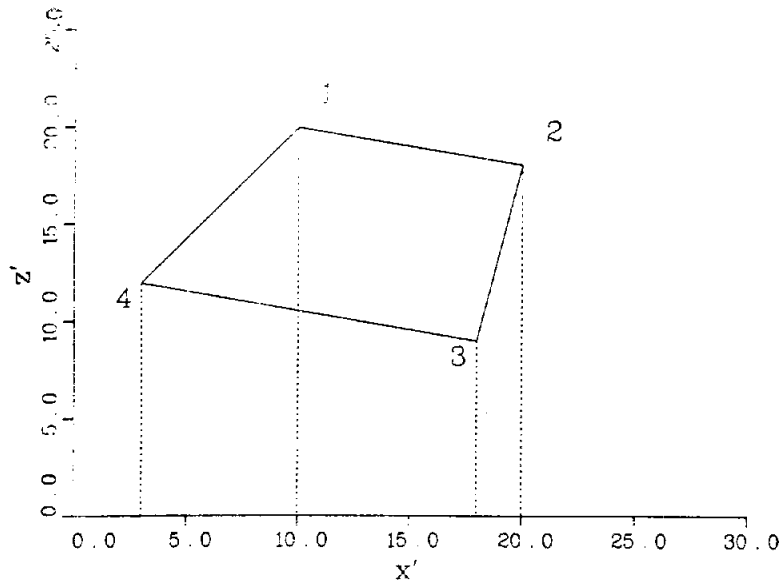


Figure 7-9. Shadowing Projection for a Heliostat

The coordinate pairs ($X'_i, Z'_i, i = 1, 4$) are available from the projection. One method of calculating the enclosed area involves direct calculation of edge lengths and angles. This approach requires square roots and perhaps the evaluation of trigonometric functions. Consider the following alternate approach.

The area may be decomposed into the sum of the areas of four oriented trapezoids. Project each vertex onto the X' - axis giving points X'_i where $1 \leq i \leq 4$. The area is given by

$$A = A_{12} + A_{23} + A_{34} + A_{41} \quad (7.4-1)$$

where

$$A_{ij} = 0.5 (Z'_i + Z'_j)(X'_j - X'_i) \quad (7.4-2)$$

A simple way to avoid complications when generalizing to other quadrants is to translate the Z'_i values to insure that all Z'_i are positive. Quadrilaterals with vertices numbered in a clockwise (counterclockwise) manner will then have a positive (negative) area as given above. The orientation for an individual trapezoid is given by the sign of $(X'_j - X'_i)$.

The four oriented trapezoids formed above are designated by the A_{ij} . The area of intersection of two quadrilaterals can now be found by treating the simpler problem of finding the areas of intersection of pairs of trapezoids. The overlap test is then simple, a nonzero (zero) area of overlap indicates that the quadrilaterals do (do not) overlap.

7.4.2 The Overlap Test

The method for measuring overlap was developed by D. S. Mason.^{7.5} Take two quadrilaterals designated by areas B and C . Each may be subdivided into four oriented trapezoids as before.

$$B = B_{12} + B_{23} + B_{34} + B_{41} \quad (7.4-3)$$

$$C = C_{12} + C_{23} + C_{34} + C_{41} \quad (7.4-4)$$

The area of intersection, I , of B and C may be expressed in terms of the overlap of the subdivisions, D_{ij} .

$$I = \sum_{i=1}^4 \sum_{j=1}^4 \text{sign}(i, j) D_{ij} \quad (7.4-5)$$

The sign (i, j) is ± 1 depending upon the orientation of the sides in the two oriented trapezoids (i. e., x is increasing for both $[+]$, decreasing for both $[+]$, or increasing for one and decreasing for the other $[-]$). A side is oriented positively (negatively) if the x coordinates of its ends are increasing (decreasing).

As discussed by Mason, the area D_{ij} will depend upon whether the quadrilateral edges that determine B_{im} and C_{jn} intersect. When they do not intersect, the situation is illustrated in Figure 7-10.

$$\text{Let } x_3 = \min(x_{iB}, x_{jC}) \quad (7.4-6)$$

$$x_4 = \max(x_{mB}, x_{nC}) \quad (7.4-7)$$

These values are $x_3 = x_{iB}$, $x_4 = x_{nC}$ in the example. If $x_3 < x_4$, the $D_{ij} = 0$. If $x_4 < x_3$, the intersection is a trapezoid with base $x_3 - x_4$ and with altitudes

$$z_3 = \min[z_{iB}, z(C_{jn} \text{ at } x_3)] \quad (7.4-8)$$

$$z_4 = \min[z_{nC}, z(B_{im} \text{ at } x_4)] \quad (7.4-9)$$

where $x(C_{jn} \text{ at } x_3)$ is the value of x corresponding to z_3 on the edge C_{jn} and where $z(B_{im} \text{ at } x_4)$ is the value of z corresponding to x_4 on the edge B_{im} . Then

$$D_{ij} = (x_3 - x_4) \frac{z_3 + z_4}{2} . \quad (7.4-10)$$

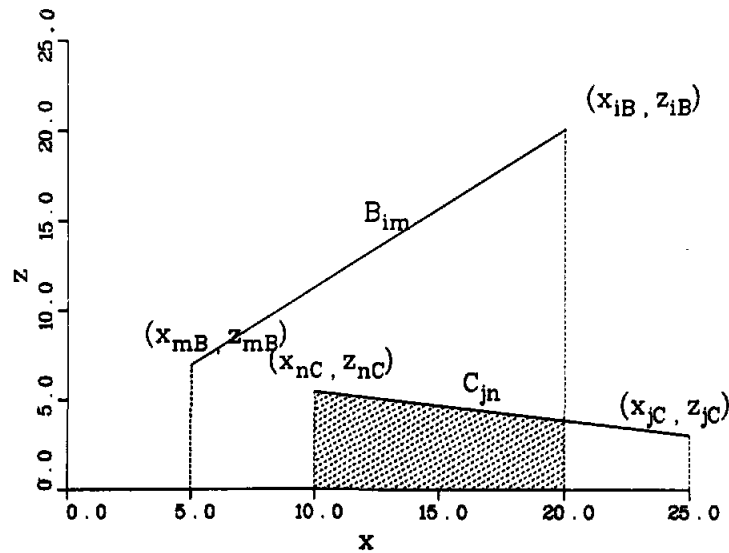


Figure 7-10. Subdivision Overlap When Quadrilateral Edges do not Intersect

The situation for intersecting quadrilateral edges is given in Figure 7-11. If the coordinates of the intersection are x_{int} , z_{int} , the area of intersection of the subdivisions is

$$D_{ij} = (x_3 - x_{int}) \frac{z_3 + z_{int}}{2} + (x_{int} - x_4) \frac{z_{int} + z_4}{2} \quad (7.4-11)$$

using the earlier notation. Thus the area of intersection of two quadrilaterals is evaluated using only addition, subtraction, and comparisons to determine maxima and minima. The method may be easily extended to polygons of n sides just by dividing each polygon into n oriented trapezoids and proceeding as before.

7.4.3 Shadowing

With the area of each quadrilateral in each pair and their overlap available, an approximation to the effect of shadowing is easily obtained. When the overlap is nonzero, the shadowed heliostat must be identified. In Figure 3-15, let \vec{r}_T (\vec{r}_S) represent the vector to the first vertex

of the first (second) heliostat. The distances from these vertices to the $x' - z'$ plane are

$$d_1 = -\hat{V}_S \cdot \vec{r}_T \quad (7.4-12)$$

and

$$d_2 = -\hat{V}_S \cdot \vec{r}_S \quad (7.4-13)$$

If $d_1 > d_2$, the shadowed heliostat is the first (labeled T). If $d_2 > d_1$, the shadowed heliostat is the second (labeled S).

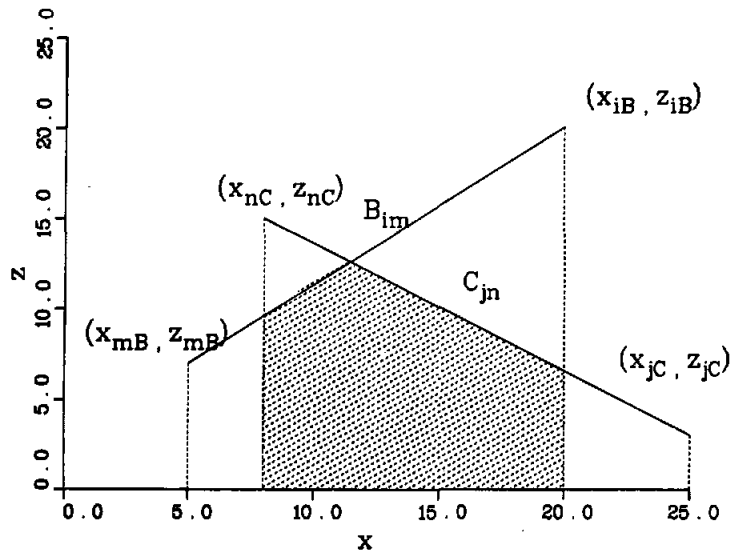


Figure 7-11. Subdivision Overlap When Quadrilateral Edges Intersect

Let A_o represent the overlap area and A represent the area of the shadowed heliostat in the $x' - z'$ plane. Then as an approximation to the effect of shadowing, the energy flux reflected from the shadowed heliostat is reduced by the ratio A_o/A . This approximation assumes that

- a. The distribution of power on the target surface resulting from the unshaded portion of the heliostat may be estimated by the distribution for the complete heliostat (neglecting shadowing) reduced by the factor $1 - A_o/A$.
- b. The ratio of the shaded facet area to facet area is the same as the ratio of heliostat shaded area to heliostat area.

The quadrilateral for each heliostat is tested for overlap with each of the others and with the tower. For times from 10 a.m. to 2 p.m., several cases examined indicate that when a heliostat is shadowed by more than one heliostat or tower, the proper A_{\circ} should be the sum of the overlapped areas (restricted to a maximum of A). However, for late times and for safety calculations where an upper limit is desired, multiple shadows on a heliostat should be treated as overlapping with A_{\circ} taken as the largest shadowed area. These two options are available in HELIOS.

7.4.4 Blocking

The chapter on coordinate systems introduced the unit sphere centered about the aim point. Assuming the edges of a heliostat lie in a plane, the projection of the edges onto the unit sphere will result in a spherical quadrilateral where the sides are arcs of great circles on the sphere. The overlap of two of these spherical quadrilaterals indicates that one heliostat blocks the power from the other, preventing the power from reaching the aim point.

In order to calculate blocking effects exactly, a unit sphere should be placed about each target point with each point treated separately. The intersection of each pair of spherical quadrilaterals must also be calculated, with sufficient detail to define the proper blocked area when the power from one heliostat is blocked by more than one other heliostat. The portion of the heliostat contributing to the blocked energy flux must also be compared with the portion of that same heliostat that may be shadowed so only the effective portion of the heliostat contributes to the collected power.

In analogy with the calculation of shadowing, let us first calculate the area of a spherical triangle with the pole ($\theta = 0$) as one vertex. Consider two points on the unit sphere (θ_1, ϕ_1) and (θ_2, ϕ_2) . The great circle path between the two points gives a curve where θ varies with ϕ . A spherical triangle is then formed by connecting each point with the pole ($\theta = 0$), as in Figure 7-12. The area of the spherical triangle is

$$\sigma = R^2 [A + B + C - \pi] \quad (7.4-14)$$

where $R = 1$.

The lower case angles are determined by $a = \theta_2$, $b = \theta_1$, and $\cos c = \cos \theta_1 \cos \theta_2 + \sin \theta_1 \sin \theta_2 \cos (\phi_1 - \phi_2)$. The spherical angles are then found from

$$\cos A = \frac{\cos a - \cos b \cos c}{\sin b \sin c}, \quad 0 \leq A \leq \pi ; \quad (7.4-15)$$

$$\cos B = \frac{\cos b - \cos c \cos a}{\sin c \sin a}, \quad 0 \leq B \leq \pi ; \quad (7.4-16)$$

$$\cos C = \frac{\cos c - \cos a \cos b}{\sin a \sin b}, \quad 0 \leq C \leq \pi/2. \quad (7.4-17)$$

This method leads to time consuming evaluation of trigonometric functions.

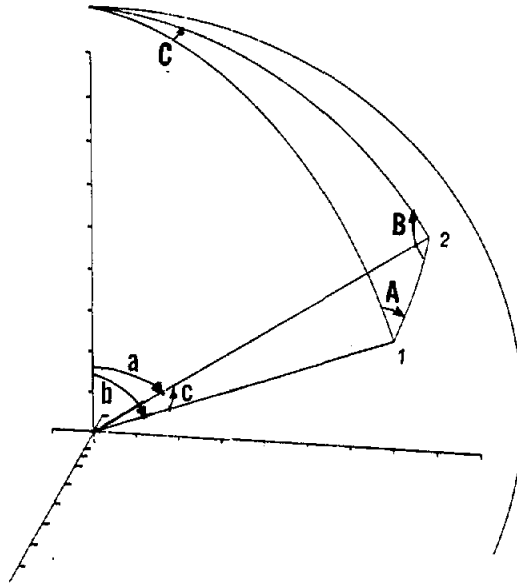


Figure 7-12. The Spherical Triangle

One might consider numerical integration over the spherical triangle to evaluate the area. If the integration is expressible in a simple form, perhaps a gain in computation speed will result. In this form

$$\sigma = R^2 \int_{\varphi_1}^{\varphi_2} \int_0^{\theta(\varphi)} \sin \theta \, d\theta \, d\varphi. \quad (7.4-18)$$

Here $\theta(\varphi)$ must be evaluated. Let \vec{n} be the cross product of unit vectors from the origin to points 1 and 2. Then $\vec{n} \cdot \hat{e}_r = 0$ for all \hat{e}_r that terminate along the great circle path between points 1 and 2. This yields a transcendental equation to be solved for $\theta(\varphi)$.

$$\begin{aligned} \sin \theta \cos \varphi \left\{ \sin \theta_1 \sin \varphi_1 \cos \theta_2 - \sin \theta_2 \sin \varphi_2 \cos \theta_1 \right\} \\ + \sin \theta \sin \varphi \left\{ \cos \theta_1 \sin \theta_2 \cos \varphi_2 - \cos \theta_2 \sin \theta_1 \cos \varphi_1 \right\} \\ + \cos \theta \left\{ \sin \theta_1 \sin \theta_2 \sin (\varphi_2 - \varphi_1) \right\} = 0. \end{aligned} \quad (7.4-19)$$

Replacing each bracket by a_1 , we find

$$a_1 \sin \theta \cos \varphi + a_2 \sin \theta \sin \varphi + a_3 \cos \theta = 0, \quad (7.4-20)$$

and for given φ , the θ is available from

$$\tan \theta = \frac{-a_3}{a_1 \cos \varphi + a_2 \sin \varphi}. \quad (7.4-21)$$

So in addition to evaluation of trigonometric functions the numerical integration is also required. We make the following approximations:

- a. The target points are sufficiently close together so that projections on the unit sphere centered at the target center give the proportion of blocked heliostat area with sufficient accuracy for each target point.
- b. The heliostats which are sufficiently far away from the target so that blocking is a problem are also sufficiently far away from the unit sphere so that the area of the spherical quadrilateral is a small portion of the surface area of the sphere. Over such a small region the spherical surface is taken as planar.
- c. In the small region of the spherical quadrilateral where the planar approximation is made, the sides of the quadrilateral are taken as straight lines.

With these approximations, the blocking calculation becomes directly analogous to that for shadowing. The axes are θ , φ , but since only ratios of areas are of consequence, these angles can be treated directly as lengths (since length along either axis is directly proportional to the angular interval).

As occurred in the shadowing case, in several geometries examined for $10 \text{ a.m.} \leq t \leq 2 \text{ p.m.}$ when the rays from an individual heliostat are blocked by more than one other heliostat, the blocked portions do not overlap and should be added (subject to the limitation of the total area). In contrast, for safety calculations and for late times, an overlapping option is convenient where only the larger area is taken as the blocked portion. These two options are available in the code.

When a heliostat is shadowed and when its reflected power is also blocked, the shadowed and blocked portions are assumed to overlap. The larger ineffective area is used to reduce the power collected by the heliostat. For all cases examined thus far, this is a good assumption for $10 \text{ a.m.} \leq t \leq 2 \text{ p.m.}$

The earlier approximations listed for shadowing also apply to the treatment for blocking with "shadowed" replaced by "blocked." On December 21 for $10 \text{ a.m.} \leq t \leq 2 \text{ p.m.}$, for aim points near the 1-MW tower receiver and for the 78 heliostats in zone A of the STTF, shadowing and blocking reduce the effective area of the heliostats by $\lesssim 16\%$ with most of the reduction caused by total shadowing of some heliostats by the tower. The same calculations on March 21 indicate $\lesssim 7.4\%$ reduction in effective area that is caused about equally by shadowing and blocking at the extreme times in the interval. On June 21, calculations indicate shadowing and blocking give $\lesssim 1\%$ reduction, mainly due to blocking effects. Some may argue that the assumptions concerning the shadowing and blocking treatment must be eliminated in order to obtain accurate results for collected power. However, even a 10% error in that calculation results in $\lesssim 1\%$ error in the collected power. Future comparisons with experimental data or with more detailed treatments are expected to verify the adequacy of the present shadowing and blocking assumptions. At late or early times, or for aim points close to the ground where only a small portion of the mirror area is effective, the options of shadowed (or blocked) areas overlapping or not overlapping allow bounds to be placed on the results. In such cases, a more detailed treatment of interference effects is expected to yield more accurate results. The authors admit the assumptions chosen here were motivated by speed and ease of programming as well as by primary interest in accuracy around power-receiver locations for times within 2 hours of noon.

It is tedious but straightforward to extend the shadowing and blocking treatments to each individual facet. Then the contribution of each shadowed facet could be reduced appropriately, relaxing the assumptions noted earlier. Even greater detail would specify just which portion of each facet is shadowed and that portion could be deleted from the integration. This detail would eliminate the need for options concerning overlap of multiple shadows on the same heliostat. A code used at McDonnell Douglas subdivides each facet into 121 elements and tests each element for shadowing or blocking.^{7.6} It is also possible to apply a separate blocking test for each of the ~ 121 target points processed during a typical problem. Such extensions are not treated here.

7.4.5 Nearest Neighbors

In calculations for the Central Receiver Test Facility, the number of heliostats ($\lesssim 222$ now) is sufficiently small that the energy flux calculation dominates the required computer time. Hence, little penalty results from testing each heliostat for shadowing and blocking with all the other heliostats. On the other hand, pilot plant or commercial central receivers may require several thousand heliostats. Then the shadowing and blocking calculation requires more computer time and further optimization is desired.

An obvious method for increasing efficiency is to test only the n nearest neighbors for shadowing and blocking of each heliostat. The proper n is expected to vary with the distribution and size of the heliostats. The minimum appropriate n will vary with the orientation of the sun

and the choice of receiver. At times far from noon, n is expected to be large. Around noon, in some designs, very little shadowing or blocking occurs and n could be zero. HELIOS now allows $4 \leq n \leq 34$, $n = 0$, or $n =$ the number of heliostats - 1, when shadowing and blocking calculations are performed. The specific limits 4 and 34 can be easily altered by changes in a few code statements (such as parameter dimensions).

The set of nearest neighbors is determined in HELIOS by calculating the distance (squared) between each heliostat and all the others and selecting the heliostats with the smallest n distances. The same set is then used for each time of day and day of year processed. One might consider selecting the n nearest neighbors that are closer to the target center. However, application to a south field of heliostats would be incorrect. It is possible to then use two sets of neighbors--one for shadowing and one for blocking. This option is not now available in HELIOS.

As an example of the selection of the number of neighbors, n , calculations are presented for the 78 heliostats in zone A of the Central Receiver Test Facility at Sandia Laboratories, Albuquerque, NM. The effective mirror area (after cosine-effect, shadowing, and blocking) is given in Figure 7-13 for 8 a.m. on December 21 as a function of n . By 10 a.m., $n = 10$ is sufficient. On March 21, or June 21, $n = 10$ is sufficient even at 8 a.m. However, in Figure 7-13, it appears the $n \geq 15$ is required.

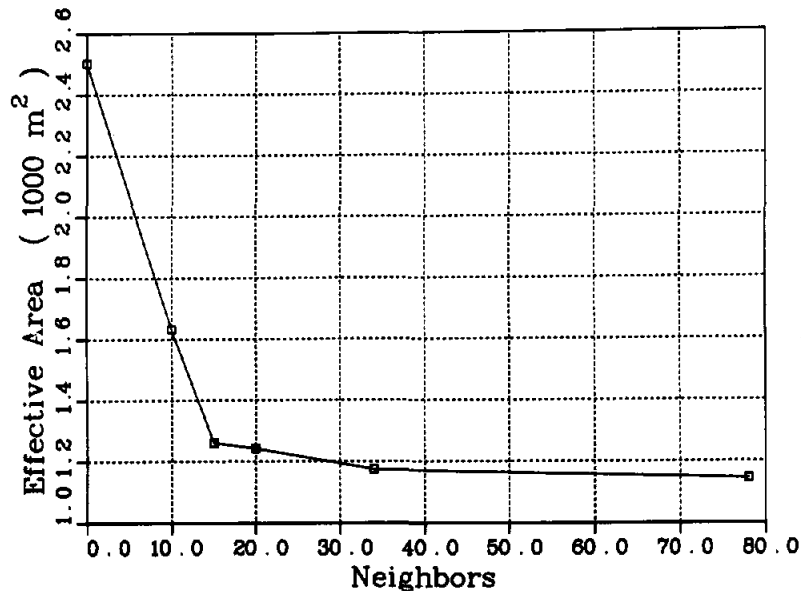


Figure 7-13. Variation of Effective Mirror Area for 1-MW CRTF With the Number of Neighbors Chosen for the Shadowing and Blocking Calculation

Consider the penalty as larger n is selected. Figure 7-14 gives the CDC 6600 computer time consumed in the shadowing and blocking calculation at 8 a.m. on December 21 as a function of n .

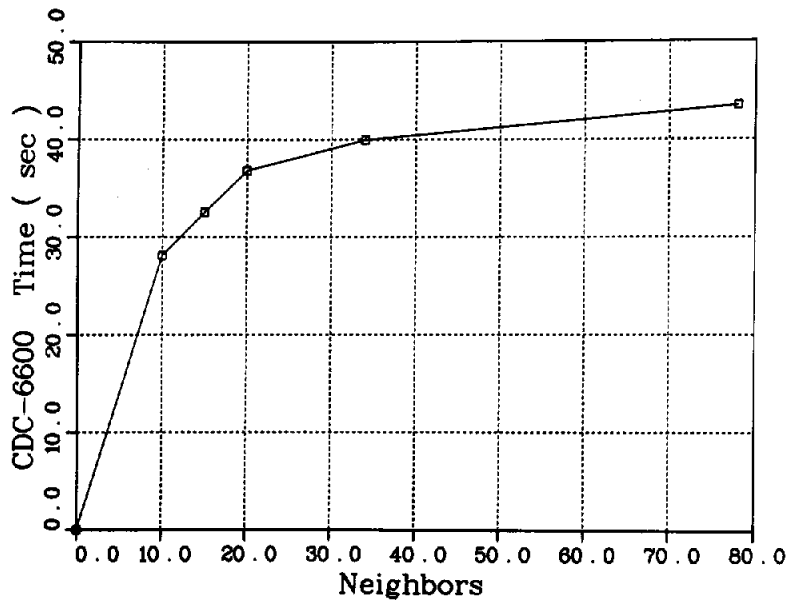


Figure 7-14. Variation of CDC 6600 Computer Time for Shadowing and Blocking With the Number of Nearest Neighbors Involved

When similar calculations are done for the 222 heliostats in Zones A and B of the CRTF with the 5-MW receiver aperture, the shadowing and blocking require computer time which increases roughly as the number of heliostats to the 1.7 power for given n . The check for overlap between two quadrilaterals proceeds quickly compared to the rest of the calculation when overlap occurs. Hence, the time required is very dependent upon the amount of shadowing and blocking present in the heliostat field. A similar check would be even more important in detailed calculations which might specify which portion of each facet is shadowed or blocked and might eliminate such portions from the integration.

References

- 7.1 G. W. Tyler, "Numerical Integration of Functions of Several variables," Canadian Journal of Mathematics, 5: 393-412 (1953).
- 7.2 A. H. Stroud, Approximate Calculation of Multiple Integrals, Prentice-Hall, Inc., p 230, (1971).
- 7.3 G. M. Ewing, "An Approximate Cubature," American Math. Monthly, 48: 134-136 (1941).
- 7.4 J. Albrecht and L. Collatz, "Zur Numerischen Auswertung Mehrdimensionaler Integrale," Z. Angew. Math. Mech., MR20 #432, 38 (1958).
- 7.5 D. S. Mason, "Determination of Areas and Volumes of Intersection of Zones in Old and New Grids," Appendix B in the TOOREZ Lagrangian Rezoning Code, SLA-73-1057, April 1974, by B. J. Thorne and B. B. Holdridge, Sandia Laboratories, Albuquerque, NM.
- 7.6 R. H. McFee, "Computer Program CONCEN for Calculation of Irradiation of Solar Power Central Receiver," Presented at the ERDA Workshop on Methods for Optical Analysis of Central Receiver Systems, University of Houston, August 10-11, 1977.

CHAPTER 8
AUXILIARY CAPABILITIES

8.1 Reconcentrators

Some receivers are designed to work with reconcentrators. A reconcentrator utilizes curved panels to redirect additional radiation onto the receiver. In this section we develop the approximation used in HELIOS for modeling receivers with reconcentrators. An example will be given in subsequent sections.

Consider a small cone of light reflected from a concentrator surface at point \vec{P}_f in Figure 8-1. Suppose that the reflected central ray of this cone reflects from point \vec{P}_r of a reconcentrator surface and continues to strike a target plane at \vec{P}_1 . The surface element ΔT defines the cone of light. The unit vectors \hat{k} , \hat{M} , and \hat{N} define the normals to the target plane, the reconcentrator surface at \vec{P}_r , and the concentrator surface at point \vec{P}_f , respectively. A dashed line through \vec{P}_r is used to indicate the intersection of a plane (the "tangent plane") with the page; this plane is tangent to the reconcentrator surface at \vec{P}_r .

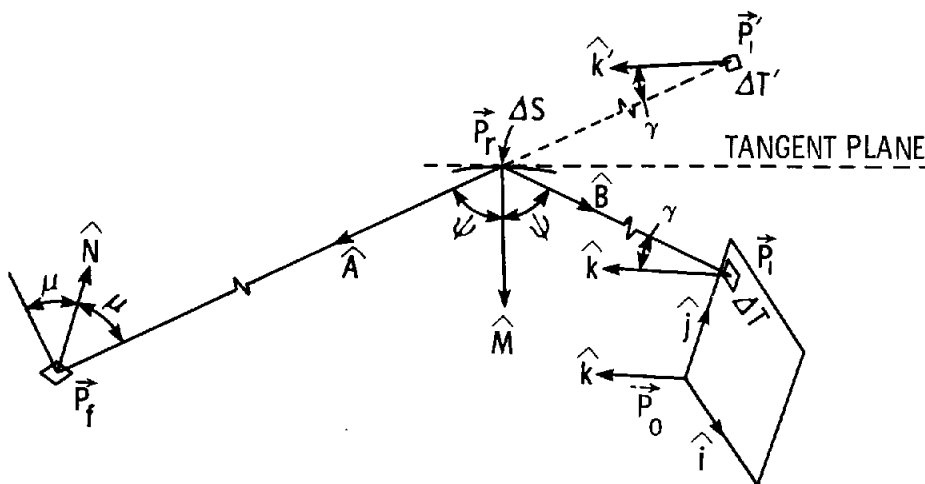


Figure 8-1. Reconcentrator Geometry

All the points so far are in the tower coordinate system. For use later, a coordinate system is defined on the target plane. Its origin is at \vec{P}_0 , its α coordinate along \hat{i} and its β coordinate along \hat{j} . In order to relate this target system $\alpha - \beta$ to the concentrator system

x - y - z, it is necessary to specify one more vector about \vec{P}_0 ; we select \hat{i} . Once the point \vec{P}_0 and the unit vectors \hat{k} and \hat{i} are specified in the concentrator system, any point (α, β) in the target system is transformed to it by the relationship

$$\vec{P} = \vec{P}_0 + \hat{i}\alpha + \hat{j}\beta \quad (8.1-1a)$$

The unit vector \hat{j} is obtained from the cross product

$$\hat{j} = \hat{k} \times \hat{i} \quad (8.1-1b)$$

The reflection of the element ΔT , its surface normal \hat{k} , and the point \vec{P}_1 in the tangent plane is shown by $\Delta T'$, \hat{k}' , and \vec{P}'_1 , respectively, in Figure 8-1.

Given the points \vec{P}_f , \vec{P}_r , and \vec{P}_0 and the unit vectors \hat{M} and \hat{k} , we first solve for the point at which the ray reflected along \vec{B} intercepts the target plane. Since \hat{k} is perpendicular to the target plane whereas the vector $\vec{P} - \vec{P}_0$ lies in it, the dot product

$$\hat{k} \cdot (\vec{P} - \vec{P}_0) = 0 \quad (8.1-2a)$$

or

$$\hat{k} \cdot \vec{P} = \hat{k} \cdot \vec{P}_0 \quad (8.1-2b)$$

for any point \vec{P} in the target plane. An equation of the line through \vec{P}_r in the direction of the unit vector \hat{B} is

$$\vec{R} = \vec{P}_r + t\hat{B} \quad (8.1-3)$$

where t is a parameter that gives the distance of point \vec{R} from point \vec{P}_r . When $\vec{R} = \vec{P} = \vec{P}_1$, we get (from Eqs. [8.1-2b] and [8.1-3])

$$\hat{k} \cdot \vec{P}_1 = \hat{k} \cdot \vec{P}_r + t\hat{k} \cdot \hat{B} = \hat{k} \cdot \vec{P}_0 \quad (8.1-4a)$$

from which

$$t = \frac{\hat{k} \cdot (\vec{P}_0 - \vec{P}_r)}{\hat{k} \cdot \hat{B}} \quad (8.1-4b)$$

This value of t in Eq. (8.1-3) gives

$$\vec{P}_1 = \vec{P}_r + \hat{B} \left\{ \frac{\hat{k} \cdot (\vec{P}_0 - \vec{P}_r)}{\hat{k} \cdot \hat{B}} \right\} \quad (8.1-5)$$

The vector \hat{B} is calculated from \hat{A} and \hat{M} by using Eq. (4.2-6).

The coordinates (α, β) in the target system are given by

$$\alpha = \hat{i} \cdot \vec{C} \quad (8.1-6a)$$

and

$$\beta = \hat{j} \cdot \vec{C} \quad (8.1-6b)$$

where

$$\vec{C} = \vec{P}_1 - \vec{P}_0 = \vec{P}_r - \vec{P}_0 + \hat{B} \left\{ \frac{\hat{k} \cdot (\vec{P}_0 - \vec{P}_r)}{\hat{k} \cdot \hat{B}} \right\} .$$

The approximation presently used in HELIOS is to specify a grid of points on the reconcentrator surface and to divide the receiver target into an array of cells as indicated in Figure 8-2. For given points \vec{P}_f on the concentrator surface and \vec{P}_r on the reconcentrator surface, the location (α, β) of the intersection of the reflected ray with the receiver target is determined. The cell indices ij are then determined by

$$\alpha_i \leq \alpha < \alpha_{i+1} \quad (8.1-7a)$$

$$\beta_j \leq \beta < \beta_{j+1} . \quad (8.1-7b)$$

When \vec{P}_1 (Figure 8-1) falls within cell ij , the flux density at the center of the cell

$$\alpha = \frac{\alpha_i + \alpha_{i+1}}{2} \quad (8.1-8a)$$

$$\beta = \frac{\beta_j + \beta_{j+1}}{2} \quad (8.1-8b)$$

is incremented by an amount $\Delta F(\Delta S/\Delta T)\rho$ where ΔF is an increment of the integral (5.5-3) as calculated by HELIOS for given points \vec{P}_f and \vec{P}_r . The quantity ΔS is an increment of area associated with the point \vec{P}_r on the reconcentrator, ΔT is the cell area on the receiver target, and ρ is the reflectivity of the reconcentrator surface at \vec{P}_r for the angle of incidence ψ .

8.1.1 Calculation Method Used in HELIOS

The basic geometry is given in Figure 8-3. Unit vectors in the sun-reflector coordinate system are labeled as $\hat{e}_x, \hat{e}_y, \hat{e}_z$. (Recall that in this system the origin is at the facet center, \hat{e}_z is normal to the facet center, \hat{e}_y is in the plane of incidence, and \hat{e}_x completes the right-handed system.) The vector from this origin to the facet element of area is designated by RLP ($I = 1, 3$) in the HELIOS FACET function routine. In the illustration here, RLP ($I = 1, 3$)

is zero. These coordinates are specified in the facet coordinate system (where x is horizontal along a facet edge, z is normal at the facet center, and y completes the right-handed system). The corresponding facet-coordinate unit vectors are formed in Program C of HELIOS as $VX(I = 1, 3)$, $VY(I = 1, 3)$, and $VZ(I = 1, 3)$, in terms of the tower coordinates.

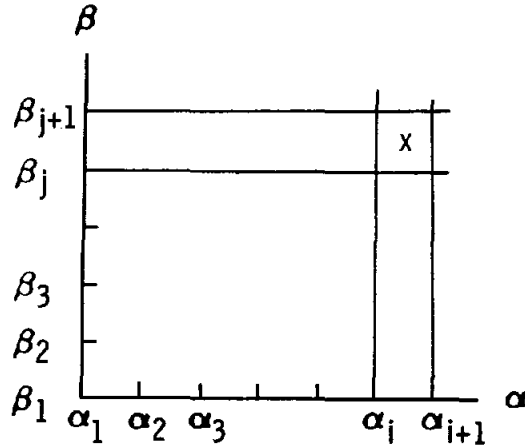


Figure 8-2. Receiver Target Cell Structure

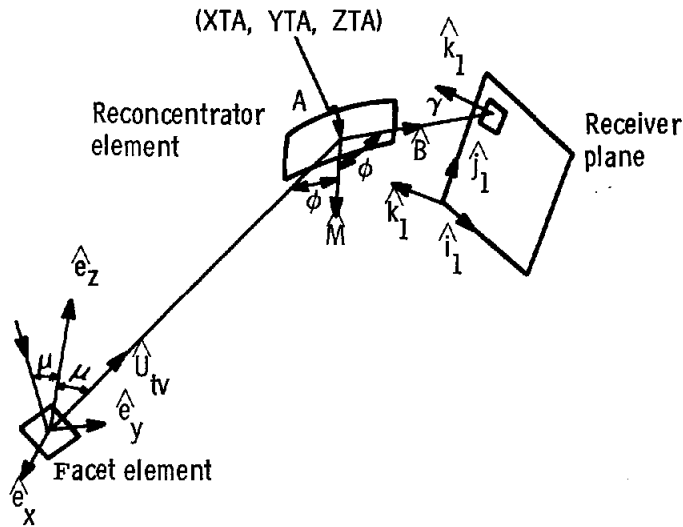


Figure 8-3. Reconcentrator Geometry

A vector from the facet center to the integration element expressed in tower coordinates is

$$VFE(I) = RLP(1) * VX(I) + RLP(2) * VY(I) + RLP(3) * VZ(I) \quad (8.1-9)$$

for $I = 1, 3$. Addition of the respective tower coordinates of the facet center (X1P, Y1P, Z1P) gives the tower coordinates of the facet integration element.

$$\begin{aligned} F_1 &= VFE(1) + X1P \\ F_2 &= VFE(2) + Y1P \\ F_3 &= VFE(3) + Z1P \end{aligned} \quad (8.1-10)$$

The function RVN furnishes the normal (\vec{V}_n) to the facet element in the facet coordinate system. The normal in the tower system is then

$$\vec{n}_t = V_n(1) \hat{e}_x + V_n(2) \hat{e}_y + V_n(3) \hat{e}_z \quad (8.1-11)$$

Now the initial reflection point at the facet in Figure 8-3 and the orientation are specified.

We choose one of the 121 target points on the reconcentrator surface as our target point. A unit vector directed toward the target point is specified by $UTV(I = 1, 3)$ and the target-point coordinates are specified (in the tower system) by XTA, YTA, ZTA. The contribution to the flux density (W/cm^2) at the target are then calculated at the target point (as done before reconcentrators were added). This requires calculation of the unit normal to the target (i. e., \hat{M} in Figure 8-3).

When the element of flux density is greater than 0, the cosine of the angle between M and $UTV(I = 1, 3)$ ($-\cos \phi$, designated by CO in FACET) specifies the unit vector \hat{B} in Figure 8-3

$$\hat{B} = 2 \cos \phi \hat{M} + \hat{U}_{tv} \quad (8.1-12)$$

The receiver normal, \hat{k}_1 (specified by RECN [$I = 1, 3$] in FACET) is determined from the TARGET subroutine. The distance, t , along \hat{B} to the receiver intersection point is determined from two expressions for the perpendicular distance from the reconcentrator point to the plane of the receiver

$$\begin{aligned} t \hat{B} \cdot \hat{k} &= RECN(1) * (X_{to} - XTA) \\ &+ RECN(2) * (Y_{to} - YTA) \\ &+ RECN(3) * (Z_{to} - ZTA) \end{aligned} \quad (8.1-13)$$

where subscripts "to" refer to the receiver center. The tower coordinates of the receiver intersection point are then given by

$$XI = t * B(1) + XTA$$

$$YI = t * B(2) + YTA$$

$$ZI = t * B(3) + ZTA \quad . \quad (8.1-14)$$

When these coordinates are known, the user is ready to determine if the coordinates lie inside the receiver boundaries and, if so, into which section of the receiver the contribution goes and how large the contribution is.

In the example given later, the receiver is a vertical plane facing north at $y = 3.0$ m. The vertical extent is $ZEXT = 12.5$ m; i. e., from $z = 66.7$ to 79.2 m. The horizontal extent is $XEXT = 0.889$ m; i. e., from $x = -0.4445$ to $+0.4445$ m. The receiver is divided into an 11×11 array of equal area cells with midpoints corresponding to the 121 target points in the receiver. Hence, the cell area is slightly larger than the receiver itself. After a check that the receiver intersection point has $YI = 3.0$ m, the XI and ZI are used to determine the cell indices of the intersection. If the intersection does not occur within the cells, no contribution to the collected flux density occurs. This decision is made in the BASKET subroutine. If a cell receiving a contribution is found, the contribution to its flux density must be estimated.

The contribution to the flux density at a particular cell is determined in the FACET subroutine. The flux density (W/cm^2) reflected from the reconcentrator point is multiplied by the reconcentrator reflectivity (taken here as 0.9) and by the ratio of areas determined in subroutine RARE. The ratio of areas is the ratio of the reconcentrator element of area ($A \equiv \Delta S$) to the individual cell area ($A_p \equiv \Delta T$). Referring to Figure 8-3, the element of power incident upon the reconcentrator element is the flux density times the element of area A . All that power is assumed to flow into the same cell and is distributed over that cell area A_p ; therefore, the element of flux density reaching the receiver requires multiplication by the ratio of these areas. The reconcentrator has a portion of its target points on edges and corners; therefore, these points have reduced effective area elements (A). The cells are all taken to be the same size.

Advantage is taken of the fact that the cells have receiver target points at their centers. The flux density within each cell is chosen as the value at its center. The reconcentrator contribution to the flux density is then added to the direct contribution to get the total distribution of power over the receiver. Integration schemes developed in Section 7.1 are then directly applicable for finding the total collected power.

In some applications the assumption may not be valid that the element of power from a reconcentrator element all flows into one cell. This is reasonable when the projected area elements are roughly the same size ($A \sin \phi \leq A_b \cos \gamma$) and the propagation distances (t) are not large. If t becomes large or if $A_b \cos \gamma \ll A \sin \phi$, it may be necessary to spread the elements of flux density over several cells to obtain reasonable estimates. Inclusion of multiple reflections would also require a more detailed analysis.

8.1.2 Four-Panel Reconcentrator

The two-aperture reconcentrator design is indicated in Figure 8-4. The upper aperture consists of two panels (reflectors) and is aimed at 22.5° east of north with edges that pass through $(-0.594, 4.92, Z)$ and $(1.254, 4.157, Z)$. The lower aperture is aimed at 22.5° west of north with edges at $(-1.254, 4.157, Z)$ and $(0.594, 4.92, Z)$. Each panel has a height of 6.25 m. Each horizontal cross section is modeled as a circle with radii of curvature as indicated in Figure 8-4 (in meters). Each reconcentrator panel is numbered in Figure 8-4 for convenience later.

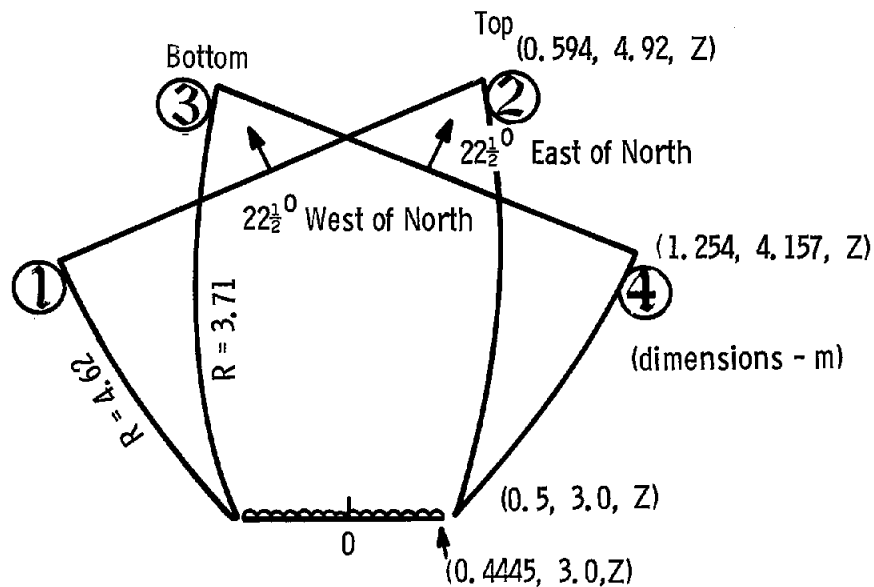


Figure 8-4. Top View of Two Aperture Reconcentrators. Apertures centered at $(-0.33, 4.54, 76.075)$ for the top and $(0.33, 4.54, 69.85)$ for the bottom. The Z values are then reduced by 1.5 m to aid energy collection

The reconcentrator surfaces are modeled as indicated in Figure 8-5. The tower coordinates of the center of curvature for each circular section are noted in the USERTG subroutine as (A, B) in the HELIOS permanent file HELIOSJ. Each reconcentrator panel is divided into an 11×11 grid of reconcentrator points as indicated in Figure 8-5. The effective area of the 14th reconcentrator point is designated by A in Figure 8-5. Points on the edges (corners) have effective area $A/2$ ($A/4$).

A - EFFECTIVE AREA OF RECONCENTRATOR
TARGET POINT 14

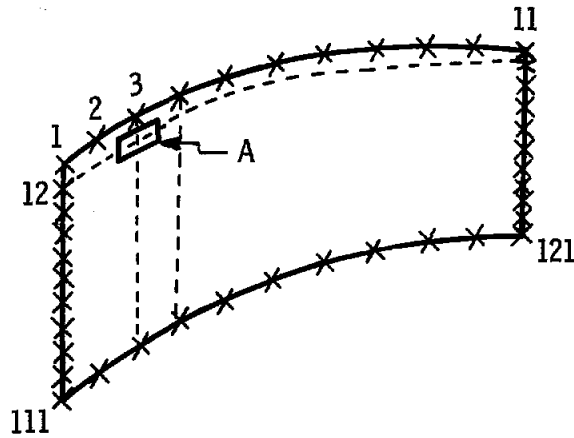


Figure 8-5. A Reconcentrator Panel

8.1.3 Receiver

The receiver itself is modeled as flat, facing north, with a height of 12.5 m and a width of 0.889 m. It is actually one panel from the McDonnell Douglas receiver as indicated in Figure 8-6 with the expanded view in Figure 8-7.

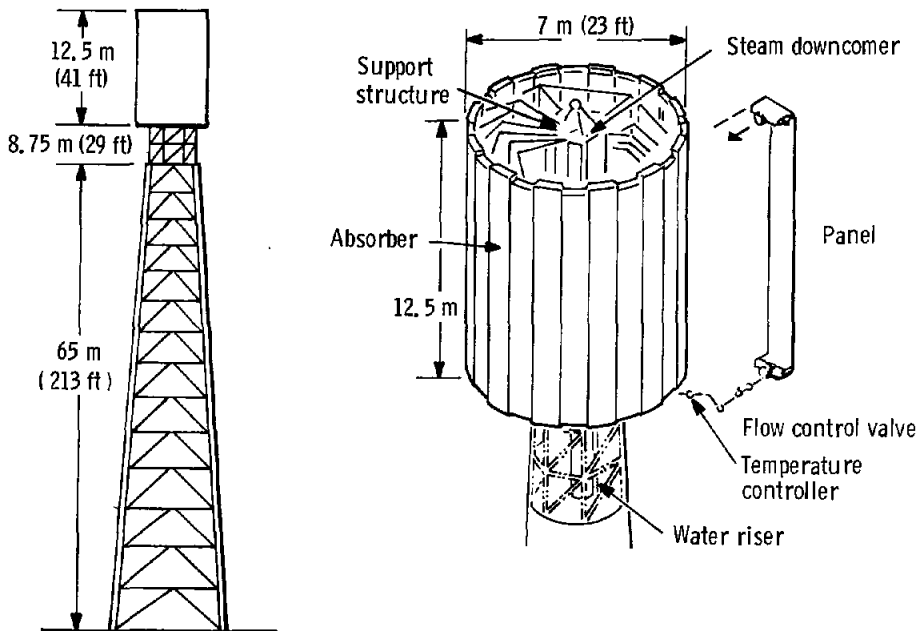


Figure 8-6. Pilot Plant Receiver

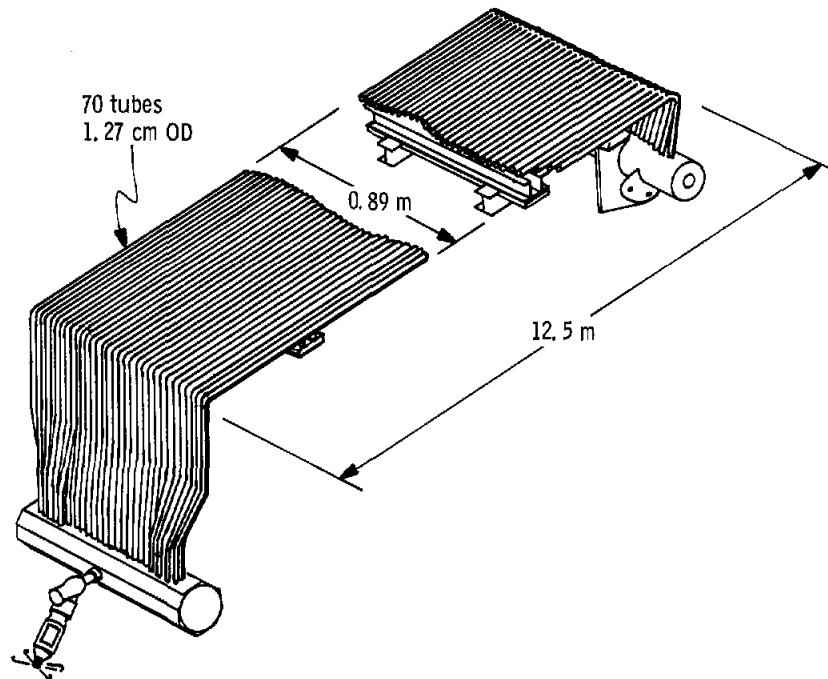


Figure 8-7. Pilot Plant Receiver Panel

The direct contribution to the receiver is calculated as with the regular HELIOS code. Any blocking caused by the reconcentrator panels is neglected. The indirect contribution to the receiver resulting from reflections from the reconcentrator are treated separately. For the indirect contribution, the receiver is divided into rectangular cells with their centers consisting of the 121 mesh points in the direct calculation. When the central ray from an integration subdivision for a facet is reflected from the reconcentrator and strikes one of the cells, the contribution of that facet subdivision is added to that cell. The reflectance of the reconcentrator has been taken as 0.9, independent of angle of incidence. When more data are available, improved reflectance may be inserted in the facet subroutine. Of course the cells can be further subdivided for greater detail and the contributions of individual facets can be spread among several neighboring cells for reduced statistical fluctuations. If needed, such refinements may be added later.

The receiver structure is mounted on top of the CRTF tower as indicated in Figure 8-8 for this example.

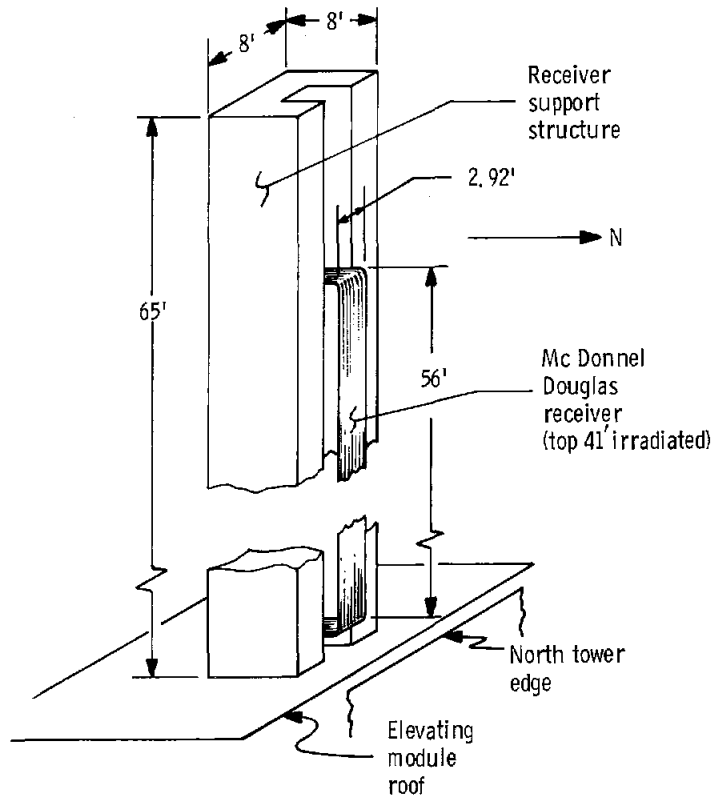


Figure 8-8. Schematic of MDAC Receiver and Support Structure Atop CRTF Tower

8.1.4 Heliostats for Four-Panel Reconcinator

The 222 heliostats in the north field of the CRTF are used in the calculation. They are diagrammed in Figure 8-9. In this configuration the centers of the reconcentrator apertures are at $(0.33, 4.54, Z_1)$ and $(-0.33, 4.54, Z_2)$ for the eastward and westward facing apertures. The $Z_1 = 68.325$ m and $Z_2 = 74.575$ m, placing the reconcentrator discontinuity at 1.5 m below the altitude of the receiver center. The aim points for this example are given in Table 8-I. The heliostats of the eastern sector are divided among the first five aim points while the western sector of heliostats utilize aim points 6 through 10.

TABLE 8-I

Aim Points for Two-Aperture Reconcinator

Point	x(m)	y(m)	z(m)	Point	x(m)	y(m)	z(m)
1	0.33	4.54	66.90	6	-0.33	4.54	71.96
2	0.33	4.54	67.92	7	-0.33	4.54	72.97
3	0.33	4.54	68.93	8	-0.33	4.54	73.98
4	0.33	4.54	69.94	9	-0.33	4.54	74.99
5	0.33	4.54	70.95	10	-0.33	4.54	76.00

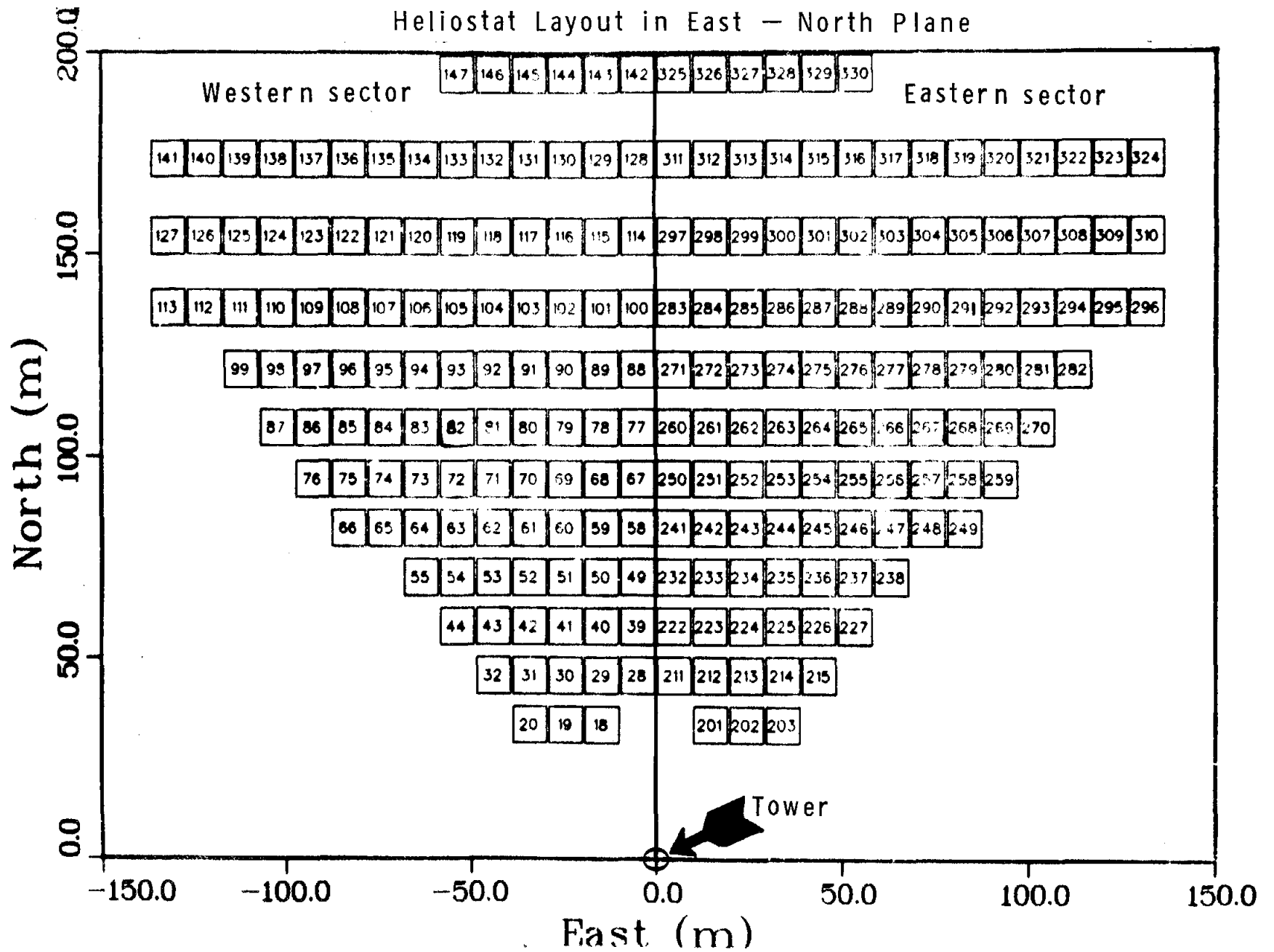


Figure 8-9. Heliostat Distribution

8.1.5 Result for Heliostat 18 and the Four-Panel Reconcentrator

As a test of the HELIOS model of the four-panel reconcentrator, results are examined for heliostat 18 alone. Its aim point is (-0.33, 4.54, 73.98). Prealignment time is noon on March 21 with alignment point (0.0, 3.2, 72.442). Calculation time is 10:00 a.m. on June 21. The receiver center remains at (0.0, 3.0, 72.95).

Heliostat 18 gives a direct power of 15.3 kW to the receiver. The reconcentrators add 4.6 kW (i.e., 57% of the power incident upon the reconcentrators). The power distribution is summarized in Table 8-II. Consistent with the geometry, the spillage occurs mainly over the top of the receiver and at the edge of the eastern side of the upper reconcentrator.

TABLE 8-II

Power Distribution for Heliostat 18

<u>Identification</u>	<u>Power (kW)</u>
Intercepted by facets	36.6
Reflected from facets	29.3
Lost by propagation	0.4
Incident upon receiver directly	15.3
Incident upon reconcentrator panel 1	0.2
Incident upon reconcentrator panel 2	7.9
Incident upon reconcentrator panel 3	0.0
Incident upon reconcentrator panel 4	0.0
Reconcentrated upon receiver	4.6
Total Collected Power	19.9
Spillage	5.5

The calculation of the reconcentrated power that is collected by the receiver only includes contributions from single reflections. Analysis of a truncated two-dimensional compound parabolic concentrator indicates as the acceptance half angle varies from 4° to 36°; the average number of reflections for accepted rays varies from 1.4 down to 0.6. The number is < 1 for $\theta > 12^\circ$. Here the acceptance half angle is near 25°, hence treatment of only the first reconcentrator reflection is reasonable. If the reconcentrator of interest is fully analyzed, then the average number of reflections for collected rays might be known and a correction factor could be applied to the additional 4.6 kW collected; in that way, accuracy could be improved. Of course, more detailed analysis in the code could also account for multiple reflections.

8.1.6 Results for Zones A and B

Results for June 21 at 10 a. m. are summarized in Table 8-III. Figure 8-10 shows a plot of flux density versus vertical distance z at the eastern edge of the receiver ($x = +0.4445$ m). The bottom of the receiver is at $z = 0$. Separate solid curves are shown for each reconcentrator as well as for their total. A dashed curve shows the corresponding slice across the direct flux-density pattern. The panel numbers are identified in Figure 8-4. The power intercepted by a panel is obtained by integrating the incident flux density over its surface. The evaluation of this integral requires several slices across the flux-density in addition to the one shown in Figure 8-10.

TABLE 8-III

Two-Aperture Power Distribution From Zones A and B

Identification	Power (MW)
Intercepted by facets	7.21
Reflected from facets	5.77
Lost by shadowing and blocking	0.26
Direct incidence upon receiver	2.08
Received from reconcentrator panel 1	0.12 (0.24 MW incident)
Received from reconcentrator panel 2	0.58 (0.98 MW incident)
Received from reconcentrator panel 3	0.55 (0.92 MW incident)
Received from reconcentrator panel 4	0.07 (0.12 MW incident)
Reconcentrated upon receiver	1.32 (2.26 MW incident)
Total Collected Power	3.40
Spillage and Propagation Loss	1.17

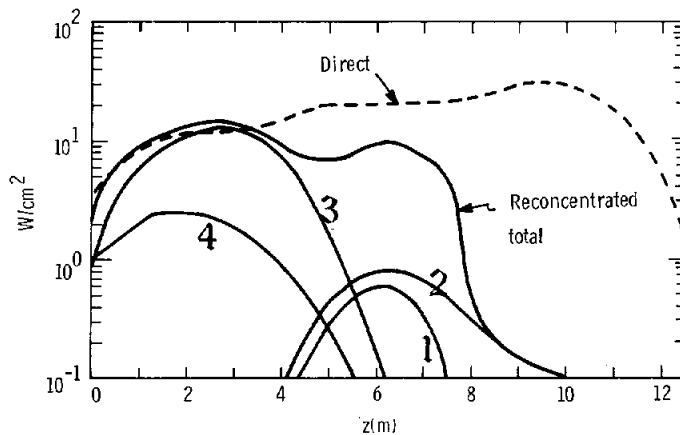


Figure 8-10. Distribution of Reconcentrated Power Along a Vertical Line at the Eastern Edge of the Receiver ($x = +0.4445$ m) Caused by Each of the Four-Reconcentrator Panels. $z = 0$ is the bottom of the receiver

8.2 Plotting Capability

The Helios model includes a large number of effects. The associated computer code is capable of generating huge amounts of data. Several auxiliary computer codes have been developed to aid in analyzing these data. The resulting graphic output allows greater insight and more rapid interaction with the code. This output also serves to alert the user when the input data do not represent the problem of interest.

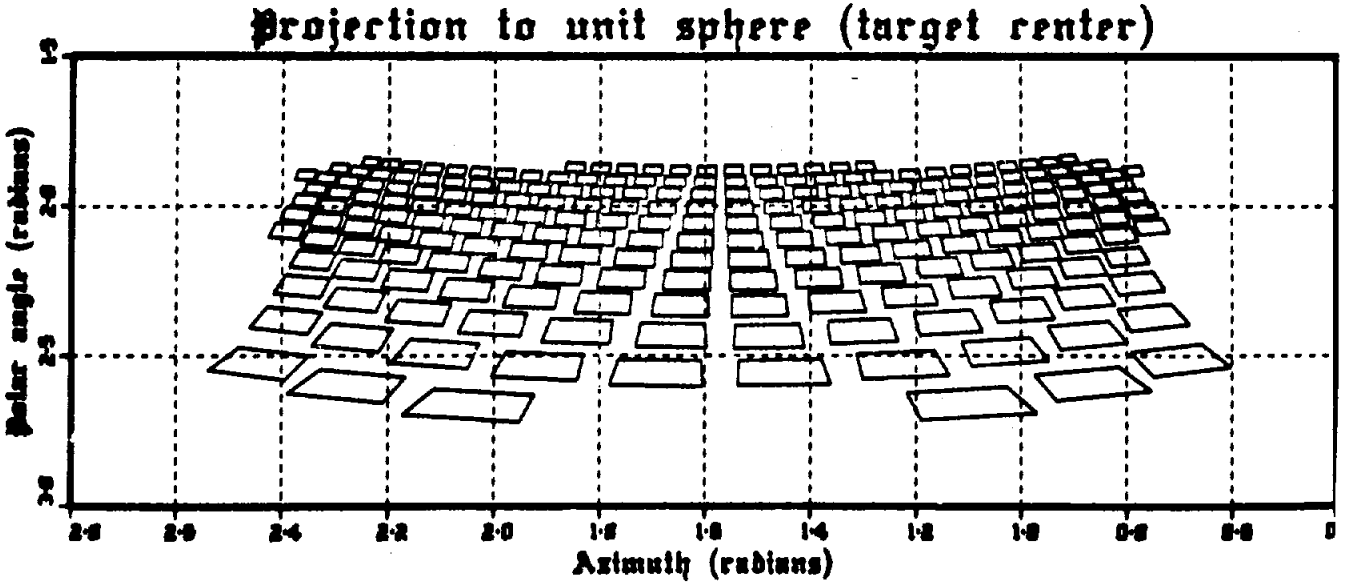
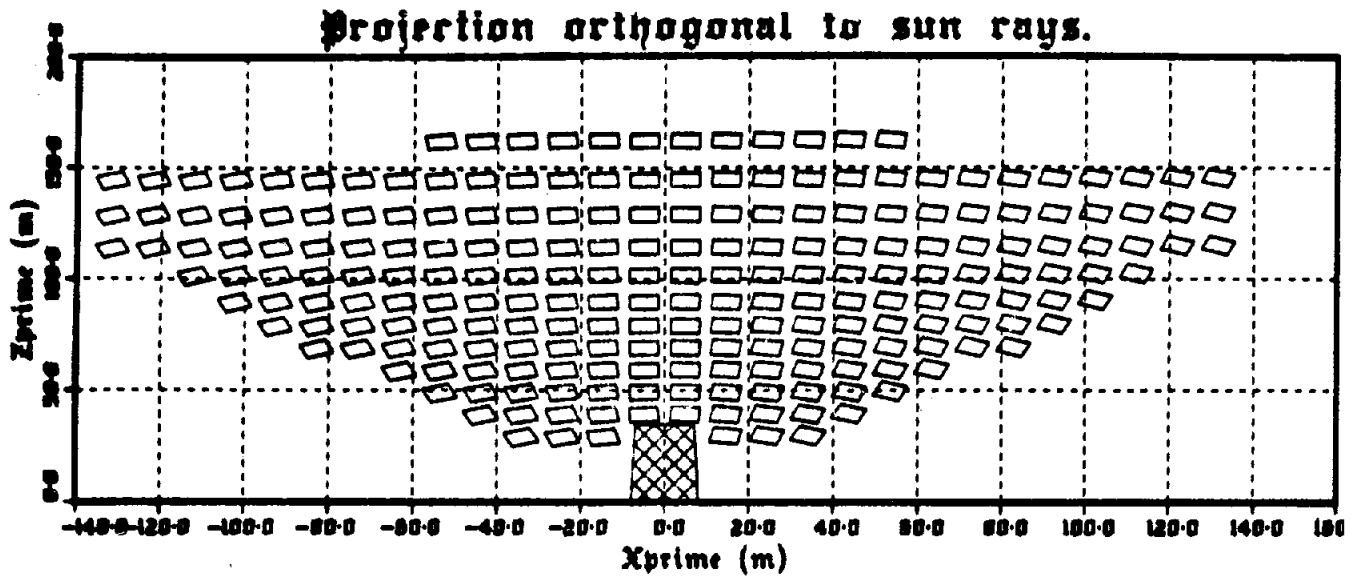
8.2.1 The PLO Plotting Package

The PLO plotting package was developed to furnish graphical output of several built-in features of HELIOS as well as of three-dimensional flux-density distributions, power variations with time, sunshape, and shadowing and blocking. The built-in features that may be examined include variation of the solar declination, solar azimuthal and elevation angles, air mass traversed, and insolation. Graphical examples are available elsewhere.^{8.2}

The plotting routines use DISSPLA (Display Integrated Software System and Plotting Language) developed by the Integrated Software Systems Corporation. The DISSPLA computer routines are proprietary and cannot be furnished with HELIOS but are available from their originator.^{8.3} Sandia has recently extended its own SCORS plotting routines; these routines are not proprietary and could be transferred to outside users with HELIOS.^{8.4} Therefore, in the future the PLO routines may be converted to the SCORS system for easier transfer.

8.2.2 Shadowing and Blocking Movies

As one example of PLO capabilities, several shadowing and blocking diagrams are shown. Let us refer to Figures 8-11 through 8-14. The shadowing effect is shown by the projection orthogonal to the sun's rays. The view seen from the target center gives the blocking as a projection onto the indicated unit sphere. The area subplot gives the effective mirror area (in square meters) before and after shadowing and blocking. The intercepted power subplot gives the power (in watts) intercepted by the mirrors and (when calculated) the power incident upon the target surface. Figure 8-14 indicates the large shadowing effect near sundown. Very little shadowing and blocking occur in the other diagrams. It is possible to use the HELIOS-PLO combination to generate movies to show the evolution of such shadowing and blocking diagrams during a day. As expected, the movies indicate little change in the blocking diagrams (other than rotation of the heliostats) while the shadowing diagrams change dramatically.



Time = 0.000

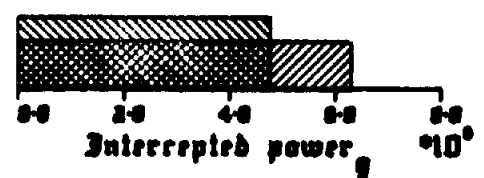
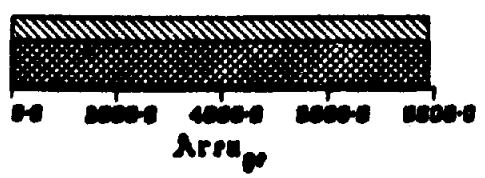


Figure 8-11. Shadowing and Blocking Diagram for Noon on March 21 With Zones A and B of the CRTF

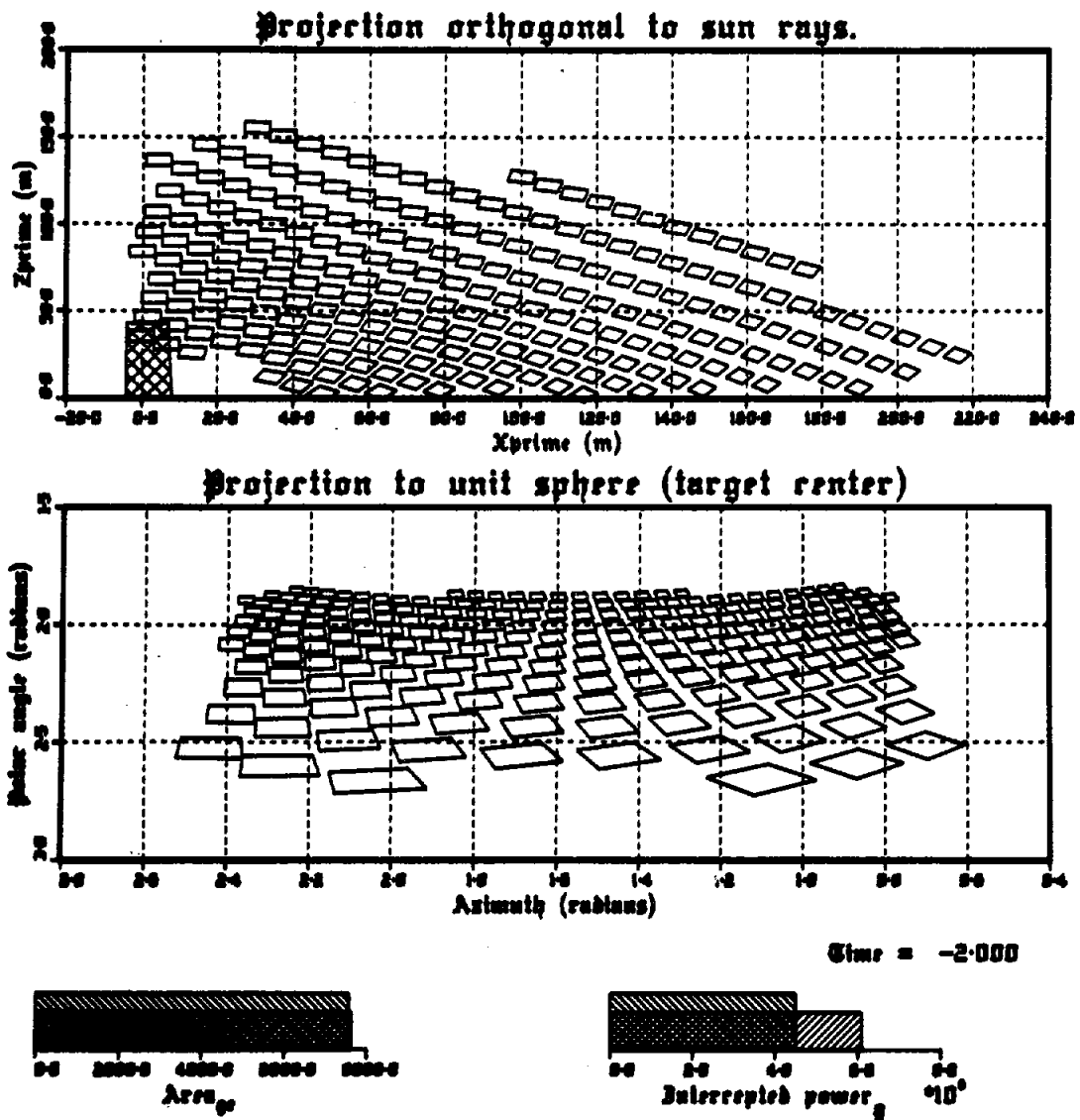


Figure 8-12. Shadowing and Blocking Diagram for 10 a.m. on March 21 With Zones A and B of the CRTF

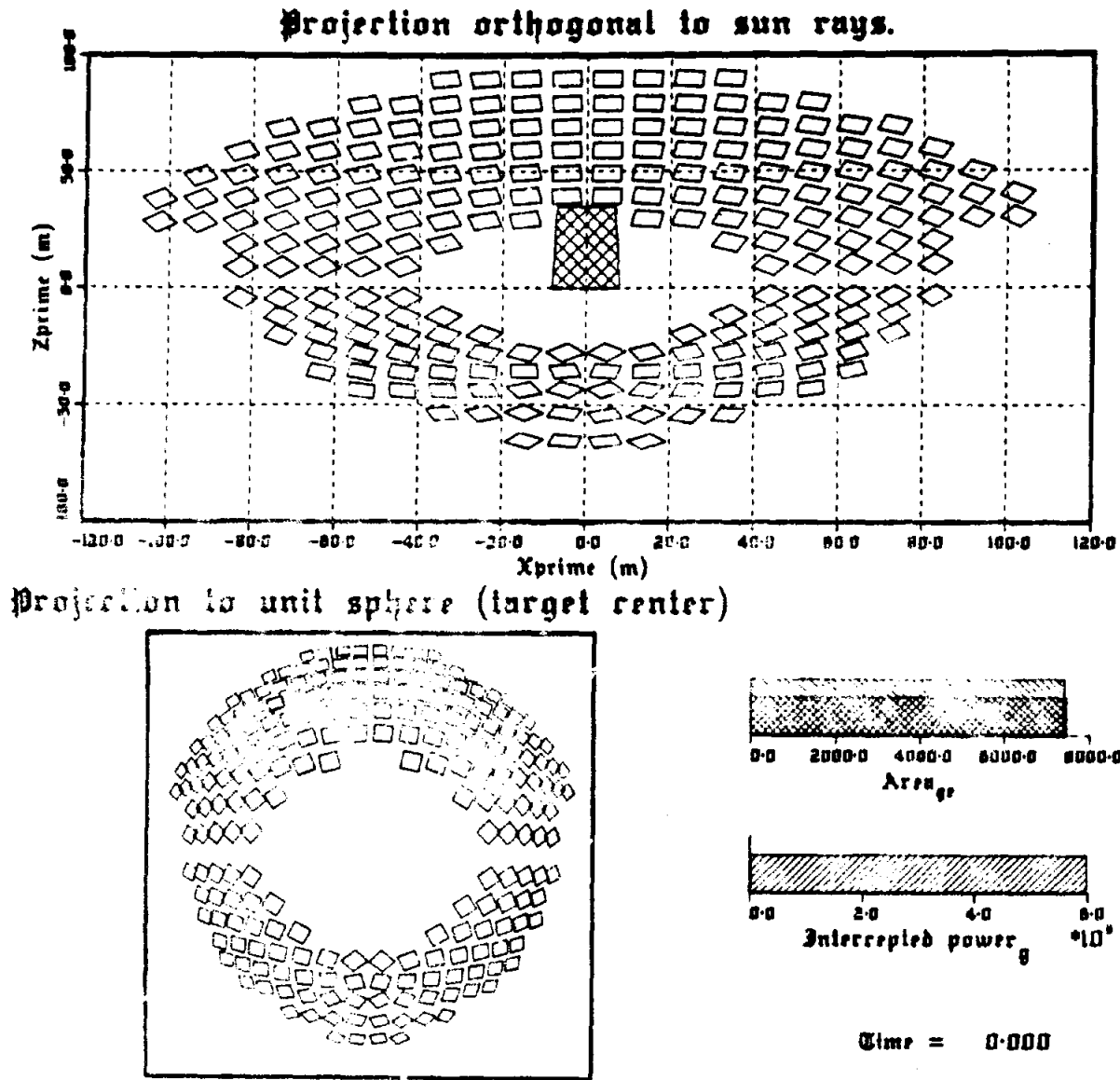


Figure 8-13. Shadowing and Blocking Diagrams for Noon on March 21 With Zones A, C, D, and E of the CRTF

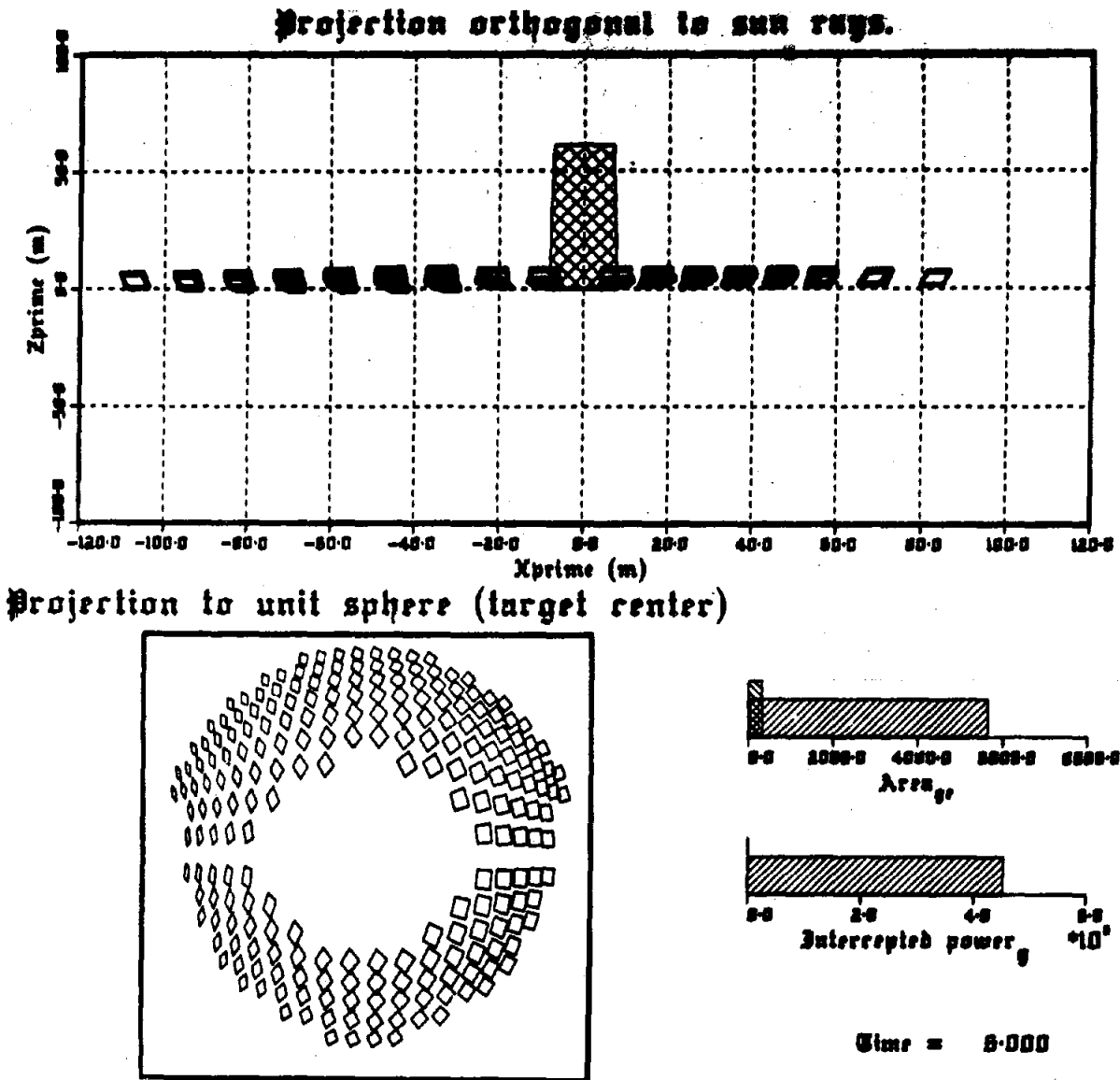


Figure 8-14. Shadowing and Blocking Diagram for 6 p. m. on March 21 With Zones A, C, D, and E of the CRTF

8.3 NOS Routines

The NOS is a large scale time-sharing facility that supports many users. At Sandia Laboratories the system is accessed via a standard telephone system. It allows the user access to a CONTROL DATA 6600 Central Processor. Because of its convenience for many tasks, several computer codes associated with HELIOS have been created for NOS.

8.3.1 NOS Version of HELIOS

Computer costs are often proportional to the amount of computer core storage required to run a computer code. This prompted effort to make HELIOS core requirements as small as possible. To date the core requirements of HELIOS have been reduced to 103 k octal words. The NOS at Sandia Laboratories imposes a limit of 107 k octal words on any job (during prime time). The complete HELIOS code is now available on this interactive system.

The computer core requirements needed to numerically convolve a sunshape with an error cone used up most of the storage space allotted to the earlier versions of HELIOS. This capability has been altered by reduction of the matrix dimensions required for fast Fourier transforms. Comparisons with earlier calculations of effective sunshape under the most trying conditions (very small dispersion for the error cone) indicate less than 1% variation in the effective sunshape. Special printing options have also been developed for the greater convenience of the NOS users.

8.3.2 NOS Input

The HELIOS users manual^{8.2} gives considerable detail concerning how to structure an input deck for HELIOS. An alternative to punched card input is the interactive response on NOS to a series of questions posed by the DGENH (Data GENERation for Helios) code. The file generated on Tape 5 may then be punched for later use or may be directly inserted into the NOS version of HELIOS.

8.3.3 NOS Plotting

A series of plotting codes have been developed to accomplish most of the tasks earlier assigned to the PLO plotting package. Use with NOS has the advantage that plots are available in just a few minutes. In some applications this will allow better interaction with the code and faster construction of the desired graphs.

8.4 Shadowing and Blocking Within a Parabolic Dish

Requirements in several HELIOS applications have prompted an extension of the treatment of parabolic reflectors. In some applications the dishes are rather deep. This in itself poses no problem, for usually (with deep parabolas) the optical axis is aligned toward the sun and no shadowing or blocking is caused by the parabola itself. However, in safety calculations the reflector may be oriented so that the reflected rays are nearly horizontal. These steps are taken to study possible hazards to personnel or machinery. Neglect of this shadowing and blocking will give a worst-case estimate. However, in some applications better estimates are desired. One example is the problem of maximizing in a limited space the power collected by a small central receiver, which will offer no hazard to a nearby inhabited area. The PHI subroutine of HELIOS (that is a portion of overlay 3) utilizes this treatment of parabolic-dish reflectors.

8.4.1 The Shadowing Effect

The sun-concentrator coordinate system was introduced in Figure 3-14. In the present application we require slightly more detail than given earlier. In Figure 8-15 the sun-concentrator system is shown with its origin at the reflector center. The incoming central ray from the sun that strikes the origin is in the $y - z$ plane (z is normal to the reflector surface at its center).

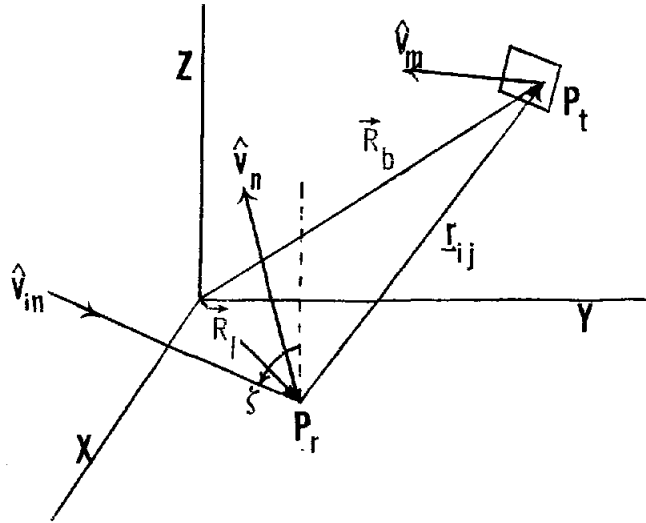


Figure 8-15. The Sun-Concentrator System. The system indicates the incident central solar ray \hat{V}_{in} , the local reflector normal \hat{V}_n , and the vector \underline{r}_{ij} from the reflection point, P_r , to the target point, P_t

The reflection point, P_r , is at \vec{R}_l with respect to the origin, and has a local unit normal \hat{V}_n . The unit vector along the incoming central solar ray that strikes the origin is designated by \hat{V}_{in} . In this coordinate system, $V_{inx} = 0$. At a general reflection point, P_r , the angle between the incoming central ray and the line through P_r parallel to z is designated by ζ . When P_r is at the origin $V_{iny} = \sin \zeta$, $V_{inz} = -\cos \zeta$. For a general position of P_r , the ζ differs very slightly because the incoming central ray may not be in the $y - z$ plane. Since the reflector dimensions are so small compared to the earth-sun distance, this variation of ζ is ignored. Then in this coordinate system the tangent of the solar elevation angle ($\zeta_e = \pi/2 - \zeta$) is given by

$$\tan \zeta_e = -V_{inz} / V_{iny} \quad (8.4-1)$$

If the dish radius is R , the projection of a portion of the vectors in Figure 8-15 onto the $x - y$ plane would be that given in Figure 8-16.

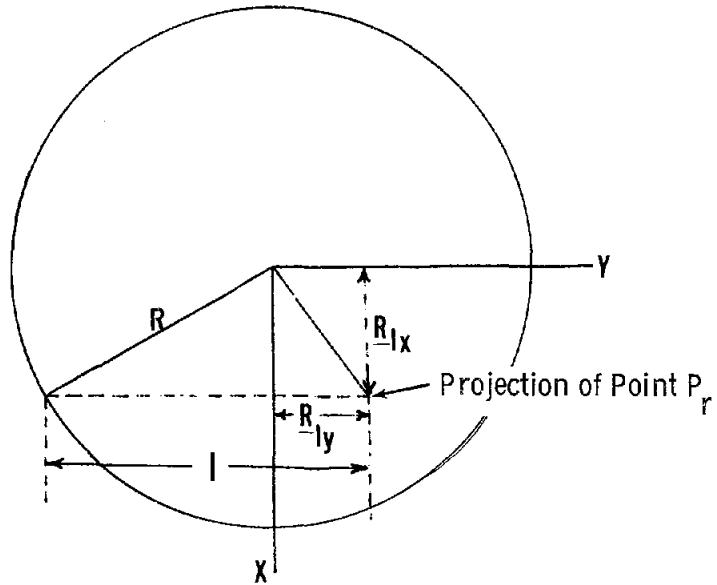


Figure 8-16. Projection Onto x - y Plane for Self-Shadowing

In Figure 8-16,

$$l = R_{ly} + \left[R^2 - R_{lx}^2 \right]^{1/2} . \quad (8.4-2)$$

At the edge of the dish, the central incoming ray that strikes the reflection point, P_r , will have a height

$$Z_{in} = l \tan \zeta_e + R_{lz} . \quad (8.4-3)$$

The Z value for the edge of the dish (Z_{edge}) is obtained from the reflector shape routine (VALRL3). Self-shadowing then occurs if $Z_{edge} \geq Z_{in}$ for the central solar ray.

Use of such a simple test does not consider the sun's shape. Shadowing of the central ray does not necessarily require that the entire sun be shadowed at the reflection point, P_r . However, if a large number of integration sections are chosen on the reflection surface, rejection of portions not shadowed should be compensated for by the addition of portions that are shadowed. Typically, when such effects are studied, the parabolic dish has been divided into from 527 up to 839 integration sections.

8.4.2 The Blocking Effect

Once it is clear that the incoming ray will reach the reflection point, the outgoing ray to the target point of interest is then tested to see if it will pass over the lip of the reflector. The base vector, \vec{R}_b , in Figure 8-15 is from the origin to the target point, P_t . Projection of several vectors onto the x - y plane now results in Figure 8-17. The primes denote vector projections onto the x - y plane.

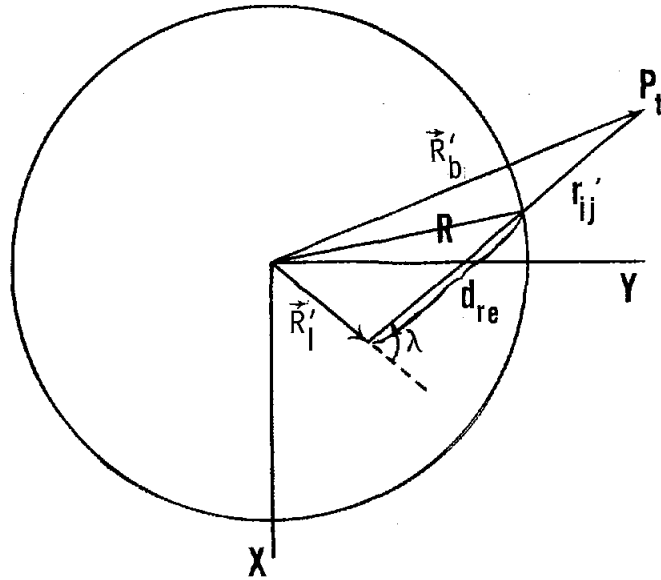


Figure 8-17. Projection Onto x - y Plane for Self-Blocking

The angle λ is available from the law of cosines

$$r_3^2 = r_1^2 + r_2^2 + 2r_1r_2 \cos \lambda \quad (8.4-4a)$$

where

$$r_1^2 = R_{1x}^2 + R_{1y}^2$$

$$r_2^2 = r_{ijx}^2 + r_{ijy}^2$$

$$r_3^2 = R_{bx}^2 + R_{by}^2 \quad (8.4-4b)$$

Since $0 \leq \lambda \leq \pi$, $\sin \lambda = \left(1 - \cos^2 \lambda\right)^{1/2}$, while the sign of $\cos \lambda$ is obtained directly from the law of cosines. If $r_3 < R$, no self-blocking is possible (this would likely be the case if the parabolic dish is tracking the sun).

The distance along the reflected ray projected into the x - y plane from the reflection point to intersection with the projection of the edge of the reflector is

$$d_{re} = -r_1 \cos \lambda + \left[R^2 - r_1^2 \sin^2 \lambda \right]^{1/2}, \quad (8.4-5)$$

where $r_1 = |\vec{R}'_1|$. The tangent of the elevation angle for the outgoing ray is

$$\tan \zeta_1 = \frac{r_{ijz} - R_{1z}}{r_2} \quad (8.4-6)$$

with $r_2 = |\vec{r}'_{ij}|$. At the edge of the parabolic dish, the outgoing ray has attained the height

$$Z_{out} = d_{re} \tan \zeta_1 + R_{1z}. \quad (8.4-7)$$

Blocking of the ray toward the target point then occurs if $Z_{edge} \geq Z_{out}$. As before, division of the reflector into a large number of integration segments allows neglect of the sunshape, and allows shadowing to be estimated from calculation of only the central ray to the target point.

8.4.3 Receiver Shadowing

In one application HELIOS was used for a situation where the receiver was mounted along the dish axis at some distance above the parabolic dish. The dish tracked the sun; hence, the receiver itself cast a shadow upon the reflecting surface. In a similar situation the parabolic dish had a hole cut from its center. The hole was utilized by a portion of the structure supporting the receiver. In both cases HELIOS adjusted the radius of the central integration-mesh element to be that of the ineffective area. Receiver shadowing or the effect of the hole is then included by neglecting the contribution from this central element.

References

- 8.1 A. Rabl, Optical and Thermal Properties of Compound Parabolic Concentrators, Report 50L 75-01, Argonne National Laboratory, 1975.
- 8.2 C. N. Vittitoe, F. Biggs, and R. E. Lighthill, HELIOS: A Computer Program for Modeling the Solar Thermal Test Facility - A Users Guide, Third Edition, SAND76-0346, Sandia Laboratories, Albuquerque, NM, October 1978.
- 8.3 DISSPLA Manuals, Integrated Software Systems Corporation, P.O. Box 9906, San Diego, CA, Fifth Printing, July 1975.
- 8.4 S. L. Thompson, RSCORS - A Revised SCORS Plot System, SAND77-1957, Sandia Laboratories, Albuquerque, NM, May 1978.

CHAPTER 9

COMPARISON OF DATA WITH HELIOS PREDICTIONS

During the evolution of the HELIOS program, there have been some comparisons of measurements with the corresponding computer calculations. Some comparisons have also been made between HELIOS results and the results from the MIRVAL code of J. D. Hankins.^{9, 1} The MIRVAL code uses a Monte Carlo method of treating statistical variations, whereas HELIOS is an analytical approach. Results from the two codes were in agreement. The agreement between calculations and measurements has been within the error tolerances of measurements.

The following list summarizes checks of the validity of HELIOS predictions.

Check Points for HELIOS

1. Scale model experiments for one heliostat by E. A. Igel, G. F. Bott, and R. L. Hughes, April 1977.
2. MIRVAL computer code for one heliostat by J. D. Hankins, January 1977.
3. Comparisons with shape of hole in a steel plate by John Holmes, May 1977.
4. Shape comparisons with image formed by 80-in. focal length spherical mirror by Larryl Matthews, April 1976.
5. Comparisons with Martin-Marietta data for one facet by W. Hart and C. N. Vittitoe, April 1977.
6. Single heliostat comparisons by D. E. Arvizu, September 1978.

Several verifications of the shape of the flux density pattern for a single spherical mirror were made by Larryl Mathews of Sandia Laboratories (Item 4 in the above list). Flux-density patterns were checked near the sagittal and tangential focal planes at several off-axis angles of reflection. In a demonstration, the Zone A field of 78 heliostats at the CRTF was used to melt a hole in a steel plate. The shape of the hole agreed with the shape of the flux-density contours from HELIOS (Item 3 in the check point list). More details of Items 1, 5, and 6 of the list will be given below.

9.1 Scale-Model Experiments for One Heliostat

In April of 1977, E. A. Igel and R. L. Hughes^{9.2} of Sandia Laboratories used a laboratory-scale model experiment to investigate the image performance of a spherical heliostat operating at large angles of incidence. Certain results of this experiment were recorded photographically. HELIOS was used to model this experiment and the calculations were compared with the measurements.

A heliostat was modeled on an optical bench using a collimator to simulate the 1/2-degree angle subtended by the solar disk. A spherical mirror was selectively masked to study the energy distribution in a focal plane when the angle of incidence was large (i. e. , 40 and 50°). Figure 9-1 shows the facet pattern used and the corresponding images.

This experiment was simulated using HELIOS. The same facet pattern and incident angles were used as input and the resulting flux-density pattern on a plane normal to the principal ray from the heliostat to the target was computed. A 3-D plot of these results is shown in Figure 9-2. Corresponding contour plots are given in Figure 9-3.

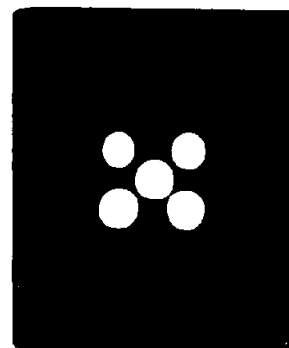
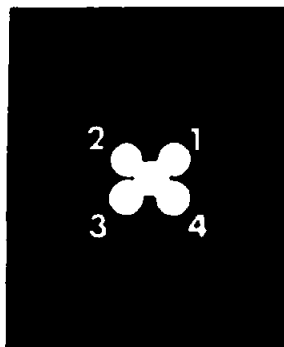
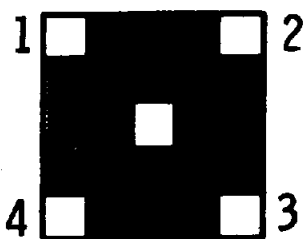
The agreement between the flux-density pattern calculated by HELIOS and the experiment is excellent. The separation of the energy into individual peaks for each facet in the pattern and the relative separation and orientation of the pattern in the computer plots of Figure 9-3 is identical to the experimental photographs in Figure 9-1. The reason that some of the peaks are truncated more than others in the computer-drawn graphs of Figure 9-2 is that the mesh points used to evaluate the flux-density patterns fall at different heights on each peak. The mesh points are located at the intersection of the grid of lines on the base of each drawing.

This experiment not only provides a valuable check for the simulation code HELIOS, but is also an excellent illustration of astigmatic aberrations caused by off-axis effects. At a zero angle of incidence, the images from all five facets coalesce into a single peak as shown in Figure 9-3. At large angles of incidence, the image from the center "reference facet" is held fixed on the center of the target but the contributions from the other facets spread out as indicated in Figures 9-1 through 9-3.

9.2 A Single-Facet Experiment

HELIOS calculations were performed for comparison with Martin-Marietta's measurements of the flux-density pattern produced by a single facet. The sunshape at the time of the measurement is not known, the exact time of the measurement is not available, and the distribution of slope errors is also not known. Using a sunshape measured in Albuquerque, NM (see Section 5.2.5) and a circular normal error cone of dispersion $\sigma = 2.83$ mrad, HELIOS predicted the dashed curves in Figure 9-4. The squares and solid curve indicate the experimental data.

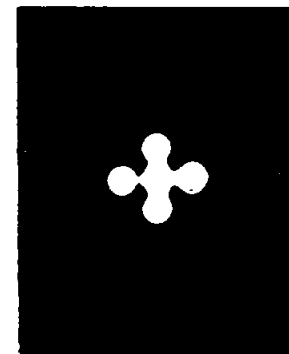
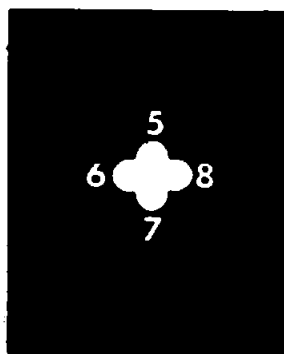
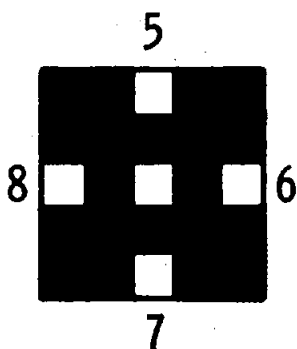
HELIOSTAT MASK



ANGLE OF INCIDENCE, φ

40°

50°



LIGHT SQUARES ARE IRRADIATED FACETS

Figure 9-1. Location of Simulated Sun Images as Produced by Specified Facets of Lab-Heliostat

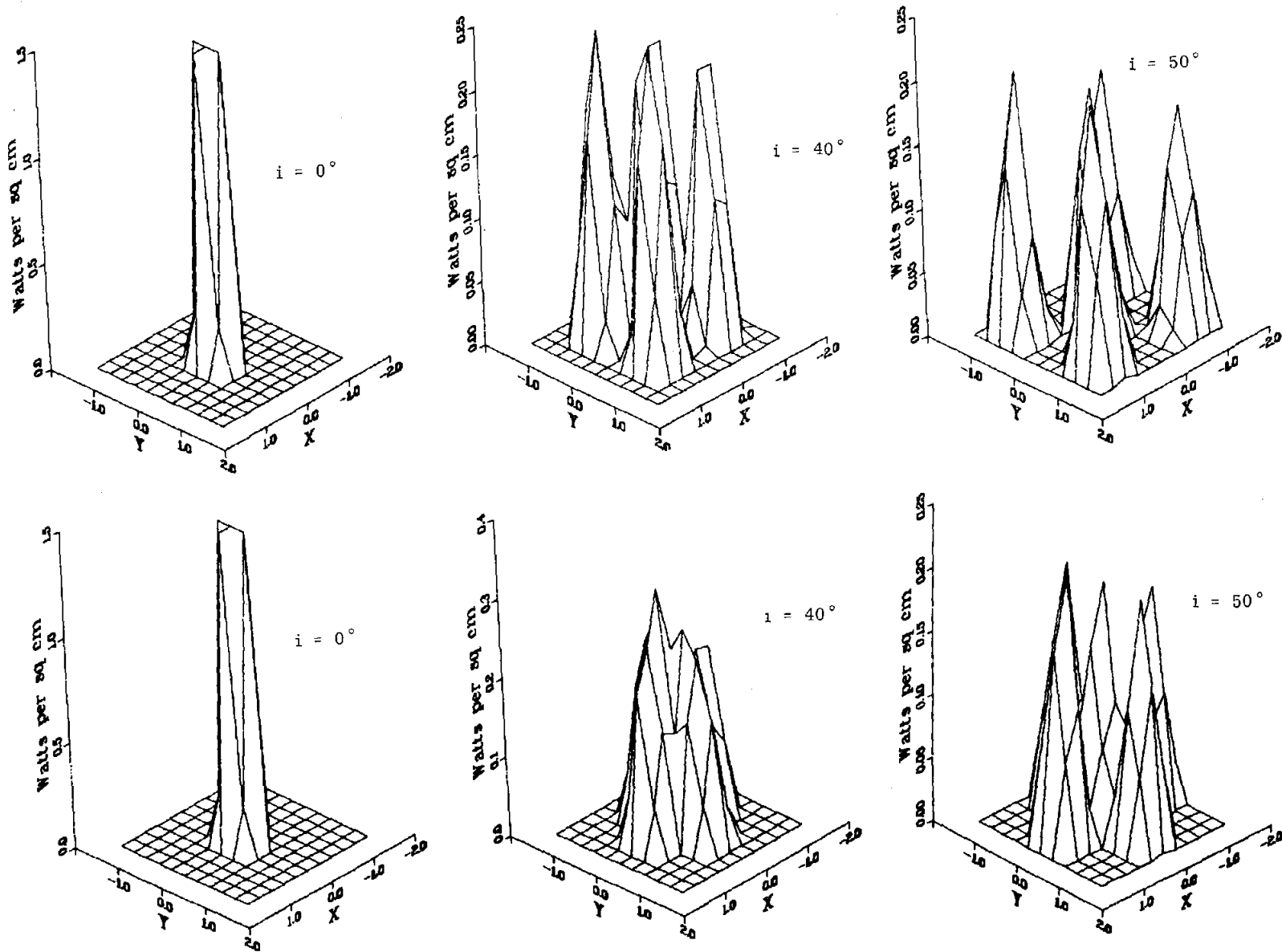


Figure 9-2. Flux-Density Patterns Calculated by HELIOS Corresponding to the Measurements Shown in Figure 9-1

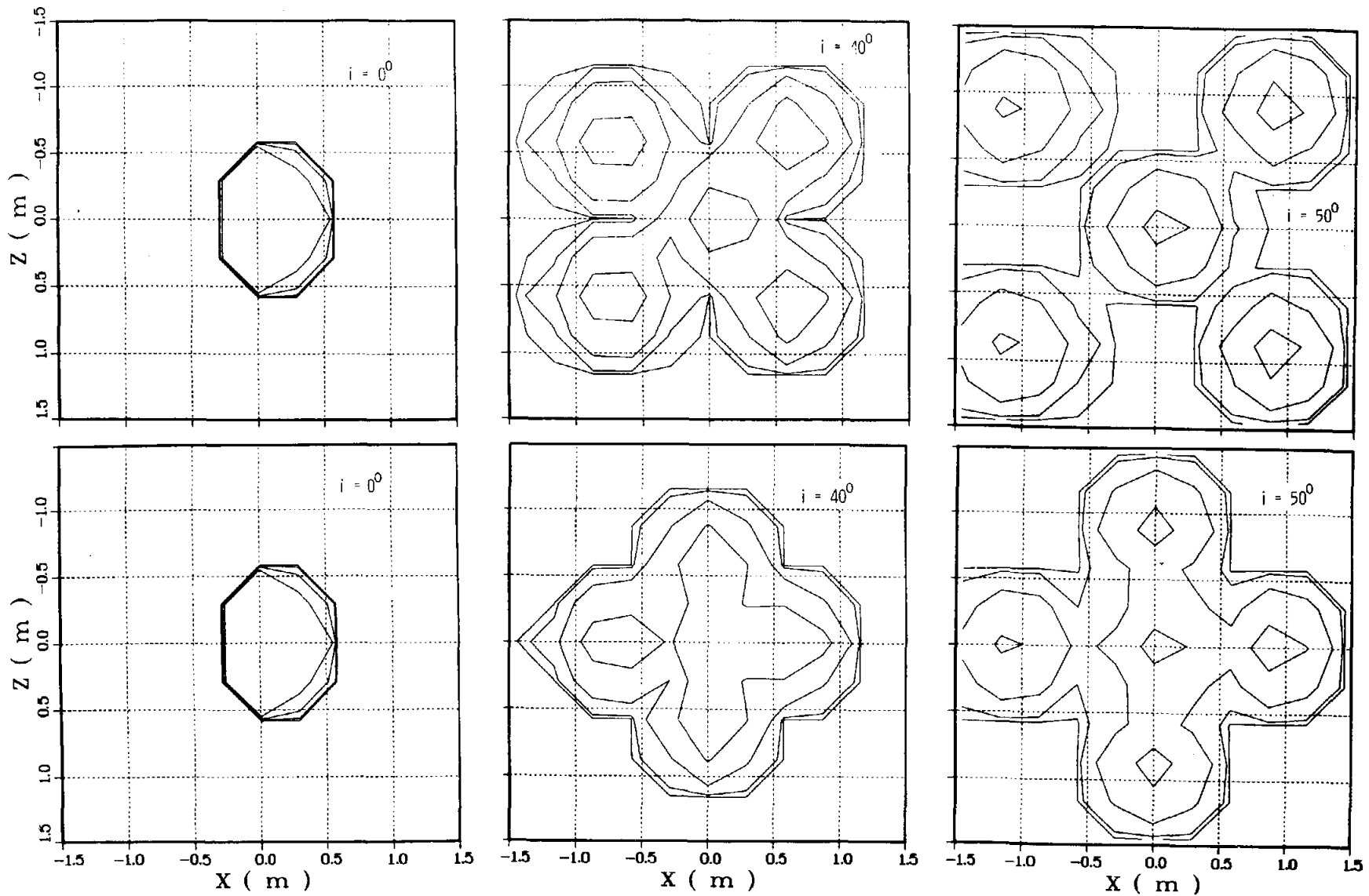
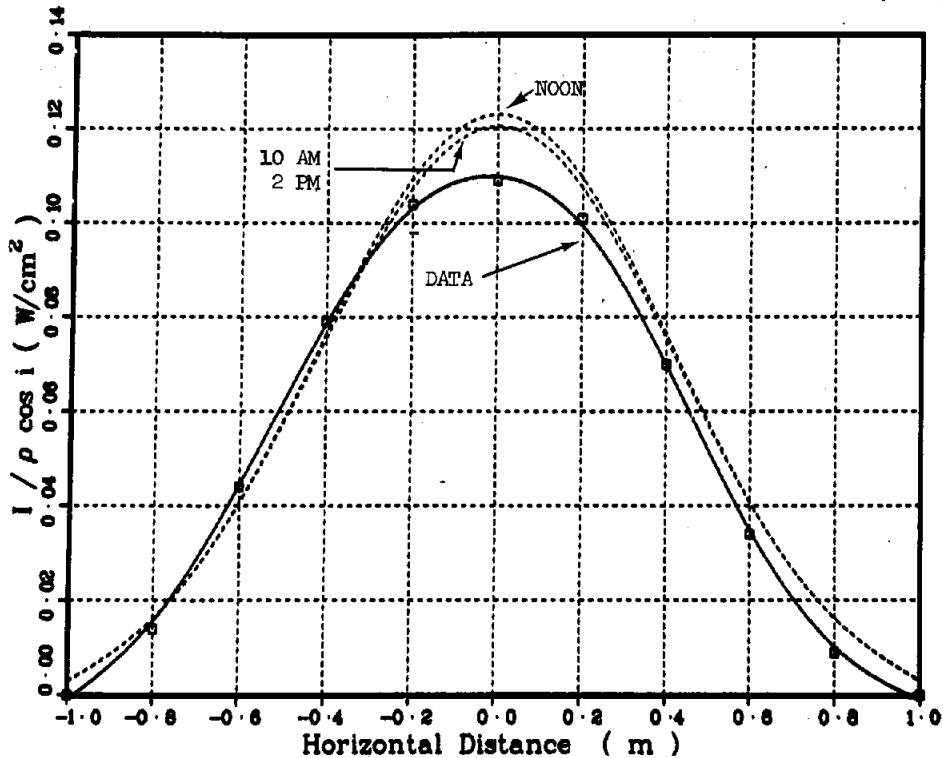


Figure 9-3. Flux-Density Contours. These contours were calculated by HELIOS corresponding to the measurements shown in Figure 9-1. The contour levels are 0.15, 0.05, 0.01, and 0.001 W/cm². Smoother contours would be expected if the target mesh had more than 121 points in the grid



Target is 106.68 m along a line 34° to the east of south of the facet. Insolation is normalized to 0.08 W/cm^2 . Latitude is 39.8° N as for Denver, Colorado. Target and facet heights are identical. The horizontal distance is across the target center. The planar target faces the facet.

Figure 9-4. Energy Flux Comparison With Martin-Marietta Data Collected on September 28, 1976

There was no attempt to adjust the insolation, the error cone, or the sunshape to improve the agreement. Of course, the agreement could be made arbitrarily close by properly choosing these quantities. We conclude that the agreement is within the tolerance bounds of the input information in the calculation.

9.3 A Single-Heliostat Experiment

A recent comparison of measurements with HELIOS was performed on single heliostats at the CRTF in Albuquerque, NM. Some preliminary results from these experiments were reported by D. E. Arvizu.^{9.3} A typical set of these measurements is given here.

This experiment was performed by using a stationary vertical bar with radiation gages spaced at intervals along the bar. The solar image produced by one Martin-Marietta heliostat was swept horizontally across the bar. This heliostat consists of a 5×5 array of 1.2- by 1.2-m facets. Each gage recorded a flux density versus time. Thus the reading from each gage

represented a different slice across the flux-density pattern. The insolation was measured separately and used together with a measured heliostat reflectivity of 0.81 as input to the HELIOS code to calculate the corresponding flux-density pattern. The results are compared in Figure 9-5.

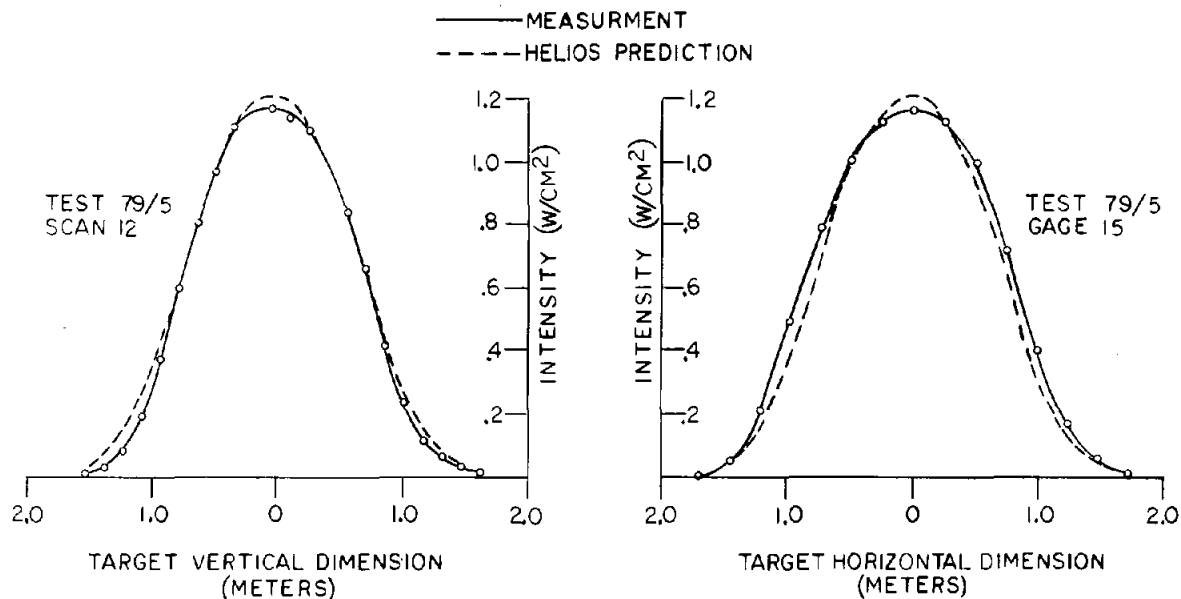


Figure 9-5. Measured vs Predicted Beam Shape

9.4 Remaining Verification

Although HELIOS has given results consistent with each of the checkpoints noted earlier, there are several features of the code that have not been subjected to test. Other than the pattern-shape test by John Holmes, each comparison was for a single mirror or a single heliostat. These give no check of shadowing and blocking features. A consistency check is possible by comparing results with MIRVAL calculations for a large array of heliostats. Such a comparison is planned. More detailed flux-pattern measurements are planned for the CRTF using large heliostat arrays. Then accurate intensity measurements with concurrent sunshape data will offer a definitive test of shadowing and blocking features.

The reconcentrator features have not been tested experimentally. However, reconcentrator experiments should be completed by the spring of 1979 giving additional data for comparison.

Thus far, the various uncertainties that contribute to the error cone in experimental tests have been treated as not well defined. In some cases the error cone was adjusted to improve agreement with data. The resultant error cone was then only examined for consistency with

readily available information about errors associated with the heliostat and the sunshape. Typically the resultant cylindrically symmetric error cone has a dispersion near 2 mrad, consistent with estimates for heliostats at the CRTF. Tests would be still more definitive if this degree of freedom were removed. In other situations it may be possible to use HELIOS results to estimate one contribution to the error provided the other contributions are known. These capabilities of HELIOS will be tested in the future.

Other possibilities for testing HELIOS are expected at several solar facilities now being developed. The authors are interested in any comparisons of HELIOS with measurements. In addition, if experimental data and heliostat field, receiver, and sun definition can be provided, the authors would welcome the opportunity for additional validation.

References

- 9.1 J. D. Hankins, "MIRVAL -- A Monte Carlo Ray Trace Program," Proceedings of the ERDA Solar Workshop on Methods for Optical Analysis of Central Receiver Systems, University of Houston, August 10-11, 1977, pp 243-247.
- 9.2 R. L. Hughes and E. A. Igel, Sandia Laboratories Memorandum of Record to Distribution, Albuquerque, NM, April 28, 1977.
- 9.3 D. E. Arvizu, "The Solar Central Power Test Facility Heliostat Development," Proceedings of the International Symposium on Concentrating Solar Collector Technology, the Solar Energy Research Institute, Golden, CO, June 14, 1978.

APPENDIX A
GLOSSARY OF TERMS

APPENDIX A
GLOSSARY OF TERMS

In this Appendix definitions are provided for terms and expressions. Some of these are defined for special use in expressing ideas in the Helios model. Others, although they are fairly standard terms, take on a special connotation when applied to Helios concepts. Certain terms are defined in the text where they first appear, but they are consolidated here for easy reference.

The Glossary entries that occur within the definition or discussion of another entry are underlined to facilitate cross referencing. Several of the entries have one or more references to the text. Some of these references are given because the Glossary definition is short and a more complete one is provided in the report. In other cases, the reference simply means the entry is used in the referenced section and provides an example of its use. Many entries contain no reference to the text. Most of these are of a general nature and are adequately defined in the Glossary. A portion of the entries is clarified by listing their metric units. One purpose of this Glossary is to facilitate the use of the report by providing a convenient reference to special terms. Another purpose is to help establish terminology for use in communication among engineers interested in the modeling of solar concentrators and related concepts. We welcome constructive criticism on improving and extending this Glossary.

AIM POINT: A point in space usually on or near the receiver that is used as a reference for the alignment of one or more heliostats or for the prealignment of facets. Central rays reflected from the center of the reference surface are directed to the aim point.

AIM-POINT STRATEGY: Any strategy for specifying the alignment of heliostats on their respective aim points. For example, a multiple aim-point strategy may be used to shape the flux-density pattern on a central receiver.

ALIASING (Undersampling): A condition caused by the sample spacing in which high frequencies masquerade as low frequencies. A high-frequency component of a function can vanish at every sample point of an equally-spaced grid and, therefore, not be detectable without using a finer sample spacing.

BLOCKING: The act of intercepting sunlight reflected from a concentrator before it reaches the receiver. For example, one heliostat may block some of the light reflected from another heliostat and prevent it from reaching the receiver.

CENTRAL RAY: A ray of light originating from the center of the solar disk.

CENTRAL RECEIVER: A solar collector in which the maximum dimension of the receiver (or maximum distance between parts of the receiver subsystem) is small compared to the maximum dimension of the concentrator (or maximum distance between parts of the concentrator subsystem) and the receiver is stationary with respect to the earth.

CIRCLE OF LEAST CONFUSION: The point along the principal ray of an astigmatic system where the diameter of the reflected sagittal-ray fan is equal to that of the tangential-ray fan when the incident light is a collimated beam.

CIRCULAR-NORMAL DISTRIBUTION: The special case of the elliptic-normal distribution that has equal standard deviations along both of its principal axes (Section 5.2.4).

CONCENTRATOR: Any optical element that changes the direction of a ray of sunlight for the purpose of intensifying the flux density over that of direct insolation. A heliostat is a part of the concentrator system of a central-receiver solar collector.

CONCENTRATOR REFERENCE SYSTEM: A coordinate system defined with respect to the concentrator. In a heliostat, for example, it is defined with respect to the heliostat frame.

CONCENTRATION: The ratio of flux density at a point on the absorber to the incident normal direct insolation.

CRTF: An acronym for the Central Receiver Test Facility at Sandia Laboratories in Albuquerque, New Mexico. This test facility was formerly known as the Solar Thermal Test Facility (STTF).

DISPERSION: A parameter used in the circular-normal distribution (Section 5.2.4).

DISTRIBUTION: A statistical description of a cone or bundle of directions of quantities such as light rays or surface normals.

DRIFT: The motion of the flux-density pattern as it moves off the receiver when the heliostats experience a lock condition.

EFFECTIVE SUNSHAPE: A distribution in the reflected-ray reference system obtained by convolving the sunshape with the error cone. The effective sunshape includes the averaged effect of nondeterministic factors, such as suntracking errors and reflecting-surface slope errors.

ELLIPTIC-NORMAL DISTRIBUTION: A two dimensional distribution for which random excursions along two mutually perpendicular axes are normally distributed (Section 5.2.3).

ERROR CONE: A distribution that includes the effects of all the nondeterministic factors influencing the optical behavior of a concentrator system (Section 2.5.2).

FACET: An individual mirror on a heliostat.

FAST FOURIER TRANSFORM: A numerical procedure for calculating the discrete Fourier transform. It is especially efficient for computer use in calculating convolutions (Section 7.3).

FLUX (Radiant) (or Radiant Power): The time rate of radiant energy flow (watts).

FLUX DENSITY (Irradiance): Radiant flux incident per unit area (W/m^2).

HELIOS: The designation given to the computer program that implements the Helios model.

Helios: The designation of a simulation model for the optical behavior of reflecting solar concentrators.

HELIOSTAT: A reflecting concentrator element which can utilize tracking axes to keep redirected solar radiation fixed on the receiver.

HELIOSTAT RESPONSE FUNCTION: The response of an error-free heliostat to a collimated incident beam of light. It is calculated by projecting the resulting flux-density pattern onto a target grid when the shape of the reflecting surface is taken to be the reference surface of the heliostat. It is normalized to correspond to unit insolation and unit reflectance.

INSOLATION (Solar Radiation): The solar energy incident on a unit surface in unit time (W/m^2).

- a. Circumsolar Radiation: When passing through a turbid atmosphere with a large amount of aerosols, there is a broadening of the angular cone through which the sun's rays arrive at the earth's surface. Under turbid sky conditions, a significant amount of the direct insolation is scattered into a cone of roughly $\pm 5^\circ$ about the central ray. This part of the diffuse insolation is referred to as circumsolar radiation. This component of solar insolation has similar general angular time variations as the direct component. Although it is usable with some types of concentrators, it is not usable by highly concentrating collectors and may contribute to spillage radiation problems.
- b. Direct Insolation: The insolation that comes from within the solid angle subtended by the solar disk (a cone of approximately $\pm 1/4^\circ$ about the central ray).
- c. Diffusion Insolation: Any contribution to the insolation that is not direct, excluding specular reflections from other objects.
- d. Horizontal Insolation: The insolation on a surface parallel to the surface of the earth.
- e. Normal Insolation: The insolation on a surface perpendicular to a central ray from the sun.
- f. Total Insolation: The total radiant power per unit area. It includes direct, diffuse, and background radiation.
- g. Background Radiation: The contribution to the total insolation that is reflected from objects on the earth.

These terms can be used in combinations such as direct-normal insolation.

IRRADIANCE (Flux Density): The radiant flux incident per unit area (W/m^2).

LINE-FOCUS COLLECTOR: A solar collector in which the receiver is located along a focal line of its concentrator.

LOCK: A condition where the heliostats stop tracking the sun and remain fixed.

OPTICAL ELEMENT: Any element that alters the direction or magnitude of an incident ray of sunlight.

PLANE OF INCIDENCE: A plane defined by the incident central ray and the normal to the surface at the point of reflection. It also contains the reflected central ray.

PREALIGNMENT: The relative orientation of the facets with respect to the heliostat frame. Prealignment can be executed for any sun-heliostat-receiver geometry specified by a date and time of day. An "on-axis" prealignment is one in which parallel rays of light incident parallel to the optical axis of a heliostat will reflect from the center of each facet to intersect at the aim point specified on the optical axis.

PRINCIPAL RAY: A central ray from the sun that strikes the center of a heliostat or the center of the aperture stop of any optical element.

RADIANT FLUX: See Radiant Power.

RADIANT POWER (also Radiant Flux or Flux): The time rate of radiant energy flow (watts).

RECEIVER: That element of a collector system to which the solar radiation is directed and where it is converted to another form of energy.

RECEIVER APERTURE: A surface, usually a plane, that defines the opening of a cavity receiver or the periphery of an external receiver.

RECONCENTRATOR: Reflectors used near the receiver for the purpose of increasing the concentration of sunlight on the receiver.

REFERENCE FACET: A facet that is kept aligned by the sun-tracking mechanism so that the central ray from the sun will reflect from the center of it to intercept the aim point.

REFLECTED-RAY REFERENCE SYSTEM: A coordinate system defined with respect to the reflected ray (Section 5.4.1).

REFERENCE PLANE: A plane perpendicular to and intercepting some reference direction at unit distance from the origin. (This reference direction may be, for example, the z-direction of a coordinate system.) The reference plane is useful for specifying two-dimensional distributions (Section 5.2.1).

REFERENCE SURFACE: A surface used as a reference for specifying slope errors for a concentrator.

ROOT-MEAN-SQUARE (RMS) WIDTH: For a two-dimensional distribution $F(x, y)$ with axes of symmetry along x and y , the corresponding RMS widths are $\sqrt{\langle x^2 \rangle}$ and $\sqrt{\langle y^2 \rangle}$ where

$$\langle x^2 \rangle = \int_{-\infty}^{\infty} \int_{-\infty}^{\infty} x^2 F(x, y) dx dy$$

and y^2 is calculated in the same way with y^2 used in place of x^2 (Appendix B).

ROOT-MEAN-SQUARE (RMS) RADIUS: A two-dimensional distribution $F(p)$ that has azimuthal symmetry is a function of one radial variable and has a RMS radius of $\sqrt{\langle p^2 \rangle}$ where

$$\langle p^2 \rangle = 2\pi \int_0^{\infty} p^3 F(p) dp$$

A distribution $F(x, y)$ that is a function of two variables has an average RMS radius of $\sqrt{\langle p^2 \rangle}$ where

$$\langle p^2 \rangle = \int_{-\infty}^{\infty} \int_{-\infty}^{\infty} (x^2 + y^2) F(x, y) dx dy$$

These distributions are normalized to unit value when integrated over their reference planes (Appendix B).

SAGITTAL FOCUS: A line formed by the intersection of rays in the sagittal-ray fan.

SAGITTAL-RAY FAN: The sagittal-ray fan is the plane that contains the principal ray and is perpendicular to the tangential-ray fan (Section 4.3.2).

SHADOWING: The act of casting a shadow across any portion of a concentrator.

SLANT PATH: A line between the center of a heliostat and a reference point. This reference point may be an aim point or some point on the receiver.

SLANT RANGE: The length of the slant path.

SLOPE ERROR: The angle between the normal to the reflecting surface and the normal to the reference surface at a point on a concentrator. For a more complete specification of a slope error, a reference surface is used (Section 5.1).

SOLAR COLLECTOR: A structure which collects and converts solar energy into an alternate form.

SOLAR TIME: The time as reckoned by the apparent position of the sun. Solar noon is the instant at which the sun reaches its largest elevation angle.

SPILLAGE: Radiation emanating from the concentrator system, but which misses the receiver aperture.

SUN-CONCENTRATOR SYSTEM: A coordinate system where the plane of incidence defines the $y - z$ plane; the $x - y$ plane is tangent to the concentrator surface at the point of reflection (Section 3.4).

SUN POSITION: The azimuth and elevation angles for specifying the direction anti-parallel to the central ray from the sun (Section 3.1.2).

SUNSHAPE: A distribution describing the angular distribution of light rays from the sun (Sections 2.5.1 and 5.2.5).

SUPER-SMART FACET: An idealization in which the facet shape varies as the sun-alignment geometry changes to maintain a correct focus (Section 7.2).

TANGENTIAL-RAY FAN: A fan of light rays reflected from a spherical reflector. The fan lies in a plane containing the incoming principal ray and the central normal of the reflector (Section 4.3.1).

TANGENTIAL FOCUS: A focal line for light rays in the tangential-ray fan.

TARGET GRID: A grid of points on the receiver (or on an arbitrary surface) where flux-density calculations are to be performed.

TARGET PLANE: A plane surface (real or imagined) on which a target-grid is to be defined.

TEST AREA: An area that distinguishes between "small-scale" and "medium-scale" surface irregularities. Medium-scale measurements average over the test area, whereas small-scale measurements apply within it (Section 5.1).

APPENDIX B

THE COMPOSITION OF MEAN-SQUARE VALUES UNDER
TWO-DIMENSIONAL CONVOLUTION

APPENDIX B

THE COMPOSITION OF MEAN-SQUARE VALUES UNDER TWO-DIMENSIONAL CONVOLUTION

The two-dimensional convolution of functions f and g is defined by

$$f * g = \int_{-\infty}^{\infty} \int_{-\infty}^{\infty} f(\mathbf{x} - \eta, y - \xi) g(\eta, \xi) d\eta d\xi . \quad (\text{B-1})$$

The general properties of convolution can be found in most books on Fourier analysis such as the one by Bracewell.^{B. 1} In this appendix we investigate the manner in which mean-square values of variables add up under convolution of two-dimensional distributions.

Since the integration limits for all the integrals used in this appendix run from minus infinity to plus infinity, we will leave off the notation for brevity in writing and leave this information as understood. The equations developed here form definitions for any distribution so we will use h with the understanding that f , g , or any other distribution can be used in place of h .

Recall that the distributions of interest to us are normalized so that

$$\iint h(x, y) dx dy = 1 . \quad (\text{B-2})$$

The mean-square value of x with respect to distribution h is defined by

$$\langle x^2 \rangle_h = \iint x^2 h(x, y) dx dy . \quad (\text{B-3})$$

The mean-square value of y with respect to the distribution h is calculated by replacing x^2 by y^2 in Eq. (B-3).

It is convenient to use Fourier analysis to calculate mean-square values with respect to the distribution $f * g$. The two-dimensional Fourier transform $H(u, v)$ of the function $h(x, y)$ is defined by

$$H(u, v) = \iint h(x, y) \exp[-2\pi i(ux + vy)] dx dy \quad (\text{B-4})$$

where u and v are the transform variables and $i = \sqrt{-1}$. Note that we are using the convention that the capital letter H represents the transform of the function h . It is convenient to use several properties of two-dimensional Fourier transforms taken from Table 12.1 of Bracewell.^{B.1}

$$\int h(x, y) dx dy = H(0, 0) = 1. \quad (\text{B-5})$$

We have used Eq. (B-2) on the last part of this result. The mean value of x with respect to the distribution h is

$$\langle x \rangle_h = -\frac{1}{2\pi i} \frac{\partial H(0, 0)}{\partial u} \quad (\text{B-6})$$

and the corresponding mean value of y is

$$\langle y \rangle_h = -\frac{1}{2\pi i} \frac{\partial H(0, 0)}{\partial v}. \quad (\text{B-7})$$

The mean-square value of x with respect to the distribution h is

$$\langle x^2 \rangle_h = -\frac{1}{4\pi^2} \frac{\partial^2 H(0, 0)}{\partial u^2} \quad (\text{B-8})$$

and the corresponding mean-square value for y is

$$\langle y^2 \rangle_h = -\frac{1}{4\pi^2} \frac{\partial^2 H(0, 0)}{\partial v^2}. \quad (\text{B-9})$$

Now using distribution $f * g$ in place of h in Eqs. (B-3) and (B-8) gives

$$\langle x^2 \rangle_{f * g} = \iint x^2 f * g dx dy = -\frac{1}{4\pi^2} \frac{\partial^2}{\partial u^2} [FG]_{0,0}. \quad (\text{B-10})$$

Note that the Fourier transform of the convolution $f * g$ is the product FG . The subscript notation $0,0$ on the brackets indicates that after the indicated differentiation both u and v are set equal to zero. Performing the differentiations in Eq. (B-10) gives

$$\langle x^2 \rangle_{f * g} = -\frac{1}{4\pi^2} \left[G(0, 0) \frac{\partial^2 F(0, 0)}{\partial u^2} + 2 \frac{\partial F(0, 0)}{\partial u} \frac{\partial G(0, 0)}{\partial u} + F(0, 0) \frac{\partial^2 G(0, 0)}{\partial u^2} \right]. \quad (\text{B-11})$$

Using properties (B-5), (B-6), and (B-8) in Eq. (B-11) gives

$$\langle x^2 \rangle_{f*g} = \langle x^2 \rangle_f + 2 \langle x \rangle_f \langle x \rangle_g + \langle x^2 \rangle_g . \quad (\text{B-12})$$

A similar development gives the mean-square value of y with respect to the distribution $f*g$ as

$$\langle y^2 \rangle_{f*g} = \langle y^2 \rangle_f + 2 \langle y \rangle_f \langle y \rangle_g + \langle y^2 \rangle_g . \quad (\text{B-13})$$

In the important special case where either $\langle x \rangle_f$ or $\langle x \rangle_g$ or both equal zero, Eq. (B-12) becomes

$$\langle x^2 \rangle_{f*g} = \langle x^2 \rangle_f + \langle x^2 \rangle_g . \quad (\text{B-14})$$

If either $\langle y \rangle_f$ or $\langle y \rangle_g$ or both equal zero, Eq. (B-13) becomes

$$\langle y^2 \rangle_{f*g} = \langle y^2 \rangle_f + \langle y^2 \rangle_g . \quad (\text{B-15})$$

The polar radius ρ is related to the rectangular coordinates x and y by

$$\rho^2 = x^2 + y^2 . \quad (\text{B-16})$$

We can apply the results of Eqs. (B-14) and (B-15) to Eq. (B-16) to get

$$\begin{aligned} \langle \rho^2 \rangle_{f*g} &= \langle x^2 \rangle_{f*g} + \langle y^2 \rangle_{f*g} \\ &= \langle x^2 \rangle_f + \langle x^2 \rangle_g + \langle y^2 \rangle_f + \langle y^2 \rangle_g \\ &= \langle \rho^2 \rangle_f + \langle \rho^2 \rangle_g . \end{aligned} \quad (\text{B-17})$$

For distributions that have circular symmetry, the averages $\langle x \rangle$ and $\langle y \rangle$ vanish. Therefore, Eqs. (B-14) and (B-15) always apply for such distributions.

Reference

B.1 Ron Bracewell, The Fourier Transform and Its Applications, McGraw Hill, 1965.

APPENDIX C

THE CONVOLUTION OF ELLIPTIC-NORMAL DISTRIBUTIONS

APPENDIX C

THE CONVOLUTION OF ELLIPTIC-NORMAL DISTRIBUTIONS

In combining the effects of sun-tracking errors, surface slope errors, and reflectance errors, it is necessary to convolve the corresponding error distributions. In general, the two-dimensional fast Fourier transform is used in HELIOS to numerically convolve these distributions. Some or all of these distributions are often elliptic normal and can be convolved analytically, thereby saving on computing time and memory requirements. In this appendix we develop the analytical form for the convolution of two elliptic-normal distributions.

The distributions to be convolved are

$$F(\hat{u}, \hat{v}) = \frac{1}{2\pi\sigma_u\sigma_v} \exp \left\{ -\frac{1}{2} \left[\frac{\hat{u}^2}{\sigma_u^2} + \frac{\hat{v}^2}{\sigma_v^2} \right] \right\} \quad (C-1)$$

and

$$G(\hat{x}, \hat{y}) = \frac{1}{2\pi\sigma_x\sigma_y} \exp \left\{ -\frac{1}{2} \left[\frac{\hat{x}^2}{\sigma_x^2} + \frac{\hat{y}^2}{\sigma_y^2} \right] \right\} . \quad (C-2)$$

The $\hat{u} - \hat{v}$ and $\hat{x} - \hat{y}$ coordinate systems are related by a rotation as shown in Figure C-1 and by Eqs. (C-3).

$$\hat{u} = \hat{x} \cos \theta + \hat{y} \sin \theta \quad (C-3a)$$

$$\hat{v} = -\hat{x} \sin \theta + \hat{y} \cos \theta . \quad (C-3b)$$

In Figure C-1, one quarter of an ellipse is shown on each set of axes; these graphs represent equations obtained by equating the bracketed terms of Eqs. (C-1) and C-2) to unit values. The \hat{u} and \hat{v} intercepts are given by σ_u and σ_v and the \hat{x} and \hat{y} intercepts are equal to σ_x and σ_y as indicated in the figure. These ellipses are contours of equal probability density for the respective distributions.

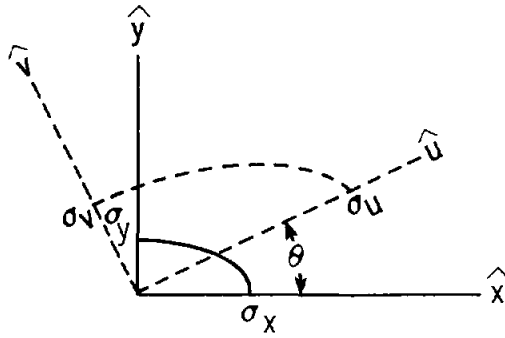


Figure C-1. Contours of Equal Probability Density for the Elliptic-Normal Distributions of Eqs. (C-1) and (C-2)

In order to simplify the subsequent development, we use the dimensionless variables

$$\hat{u} = \sigma_u u \quad (C-4a)$$

$$\hat{v} = \sigma_v v \quad (C-4b)$$

$$\hat{x} = \sigma_x x \quad (C-4c)$$

$$\hat{y} = \sigma_y y \quad (C-4d)$$

In terms of these variables the probability-density functions become

$$F(u, v) = \frac{1}{2\pi} \exp \left\{ -\frac{1}{2} [u^2 + v^2] \right\} \quad (C-5)$$

and

$$G(x, y) = \frac{1}{2\pi} \exp \left\{ -\frac{1}{2} [x^2 + y^2] \right\} \quad (C-6)$$

We have used the Jacobians

$$\frac{\partial(\hat{x}, \hat{y})}{\partial(x, y)} = \sigma_x \sigma_y \quad (C-7a)$$

and

$$\frac{\partial(\hat{u}, \hat{v})}{\partial(u, v)} = \sigma_u \sigma_v \quad (C-7b)$$

in order to adjust the normalization constants that multiply the distributions. In terms of the new variables in Eq. (C-4), the transformation (C-3) becomes

$$u = ex + fy \quad (C-8a)$$

$$v = -gx + hy \quad (C-8b)$$

where

$$e = \frac{\sigma_x}{\sigma_u} \cos \theta \quad (C-9a)$$

$$f = \frac{\sigma_y}{\sigma_u} \sin \theta \quad (C-9b)$$

$$g = \frac{\sigma_x}{\sigma_v} \sin \theta \quad (C-9c)$$

$$h = \frac{\sigma_y}{\sigma_v} \cos \theta . \quad (C-9d)$$

Using Eqs. (C-8) to change the variables in F to x and y gives

$$F = \frac{1}{2\pi} \exp \left\{ -\frac{1}{2} \left[x^2(e^2 + g^2) + 2xy(ef - gh) + y^2(f^2 + h^2) \right] \right\} . \quad (C-10)$$

The convolution of G and F is

$$G * F = \int_{-\infty}^{\infty} \int_{-\infty}^{\infty} G(x - u, y - v) F(u, v) du dv . \quad (C-11)$$

Substituting from Eqs. (C-6) and (C-10) for G and F in Eq. (C-11) gives

$$G * F = \frac{\exp \left\{ -\frac{1}{2} (x^2 + y^2) \right\}}{4\pi^2} \iint \exp \left\{ -\frac{1}{2} \left[Au^2 + 2Cuv + Bv^2 - 2xu - 2vy \right] \right\} du dv , \quad (C-12)$$

where we define

$$A = 1 + e^2 + g^2 \quad (C-13a)$$

$$B = 1 + f^2 + h^2 \quad (C-13b)$$

$$C = ef - gh \quad (C-13c)$$

$$D = AB - C^2 \quad (C-13d)$$

The parameter D is not used in Eq. (C-12) but will be useful later.

In order to "complete the squares" with respect to the integration variables, we make the change of variables

$$u = w + \alpha \quad (C-14a)$$

$$v = t + \beta \quad (C-14b)$$

Substituting Eqs. (C-14) into (C-12) and equating the coefficients of the new integration variables t and w to zero gives the system of equations

$$\alpha A + \beta C = x \quad (C-15a)$$

$$\alpha C + \beta B = y \quad (C-15b)$$

Solving this system of equations for α and β gives

$$\alpha = \frac{Bx - Cy}{D} \quad (C-16a)$$

and

$$\beta = \frac{Ay - Cx}{D} \quad (C-16b)$$

The convolution integral Eq. (C-12), before elimination of the parameters α and β , becomes

$$G * F = \frac{\exp \left\{ -\frac{1}{2} \left[x^2 + y^2 + A\alpha^2 + 2\alpha\beta C + \beta^2 B - 2\alpha x - 2\beta y \right] \right\}}{4\pi^2} \quad (C-17)$$

where I is the integral

$$I = \int_{-\infty}^{\infty} \int_{-\infty}^{\infty} \exp \left\{ -\frac{1}{2} \left[Aw^2 + 2Cwt + Bt^2 \right] \right\} dw dt . \quad (C-18)$$

which is a constant (i. e., not a function of x or y). Now we use Eqs. (C-16) to eliminate the parameters α and β in Eq. (C-17) and obtain

$$G*F = \text{const} \exp \left\{ -\frac{1}{2} \left[x^2 \left(\frac{D-B}{D} \right) + 2xy \frac{C}{D} + y^2 \left(\frac{D-A}{D} \right) \right] \right\} . \quad (C-19)$$

In terms of the original variables, Eq. (C-19) becomes (using Eqs. (C-4))

$$G*F = \text{const} \exp \left\{ -\frac{1}{2} \left[\hat{a}x^2 + 2k\hat{x}\hat{y} + \hat{b}y^2 \right] \right\} , \quad (C-20)$$

where we define

$$a = \frac{D-B}{D\sigma_x^2} \quad (C-21a)$$

$$b = \frac{D-A}{D\sigma_y^2} \quad (C-21b)$$

$$k = \frac{C}{D\sigma_x\sigma_y} . \quad (C-21c)$$

The quadratic form in Eq. (C-20) is

$$Q = \hat{a}x^2 + 2k\hat{x}\hat{y} + \hat{b}y^2 . \quad (C-22)$$

We can eliminate the cross term in Q by the proper selection of η in the coordinate transformation (rotation).

$$\begin{bmatrix} \hat{x} \\ \hat{y} \end{bmatrix} = \begin{bmatrix} \cos \eta & -\sin \eta \\ \sin \eta & \cos \eta \end{bmatrix} \begin{bmatrix} t \\ w \end{bmatrix} \quad (C-23)$$

which is shown in Figure C-2.

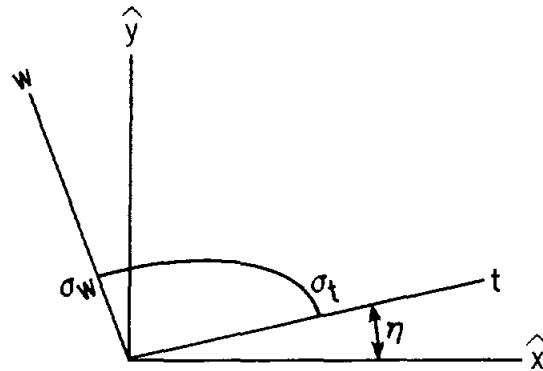


Figure C-2. The Principal-Axis System $t - w$ for the Quadratic Form of Eq. (C-20)

The $t - w$ coordinate axes are the principal axes of the quadratic form Q . We will use results from Chapter 12 of Noble^{C.1} to establish that the quadratic form is elliptic, to solve for the standard deviations corresponding to the principal axes of this quadratic form, and to find the angle of rotation η .

When the axes t and w correspond to the principal axes of the quadratic form, Q becomes

$$Q = \lambda_t t^2 + \lambda_w w^2 \quad (C-24)$$

where λ_t and λ_w are the eigenvalues of the matrix

$$M = \begin{bmatrix} a & k \\ k & b \end{bmatrix} . \quad (C-25)$$

The axes t and w lie along the eigenvectors of M .

The curve

$$Q = 1 = \lambda_t t^2 + \lambda_w w^2 \quad (C-26)$$

is an ellipse provided that λ_t and λ_w are positive. The eigenvalues of M are

$$\lambda = \frac{1}{2} \left\{ a + b \pm \sqrt{(a + b)^2 - 4(ab - k^2)} \right\} \quad (C-27a)$$

which can also be written

$$\lambda = \frac{1}{2} \left\{ a + b \pm \sqrt{(a - b)^2 + 4k^2} \right\} . \quad (\text{C-27b})$$

In terms of the parameters of Eq. (C-13), these eigenvalues are

$$\lambda = \frac{1}{2D} \left\{ \frac{D - B}{\sigma_x^2} + \frac{D - A}{\sigma_y^2} \pm \left[\left(\frac{D - B}{\sigma_x^2} - \frac{D - A}{\sigma_y^2} \right)^2 + \left(\frac{2C}{\sigma_x \sigma_y} \right)^2 \right]^{1/2} \right\} . \quad (\text{C-27c})$$

We now proceed to establish that both of these eigenvalues are positive. In order to fix the signs of a and b , we examine Eq. (C-21). From Eq. (C-13) we get

$$D - B = B(A - 1) - C^2 = e^2 + g^2 + (fg + eh)^2 > 0 \quad (\text{C-28a})$$

and

$$D - A = A(B - 1) - C^2 = f^2 + h^2 + (fg + eh)^2 > 0 . \quad (\text{C-28b})$$

From Eqs. (C-28a) and (C-28b)

$$D > B \quad (\text{C-29a})$$

$$D > A \quad (\text{C-29b})$$

and from the definition Eq. (C-13b), $B > 0$. Hence

$$D > 0 . \quad (\text{C-30})$$

Therefore

$$a > 0 \quad (\text{C-31a})$$

and

$$b > 0 . \quad (\text{C-31b})$$

Since the eigenvalues of a real symmetric matrix are real, the quantity under the square root of Eq. (C-27a) must not be negative. The eigenvalue corresponding to the plus sign in Eq. (C-27a) is obviously positive. If we can show that $ab - k^2 > 0$, this will be sufficient to prove that the other eigenvalue is positive. In this case we would be subtracting from the positive quantity $(a + b)$ another positive quantity that is less than $(a + b)$. Now note that

$$ab - k^2 = \det M = \lambda_t \lambda_w . \quad (C-32)$$

The last form of this equation, which will be useful later, is true because of the invariance of the determinant of M under the rotation of coordinates used to transform Q from its form in (C-22) to that of Eq. (C-24). Substituting from Eq. (C-21) into Eq. (C-32) gives

$$\lambda_t \lambda_w = \frac{D + 1 - A - B}{D \sigma_x \sigma_y} . \quad (C-33)$$

The numerator of this becomes, using Eq. (C-13)

$$D + 1 - A - B = (eh + fg)^2 > 0 . \quad (C-34)$$

Since the denominator of Eq. (C-33) is positive because $D > 0$ (Eq. C-30), the ratio is also positive establishing both that $ab - k^2 > 0$ and that the eigenvalues are positive.

An alternative way to establish that the eigenvalues are positive is to prove that the matrix M is positive definite.^{C.1} This is true if $a > 0$ and if $\det M > 0$ which we showed in the above development.

Equation (C-26) is, therefore, an ellipse; it is convenient to write it as

$$Q = 1 = \lambda_t t^2 + \lambda_w w^2 = \frac{t^2}{\sigma_t^2} + \frac{w^2}{\sigma_w^2} , \quad (C-35)$$

where

$$\sigma_t^2 = \frac{1}{\lambda_t} \quad (C-36a)$$

and

$$\sigma_w^2 = \frac{1}{\lambda_w} . \quad (C-36b)$$

Here σ_t and σ_w are standard deviations of the resultant elliptic-normal distribution.

In terms of the coordinates t and w , Eq. (C-20) takes its standard form (such as the form of Eqs. (C-1) and (C-2))

$$G * F = \frac{1}{2\pi\sigma_t\sigma_w} \exp \left\{ -\frac{1}{2} \left[\frac{t^2}{\sigma_t^2} + \frac{w^2}{\sigma_w^2} \right] \right\} . \quad (C-37)$$

It is also useful to use Eqs. (C-36) and (C-33) in (C-37) to identify the constant for Eq. (C-20) to get

$$G * F = \frac{1}{2\pi\sigma_x\sigma_y} \sqrt{\frac{D+1-A-B}{D}} \exp \left\{ -\frac{1}{2} \left[a\hat{x}^2 + 2k\hat{x}\hat{y} + b\hat{y}^2 \right] \right\} . \quad (C-38)$$

Since the axis t in Figure C-2 lies along the eigenvector of M that corresponds to the eigenvalue λ_t , the angle η is given by

$$\eta = \arctan \left(\frac{\lambda_t - a}{k} \right) \quad (C-39)$$

or

$$\eta = \arctan \left(\frac{k}{\lambda_t - b} \right) .$$

These results are used in Section 5.3.2.

In the important special case where $\theta = 0$, the convolution of elliptic-normal distributions simplifies somewhat. Equations (C-9) give

$$e = \frac{\sigma_x}{\sigma_u} \quad (C-40a)$$

$$f = 0 \quad (C-40b)$$

$$g = 0 \quad (C-40c)$$

$$h = \frac{\sigma_y}{\sigma_v} . \quad (C-40d)$$

Using these in Eqs. (C-13) give

$$A = \frac{\sigma_u^2 + \sigma_x^2}{\sigma_u^2} \quad (C-41a)$$

$$B = \frac{\sigma_v^2 + \sigma_y^2}{\sigma_v^2} \quad (C-41b)$$

$$C = 0 \quad (C-41c)$$

$$D = \frac{(\sigma_u^2 + \sigma_x^2)(\sigma_v^2 + \sigma_y^2)}{\sigma_u^2 \sigma_v^2} . \quad (C-41d)$$

From the fact that $C = 0$ we can already see in Eqs. (C-16) that with the change in integration variables Eqs. (C-14) will simplify so that a simple product of integrals, one for each dimension, is readily obtained. This is what one would expect physically in this case, the problem decouples so that a one-dimensional convolution can be done along each axis separately to effect the two-dimensional convolution. Rather than go back to the integral, we shall interpret this as a special case of the two-dimensional results.

Using Eqs. (C-41) in Eqs. (C-21) gives, with a little algebra,

$$a = \frac{1}{\sigma_u^2 + \sigma_y^2} , \quad (C-42a)$$

$$b = \frac{1}{\sigma_v^2 + \sigma_x^2} , \quad (C-42b)$$

$$k = 0 . \quad (C-42c)$$

The matrix M of Eq. (C-25) is diagonal with $k = 0$ which makes one of the eigenvalues equal to a and the other one equal to b . The case $\lambda = a$ corresponds to the \hat{x} direction as is evident from Eq. (C-22) with $k = 0$ and the other eigenvalue $\lambda = b$ corresponds to the \hat{y} direction. The t and w directions are the same as the \hat{x} and \hat{y} directions (Figure C-2) because $\eta = 0$. Now using Eq. (C-36), we get

$$\sigma_t^2 = \frac{1}{a} = \sigma_u^2 + \sigma_x^2 \quad (C-43a)$$

$$\sigma_w^2 = \frac{1}{b} = \sigma_v^2 + \sigma_y^2 . \quad (C-43b)$$

In the case $\theta = 90^\circ$, the results also simplify in a similar way. It becomes the same as above with $\theta = 0$ simply by interchanging σ_u and σ_v .

Reference

C.1 Ben Noble, Applied Linear Algebra, Prentice-Hall, Inc., 1969.

DISTRIBUTION:

Fernando Delgado
INITEC Padilla 17
Madrid-6, Spain

A. F. Baker
c/o DFVLR
Linder Hohe
5000 Cologne 90, Germany

R. N. Singh
Department of Physics
Indian Institute of Technology
New Delhi-29, India

Dr. Ashok K. Seth
Department of Physics
Centre of Energy Studies
Indian Institute of Technology
Hauz Khas, New Delhi-110029, India

D. Suresh
Dept of Mechanical Engineering
Indian Institute of Science
Bangalore-560012, India

Jose Luis Hidalgo
c/Santiago de Compostela 60
11 C
Madrid-34, Spain

Gershon Grossman
Israel Institute of Technology
Faculty of Mechanical Engineering
Technion City, Haifa 32000, Israel

A. K. Chhabra
BHABHA Atomic Research Center
DESAL, and EFFL, ENGG, DIVN
BARC., Trombay, Bombay-400085, India

Byung Chan Son
KSRI
P. O. Box 333
Da Jun, Coong Nam, Korea

Dr. J. S. Vaishya
National Physical Laboratory
Hill Side Road, New Delhi-12, India

McDonnell Douglas Co.
5310 Bolsa
Huntington Beach, CA 92647
Attn: J. B. Blackman

F. A. Blake
7102 South Franklin St
Littleton, CO 80122

Denver Research Institute
University of Denver
University Park
Denver, CO 80210
Attn: J. Butz

SERI (6)
1536 Cole Boulevard
Golden, CO 80401
Attn: B. Butler
F. Kreith
K. Masterson
A. Robl
K. Touryan
R. Pitts

General Electric ESPD
Building 6, Room 329
Schenectady, NY 12345
Attn: T. Curinga

Black & Veatch Consulting Engineers
P.O. Box 8405
Kansas City, MO 64114
Attn: J. T. Davis

Sanders Associates (2)
MER 12 1214
95 Canal Street
Nashua, NH 03060
Attn: S. B. Davis
N. McHugh

C. T. I. P. International
30 Rockefeller Plaza
New York, NY 10020
Attn: A. Divecchia

General Electric
Building 2, Room 517
Schenectady, NY 12345
Attn: S. Finnigan

Foster Wheeler Development Corp.
12 Peach Tree Hill Road
Livingston, NJ 07039
Attn: G. D. Gupta

Colorado State University
Mechanical Engineering Dept
Ft. Collins, CO 80523
Attn: J. Harris

Martin Marietta
P.O. Box 179
Denver, CO 80201
Attn: W. Hart, Mail Stop S0510

Booz, Allen & Hamilton, Inc.
8801 E. Pleasant Valley Rd
Cleveland, OH 44131
Attn: C. G. Howard

DISTRIBUTION: (cont)

Solar Energy Research Institute (2)
Resource Assessment Branch
1536 Cole Boulevard
Golden, CO 80401
Attn: R. Hulstrom
J. Williamson

Westinghouse Advanced Energy Systems Div (4)
P.O. Box 10864
Pittsburgh, PA 15236
Attn: D. Hofer
W. F. Parker
W. Pierce
C. C. Silverstein

The Singer Company
Corporate R&D Laboratory
286 Eldridge Road
Fairfield, NJ 07006
Attn: W. Kahan

University of Oregon
Dept of Physics
Eugene, OR 97230
Attn: Dr. H. K. Kaehn

General Electric
Building 23, Room 334
Schenectady, NY 12345
Attn: W. F. Knightly

Bechtel National, Inc.
P.O. Box 3965
San Francisco, CA 94110
Attn: R. L. Lessley 301-3

Solar Engineering & Materials Science Div
Engineering Experiment Station
Georgia Institute of Technology
Atlanta, GA 30322
Attn: B. G. Levi

Black & Veatch
P.O. Box 8405
Kansas City, MO 64114
Attn: S. L. Levy

University of Houston
Solar Energy Laboratory
4800 Calhoun
Houston, TX 77004
Attn: F. Lipps

C. L. Lourence
2350 East El Segundo Blvd
P.O. Box 92957
Los Angeles, CA 90009

Energy Management & Control Corporation
634 Harrison Street
Topeka, KN 66603
Attn: L. McQueen

Helio Associates, Inc.
P.O. Box 17960
Tucson, AZ 85731
Attn: D. B. McKenney

Foster-Miller Associates
135 Second Avenue
Waltham, MA 02154
Attn: L. Bystock

General Electric Co.
P.O. Box 8661
Philadelphia, PA 19101
Attn: M. A. Van Horn

General Electric Co.
1 River Road
Schenectady, NY 12345
Attn: R. H. Horton

ITT Research Institute
10 West 35th Street
Chicago, IL 60680
Attn: D. J. Ljubenko

Martin Marietta Aerospace
P.O. Box 179
Denver, CO 80201
Attn: G. A. Roe

McDonnell Douglas Astronautics Company
5301 Bolsa Avenue
Huntington Beach, CA 92647
Attn: J. R. Campbell

Northrup, Inc. (2)
302 Nichols Drive
Hutchins, TX 75141
Attn: J. L. Northrup
J. H. McDowell, Jr.

Schumacher & Associates, Inc.
2550 Fair Oaks Blvd
Suite 120
Sacramento, CA 95825
Attn: J. G. Schumacher

Solaramics
1301 East El Segundo Blvd
El Segundo, CA 90245
Attn: H. E. Felix

Sun Power Corporation
55 Miller Street
Fairfield, CT 06430
Attn: C. L. Whiteford

DISTRIBUTION: (cont)

University of Houston
Houston, TX 77004
Attn: L. Vant-Hull

BDM Corporation
Library
7915 Jones Branch Drive
McLean, VA 22101
Attn: M. Minster

Martin Marietta (3)
P.O. Box 179
Denver, CO 80201
Attn: J. Montague, Mail Stop S0403
P. Norris, Mail Stop S0403
T. Oliver, Main Stop S0403

New Mexico State University
Dept of Mechanical Engg
Box 3450
Las Cruces, NM 81803
Attn: G. P. Mulholland

General Electric Co.
Space Division
Room 7246 CC&F 7
P.O. Box 8555
Philadelphia, PA 19101
Attn: A. J. Poche

Jet Propulsion Laboratory
4800 Oak Grove Drive
Pasadena, CA 91103
Attn: P. Poon, Mail Stop 125-140

Oak Ridge National Laboratory
4500-S; B-248
P.O. Box X
Oak Ridge, TN 37830
Attn: Dr. A. S. Ray

University of Pennsylvania
Dept of Mechanical Engg
Philadelphia, PA 19171
Attn: G. L. Schrenk

ANCO Engineers, Inc.
1701 Colorado Avenue
Santa Monica, CA 90404
Attn: Dr. B. Taylor

Dynatherm Corporation
One Industry Lane
Cockeysville, MD 21030
Attn: D. Wolfe

Gruman Energy Systems
4175 Veterand Memorial Highway
Ronkonkona, NY 11779
Attn: G. Yenatchi

Acurex Corporation
485 Clyde Avenue
Mountain View, CA 94042
Attn: D. R. McCullough

E-Systems
P.O. Box 6118
Dallas, TX 75222
Attn: C. Y. Reeves

Beckman Instruments, Inc.
Advanced Technology Operations
1630 S. State College Blvd
Anaheim, CA 92806
Attn: S. C. Guenther

Boeing Engineering & Const.
P.O. Box 3707
Seattle, WA 98124
Attn: E. J. Valley

Busche Energy Systems
7288 Murdy Circle
Huntington Beach, CA 92647
Attn: K. Busche

FMC Corporation
Engineered System Div
328 Brokaw Road
Box 450
Santa Clara, CA 95052
Attn: D. G. Curphey

Ford Corporation
Ford Aerospace & Communications
3939 Fabian Way
Palo Alto, CA 94303
Attn: T. L. Fitch

1127 D. J. Kuehl
1521 J. L. Mortley
1537 N. R. Keltner
1550 F. W. Neilson
1552 B. D. Hansche
1556 E. A. Igel
1556 R. L. Hughes
3151 B. J. Tolman
4200 G. Yonas
4230 M. Cowan
4231 J. H. Renken
4231 F. Biggs (25)

DISTRIBUTION: (cont)

4231	C. N. Vittitoe	(25)	4725	J. A. Leonard	
4700	J. H. Scott		5133	K. W. Mitchell	
4713	B. W. Marshall		5512	A. C. Ratzel	
4713	R. D. Aden		5512	J. C. Dunn	
4713	D. E. Arvizu		5512	R. J. Gross	
4713	J. E. Clark		5524	J. R. Koteras	
4713	D. B. Davis		5842	R. B. Pettit	
4713	R. M. Edgar		5844	R. E. Allred	
4713	J. T. Holmes		5844	F. P. Gerstle, Jr.	
4713	D. L. King		8122	W. R. Delameter	
4713	L. K. Matthews	(25)	8326	E. D. Eason	
4713	W. L. McAttee		8326	P. J. Eicker	
4713	J. E. Myers		8326	M. J. Fish	
4713	D. R. Porter		8326	J. D. Hankins	
4713	D. L. Risvold		8420	C. S. Selvage	
4713	L. O. Seamons		8450	D. N. Tanner	
4713	J. M. Stomp		8450	R. C. Wayne	
4716	H. M. Dodd		8451	T. D. Brumleve	
4719	E. C. Boes		8451	T. A. Dellin	
4719	D. G. Schueler		8451	C. L. Mavis	
4719	B. D. Shafer		8451	C. J. Pignolet	
4720	V. L. Dugan		8451	W. G. Wilson	
4721	J. V. Otts		8452	A. C. Skinrood	
4722	J. F. Banas		8453	J. D. Gilson	
4722	R. W. Harrigan		8266	E. A. Aas	
4722	G. W. Treadwell		3141	T. L. Werner	(5)
4722	J. C. Zimmerman		3151	W. L. Garner	(3)
4722	E. L. Harley				for DOE/TIC (Unlimited Release)
4723	R. R. Peters				DOE/TIC (25)
4723	W. P. Schimmel				(R. P. Campbell, 3172-3)